UiT The Arctic University of Norway

Faculty of Health Sciences

The Tumor Immune Microenvironment as a Regulator of Oral Cancer Progression

Kjersti Sellæg

A dissertation for the degree of Philosophiae Doctor (PhD)   September 2024

The Tumor Immune Microenvironment as a Regulator of Oral Cancer Progression

Kjersti Sellæg

A dissertation for the degree of Philosophiae Doctor

Table of Contents

Acknowledgements

I would first like to express my sincere gratitude to my main supervisor, Associate Professor Synnøve Norvoll Magnussen. Your office door has always been open to me for any questions I may have had during this process, or just a chat. I will look back on those student-supervisor moments with joy. I am deeply thankful for your time, encouragement, help, and patience these past five years. Although I may not have fully appreciated it in the moment, you have challenged me to articulate my thoughts and draw conclusions. There is no question that you have played a significant role in raising me as an independent researcher. Your curiosity and drive are contagious, and I admire your eager to constantly grow, as a supervisor, researcher, and lecturer. You have a special ability to dive deep into the details of your work, which is also reflected in your almost molecular approach to gardening. I am grateful that you saw the potential in me for this project.

I would also like to thank my co-supervisors Associate Professor Gerd Berge, and Associate Professor II/Dr. Anna M. Wirsing. Gerd, you have a refreshing and a bit untraditional approach to academia. You have taught me that research is not only about the results, but also about the process and our mindset. You have provided valuable insights into my project with your detailed knowledge in immunology and you have pushed me to look at the bigger picture. You have a special gift of making people feel seen and I have appreciated our talks in your office. Anna, you are a force of nature, and you have a capacity like no other. Despite your busy schedule, you always made time to supervise my project, even in Teams meetings with a baby on your lap. I also want to thank Professor Elin Hadler-Olsen for her key insights and helpful advice during revisions of the papers included in this thesis.

I want to give a huge thanks to everyone that has been a part of the Tumor Biology Research Group (TBRG) these past five years. I am really proud of where we are as a team, and the effort we put into continuously improving ourselves. To the members of TBRG, you have made it enjoyable to go to work every day, even during the Covid lockdown where we "met" on Teams for morning coffee, and even if (or I should say when), the seagulls woke me up in the middle of the night. I know I haven't let this go by in silence, as with most things. When I look back at the time that has passed since I first came to Tromsø on a dark and stormy winter evening (literally), it feels like I really grew up here, and I know that I have been exactly where I was supposed to be. Therefore, I am glad to have the opportunity to stay for a little while longer.

I want mention a few that has been extra special to me throughout this journey: May-Britt, my "work-wife". We have shared many cups of coffee, though less snobby than what you have at home, laughs, frustrations, and gossip. You are one of the most organized persons I know, and my main motivation on leg-days (slay). Thank you for keeping me humble. Susannah, my dear friend and office mate. You and Ingar have invited me into your circle and introduced me to bouldering, fancy wines, and new friends. Susannah, you have taught me to be a better listener, and you are someone who always shows up. I don't take that for granted. Beate, I've had so much fun with you in the lab and on our many hikes. You always have a smile on your face and a genuinely caring spirit. I would also like to

Abstract

Oral squamous cell carcinoma (OSCC) is a global public health challenge, and according to the EU mission: Cancer (European Cancer Information System) the burden is estimated to increase over the next two decades, especially in younger people. The immune system plays a key role in the progression of solid malignancies and patients with tumors densely infiltrated with T lymphocytes show better clinical outcomes and enhanced responses to immunotherapy. The specialized lymphocyte-recruiting tumor vasculature, termed tumor-associated high endothelial venules (TA-HEVs), express the lymphocyte homing ligand PNAd and permits the entry of lymphocytes into the tumor. The presence of TA-HEVs has been associated with an inflamed tumor microenvironment and improved patient prognosis in OSCC. The main goal of this thesis is to gain a better understanding of TA-HEV development in OSCC of the tongue (OTSCC) and their interaction with the surrounding microenvironment. To determine the prognostic value of TA-HEVs as an independent marker or in combination with immunosuppressive cell types, we scored the density of TA-HEVs, regulatory T cells (Tregs) and tumor-associated macrophages (TAMs) in 126 OTSCC tumors. A high density of TA-HEVs combined with a low density of FoxP3+ regulatory Tregs (Treg) identified patients with superior five-year survival, while patients with a low TA-HEV and high FoxP3 score had particularly low five-year survival. FoxP3+ Tregs were an independent prognosticator in OTSCC. We used a carcinogen-induced mouse tumor model to characterize the spatial distribution and density of HEVs and the lymphocytic infiltrate during oral carcinogenesis. The presence of HEVs and lymphocytes corresponded with the site and severity of oral epithelial lesions, but only HEVs increased significantly in SCC compared to non-malignant lesions. Organized lymphoid structures, termed tertiary lymphoid structures (TLS) did not develop in the carcinogen-exposed mice. To analyze the regulation of HEVs in the tumor microenvironment, we analyzed the co-localization of PNAd with the PNAd synthesizing enzyme GlcNAc6ST-2 in mouse and human OTSCC and assessed the influence of the surrounding environment at the cellular-, protein-, and gene levels. A subset of TA-HEVs in OTSCC lacked GlcNAc6ST-2 protein- or mRNA expression. GlcNAc6ST-2 expression in TA-HEVs did not correlate with the density of cells surrounding the HEVs, but the absence of T cells in immune deficient mice precluded the formation of TA-HEVs. Human OTSCC tumors enriched in proteins involved in inflammatory processes favored the presence of TA-HEVs, while cell culture conditions had little effects on HEV-related genes. Our findings support the involvement of TA-HEVs in OTSCC progression and GlcNAc6ST-2 might serve as a potential marker for refining patient prognosis. A deeper understanding of the role of GlcNAc6ST-2 may enable targeted manipulation of

HEVs in solid tumors and offer new therapeutic strategies. We hypothesize that the interaction between TA-HEVs and the OTSCC microenvironment, leading to downregulation of GlcNAc6ST-2 and PNAd, possibly leading to impaired lymphocyte recruitment to the TME.

List of papers

This thesis is based on the following papers:

Paper I   Abdulsalam, I.A., Sellæg, K., Benebo, F.O., Ojei, N.C., Hegge, B., Steigen, S.E, Uhlin-Hansen, L., Bjerkli, I.H., Wirsing, A.M., Norvoll Magnussen, S., Hadler-Olsen, E. **FoxP3+ regulatory T cells were independent predictors of disease-free survival in oral tongue squamous cell carcinoma whereas tumour-associated CD163+ macrophages and -high endothelial venules were not**. *Manuscript.*

Paper II   Sellæg, K., Schwienbacher, R., Kranz, M., Engan Aamodt, A., Wirsing, A.M., Berge, G., Hadler-Olsen, E. & Norvoll Magnussen, S. (2024). **4-nitroquinoline 1-oxide-induced oral epithelial lesions exhibit time- and stage-dependent changes in the tumor immune microenvironment.** *Frontiers in Oncology, 14.* https://doi.org.10.3398/fonc.2024.1343839

Paper III   Sellæg, K., McLaren Berge, A.K., Knutsen, E., Five, MB., Hadler-Olsen, E., Norvoll Magnussen, S. **Tumor-associated high endothelial venules in oral squamous cell carcinoma can be distinguished by Chst4 expression**. *Manuscript.*

Abbreviations

CCL	C-C motif ligand
CXCL	C-X-C motif ligand
CD	Cluster of differentiation
DC	Dendritic cell
DSS	Disease-specific survival
FFPE	Formalin-fixed, paraffin embedded
GlcNAc6ST	N- acetylglucosamine-6-O-sulfotransferase
HEV	High endothelial venule
ICAM-1	Intercellular cell adhesion molecule 1
IHC/IF	Immunohistochemistry/immunofluorescence
LIGHT	Homologous to **L**ymphotoxin, exhibits **I**nducible expression and competes with Herpes Simplex virus **G**lycoprotein D for **H**erpes virus entry mediator, a receptor expressed by **T** cells
LTα1β2	Lymphotoxin alpha 1 beta 2
LTβR	Lymphotoxin beta receptor
MECA-79	Mouse endothelial cell antigen 79
MAdCAM-1	Mucosal addressin cell adhesion molecule 1
OPMD	Oral potentially malignant disorder
OSCC	Oral squamous cell carcinoma
OTSCC	Oral tongue squamous cell carcinoma
PNAd	Peripheral node addressin
PET	Positron emission tomography
SLO	Secondary lymphoid organ
TAM	Tumor-associated macrophage
TIL	Tumor-infiltrating lymphocyte
TLS	Tertiary lymphoid structure
TME	Tumor microenvironment
TNFα	Tumor necrosis factor alpha
TNFR	Tumor necrosis factor receptor
Treg	Regulatory T cell
VCAM-1	Vascular cell adhesion molecule 1
4NQO	4-nitroquinoline 1-oxide
6 sulfo sLeX	6 sulfo sialyl Lewis

1 Introduction

1.1 Oral squamous cell carcinoma

Most malignancies arising in the head and neck region are oral squamous cell carcinomas (OSCC) (1). OSCC originates from the stratified squamous cell lining of the oral cavity, which together with the underlying lamina propria forms the oral mucosa (2). The anatomical subsites that define the oral cavity are the hard palate, the gingiva and alveolar ridge, the inside of the lips and cheeks, the mobile tongue, the floor of the mouth, and the retromolar trigone (3, 4) (Fig.1). The mobile tongue is the most common site of OSCC, accounting for approximately half of all cases (3, 5). Early tumor invasion and lymph node metastasis is associated with increased morbidity and mortality in OSCC patients. OSCCs are aggressive in nature due to their anatomical location within the oral cavity, where invasion into neighboring structures and metastatic spread to lymph nodes in the head and neck region frequently occur (6, 7).
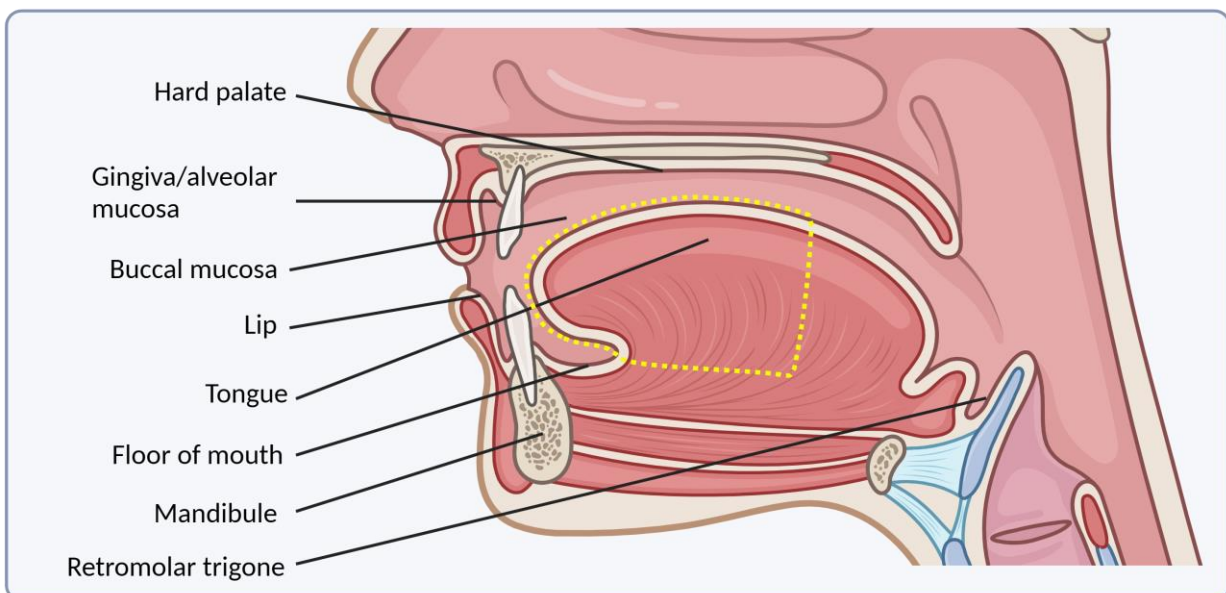
Figure 1. Anatomical location of oral squamous cell carcinoma. OSCC develop from the oral mucosa that lines the inside of the lips and cheeks (bucca), the gingiva and alveolar ridge in the upper and lower gum, hard palate in the anterior roof of the oral cavity, mobile part of the tongue (yellow dotted line), floor of the mouth, and the area posterior to the molars termed the retromolar trigone. Created with BioRender.

The papers included in this thesis are primarily based on analyses of tissue from patients with OSCC of the mobile tongue (OTSCC) (**Paper I and III**) and mouse tongue tissue (**Paper II and III**). As will be discussed later in this introduction, the etiology and risk factors for oral cavity cancers differ from other cancers of the head and neck. We chose to focus on OTSCC due to its high prevalence among oral cavity cancers, as well as concentrating on a single subsite allows for the study of cancers with potentially less biological heterogeneity. Because most of the literature on oral cancer does not

distinguish between OSCC subsites, the introduction will address OSCC in general unless sublocations are specified.

1.1.1 Epidemiology and survival

According to the latest report by the Global Cancer Observatory, the annual incidence of lip and oral cavity cancers was estimated to be nearly 390 000 cases, representing 2.1% of all new cancer cases (8). About half (48.3%) of these patients are predicted to die from the disease (8). Oral cancer affects over twice as many men than women and most cases of OSCC occur in people aged 50 and older (9). As with most human solid cancers, the risk of developing OSCC increases with age, however, a rising trend is seen in the younger people (10). The highest incidence rates of OSCC are found in South Central Asian and Oceanian countries, such as India, Pakistan, and Papua New Guinea (11). The high frequency of oral cavity cancers in these countries is mainly linked to the exposure to risk factors (discussed in section 1.1.2), which also causes the high incidence of OSCC seen in some Western and Eastern European countries (11). Incidence rates of oral cancers have stabilized and begun to decrease in many countries over the past twenty years, likely reflecting increased efforts to prevent and reduce risk factor exposure (9, 12). In the Norwegian population the incidence has shown an increasing trend since the early 2000s, however, it is encouraging that the survival rates follow a similar tendency (13). The global OSCC survival rates have remained stable over the past two decades at about 50% (8, 14) and the global burden of OSCC is estimated to increase with nearly 40% until 2040 along with a rise in mortality (15). Hence, OSCC is an ongoing challenge to the global public health.

1.1.2 Risk factors

Regular use of tobacco and alcohol are the most important risk factors for developing OSCC, and especially the combination of heavy alcohol consumption and smoking significantly increases the risk for OSCC development (16). Smokeless tobacco products, such as toombak, chewing tobacco and the Scandinavian wet snuff (snus) has also been linked to an increased risk of developing OSCC (17, 18). However, the potential of smokeless tobacco to cause cancer in humans is a subject of debate (19-21). The practice of chewing betel quid, which typically contains a mix of areca nut, betel leaf, slaked lime and tobacco leaves (22), is common in South and Southeast Asia and is associated with the particularly high incidence of oral cancers in this region (23). Infection with high-risk Human Papilloma virus (HPV) subtypes 16 and 18, which are associated with cancers in the oropharynx and cervix (24), have been reported in OSCC patients but is generally uncommon (25-28). Epstein-Barr virus (EBV) DNA have also been detected in OSCC tissue and is strongly implicated in

carcinogenesis in lymphomas, nasopharyngeal- and gastric cancers (25, 29, 30). However, the role of EBV in OSCC development is not clear. Discrepancies in viral infection status in OSCC is likely due to studies combining cancers of the oral cavity with other subsites of the head and neck a causative role of viral infections is established. Cancers of the lips are often grouped with oral cavity cancers (8). However, because lip cancers can originate from the skin in perioral areas of the face and may be caused by ultraviolet (UV) radiation, the etiology differs from that of OSCC. The risk of developing OSCC has also been linked to poor oral hygiene and oral microbes (31, 32).

The ethanol metabolite acetaldehyde and tobacco-specific nitrosamines and aromatic compounds are considered the primary components involved in alcohol- and tobacco-induced carcinogenesis (33, 34). Acetaldehyde has been shown to be cytotoxic and mutagenic and can accumulate in the oral cavity after heavy alcohol consumption (33). Alcoholic beverages can have a dehydrating effect on the oral mucosa and damage the outer layer of the epithelium, which disrupts its barrier function and can promote cell proliferation and mutagenesis (35). Hence, alcohol might act as a promoter and increase the risk of exposure to damaging substances found in tobacco. Nitrosamines, polycyclic carbons, and aromatic amines in tobacco can bind to DNA and cause DNA adducts that in turn leads to mutations and dysregulation of oncogenic or tumor-suppressor pathways (15, 22). In **Paper II**, we used the synthetic progenitor carcinogen 4-nitroquinoline 1-oxide (4NQO) to induce oral carcinogenesis in mice (36). Like tobacco carcinogens, 4NQO metabolites can cause DNA adducts, as well as induce DNA-damaging reactive oxygen species (37), that induces similar histological changes and genetic alterations in mice as those observed in human OSCC (38, 39).

1.1.3 Histopathology and clinical features

OSCC develops from normal epithelium through the accumulation of genetic alterations, which over time can result in malignant transformation of the epithelial cells (40). The molecular landscape of OSCCs is generally heterogenous and display a range of somatic mutations (41, 42). Mutations in the tumor suppressor gene TP53 is found in nearly 80% of HPV-negative OTSCCs, and epidermal growth factor receptor (EGFR) overexpression is found in nearly 60% of OSCCs (40, 42). Altered expression of other genes and pathways, such as CDKN2A, p16, PIK3CA, CCND1, and FAT1 have also been indicated as drivers of oral carcinogenesis (40, 42). A gradual transition of normal tissue is evident in a series of increasingly severe histopathological changes, ranging from different grades of oral epithelial dysplasia to development of invasive OSCC. Clinical signs of altered epithelium that can progress into cancer are red (erythroplakia) or white (leukoplakia) areas of the oral mucosa. Leukoplakia is the most common type of oral potentially malignant diseases (OPMD) and is generally

asymptomatic (43). The malignant potential of OPMDs is determined by the histological diagnosis (44). Oral epithelial dysplasia is graded as mild, moderate, or severe based on the extent of architectural changes in the epithelial layers and the presence of atypic cytological features (45). Due to variable reproducibility and subjectivity in grading of dysplasia, the three-tier system can be supplemented with a binary grading into low- and high-risk dysplasia, in which the latter combines moderate- and high-grade dysplasia (46). A higher dysplasia grade is believed to have a higher potential for malignant transformation, but the risk stratification of OPMDs is not well defined (44). Indeed, most OPMDs do not develop into cancer and dysplasias can regress without intervention.

Invasive OSCC is established once malignant cells have invaded into the underlying tissue beyond the basal membrane. Tumor cells can invade into the tissue in different ways, presenting as a delineated pushing border, strings of tumor cells penetrating the surrounding tissue or small clusters of tumor cells (47). Macroscopically, OSCCs appear as flat (endocytic) or elevated (exophytic) growths that can present with non-healing wounds and ulceration (48). As the tumor progresses, more severe symptoms such as pain and bleeding may appear and depending on the tumor site, patients can experience loosening of teeth and difficulties with chewing and swallowing. OSCCs frequently metastasize to draining lymph nodes in the head and neck, which is often detected as a lump on the neck on the same side (ipsilateral) or both sides of the neck (contralateral) (48). About 40% of the patients present with lymph node metastasis at the time of diagnosis, which is critically linked to an adverse prognosis (7). Metastasis to other organs is a dismal prognosis, though less common (49).

Compared to other malignancies, OSCC patients are highly prone to developing second primary tumors (50). This phenomenon is explained as field cancerization, which refers to areas with genetically altered cells near the primary tumor that can give rise to new primary tumors (51, 52). Other second tumors can arise from residual cancer cells after surgical removal of a primary tumor and is referred to as local recurrence.

1.1.4 Prognostic factors

The main prognostic tool in OSCC is the TNM classification system, which uses the size and depth of invasion (DOI) of the primary tumor (T), the extent of spread to regional lymph nodes (N), and presence of distant metastasis (M) to determine the disease stage (Table 1) (4). DOI of the primary tumor and extranodal extension, the latter referring to the spread of metastatic cells outside the lymph node capsule, was first introduced in the current 8th TNM edition (53). TNM stage ranges from stage I-IV and is strongly associated with patient prognosis. Early-stage OSCC (stage I-II) typically confer

a better prognosis compared to more advanced disease (stage III-V), but clinical outcomes and treatment responses may vary even among patients with same-stage tumors (3, 54, 55).

Table 1. Eighth edition of the TNM classification of malignant tumors of the oral cavity (4).

Primary tumor	
T1	Size ≤2cm, DOI ≤5mm
T2	Size ≤2cm, DOI 5-10mm, or size >2-4cm, DOI ≤10mm
T3	Size >4cm or DOI >10mm
T4a/b	Tumor invades adjacent structures subclassified as (a) moderately- and (b) advanced local disease
Regional lymph node metastasis	
N0	No regional lymph node involvement
N1	Ipsilateral, single ≤3cm and no extranodal extension
N2a/b/c	(a) Ipsilateral, single >3-6cm, (b) Ipsilateral, multiple ≤6cm, or (c) bilateral, ≤6cm and no extranodal extension
N3	>6cm and no extranodal extension, or any N with extranodal extension
Distant metastasis	
M0	No distant metastasis
M1	Distant metastasis
Stage group	
Stage I	T1, N0, M0
Stage II	T2, N0, M0
Stage III	T3, N0, M0, or T1-T3, N1, M0
Stage IVA/B/C	Any T4, Any N2-N3, M1

Grading of OSCC differentiation is often used in addition to the TNM system to predict patient outcome (WHO Classification of Head and Neck tumors (48, 56). Tumors are graded as well, moderate, or poor, based on the degree to which the cancer cells resemble normal epithelial cells (48). Most OSCCs display well or moderate differentiation (5). Poorly differentiated tumors are considered the most adverse, however, a strong correlation between differentiation grade and clinical outcomes in OSCC patients is lacking (54, 57).

Histological parameters describing interactions between the tumor and the host tissue has shown promise for risk stratification of OSCC patients, such as tumor invasion patterns, vascular and neural invasion, and infiltrating lymphocytes (47, 55, 58). Tumor budding refers to the presence of single

cells or small clusters of cells within the stroma at the invading tumor front and has been associated with poor prognosis (54, 59, 60). According to the worst pattern of invasion (WPOI) grading, larger clusters of invading cancer cells also indicate high-risk invasive patterns and are associated with poor clinical outcomes (61). The prognostic value of a multifactorial histopathological risk-assessment score including WPOI, perineural invasion, and lymphocytic infiltrate has also been proposed but produced varying results across studies (47, 54, 62). Recently, immune biomarkers have shown independent effects on OSCC patient survival. Tumors with a prominent lymphocytic infiltrate, and particularly high densities of T cells expressing cluster of differentiation (CD)3, CD8, and CD4, are associated with favorable patient outcomes (63-67). OSCC patients with tumors nearly devoid of immune cells have poor prognosis (68). The presence of other immune cell types, such as natural killer (NK) cells, macrophages, and regulatory T cells (Tregs) has also been shown to predict patient prognosis in OSCC (66, 69-71).

Many potential biomarkers have been explored to identify OSCC patients at higher risk of adverse disease, but none of them have been implemented into clinical routine. The clinical application of histological parameters is often limited by poor inter-operator reproducibility, and the TNM classification system can only be used to assess the anatomical extent of the disease. Other prognostic markers that better describes the tumor-host relationship in the TME could be valuable for guiding clinical decisions in combination with TNM staging and histological features.

1.1.5 Treatment and treatment-related side effects

The primary choice of treatment for OSCC is surgery when the tumor is not metastasized, while locally advanced and advanced-stage disease is often treated with surgery combined with adjuvant radiotherapy with or without chemotherapy (72). Neoadjuvant radiation or radio-chemotherapy is sometimes used to shrink large tumors before surgery. In some patients with advanced-stage disease, standard treatment can be combined with targeted approaches, including inhibitors of oncogenic pathways and immunotherapy (73, 74). Side-effects related to OSCC treatment can severely impact the patients' quality of life and may include impaired speech, swallowing, and chewing after oral surgery, as well as facial deformation and dental health problems (75). Complications after radiotherapy can include inflammation and painful ulcers of the oral mucosa, which may lead to an increased susceptibility to oral infections (76). Irradiation of salivary glands and bone can also have debilitating effects, causing mouth dryness and problems with eating, and irreversible bone necrosis (osteoradionecrosis), respectively (77). Physical treatment-related side effects can influence the

patients' psychological health and social interactions (78), which may lead to isolation, anxiety, and depression.

Besides the patient's health status and individual desires, the treatment of OSCC is largely determined by the clinical, pathological, and radiological findings that form the basis for the TNM staging (79). Tissue biopsies and clinical examination of the primary site is used to set the diagnosis of a suspected malignancy in the oral cavity, determine the extent of the tumor once verified, as well as assessing operability. Different imaging techniques can be used to assess the primary tumor size and DOI and to determine lymph node involvement. This includes ultrasound, computed tomography (CT), and magnetic resonance imaging (MRI) for anatomical imaging, and functional positron emission tomography (PET) imaging which enables the detection of metabolically active cells by using radioactive tracers (79).

1.2 Tumor microenvironment

From the earliest systematic descriptions in the late 19th century, solid tumors were regarded as masses of cells that acquired properties that enable uncontrolled growth (80). Consequently, cancer research was initially focused on the genetic alterations within the malignant cells which were believed to be sufficient for cancers to develop (81). Over time, it became evident that tumor cells could be affected by the local tissue microenvironment. The concept of the tumor microenvironment (TME) as an active player in tumor progression is now widely recognized and constitute the interactions between the cancer cells, non-cancerous resident and recruited cells, the soluble molecules produced by these cells, and the extracellular matrix ECM) (82) (Fig.2).

Due to the increased demand for energy and biomass in the growing tumor, the TME features altered physiological conditions, such as low oxygen levels (hypoxia) in the tumor center, low pH and high interstitial pressure. Alterations in metabolic pathways are also common in tumors, including increased glucose uptake and altered fatty acid metabolism (82).
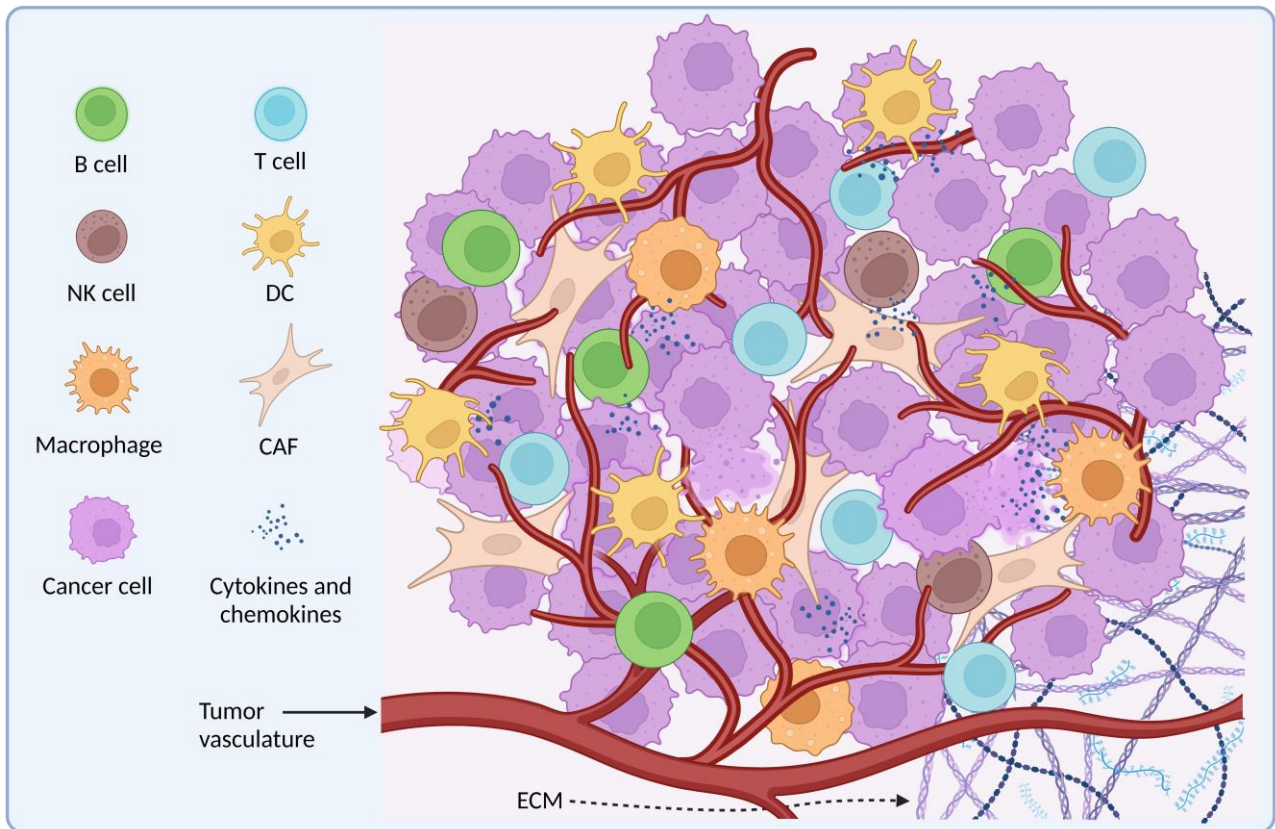
Figure 2. Components of the tumor microenvironment. The major components that form the tumor microenvironment (TME) in solid tumors are the cancer cells, cancer-associated fibroblasts (CAFs), innate and adaptive immune cells, cytokines and chemokines (secreted or surface expressed), and the tumor vasculature, all embedded within an extracellular matrix (ECM). Inspired by Zhang, J., and Veeramachaneni, N. (83). Created with BioRender.

Cancer-associated fibroblasts (CAFs) are an abundant cell type in the tumor stroma and share similarities with normal fibroblasts during wound healing and inflammation (84). Fibroblasts are essential for tissue repair and regeneration, but remodeling of the tumor stroma by CAFs can promote the survival and invasion of tumor cells (85, 86). CAFs can also stimulate the formation of new blood vessels, known as angiogenesis (87, 88). Other major cell types in the TME includes various types of immune cells and the endothelial cells forming the tumor vasculature and lymphatics. The following sections will focus on tumor-infiltrating immune cells, their organization within the TME, and the specialized tumor vasculature mediating immune cell recruitment.

1.2.1 Tumor-infiltrating immune cells

The cells of the immune system are tailored to protect the host from pathogens and harmful substances from the outside environment, as well as eliminating abnormal cells within the host that are recognized as non-self. Due to the potential damaging effects of an ongoing immune response to the affected tissue, the immune response needs to be tightly regulated. In the cancer setting, the TME

comprise immune cells with tumor-suppressive and tumor-promoting properties, the so-called tumor immune microenvironment

1.2.2 Anti-tumor immunity

Mutations or dysregulated genes within tumor cells result in the production of abnormal or inappropriately expressed proteins, often referred to as neoantigens or tumor antigens (89). Tumor antigens are captured at the tumor site by antigen-presenting cells specialized in processing of intracellular antigen, such as dendritic cells (DCs). The DCs migrate to the draining lymph node via the lymphatic system and present processed antigen on major histocompatibility complex (MHC) molecules, MHC I and/or MHC II, to naïve CD8+ and CD4+ T cells, respectively (90). This interaction leads to the priming and activation of antigen-specific T cells. The CD4 T helper 1 (Th1) subset provides the necessary co-stimulatory signals for activation of CD8+ cytotoxic T lymphocytes which then undergo clonal proliferation (91). The cytotoxic T cells leave the lymph node and enter the tumor where they recognize and eliminate cancer cells expressing the specific antigen on MHC I by perforin/granzyme-mediated lysis or induction of apoptosis via Fas-Fas ligand (FasL) interaction (92). Tumor-infiltrating CD8+ T cells are the most important host-protective cells against cancer.

CD4+ T cells are typically abundant in solid tumors and are important for driving and enhancing cytotoxic CD8+ T cell responses (93). CD4+ T cells can differentiate into various subtypes with diverse functions in the TME, such as interleukin (IL)-17 expressing Th17 cells and FoxP3+ regulatory T cells (Tregs) (94, 95). Tumor-reactive CD4+ T cells with cytotoxic activity have also been found in murine tumors (96-98). In the lymph node, CD4+ T helper 2 cells are important for activation of humoral immunity mediated by B cells. Once activated, B cells undergo clonal expansion within lymphoid follicles and mature within newly formed germinal centers (GCs). Selection of high-affinity B cells takes place in the GCs and is assisted by CD4+ T follicular helper cells (Tfh) and follicular DCs (FDC) (99). This process leads to the generation of antibody-producing plasma cells (100). Antibodies coating the surface of tumor cells can lead to the elimination of cancer cells by phagocytosis or release of cytotoxic granules by innate immune cells, such as macrophages, neutrophils and natural killer (NK) cells (101). The role of tumor-infiltrating B cells is not well defined. However, their presence in the TME seems to favor anti-tumor responses and inflammation (102-104), and they are often aggregated with T cells in lymphoid follicle-like structures (discussed in more detail in section 1.4) (105).

In addition to their phagocytic activity, cells of the innate immune system are crucial for the activation of adaptive immunity. Classically activated tumor-associated macrophages (TAMs), known as M1 TAMs, mediate recruitment of DCs to the tumor site, aiding in the initiation and acceleration of anti-

tumor immune responses. Antigen-presentation and release of proinflammatory cytokines by M1 TAMs also promotes T cell function within the TME (106).

1.2.3 Tumor promoting immunity

Suppression of the anti-tumor immune response by regulatory immune cells promotes tumor immune evasion and progression. CD4+FoxP3+ Tregs are key players in maintaining self-tolerance and dampening of immune responses (107). Maintaining tolerance is especially important in the oral cavity, which is inhabited by commensal microbes and is constantly exposed to allergens and foreign substances from food and the external environment (108). By expressing the inhibitory receptor Cytotoxic T lymphocyte-associated antigen (CTLA-4), which competes with antigen-presenting cells (APCs) for binding co-stimulatory ligands on T cells, Tregs can hinder the activation of tumor-reactive T cells (109). Release of anti-inflammatory cytokines, such as IL-10, IL-15, and TGFβ, can also inhibit effector T cell functions (110, 111). Within the TME, the release of cytokines by CD4+ Th2 cells, granulocytes and tumor cells, such as IL-4, IL-13, colony stimulating factor (CSF) and TGFβ, can drive the polarization of M1 macrophages to M2 TAMs with immunosuppressive functions (112-115). Similar to Tregs, M2 macrophages can induce T cell dysfunction by producing suppressive cytokines. Hypoxic conditions within the TME also promotes M2 TAMs (116). Other tumor-promoting cell types in the TME, such as regulatory B cells (Bregs) and myeloid-derived suppressive cells (MDSCs) have been identified in human cancers (117, 118) and have been shown support the induction of Tregs from resting CD4+ T cells (117, 119) and/or exert inhibitory activity to T cells (120-123).

The dynamic nature of the TME is evident in the changes that occur over time – at early stages of tumor development, the microenvironment is tumor suppressive, while in late-stage tumors the microenvironment tends to promote tumor progression (124). The pressure of the anti-tumor immune system at early stages drives the adaptation and selection of cancer cells that can escape recognition, which is further promoted by immunosuppressive cells. Effective ways for cancer cells to evade elimination is to downregulate MHC I and upregulate inhibitory molecules, such as the programmed death ligand 1 (PD-L1) (125). Binding of PD-L1 on the cancer cells with its receptor PD-1 on T cells causes T cell dysfunction. Upregulation of FasL by the tumor cells can also induce apoptosis in tumor-reactive T cells carrying the Fas receptor (126). The entry and migration of tumor-reactive lymphocytes into the tumor can also be restricted by the tumor vasculature and stroma (125).

1.3 Tertiary lymphoid structures

In some tumors, TILs can be found in organized immune aggregates known as tertiary lymphoid structures (TLSs) (127) (Fig.3). TLSs share many morphological and functional features with lymphoid follicles in secondary lymphoid organs (SLOs), particularly lymph nodes, and consist of a B cell follicle surrounded by a T cell zone. FDCs and mature DCs are typically found within the B- and T cell zone, respectively, and a specialized type of post-capillary venules termed high-endothelial venules (HEVs) are found in the vicinity of the TLS (105) (Fig.3). In contrast to lymph nodes, which develop embryonically and mature during the postnatal period (128), TLSs are inducible and develop in tissues affected by chronic inflammation, including autoimmune diseases, infection, transplant (allograft) rejection, and solid malignancies (105). TLSs are generally associated with increased severity in inflammatory conditions (129), while the presence of TLS has been identified as a positive prognosticator in various cancer types, including OSCC (130-134).
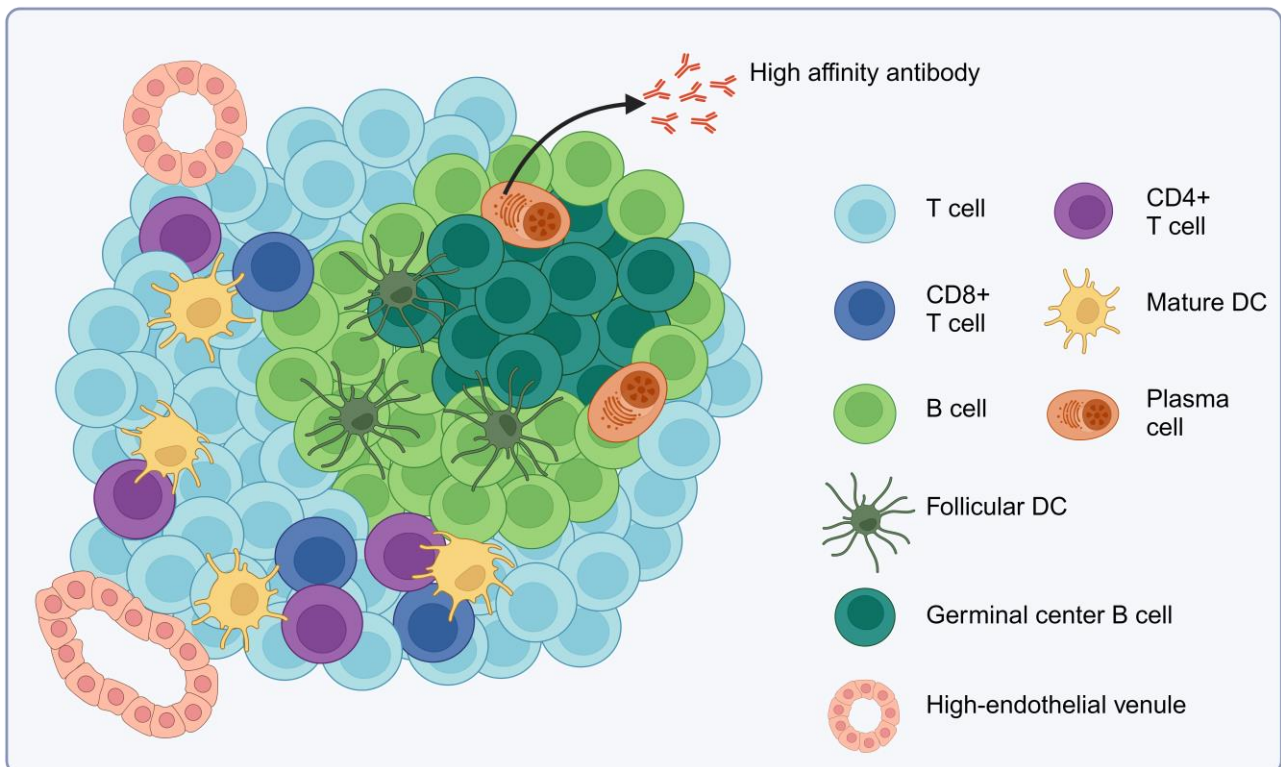
Figure 3. Schematic representation of tertiary lymphoid structure. Mature tertiary lymphoid structures (TLS) are formed in non-lymphoid tissues following prolonged antigen exposure. TLSs are organized into clusters of T and B cells, along with mature and follicular dendritic cells (DCs), and resemble lymphoid follicles found in lymph nodes. High endothelial venules (HEVs) are found in the periphery of the TLS. TLSs facilitate the activation of CD4+ and CD8+ effector T cells, and the maturation and differentiation of B cells within germinal centers, leading to the generation of high affinity antibodies by plasma cells and memory B cells. Inspired by Fridman et al. (105). Created with Biorender.

Accumulating evidence suggest that TLSs serve as local sites for activation of humoral and cell-mediated immunity (105). TLSs likely facilitate the interaction between naïve or memory T cells with antigen-presenting DCs (135). Because TLSs lack a capsule separating them from the surrounding tissue, they might also be exposed to unprocessed antigens (127). Most B cells in the TME are confined to TLSs (105) wherein they have been shown to express the transcription factor B cell lymphoma 6 (BCL-6) (131, 136) and the enzyme (activation-induced) cytidine deaminase (137), which are important for GC formation and generation of high affinity antibodies, respectively (138-140). Activated CD4+, CD8+, and tumor reactive CD8+ T cells have also been identified within TLSs (141-144), suggesting that the TLSs can facilitate antigen-specific immune responses independently of SLOs at the tumor site. However, the development and function of TLS in cancers is not fully understood. For instance, different areas of the tumor might have different susceptibilities for TLS formation as TLSs are more frequently found in the tumor-periphery and/or invasive front in different cancers (ref). Furthermore, the composition of TLSs differ depending on the degree of maturation (105) and some tumors lack or have low numbers of TLSs (131, 145), suggesting that some tumors might harbor a TME that is insufficient or restrictive for TLS development.

1.4 Tumor vasculature

Angiogenesis is a hallmark of cancer and describes the formation of new blood vessels from the preexisting capillary network at the tumor site (82). Angiogenesis is crucial for the growth and survival of tumor cells by providing oxygen and nutrients while removing metabolic waste products. Tumors can also obtain sufficient blood supply by other means, such as growing along existing blood vessels, a concept known as vessel co-option (146), or by vascular mimicry in which the tumor cells trans-differentiate and assume endothelial-like properties (147). Vascular endothelial growth factor A (VEGF-A) is the most important angiogenic stimulant, which upon binding to VEGF receptors (VEGFR) 1 and 2 on endothelial cells triggers their proliferation and organization into vascular tube structures (148). In their normal state, endothelial cells display little to no proliferative activity and are one of the most quiescent cells of the body (149). In response to the increasing need for new blood vessels in a growing tumor, angiogenesis is accelerated by the upregulation of VEGF-A and other pro-angiogenic factors by various cells in the TME, including tumor cells, macrophages and neutrophils (150). Hypoxia also triggers angiogenesis via hypoxia-inducible factor 1 (HIF1) - mediated upregulation of VEGF-A and VEGFR2 (151, 152).

The resulting new vasculature is often leaky and disorganized, which causes increased interstitial pressure within the tumor and worsen the hypoxia due to poor diffusion (148). The abnormal tumor vasculature itself and the resulting conditions within the TME favors tumor progression and presents challenges to effective cancer therapy. For instance, tumor endothelial cells can inhibit the function of tumor-infiltrating T cells by upregulating PD-L1 and FasL (125). Tumor endothelial cells also become anergic and display reduced expression of cytokines, chemokines, and adhesion molecules that are important for the recruitment of immune cells to the tumor site (153). Hence, reducing the efficacy of immunotherapies aimed at boosting the patients' anti-tumor immune response.

1.5 High endothelial venules

High endothelial venules were first described in the late 1890s in the lymph node of macaques by their unique morphology, featuring irregularly shaped, plump and cuboidal high endothelial cells (HECs) (154) (Fig.4A). The characteristic morphology of these venules distinguishes them from the flat endothelium found in blood- and lymphatic vessels although they share some pan-endothelial markers such as CD31 and vascular endothelial (VE)-cadherin (155). HEVs are post-capillary venules present in most SLOs, including lymph nodes, tonsils, and Peyer's patches (PPs), as well as less discretely defined lymphoid aggregates associated with mucosal surfaces in the gut, bronchus, and nasopharynx (156). HEVs serve a specialized role in facilitating the entry of circulating naïve and memory lymphocytes into these tissues. This occurs through a multistep process mediated by chemokines, adhesion molecules, and lymphocyte-homing ligands that are expressed on the HEV endothelium (157). HEVs in various SLOs differ in their expression of lymphocyte homing ligands (158). Among these, the HEVs in peripheral lymph nodes (pLNs) are the most widely studied.

1.5.1 HEV development and function in lymph nodes

HEV development is initiated at the fetal stage and is critically dependent on the interaction between stromal lymphoid tissue organizer (LTo) and -inducer (LTi) cells. LTi cells are attracted to the developing lymph node by resident LTo cells and engage the lymphotoxin (LT) beta receptor (LTβR) on the LTo cells through the ligand LTα1β2 (159). This interaction leads to the secretion of lymphoid chemokines such as C-C motif ligand (CCL)19, CCL21, C-X-C motif ligand (CXCL)12 and CXCL13, and expression of adhesion molecules, including mucosal addressin cell adhesion molecule 1 (MAdCAM-1), intercellular- and vascular cell adhesion molecule 1 (ICAM-1 and VCAM-1, respectively) (156). In turn this trigger the aggregation of the LTo and LTi cells into organized clusters, which form the basis of the T and B cell zones in the mature lymph node, concomitant with development of the lymph node vasculature, including HEVs (160).

A defining feature of fully differentiated LN-HEVs is the expression of Peripheral node addressin (PNAd). PNAd is expressed at low levels in LN-HEVs after the first 24 hours in newborn mice, and its expression increases significantly at 2-7 days postpartum (158, 161). *In utero*, murine LN-HEVs are detected by MAdCAM-1. Until two weeks after birth LN-HEVs are double-positive for MAdCAM-1 and PNAd, after which MAdCAM-1 expression starts to decrease. pLN-HEVs in adult mice predominantly express PNAd while HEVs in mesenteric lymph nodes retain high expression of both MAdCAM-1 and PNAd (158). HEVs in Peyer's patches are unique in that they mostly express MAdCAM-1. PNAd is critical for the function of LN-HEVs and serves as a ligand for L-selectin, the homing receptor expressed by lymphocytes (Fig.4B) (162).

PNAd describes a set of glycoproteins on the HEV surface, often termed HEV sialomucins, that are decorated with O- and N-glycans containing the terminal modification 6-sulfo sialyl Lewis X (6 sulfo sLeX) (Fig.4C) (157). 6 sulfo sLeX is comprised of four covalently linked monosaccharides with a sulfate group on the N-acetylglucosamine (Fig.4C) (163, 164). PNAd is detected by antibodies against the Mouse Endothelial Cell Antigen (MECA-79) epitope (Fig.4C) and have been identified on several HEV sialomucins, such as CD34, GlyCAM-1 (rodent only, pseudogene in humans), endomucin, nepmucin, podocalyxin, and MAdCAM-1 (157, 165). Post-translational glycosylation of HEV sialomucins is dependent on the catalytic activity of several Golgi glycosyltransferases (166). The terminal 6 sulfo sLeX is catalyzed by sialyltransferases (167), fucosyltransferases (168), and N-acetylglucosamine-6-O-sulfotransferases (GlcNAc6ST) (169, 170) (171, 172). Sulfation by GlcNAc6ST-1 and -2 enzymes, encoded by *Chst2* and *Chst4*, respectively, is crucial for the generation of PNAd in HEVs (171, 172).
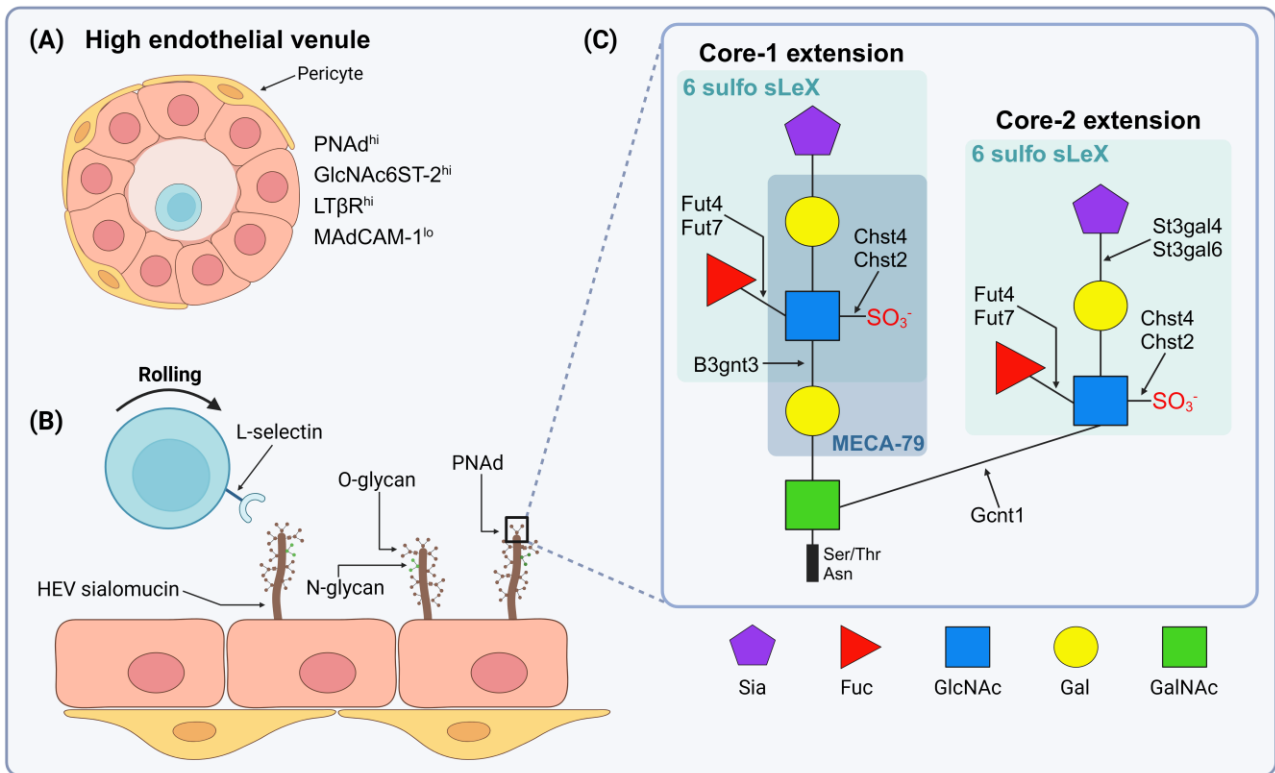
Figure 4. **(A)** High endothelial venules (HEVs) are composed of characteristic plump and cuboidal endothelial cells ensheathed with pericytes. In peripheral lymph nodes (pLNs), fully differentiated HEVs express the specific marker Peripheral Node Addressin (PNAd) which distinguishes them from other blood- and lymphatic vessels in the lymph node. Homeostatic LN-HEVs also express relatively high levels of N-acetylglucosamine-6-sulfotransferase 2 (GlcNAc6ST-2), lymphotoxin beta receptor (LTβR) and low levels of Mucosal vascular addressin cell adhesion molecule 1 (MAdCAM-1) (173). **(B)** PNAd describes a set of glycosylated proteins with a mucin-like domain, termed HEV sialomucins, that carry a specific terminal glycan modification. Interaction between PNAd and the lymphocyte homing receptor L-selectin mediates lymphocyte tethering and rolling along the HEV lumen and is the initial step in the multicascade process of lymphocyte extravasation (diapedesis) **(C)**. The structural determinant within PNAd is the 6 sulfo sialyl Lewis X moiety (6 sulfo sLeX), which is composed of N-acetylglucosamine (GlcNAc) with a sulfate group at the carbon in position 6, fucose (Fuc), and sialic acid (Sia). Catalytic activity of specific Golgi glycosyltransferases is important for the synthesis of 6 sulfo sLeX, and includes a2,3-sialyltransferases (*St3gal4* and *St3gal6*), a1,2-fucosyltransferases (*Fut4* and *Fut7*), N-acetylglucosamine-6-O-sulfotransferases (GlcNAc6ST) 1 and 2 (*Chst2* and *Chst4*). 6 sulfo sLeX is present in the extended core-1 and core-2 of biantennary O- and N-linked glycans that attaches to HEV sialomucins via serine/threonine (Ser/Thr) or asparagine (Asn) residues, respectively. The Mouse endothelial cell antigen (MECA) 79 epitope overlaps with 6 sulfo sLeX in the core-1 extension. Inspired by Blanchard, L. and Girard J.P (154), Rodriguez et al. (174), and Menzel et al. (175). Created with BioRender.

Homing of lymphocytes to the lymph node parenchyma is initiated by the interaction between PNAd and L-selectin causing the lymphocytes to tether and roll along the luminal surface of the HEV wall. Luminal expression of chemokines CCL19, CCL21, CXCL12, and CXCL13 is required for the lymphocytes to stick to the HEV wall via their cognate receptors, while firm adhesion is mediated by binding of ICAM-1 to the lymphocyte function-associated antigen 1 (LFA1) integrin on lymphocytes (154). Conformational activation of LFA-1 is induced by chemokine signaling and shear forces (176).

The lymphocytes then crawl along the HEV surface and transmigrate through the HEV endothelium via specific exit ramps (177). Compared to the tight junctions in other blood vessels, HEVs display discontinuous junctions allowing paracellular migration (178, 179). Transmigration of lymphocytes through HEV endothelial cells have also been observed (177). While PNAd expressed on the HEV lumen mediate lymphocyte tethering and rolling, the role of PNAd expressed on the abluminal side of LN-HEVs is not fully understood but appear to be involved in the migration of lymphocytes after they have entered the lymph node (177).

1.5.2 HEVs in cancer

PNAd-expressing vessels with a similar phenotype to LN-HEVs have been found in various human solid tumors (180, 181), including OSCC (182-186). Compared to classical tumor angiogenesis that promotes tumor growth, the formation of TA-HEVs has been associated with tumor regression in cancer patients and in mice (187-190). The role of HEVs within the TME is believed to be similar to their function in SLOs. In patient tumors, the presence of TA-HEVs is associated with increased numbers of TILs and they are often found within dense lymphocytic infiltrates, sometimes organized into TLS (180, 186, 191-193). A recent systematic review and meta-analysis comprising 1933 cancer patients found that TA-HEV positive tumors was correlated with prolonged overall- and disease-free survival, while negatively associated with lymph node- and distant metastasis (181). OSCC patients with TA-HEV positive tumors have also been shown to have longer survival than those with TA-HEV negative tumors (186), and the presence of TA-HEVs correlated with increased numbers of T and B cells (194). Yoshida et al. found that TA-HEVs in OSCC tumors were closely associated with CD4+ and CD8+ T cells, which also adhered to the TA-HEV lumen (182), supporting that TA-HEVs recruit lymphocytes into OSCCs. Furthermore, TA-HEVs in murine tumors have been shown to mediate lymphocyte rolling *in vivo*(195). The function of TA-HEVs in human cancers inevitably rely on correlative findings from tissue samples and remains unclear.

In contrast to the reported survival benefit of TA-HEVs in OSCC patients, Lee. et al found that the presence of dilated, flat-walled HEVs in tumor-draining lymph nodes in OTSCC patients was associated with an unfavorable prognosis (185). Similar HEV phenotypes have been observed in the lymph node of tumor-bearing mice and correlated with reduced lymphocyte adhesion to the HEV wall (196, 197). This suggests that HEVs might serve as a gateway for disseminated tumor cells and play a role in OTSCC metastasis.

TA-HEVs have been found more frequently in early-stage tumors (T1/T2) than advanced tumors (T3-T4) in OSCC patients (182, 186). Among late-stage tumors, Wirsing et al. found that two thirds lacked

TA-HEVs (186). They also found that the phenotype of TA-HEV varied based on the surrounding inflammation; in less inflamed areas of the tumor, TA-HEVs often had a flat vessel wall with patchy PNAd expression and a dilated lumen, while in highly inflamed regions they more closely resembled differentiated HEVs in lymph nodes. Heterogenous PNAd expression in TA-HEVs have also been reported in melanoma and breast cancer tissues (145, 188). This suggest that factors within the TME might influence the phenotype of TA-HEVs, which differs at different stages of tumor progression.

The regulation of TA-HEV development in cancer is not fully understood but appears to depend on some similar cues as HEVs in lymph nodes. Positioned in the paracortex and cortical-paracortical junction in the lymph node, HEVs are closely associated with lymphocytes, DCs, and a supportive network of fibroblastic reticular cells (FRCs) (178). Signaling from their surroundings is important for maintaining a differentiated HEV phenotype, especially DCs which produce the ligands LTα1β2 and LIGHT engaging the LTβR on the HEVs (198-203). Disruption of this signaling leads to dedifferentiation of the LN-HEV vasculature (175, 198, 204). A similar remodeling of LN-HEVs occur in response to inflammation and infection, whereby the HEVs temporarily loses their characteristic morphology and downregulate PNAd (173, 205). While DCs appear to be redundant for TA-HEV development (206), signaling via the LTβR has been shown to be important for TA-HEV induction in various mouse tumors (195, 207-211). Others have also proposed a role for the TNF receptor in TA-HEV formation (174, 206, 212). The primary sources of key ligands for LTβR or TNFR-mediated induction of TA-HEVs in tumors are not well defined but seems to involve tumor-infiltrating immune cells (206, 207, 212).

The mechanisms that drive the formation of TA-HEVs are not fully understood and it remains unclear how the TME permits or restricts TA-HEV development and stability during tumor progression. A deeper understanding of TA-HEV neogenesis could identify potential targets and permit the development of strategies aimed at inducing TA-HEVs, potentially improving anti-tumor responses and outcomes in cancer patients.

2 Aims

The overall aim of this project was to gain a better understanding of TA-HEV development and how their interaction with the surrounding tumor microenvironment shapes their phenotype. To study this, we used human OTSCC tissues with corresponding clinical data, mouse models of OTSCC and endothelial cells in culture. Specifically, we wanted to:

1) Determine whether TA-HEVs are independent positive prognosticators in human OTSCC and assess their prognostic value in combination with immunosuppressive Tregs and TAMs (**Paper I**).
2) Characterize the lymphocytic infiltrate and HEVs in the 4NQO mouse model of oral carcinogenesis (**Paper II**).
3) Analyze the development and regulation of HEVs in the tumor microenvironment using the established 4NQO mouse model and human OTSCC tissues **(Paper III)**.

3 Results – Summary of Papers

Paper I – FoxP3+ Regulatory T cells were independent predictors of disease-free survival in oral tongue squamous cell carcinoma whereas tumor-associated CD163+ macrophages and -high endothelial venules were not.

Manuscript
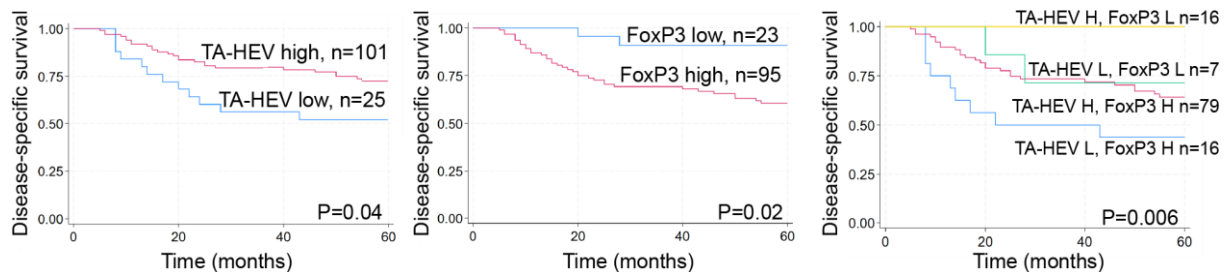
A high TA-HEV score was associated with improved survival in OTSCC patients, while a high FoxP3 score conferred poor prognosis. The combination of a high TA-HEV- and low FoxP3 score identified patients with superior five-year disease-specific survival.

In **Paper I**, we wanted to assess the prognostic value of TA-HEVs in OTSCC as an individual marker, and in combination with immunosuppressive TAMs and Tregs. We performed immunohistochemical staining for PNAd, CD163, and FoxP3 of tumor tissue from 126 OTCC patients. The number of cells or vessels were counted within five hot-spot areas in each tumor section and a low and high score was generated for each of the markers using the first quintile (20%) and the second through fifth quintile (80%) as a cut-off for low and high score, respectively. We analyzed the correlation between the score (high versus low) for each of the markers with clinicopathological parameters and found that a high FoxP3 score was significantly associated with larger tumors (T3) and a higher five-year DSS rate than FoxP3 low tumors. The five-year DSS rate for patients with TA-HEV high tumors was significantly lower than for those with TA-HEV low tumors. CD163 score was not associated with OTSCC prognosis in this cohort. A high density of FoxP3+ cells was significantly, and independently, associated with an increased risk of disease-specific death, suggesting applicability as a prognostic biomarker in OTSCC patients. TA-HEV high tumors were associated with significantly longer five-year DSS in univariate analysis but not as an independent factor. The combination of a high TA-HEV and low FoxP3 score identified patients that did not experience death during the five years after diagnosis. Conversely, low TA-HEV- and high FoxP3 scores was associated with particularly poor prognosis. In conclusion, FoxP3 score had an independent effect on OTSCC prognosis, and a combined assessment of TA-HEVs and FoxP3+ Tregs could effectively stratify patients with particularly good or poor prognosis.

Paper II – 4-Nitroquinoline 1-oxide-induced oral epithelial lesions exhibit time- and stage-dependent changes in the tumor immune microenvironment.

Published
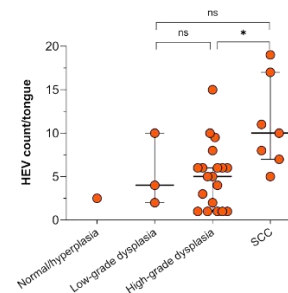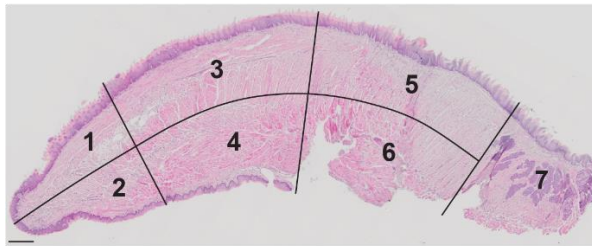
Whole-slide images of the tongues were divided into seven sectors representing different sublocations, which were assessed for the density of HEVs and lymphocytes. HEVs were present in tongues presenting with normal/hyperplastic epithelium, dysplastic lesions and SCC.

In **Paper II**, we aimed to characterize the quantity and distribution of HEVs and the lymphocytic infiltrate in different stages of oral carcinogenesis in the 4NQO mouse model. The 4NQO carcinogen was administered in the drinking water of immunocompetent mice for 16 weeks and animals were sacrificed at different timepoints during a 12-week follow-up period. Immunohistochemistry was performed on consecutive serial sections of the tongue to detect the immune cell markers CD4, CD8, FoxP3 and B220, and the HEV-specific marker PNAd. We used a novel approach to evaluate the presence of each of the markers in epithelial lesions located in different areas of the tongue presenting with different histological grades. 4NQO exposure induced epithelial lesions of varying severity on the tongue, including low-grade dysplasia, high-grade dysplasia and SCC. The density of lymphocytes and HEVs increased with time after 4NQO-exposure and the distribution corresponded to the site of epithelial lesions, but only HEVs increased significantly in SCC compared to non-malignant stages. TLSs did not develop at any time point. We used PET/MRI to evaluate its applicability to identify epithelial lesions on the tongue and lymph node metastasis. PET/MRI imaging showed active uptake of [F18]-FDG in the tongue of four 4NQO-exposed mice, and the presence of epithelial lesions was verified by IHC. Strong PET-signal in the lymph nodes was due to reactive changes, suggesting that more tumor-specific radiotracers are needed to discriminate between reactive lymph nodes and metastasis. To conclude, HEVs formed independently of TLS during both non-malignant and malignant stages of 4NQO-induced oral carcinogenesis and was accompanied by infiltrating lymphocytes.

Paper III – Tumor-associated high endothelial venules in oral squamous cell carcinoma can be distinguished by Chst4 expression.

Manuscript
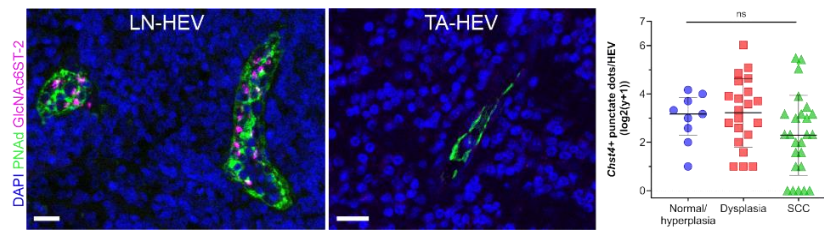
The expression of GlcNAc6ST-2 and PNAd was less abundant in TA-HEVs in human OTSCC than in normal LN-HEVs, and a subset of HEVs associated with SCC in 4NQO-exposed mice lacked expression of GlcNAc6ST-2 mRNA.

In **Paper III**, we hypothesized that the OTSCC microenvironment affects the TA-HEV phenotype, leading to reduced expression of PNAd and the key enzyme GlcNAc6ST-2 and possibly impaired TA-HEV function. We investigated the protein- and gene expression of GlcNAc6ST-2 (gene *Chst4*) in TA-HEVs in human OTSCC and in HEVs associated with oral epithelial lesions using IF or IF combined with RNAScope. We found that the expression of GlcNAc6ST-2 and PNAd was lower in TA-HEVs in human OTSCCs than normal human lymph node, a subset of TA-HEVs lacked GlcNAc6ST-2 expression. The expression of *Chst4* was absent in some HEVs associated with SCCs. Using the number of DAPI+ cells/μm^2 as an estimate of the general immune infiltrate surrounding TA-HEVs in human OTSCC, we found no association between the cell density and GlcNAc6ST-2 expression in. Transplanted tongue tumors in T cell-deficient mice lacked TA-HEVs entirely, whereas the density of CD11c+ cells did not seem to influence either the presence of HEVs or their PNAd expression level. The expression of *Fut4, Chst2* and *B3gnt3* was significantly upregulated in endothelial cells seeded on Matrigel compared to monolayer, while the expression of *Chst4, Fut7,* and *Gcnt1* could not be detected in any of the tested conditions. Proteomics analysis of 79 human OTSCC specimens revealed that HEV-high tumors were preferentially enriched in proteins associated with inflammatory processes and adaptive immunity. In conclusion, the expression of GlcNAc6ST-2 and PNAd distinguishes LN-HEVs from TA-HEVs. GlcNAc6ST-2/*Chst4* expression also differentiate between two TA-HEVs phenotypes in mouse and human OTSCC. TA-HEV formation rely on adaptive immune responses, particularly T cells.

4 Discussion

4.1 Methodological considerations

4.1.1 Patients

Since the mobile tongue is the most common site for oral cavity cancers and has a distinct etiology compared to other cancers of the head and neck, such as oropharyngeal cancers linked to HPV infection, this thesis focuses on OTSCC. Concentrating on a homogeneous patient cohort can potentially minimize the contribution of biological variability from various intraoral locations.

The OTSCC patients in **Paper I** and **Paper III** were derived from a large retrospective study, The Norwegian Oral Cancer Study (NOROC), comprising a total of 535 OSCC patients diagnosed in the period 2005-2009 at one of the four university hospitals in Norway (3). Out of the 535 OSCC patients, 240 were diagnosed with OTSCC. All patients were followed up for at least five years after the end of treatment and concluded on June 1st, 2015. Only patients with histologically verified OTSCC that had not been formerly diagnosed with, or treated for, cancers of the head and neck region were included, and only when sufficient clinical data and tissue material was available. Patients who received pre-operative or palliative treatment was excluded. This resulted in 126 and 79 eligible treatment-naïve OTSCC patients for the analyses in **Paper I** and **Paper III,** respectively. Clinical data were collected from the patients' hospital records, pathology reports, and the Norwegian Cause of Death Registry, and FFPE tissue was obtained from the archives of the Clinical Pathology departments at the different institutions. Bjerkli et al. previously demonstrated that the NOROC study cohort corresponded well with other epidemiological studies on OSCC in Europe and other western countries (3). Because patients that received palliative care were excluded from the cohorts in **Paper I** and **III**, the proportion of patients with advanced disease (stage III-IV) was lower than in the original NOROC study. Consequently, the patients in **Paper I** had longer five-year DSS compared to the NOROC cohort (70% versus 52%). Hence, the results from **Paper I** and **Paper II** might better reflect OTSCC patients with early-stage disease (stage I-II).

To be able to compare and interpret results from different studies, it is important that the clinical and histopathological parameters are standardized and up to date. As such, the TNM classification of the patients included in **Paper I** and **III** was revised according to the newest edition (4). A limitation frequently encountered with retrospective studies is that the patient data and biological material is collected for other purposes and often lacks the standardization and quality required for research. For instance, some clinical parameters were missing in some OTSCC patients in the selected cohorts in our study, leading to their exclusion from statistical analysis which might negatively affect the

statistical power and precision of our results. Patient-reported parameters, such as alcohol consumption and smoking, often carry some uncertainty because the patients might want to underestimate unhealthy habits to please the physician, or they may be reluctant to share personal information (213). Patient tissue is a valuable and limited source of information in medical research. Since NOROC is a multi-center study and includes several sub-projects, FFPE tissue was not available from all OTSCC patients or in sufficient amounts. This resulted in fewer eligible patients in **paper III** than in **paper I**.

The ethical principles outlined in The Declaration of Helsinki is considered the main framework for human research ethics (214). The principles state that the research involving human subjects and material should address relevant needs of the study group and contribute to improved health of the participants, including new knowledge that can improve clinical practices and outcomes. It is also clearly stated that the researchers and institutions must protect the subject's privacy, confidentiality, integrity, and autonomy. Human research also follows national and international legal requirements and should only be conducted by qualified personnel with appropriate training in scientific methods and ethics. In adherence to this, the previously collected patient data from electronic health reports was anonymized and the study was reviewed to The Regional Committee for Medical and Health Research of Northern Norway (REK Nord) which granted approval for the study at all four hospitals (Protocol number REK Nord: 2013/1786 and 2015/1381). All the patients that were still alive when the data was collected were informed about the study in an information-consent letter approved by REK Nord and were given the option to participate or not at any time without reprisal. Reclassification from the 6th to the 8th edition of the TNM system was performed by experienced pathologists, and experiments and analyses were performed by trained operators or operators under training with supervision. To ensure complete and transparent reporting of our findings, the study in **Paper I** broadly adhered to the REMARK guidelines (215).

OTSCC patients represent a small group of cancer patients in Norway that receive little public attention compared to other cancer types such as breast and prostate cancer, as well as other tobacco-associated cancers of the upper and lower airways. This patient group is particularly vulnerable because many patients suffer from stigmatizing treatment-related side effects and should be shielded from unnecessary burden. However, in accordance with The Declaration of Helsinki, it is stressed that the medical and scientific communities have an obligation to ensure to ensure equal opportunities for underrepresented groups to participate in research (214).

4.1.2 Animal models of oral cancer

One of the aims of this thesis was to characterize HEV development and the lymphocytic infiltrate during oral carcinogenesis, to ultimately study the regulation of HEVs in OTSCC. For this purpose, we chose to use the 4NQO mouse model which is a widely used model to study oral cancer (216). Although animal models can never perfectly replicate human biology or disease, 4NQO exposure has been shown to induce histological changes and mutation signatures resembling tobacco-associated human OSCC (39), including mutated p53, increased expression of EGFR, and decreased expression of p16 (39, 217). The 4NQO model enables the study of oral carcinogenesis from initiation to established SCC in mice with a functional immune system, which was essential for studying infiltrating lymphocytes and HEVs. We chose to administer 4NQO in the drinking water *ad libitum*, as this approach requires less handling of the animals compared to topical application. Although painting of the tongue with carcinogen could possibly induce more localized changes in the tongue and less exposure to the digestive tract, this method requires more handling of the animals and several rounds of application.

Various other chemical carcinogens belonging to the class of polycyclic aromatic hydrocarbons or nitrosamines have also been used to induce oral cancer in mice, including methyl-cholanthrene (MCA), 7,12-Dimethylbenz[a]anthracene (DMBA), and N'-nitrosonornicotine (NNN) (216, 218). Combining 4NQO with arecoline, a compound extracted from betel nut, or ethanol, have been shown to increase the tumor burden in mice and might better represent carcinogenesis in alcohol drinkers and betel quid users (219, 220).

Other methods for establishing *in vivo* models of oral cancer includes genetic engineering and transplanted tumor cells or tissues (221). Transplanting of murine oral carcinoma cells into genetically identical recipients (syngeneic), or transplanting cancer cells or -tissues from donors with other genetic backgrounds or species (xenograft), enables rapid tumor establishment, consistent tumor growth, and lower variation compared to spontaneous models. Syngeneic models can be used to study the interplay between the tumor and the host immune response, while xenograft models requires that the recipient has a defective immune response to prevent transplant rejection. However, as shown in **Paper III**, where human OSCC cells were orthotopically transplanted into the tongues of athymic Balb/c nude mice, transplanted models can be used to investigate how the absence of specific immune components influences the tumor microenvironment. An advantage of orthotopic transplantation is that it more accurately replicates the interactions between oral cancer cells and the tissue in the specific anatomical location compared to transplantation into other sites such as the flank (216). However, intra-oral injections require more extensive handling and can cause more stress to

the animals, and due to the small size of the oral cavity the tumor cannot grow to unlimited size. In general, the nature of transplanted models limits their application in early stages of oral carcinogenesis and lack a naturally formed tumor microenvironment

Mice genetically engineered to express oncogenes, lack tumor-suppressor genes, or carry mutated versions of such genes, can drive the formation of oral cancer (221). The use of genetically engineered mouse models (GEMMs) for oral cancer allows spontaneous tumor development in immunocompetent mice, either gradually throughout the animals' life or in adult mice. For instance, targeted expression of mutated *Kras* or *P53* in the oral epithelium has been achieved by inserting the gene in the promoter region of keratin 5 (gene *Krt5*) or keratin 14 (gene *Krt14*) (222, 223). Keratins 5 and 14 are highly expressed in oral epithelium and these transgene mice develop invasive SCC in the tongue (221). However, because expression of keratin 5 and keratin 14 is not restricted to epithelium in the oral cavity, these mice also develop tumors in the esophagus, skin, and forestomach. Due to the low specificity and high mortality from the effects of gene editing, GEMMs are not suitable for studying invasive OSCC. Furthermore, the tumorigenesis in these mice is driven by intentional mutations rather than accumulating genetic alterations, and GEMMs might fail to trigger strong immune responses due to a lack of tumor antigens (224). 4NQO-exposure can be combined with GEMMs to induce more specific OSCC through the deletion or overexpression of specific genes (221).

In **Paper II** and **III** we used the C57Bl/6 and Balb/c mouse strains, which are widely used genetic backgrounds in cancer and immunology research. It is important to be aware that the choice of genetic background can influence tumor development and progression in preclinical studies. Indeed, it has been shown that different mouse strains have varying susceptibility to tumor development and immune responses can differ due to natural mutations. For instance, heterozygous *p53* mutations induces breast carcinomas in Balb/c but not in C57Bl/6 mice, and while the C57Bl/6 strain favors T cell-mediated immunity, Balb/c mice exhibit more pronounced B cell responses (225, 226). The gender of the animals can also influence tumor growth rate, and female mice were shown to be more prone to lung carcinomas and more severe disease than male mice (227).

The use of *in vivo* models has provided unprecedented insights into biological processes and disease mechanisms and is an important preclinical study platform. The use of animals for research purposes is regulated by national legislation to protect the welfare of the animals and ensure that animal experiments are conducted in an ethical and humane manner. The animal study in **Paper II** was approved by The Norwegian Food Safety Authority and adhere to European Union (EU) legislation

on animal research. The EU Animal Welfare Act and The Norwegian Consensus Platform for the Replacement, Reduction, and Refinement of Animal Experiments (NORECOPA) both promote the implementation of three 3'Rs principle. The 3'Rs encourages researchers to replace animal experiments with alternative methods whenever possible, reduce the number of animals to the minimum needed for a meaningful output, and refine experimental procedures to enhance animal welfare and minimize suffering.

4.1.3 Histological assessment of mouse tongue tissue

Once we had established that HEVs developed in 4NQO-exposed mice, we aimed to map the location and quantity of HEVs and lymphocytes associated with epithelial lesions on the tongues. To assess the most severe histology in the tongue as a whole, the tongues were cut through the midline to give sagittal sections displaying the tongue from tip to base. Two sagittal tongue sections from each of the animals were H&E stained: one from the medial part of the tongue and one from a more lateral part (approximately 80µm apart). With this approach, we might have overlooked epithelial lesions on the outermost lateral surface of the tongue, which is a common site for OTSCC in humans (228). Since we only assessed the histology in tissue sections from one half of the tongue there is the possibility that the other half could contain lesions with more severe histology. To get a more extensive overview of the histology of the tongue tissues we could have sectioned it all the way through. However, this is labor-intensive. Furthermore, since the mice develop lesions at different timepoints, often several with varying histological grade, the histology in individual mice and across studies will likely differ depending on when the animals are sacrificed. Overall, our study reports similar frequency of histological grade as previous studies (38, 229, 230), suggesting that our study sufficiently represents the extent of 4NQO-induced disease.

Because the mice developed multiple lesions, some appearing contiguous or located adjacent to each other, we chose to divide the tongues into seven sectors. Each sector represents different sublocations in the tongue to give a more detailed overview of the spatial distribution of the lesions and the associated immune infiltrate. We modified the approach used in a study by Vered et al. on Wistar rats (231), where sagittal tongue sections were separated into anterior, middle, and posterior thirds. The anterior and middle sectors represented the mobile tongue, while the posterior section represented the tongue base which is considered an oropharyngeal site. To better replicate human OTSCC, we could have used this approach, but we chose to keep the lingual salivary glands in the posterior tongue within a separate sector because we were interested in studying the salivary glands for other purposes.

4.1.4 Staining of mouse and human tissue

Staining of fixed and paraffin embedded tissue with different techniques is the primary method used in all three papers in this thesis and includes immunohistochemistry (IHC), immunofluorescence (IF), and fluorescence in situ hybridization (FISH). Formalin-fixed, paraffin-embedded (FFPE) tissue is widely used in clinical pathology because it allows for long-term storage and preserves the tissue structure and morphology. This enables the assessment of histology and spatial distribution of markers. Formalin fixation causes protein cross-linking, which helps preserve the tissue but might also alter protein structures and lead to reduced antibody recognition. Zinc-based fixation is a non-carcinogenic alternative to formalin that better preserves the antigenicity (232). Storing of fixed tissue in tissue blocks also preserves antigenicity better than storing pre-sectioned tissue for extended periods (233). For **Paper I** and **III**, we used human tissue that was collected at different hospitals, where differences in preanalytical procedures can introduce variability in downstream analysis. However, most Norwegian hospital laboratories operate with standardized protocols, and some are accredited with International Organization for Standardization (ISO) certification to ensure consistently high quality and reliability of test results.

4.1.4.1 Immunohistochemistry and immunofluorescence

IHC and IF were used in this thesis because they are relatively simple and cost-effective methods and enables the detection of markers in intact tissues. IHC is the most frequently used method to screen for biomarkers and requires inexpensive equipment. IHC offers direct visualization of the results, and the chromogen precipitate remains stable over time without significant loss of signal (234). For IF, antibodies are conjugated with fluorophores and detection requires the sample to be illuminated with specific light sources that emits light at appropriate wavelengths to excite the fluorophores. While IF offers higher sensitivity, resolution and multiplexing, some additional considerations need to be addressed for IF compared to IHC, including autofluorescence, photobleaching, and excitation spectra.

Different chromogens are available for IHC that produce different colors after enzymatic reactions with horseradish peroxidase (HRP) and enables detection of several targets in the same sample. In **Paper III**, we used a dual IHC protocol for staining of PNAd+ HEVs and CD11c+ cells in mouse tongue tissues using 3,3'-Diaminobenzidine (DAB) and VIP. The brown and violet precipitates generated from DAB and VIP, respectively, were easily distinguishable. Multiplexing with IHC is limited by the ability to distinguish between different colors by eye, and the number of markers that can be analyzed by IHC in a single section is limited to only a few (up to three markers) (234). Multiplex IHC also poses challenges related to co-localization. However, iterative approaches with

repeated cycles of staining, imaging, and destaining have been developed (235). IF is more commonly used for multiplexing and enables the quantification of several markers within a sample even when they overlap spatially. In **Paper III**, we used multiplex IF of human OTSCC tissue to assess the co-localization of PNAd and GlcNAcST-2 in TA-HEVs and to quantify the surrounding cell infiltrate using DAPI. To enable the assessment of co-localization, it is important to select secondary antibodies conjugated with fluorophores that have different excitation spectra to be able to distinguish the signals by fluorescence microscopy. Since PNAd and GlcNAc6ST-2 is co-expressed in HEVs it is particularly important to control for unspecific binding of the antibodies. For this we used isotype controls that matched the primary antibody immunoglobulin type for the PNAd- and GlcNAc6ST-2 antibodies.

In all three papers in this thesis, we used the MECA-79 antibody to detect mouse and human PNAd (fig.4C). PNAd expression in mouse and human LN-HEVs or human tonsil HEVs always showed strong positive staining and PNAd co-localized with the blood vessel marker *Pecam1* in mouse tissues. Although MECA-79 is the most widely used antibody to study HEVs (181), it only partly overlaps with the critical structural determinant 6 sulfo sLeX and only on extended core 1 of branched glycans (164, 236). Recently, an antibody that specifically recognize both mouse and human 6 sulfo sLeX has been established (236), but we are yet to test this antibody in our laboratory.

The anti-human GlcNAc6ST-2 antibody used in **Paper III** has been validated and widely used in The Human Protein Atlas project (237). In the current study we have also confirmed the co-localization of the GlcNAc6ST-2 antibody with PNAd in human lymph node and OTSCC tissue. Co-expression of GlcNAc6ST-2 and PNAd has previously been shown in human lymph node, tonsil, and synovial tissue from patients with rheumatoid arthritis, however, the peptide sequence for the anti-GlcNAc6ST-2 differed slightly from that used in **Paper III** (238). Due to a lack of validated antibodies against mouse GlcNAc6ST-2, we instead used RNAScope combined with IF to detect GlcNAc6SST-2 mRNA (gene *Chst4*) in mouse tongue tissue. RNAScope uses FISH technology and allows for the detection of sequence specific probes bound to mRNA targets in the tissue that are visualized by fluorescent dyes. For the IHC and IF protocols with two or more markers, we used a chromogen/fluorescence minus one control where all antibodies minus one is included. Due to the high cost of RNAScope reagents and probes, this was not performed for the combined FISH/IF protocol. However, we did stain with single probes and the full FISH/IF panel in mouse lymph node tissues to assess specificity before staining of tongue tissues. Preferentially, follow-up experiments showing that protein and gene expression correlates in HEVs in human and mice should be done.

4.1.4.2 Evaluation of stained tissue

The goal in **Paper II** was to determine the presence of HEVs in the tongue of 4NQO-exposed mice and to also map the spatial distribution of HEVs and lymphocytes associated with epithelial lesions. The use of consecutive serial sections in **Paper II** enabled the assessment of different markers and cell types in the same area, albeit at some distance. We chose to count all cells or vessels within the epithelium or lamina propria within the separate sectors, including those in and around epithelial lesions. We chose this approach because most of the 4NQO-exposed mice exhibited several lesions with varying histological grade in the tongue, making it difficult to assess the exact lesion to which the immune infiltrate belonged. Due to the nature of invasive OSCCs, it is most likely that the total area of the lesion and the associated stroma is greater than for instance low-grade dysplasias. However, while the number of B220+ cells and HEVs were higher in SCC than high-grade dysplasias, the number of CD4+, FoxP3+, and CD8+ cells tended to be lower in SCC compared to high-grade dysplasias. This suggests that other factors than the mere size of the lesions affect the composition of the immune infiltrate. The use of serial sections in **Paper II** limits the accuracy in terms of co-localization of the different immune markers. Furthermore, the histology present in the individual tissue sections might differ if the lesions are very small. To counteract this, we chose to use the worst histology of the entire tongue, or the histology confined within sectors, from H&E-stained sections while the histology was not evaluated in the IHC stained sections.

In recent years, more advanced techniques are available for the identification of large numbers of markers within a single tissue section, enabling deep spatial phenotyping and cellular neighborhood analysis (239, 240). Employing these techniques will pave the way for a deeper understanding of the complexity of the TME in the future. However, the increased number of markers will inevitably increase the complexity of the generated data in terms of analysis and interpretation, as well as the costs.

4.1.5 *In vitro* cell culture of mouse endothelial cells

Cell culture is a widely applied method in biomedical research which enables the study of isolated changes in cell behavior and gene expression after stimulation with exogeneous factors, without the influence of systemic factors. Culture of animal- or human-derived cells raises less ethical concerns compared to animal studies and is relatively simple and cost-effective, allowing it to be scalable, and reproducible.

The objective of the cell culture experiments performed in **Paper III** was to study how the expression of selected HEV-associated genes was influenced by the stimulation with LIGHT, LTα1β2, or TNFα.

Stimulation with lymphotoxins and TNFα have previously been shown to influence the expression of various adhesion molecules involved in lymphocyte adhesion in cultured endothelial cells (241-244), however, evidence that cultured endothelial cells express GlcNAc6ST-2 is limited (238, 245). In culture, isolated HECs lose their characteristic cuboidal morphology after two-three days along with a gradual decrease in PNAd and several genes involved in PNAd synthesis (200, 246, 247). *In vivo*, endothelial cells form vessels and have a specific orientation with a lumen facing the interior of the vessel and an abluminal side that is anchored to a basement membrane and the surrounding tissue (248). Endothelial cells form tube-like structures (cords), sometimes with a complete lumen, on Matrigel (249), which contain a mixture of basement membrane proteins, including laminin, fibronectin, and proteoglycans (250). We therefore chose to use the tube formation assay with Matrigel to mimic *in vivo* conditions of endothelial cells to. This is a very simplistic system to study the behavior of cells but could be used to determine minimal requirements for the expression or upregulation of HEV-related genes.

For the experiments in **Paper III**, we used the bEnd.3 cell line which is derived from brain endotheliomas in mice. The bEnd.3 cells are transformed by infection with a retroviral vector expressing the polyoma middle T antigen (PyMT) to enable sustained proliferation in culture (251). Endothelial cells normally remain in a quiescent state *in vivo* and enter the cell cycle upon stimulation (149). Hence, our approach cannot be used to study endothelial cells under steady state conditions but might instead represent a more similar phenotype to actively proliferating endothelial cells during angiogenesis *in vivo*. It is important to note that cultured cells can display different phenotypes than their *in vivo* counterparts and that endothelial cells exhibit tissue-specific characteristics (252). Compared to endothelial cell lines, primary cells are more phenotypically similar to endothelial cells *in vivo*. Primary human umbilical cord vascular endothelial cells (HUVECs) are the most frequently used cells in angiogenesis assays. Because HUVECs are derived from relatively large vessels, other primary cells with a more capillary-like phenotype could be a better alternative to study HEV-related genes in future studies, such as human dermal microvascular endothelial cells (249). However, a drawback with primary endothelial cells is that they lose their angiogenic phenotype after a few passages, and they also become activated *in vitro* (252).

Other methods to study HEV-associated genes *in vitro* to potentially induce a HEV-like phenotype could be employed. For instance, a sandwich assay where endothelial cells are embedded within or between two layers of matrix would allow the cells to polarize and form tubes with a complete lumen (249). Alternatively, more advanced model systems with integrated microfluidics mimicking blood flow or organoid cultures resembling *in vivo* tissues could be used (253, 254), that also enables co-

culture with other cell types. Currently, there are no *in vitro* or *ex vivo* system available for long-term culture of high endothelial cells.

4.1.6 Quantitative real time PCR

Quantitative real time PCR (qPCR) enables the measurement of the relative abundance of specific cDNA sequences in a sample, representing the RNA content. In **Paper III**, we used qPCR to measure the expression of *Chst4, Chst2, Fut4, Fut7, B3gnt3, and Gcnt1* in RNA isolated from bEnd.3 cells. We used a protocol based on the SYBR green fluorescent dye, in which the dye binds to double stranded (ds) DNA and emits fluorescent signal thousand folds higher than non-bound dye (255). The amount of dsDNA amplicons in each quantification cycle (Cq) is proportional to the fluorescent signal, and the Cq values of the samples are used to calculate the quantity of the target mRNA relative to the expression of reference genes (256). SYBR green is more cost effective than the other qPCR method TaqMan, which is based on sequence-specific hydrolysis probes (257).

Because PNAd is a carbohydrate structure, the detection of PNAd is not possible at the mRNA level. Therefore, we used the expression of genes encoding glycosyltransferases as surrogate markers for PNAd biosynthesis. The biological importance of mRNA is somewhat obscure since the presence of mRNA does not necessarily reflect the presence of functional protein (258). However, the presence of mRNA is useful to verify active transcription of a gene and is valuable for further analyses of protein expression.

Even though the effects has not been widely studied, Matrigel has been shown to influence the quality and yield of RNA isolated from cultured cells (259). Hence, the use of Matrigel for bEnd.3 cell culture in **Paper III** may have influenced downstream gene expression. In our experiments, the average Cq value for each of the three reference genes (*Actb, Hprt, Ppia*) was slightly higher in unstimulated cells seeded on Matrigel compared to unstimulated monolayer culture, suggesting that the start concentration of mRNA in Matrigel cultured cells was lower than in monolayer cells. However, the difference between Cq values was 0.3-0.9 for the three reference genes in unstimulated Matrigel versus monolayer cells, indicating that the use of Matrigel only had minimal effects on the mRNA concentration. Other factors could also influence qPCR results, collectively known as PCR inhibitors, and includes RNA- or DNA-degrading enzymes, calcium ions, salts, and complex carbohydrates (260).

For the gene expression measurements following stimulation with LIGHT, LTα1β2, or TNFα we have yet to include a control to confirm that stimulation with the selected cytokines was successful. This can be achieved by measuring the expression of genes known to be upregulated in endothelial

cells in response to the different cytokines. For instance, ICAM-1, VCAM-1, and E-selectin has been shown to be upregulated at the protein and/or mRNA level in cultured endothelial cells stimulated with LIGHT, LTα1β2, or TNFα (242, 243, 261). The downregulation of mediators involved in NFκB signaling downstream of the LTβR could also be used as markers of successful stimulation with LIGHT or LTα1β2, such as the inhibitory protein IκB (242). We did, however, show that cells stimulated with TNFα had significantly higher expression of *Fut4* compared unstimulated cells, both when seeded on Matrigel and as monolayer. A slight upregulation of *B3gnt3* and *Chst2* in monolayer cells was also observed following LIGHT stimulation compared to unstimulated cells. Although it is unlikely that the measured expression is unrelated to any effect of stimulation, there currently remains some uncertainty regarding the bEnd.3 gene expression results in **Paper III** as discussed and they should to be validated by additional experiments.

4.1.7 Statistical analysis

Survival statistics are widely used to estimate prognosis of cancer patients and are valuable tools for researchers, clinicians, and the patients themselves. In **Paper I**, the goal was to investigate the prognostic value of TA-HEVs, CD163+ TAMs, and FoxP3+ Tregs in an OTSCC cohort. Kaplan Meier curves and Log rank tests were applied to calculate whether there were any statistically significant differences in the mean five-year DSS of OTSCC patients with a high or low score of each of the three markers, or a combination of scores. We also performed Cox regression analysis to assess whether the CD163, TA-HEV and/or FoxP3 score had independent effects on OTSCC patient survival.

Statistical analyses can be influenced by various sources of bias, such as sample size and cut-off values (262). It is generally advised to not convert continuous variables into two categories for multivariate analysis because it leads to a loss of information regarding the distribution of the variable (263). However, the use of cut-off values allows for the discrimination between low- and high-risk patients which is useful for guiding of clinical decisions (263). In our study, we chose the 20% quintile as cut-off to dichotomize the density of TA-HEVs, CD163+ TAMs, and FoxP3+ Tregs into high and low scores. We chose this approach because this gave the best separation of the variables in survival curves. Using data-driven cut-off values is debatable, especially for small sample sizes (n=40), while larger samples (n=200) generate more accurate estimates (264). Our OTSCC cohort (n=126) is not critically small, and the selected cut-off might identify patients at the extreme low end of the score with particularly good or poor prognosis. In a meta-analysis of thirteen publications reporting on the prognostic value of TA-HEVs in cancer patients, studies that used a cut-off other than the median to separate tumors into TA-HEV positive and -negative were more likely to report a positive prognosis

(181). Although the sample median is the most commonly used, there is no widely accepted method for selecting the most optimal cut-off point in statistical analysis (263). Using the same cut-off across studies would make comparisons easier and increase the reproducibility of the scoring method. However, the median will also differ between different patient cohorts. Furthermore, cut-off points are somewhat arbitrary, offering limited insight into the biological relevance of the variable, making it difficult to determine if one cut-off is objectively better than another.

For statistical analysis it is important practice thorough reporting and transparency of study limitations. In the clinical setting, the evaluation of potential of new biomarkers is often limited by the lack of standardization and validation. For this reason, The US National Cancer Institute and the European Organization for Research and Treatment of Cancer have initiated the development of reporting recommendations for tumor marker prognostic studies (REMARK) guidelines (215). The REMARK guidelines include a checklist of the minimum information that should be reported in prognostic marker studies to ensure high quality and reproducibility. The analysis in **Paper I** broadly adhere to the REMARK guidelines.

4.2 Discussion of results

It is widely accepted that cancer cells and the host immune response engage in cellular and molecular crosstalk that can both restrict and promote disease progression. These tumor-host interactions can be leveraged for cancer treatment, and specific components within the TME can predict clinical outcomes in cancer patients. Oral cavity cancers can differ in their aggressiveness and response to treatment irrespective of the tumor size, highlighting the need for biomarkers that can identify factors contributing to tumor aggression, to ultimately discriminate between patients with varying risk of disease progression and treatment needs. Analyzing tumor-associated HEVs as individual components of the TME, as well as in combination with other immune cells, can enhance our understanding of their roles in tumor progression and their prognostic values.

4.2.1 GlcNAc6ST-2 expression as an indicator for TA-HEV dedifferentiation

LN-HEVs in mice exhibit a temporary phenotypic shift in response to inflammation and interrupted LTβR signaling (173, 265). These dedifferentiated LN-HEVs display reduced PNAd expression and downregulation of several genes involved in PNAd synthesis, including *Chst4*, *Chst2, Fut7, Gcnt1*, *B3gnt3*, *GlyCAM-1*, and *Ccl21a* (173, 195, 198, 265). GlcNAc6ST-2 (gene *Chst4)* is important for the specific expression of PNAd in LN-HEVs, and mice deficient in *Chst4* exhibit low levels of PNAd and diminished lymphocyte homing to the lymph node (169, 171, 172, 266). Hence, in **Paper III**, we hypothesized that the expression of GlcNAc6ST-2 and PNAd could be a marker for a dedifferentiated TA-HEV phenotype, possibly leading to impaired function. We found that the expression of GlcNAc6ST-2 and PNAd was lower in TA-HEVs than in normal LN-HEVs, indicating different HEV phenotypes in human lymph node and OTSCC. Interestingly, GlcNAc6ST-2 expression was absent in a larger proportion of HEVs in OTSCC than in the lymph node, which might suggest that TA-HEVs expressing or lacking GlcNAc6ST-2 could represent different grades of differentiation. It has previously been shown that dedifferentiated LN-HEVs and TA-HEVs in mice have significant overlap in gene expression patterns compared to normal LN-HEVs, both featuring downregulation of genes involved in PNAd synthesis and lymphocyte homing (195). Interestingly, two independent studies reported a strong downregulation of *Chst4, Chst2, Fut7, Gcnt1,* and *Glycam1* in TA-HEVs compared to dedifferentiated- or normal LN-HEVs in mice (195, 207). Hence, TA-HEVs may be less effective at maintaining a differentiated phenotype, and these genes could potentially serve as a signature for dedifferentiated TA-HEVs. The expression of CHST4 and other HEV-associated genes (CCL21, CCL19, ICAM1, and MADCAM1) was recently demonstrated in TA-HEVs in human breast cancer tissue (145), but lacked comparison with LN-HEVs. HEV phenotypes in human cancers

are not widely explored, and further studies are needed to elucidate the characteristics that defines a dedifferentiated HEV phenotype in normal human lymph nodes and solid tumors.

4.2.2 TA-HEV development depend on anti-tumor immunity in OTSCC

The local microenvironment influences the expression of PNAd in HEVs, both in lymph nodes (198, 204) and in tumors (145, 186, 188). Our results from **Paper III** support that the OTSCC microenvironment somehow regulates the expression of PNAd as well as GlcNAc6ST-2 in TA-HEVs. We hypothesized that the immediate surroundings of TA-HEVs in OTSCC affects their phenotype. The cell density (DAPI+ cells/μm^2) surrounding TA-HEVs was used to estimate the general immune infiltrate around the HEVs. We found that the cell density around LN-HEVs was significantly higher than around TA-HEVs, but the infiltrate surrounding TA-HEVs in OTSCC did not reflect the expression of GlcNAc6ST-2. Our approach to evaluate the immune infiltrate around TA-HEVs was based on the number of DAPI stained nuclei. Even though the size and shape of the cells were considered, this approach does not allow us to distinguish between immune cell types, or stromal cells. Hence, the types of cells surrounding GlcNAc6ST-2-positive and -negative TA-HEVs might differ.

Studies in mice have demonstrated that various immune cell types contribute to the formation of TA-HEVs. Compared to lymph nodes, where DCs play an important role in HEV stability and maintenance (198), lymphocytes appear to be critically involved in TA-HEV development (267). B cells have been proposed to play a role in remodeling of LN-HEVs (173, 205), but appeared to play a lesser role in lymphocyte recruitment to transplanted melanoma (212). In **Paper III**, we showed that the absence of mature T cells in Balb/c nude mice abrogated TA-HEV formation in transplanted tongue tumors. However, since CD4+ T cells are important for B cell activation we cannot exclude that the lack of active B cells or the presence of other immune cell types prevented TA-HEV formation. Mice deficient in mature T cells and *in vivo* depletion of T cells in tumor-bearing mice have demonstrated a close relationship between TA-HEV development and T cells (141, 195, 207, 209, 212, 268). Depletion of CD4+ and CD8+ T cells in adult mice reduced the number of TA-HEVs in pancreatic β-cell carcinoma (209), breast carcinoma (212), and fibrosarcoma (195, 206). Furthermore, tumors grown in mice lacking both mature B and T cells or only lacked CD8+ T cells also lacked TA-HEVs and displayed diminished lymphocyte infiltration into tumors (195, 207, 212). However, while the presence of CD4+ T cells was shown to be essential for TA-HEV development in fibrosarcoma (195), CD8+ T cells and NK cells were shown to be important for the formation of

TA-HEVs in melanoma and breast cancer models (207, 212). This suggests that the cell types driving TA-HEV formation might differ between tumor types.

Nevertheless, adaptive immune responses appear to be important for TA-HEV formation. In support, our proteomics results from **Paper III** showed that the tumor protein expression in HEV-high OTSCCs were enriched in hallmarks and pathways associated with antigen-specific immune responses. Depletion or inactivation of Tregs in tumor-bearing mice have previously been shown to enhance the frequency and activity of CD4+ and CD8+ T cells in the TME and enabled the formation of TA-HEVs (190, 206, 268, 269). In **Paper I**, we showed that OTSCC patients with a high TA-HEV and low FoxP3 score had superior survival compared to those with TA-HEV low- and FoxP3 high tumors, which had the lowest disease-specific survival. The presence of TA-HEVs has been associated with increased numbers of TILS in various human cancers including OSCC (180, 187, 192, 194) and TA-HEV density was recently proposed as a surrogate marker for a T cell inflamed TME in gastric cancer patients (193). Hence, the unfavorable prognosis associated with a low density of TA-HEVs and a high density of FoxP3+ Tregs in OTSCC might therefore indicate that these tumors have limited capacity for lymphocyte recruitment and impaired TIL function, potentially indicating a poor response to immunotherapy in these patients. Which cell type is most important for TA-HEV neogenesis in OTSCC remains to be elucidated.

4.2.3 Prognostic potential for refining TA-HEV score based on Chst4/GlcNAc6ST-2 expression

In **Paper III**, we showed that a subset of HEVs associated with 4NQO-induced SCC lacked *Chst4* mRNA transcripts while *Chst4* was detected in all HEVs associated with normal/hyperplastic- or dysplastic epithelium. This might indicate a gradual loss of *Chst4* as these lesions advance into SCC and that the absence of *Chst4* contributes to the dedifferentiation of TA-HEVs during cancer progression. We therefore hypothesize that *Chst4* could be used as a marker to refine the TA-HEV score for more accurate prognosis prediction in OTSCC. In **Paper I**, we found that a high TA-HEV score was associated with higher five-year DSS rate compared to TA-HEV low tumors. However, TA-HEV density did not prove to be an independent risk factor for OTSCC-related death. This finding contradicts our previous findings in an OSCC cohort where large HEV-negative T3/T4 tumors predicted shorter survival than T3/T4 HEV-positive tumors (186). In light of this, it would be interesting to examine whether the proportion of GlcNAc6ST-2-positive and -negative TA-HEVs differ between OTSCC tumors and have independent effects on patient survival. The inconsistency between these findings could be due to the different locations of the tumors between the two cohorts. The current cohort is more homogeneous, consisting of only OTSCC, while the study by Wirsing et

al. included cancers of the mobile tongue plus other oral subsites (186). The use of different cut-off points between these two studies might also contribute to the inconsistent findings, and the small number of patients in the TA-HEV low group could affect the reliability of our results.

The prognostic value of HEV-associated genes was recently demonstrated in breast cancer patients (145). Sawada et al. identified a high and relatively specific expression of two genes, TSPAN7 and MEOX2, in TA-HEVs in breast cancer tissue (145). A high expression of each of these genes in breast cancer tissue was associated with improved patient survival and correlated with the expression of CCL21, CCL19 and transcripts representing T and B cells. Interestingly, the tumor expression of CHST4 was very low and did not correlate with the expression of other HEV-related genes. The authors ascribed the low CHST4 expression to the inability of bulk RNA sequencing for detecting CHST4, but it would be interesting to know if this was related to a reduced expression of CHST4 as well as PNAd in the TA-HEVs. As we show in **Paper III**, this can be achieved using RNAScope FISH technology combined with IF which enables the detection of *Chst4* mRNA in PNAd+ HEVs while preserving the tissue morphology. The potential of using HEV-associated genes for more accurate prognosis prediction is promising but largely unexplored. Hua et al. recently showed that a HEV gene signature was enriched in melanoma and non-small cell lung cancer patients that responded to immunotherapy (207), suggesting that TA-HEVs also could be used as a predictive marker. It is important to point out that data on the prognostic value of TA-HEVs in oral cancers is limited to few publications and needs to be confirmed in more studies.

4.2.4 Functional implications of reduced/loss of GlcNAc6ST-2 expression in TA-HEVs

The prognostic relevance of a marker is often related to its biological role. GlcNAc6ST-2 is involved in the luminal expression of PNAd in LN-HEVs and works cooperatively with GlcNAc6ST-1 (gene *Chst2*), which is responsible for abluminal PNAd expression (171, 172). A near-complete loss of PNAd in *Chst4* and *Chst2* double-knockout mice results in severely impaired lymphocyte homing to the lymph node (171, 172). However, lymphocyte homing in *Chst4* deficient mice is more impaired than in those lacking *Chst2*. We therefore hypothesize that loss of *Chst4* in TA-HEVs in OTSCC would have impaired ability to recruit lymphocytes to the TME. As shown by Asrir et al., TA-HEVs displayed low expression of *Chst4* compared to normal- and dedifferentiated LN-HEVs (195). However, they showed that the TA-HEVs did express luminal PNAd and were able to capture and bind circulating lymphocytes, suggesting that the HEVs did retain some function. Interestingly, the expression of *Chst2* was less downregulated in TA-HEVs compared to normal- or dedifferentiated LN-HEVs than was the expression of *Chst4* (195). It has been proposed that while both *Chst4* and

Chst2 mediates addition of a sulfate group to extended core-2 of O-glycans, sulfation in the core-1 extension is preferentially mediated by *Chst4 (172).* It is tempting to speculate that *Chst2* serve as a compensatory mechanism for luminal PNAd expression in the absence of *Chst4* in tumors and enable low-level lymphocyte transmigration. In **Paper III** we found that cultured endothelial cells expressed *Chst2,* but not *Chst4,* and that *Chst2* expression changed in response to seeding conditions. Although we cannot deduce any functional details from this experiment, this could indicate that *Chst4* is more context-dependent than *Chst2*, and that the environment in tumors affect *Chst4* expression more readily than *Chst2*. Analyzing the expression of *Chst2* in TA-HEVs in mouse and human OTSCC would provide further insight into this. Since the most widely used antibody MECA-79 only partly overlaps with the 6 sulfo sLeX on the extended core-1, it would also be interesting to test the staining patterns of other established antibodies that specifically recognize 6 sulfo sLeX (236, 270).

Although *Chst4*, followed by *Chst2*, appear to play a chief function in PNAd synthesis and lymphocyte trafficking, the coordinated activity of other enzymes involved in the generation of PNAd is also important. Indeed, *Gcnt1* and *Fut7* were strongly downregulated in TA-HEVs in tumor-bearing mice (195, 207). *Gcnt1* is important for the generation of the biantennary structure in PNAd (fig.4C), suggesting that its absence could lead to loss of 6 sulfo sLeX on the core 2 extension, without detectable reduction in MECA-79. *In vitro* and *in vivo* studies have demonstrated the importance of *Fut7* and *Fut4* in lymphocyte adhesion and homing (168, 271-273). The expression of GlcNAc6ST-2 in PNAd-negative vessels in arthritis-affected tissue might also indicate aberrations in other sugar residues than N-acetylglucosamine (238, 274). Because lymphocyte recruitment is pivotal for the health of the host, it is likely that several compensatory mechanisms exist to support this process. However, the individual or concerted roles of PNAd synthesizing enzymes in TA-HEVs are not well described.

4.2.5 TA-HEVs and TLS

TA-HEVs can be found within TLS in oral cancers and display a lymph node-like phenotype with pronounced PNAd expression (131, 183). TA-HEVs with similar phenotypes have been found in areas of OSCC tumors with high inflammation that was unrelated to TLS (186). We did not assess the presence of TLS in the human OTSCC tissue in **Paper I** and **Paper III**. Given that TLS have been associated with prolonged survival in OSCC patients (131, 183), it is possible that survival rates could differ between patients depending on whether TA-HEVs are found within or outside TLS. Mature TLSs are generally associated with better prognosis in cancer patients (275), and there was a tendency that mature TLS in OSCC patients conferred better prognosis (131). TLSs can be detected with standard hematoxylin and eosin staining but because the composition of cells within the TLS

differ by the level of maturity, additional markers are required (275). The minimal markers required to detect mature TLS in human cancer is not fully established but typically include markers for B cells, GC formation, follicular DCs, T cells, and HEVs (105, 275). It would be interesting to investigate whether TA-HEV phenotypes, characterized by the presence or absence of GlcNAc6ST-2, is related to their location within TLS or independent of TLS in OTSCC, potentially serving as a simple marker for TLS maturity. For future studies assessing the prognostic value of TA-HEVs in oral cancers it would be beneficial to evaluate whether the survival benefit of TA-HEVs is influenced by their location within or outside of TLS.

In **Paper II**, we reported for the first time the presence of HEVs in the tongue of 4NQO-exposed mice (36). Interestingly, the HEVs developed in the absence of any detectable TLS. TA-HEVs can be induced in murine tumors genetically engineered to express strong antigens, such as ovalbumin (174, 212, 269) and Polyoma Middle T antigen (208). Several studies have also shown that TA-HEVs are induced in tumor-bearing mice by stimulating LTβRs signaling alone and/or with immune checkpoint inhibitors and vessel normalization drugs (207-209, 211, 276). Most of these tumors also develop TLS or TLS-like immune aggregates or TLS was not systematically assessed. Besides our current work, only few studies have reported the development of TA-HEVs without the presence of TLS (195, 206, 268) and there are limited reports of TA-HEVs efficiently forming without some form of pharmacological intervention (190, 195, 208). The reason why TA-HEVs develop independently of TLS remains unknown, and it is unclear whether this indicates distinct regulatory mechanisms. Could the nature of the tumor antigen selectively trigger the formation of ectopic TA-HEVs rather than both TA-HEVs and TLS, possibly resulting in the recruitment of different immune cell types? The formation of TA-HEVs might instead be a byproduct of an ongoing immune response or simply represent an early phase in the formation of TLS or other immune aggregates, such as a recently described antigen-presenting niche (211, 277). Many questions regarding the regulation, timing of development, and function of TA-HEVs remains unanswered.

5 Conclusions and future perspectives

The work presented in the current thesis has shown that different TA-HEV phenotypes, marked by the presence or absence of GlcNAc6ST-2, are present in mouse and human OTSCC. The number of HEVs significantly increased in SCCs compared to less severe lesions, and while GlcNAc6ST-2 mRNA was expressed in all HEVs associated with non-malignant lesions, a subset of HEVs within SCCs lacked GlcNAc6ST-2 gene expression. These findings might indicate that loss of GlcNAc6ST-2 is involved in the dedifferentiation of TA-HEVs and is linked to the loss of PNAd, ultimately leading to impaired function. We cannot draw any conclusions on the functional consequence of the absence of GlcNAc6ST-2 in TA-HEVs from the current work. Because there are currently no model systems that can be used to study HEVs *in vitro*, this can only be achieved by *in vivo* models. Knockout of *Chst4* and/or *Chst2* in tumor-bearing mice could give insight into how loss of *Chst4* affects lymphocyte infiltration into tumors and at the same time study the influence of GlcNAc6ST-1 in TA-HEV development.

The presence of TA-HEVs in OTSCC is associated with improved patient survival rates, but not as an independent marker. OTSCCs with a high TA-HEV and low FoxP3 score had superior survival rates than tumors with a low TA-HEV- and high FoxP3 score. To investigate whether GlcNAc6ST-2/*Chst4* can be used to refine the prognostic value of TA-HEVs in OTSCC we are planning to include more patient samples and correlate GlcNAc6ST-2 expression with clinical data, both at the protein- and gene level. We are also planning to analyze the co-localization of GlcNAc6ST-1/Chst2 and PNAd in TA-HEVs in mouse and human OTSCC, to investigate whether GlcNAc6ST-1 is a compensatory mechanism in TA-HEVs in the absence of GlcNAc6ST-2/*Chst4*.

HEV development in mouse OTSCC depends on a functional immune system, particularly mature T cells, but the density of the general cell infiltrate around TA-HEVs did not reflect the expression of GlcNAc6ST-2. HEVs developed independent of TLS, and DCs appeared to play a minimal role. Although our results points to an important role of T cells for TA-HEV development in OTSCC, we cannot conclude which cell types are involved in the formation TA-HEVs. Because other cell types are also present in the local microenvironment of TA-HEVs in tumors it would be interesting to investigate which cell types surround TA-HEVs within OTSCC tumors, and if the composition and state of the cells surrounding TA-HEVs can be correlated with GlcNAc6ST-2/*Chst4* expression. This includes TLS, which requires several markers. This can be achieved with multiplexing of multiple antibodies or probes.

Although GlcNAc6ST2 appear to be the single most important factor for PNAd synthesis in LN-HEVs, other glycan modifying enzymes are likely also involved. It would be interesting to isolate high endothelial cells from murine SLOs (lymph node, tonsil, PPs), for which there are existing protocols. Analyzing the gene expression and PNAd in freshly isolated cells and at various timepoints in culture, could reveal which genes are up- or downregulated in parallel to the gradual loss of PNAd. This could be achieved using single RNA sequencing or CRISPR technology of MECA-79+CD31+ isolated cells. Cutting-edge technologies, such as single-cell spatial transcriptomics and glycoproteomics, could also provide a comprehensive understanding of how TA-HEVs interact with their local microenvironment within the TME.

Our findings provide support for the involvement of TA-HEVs in OTSCC progression and the expression of GlcNAc6ST-2/*Chst4* in TA-HEVs is a potential marker for refining the TA-HEV score in OTSCC to stratify patients with varying risk of disease progression. A better understanding of the role of GlcNAc6ST-2 could permit the development of strategies for targeted depletion of HEVs in diseases where their presence is detrimental and targeted induction of TA-HEVs in human solid malignancies.

References

1. Mody MD, Rocco JW, Yom SS, Haddad RI, Saba NF. Head and neck cancer. Lancet. 2021;398(10318):2289-99.
2. Cruchley AT, Bergmeier LA. Structure and Functions of the Oral Mucosa. In: Bergmeier LA, editor. Oral Mucosa in Health and Disease: A Concise Handbook. Cham: Springer International Publishing; 2018. p. 1-18.
3. Bjerkli IH, Jetlund O, Karevold G, Karlsdottir A, Jaatun E, Uhlin-Hansen L, et al. Characteristics and prognosis of primary treatment-naive oral cavity squamous cell carcinoma in Norway, a descriptive retrospective study. PLoS One. 2020;15(1):e0227738.
4. Brierley J, Gospodarowicz, M.K., Wittekind. TNM Classification of Malignant Tumours, 8th Edition. 8 ed. Oxford, UK: Wiley-Blackwell; 2017.
5. Mohideen K, Krithika C, Jeddy N, Balakrishnan T, Bharathi R, Sankari SL. A Meta-analysis of Oral Squamous Cell Carcinoma in Young Adults with a Comparison to the Older Group Patients (2014-2019). Contemp Clin Dent. 2021;12(3):213-21.
6. Brown JS, Lowe D, Kalavrezos N, D'Souza J, Magennis P, Woolgar J. Patterns of invasion and routes of tumor entry into the mandible by oral squamous cell carcinoma. Head Neck. 2002;24(4):370-83.
7. Cao L-M, Zhong N-N, Li Z-Z, Huo F-Y, Xiao Y, Liu B, et al. Lymph node metastasis in oral squamous cell carcinoma: Where we are and where we are going. Clinical and Translational Discovery. 2023;3(4):e227.
8. Bray F, Laversanne M, Sung H, Ferlay J, Siegel RL, Soerjomataram I, et al. Global cancer statistics 2022: GLOBOCAN estimates of incidence and mortality worldwide for 36 cancers in 185 countries. CA Cancer J Clin. 2024.
9. Huang J, Chan SC, Ko S, Lok V, Zhang L, Lin X, et al. Disease burden, risk factors, and trends of lip, oral cavity, pharyngeal cancers: A global analysis. Cancer Med. 2023;12(17):18153-64.
10. Hussein AA, Helder MN, de Visscher JG, Leemans CR, Braakhuis BJ, de Vet HCW, et al. Global incidence of oral and oropharynx cancer in patients younger than 45 years versus older patients: A systematic review. Eur J Cancer. 2017;82:115-27.
11. Sung H, Ferlay J, Siegel RL, Laversanne M, Soerjomataram I, Jemal A, et al. Global Cancer Statistics 2020: GLOBOCAN Estimates of Incidence and Mortality Worldwide for 36 Cancers in 185 Countries. CA Cancer J Clin. 2021;71(3):209-49.
12. Bosetti C, Carioli G, Santucci C, Bertuccio P, Gallus S, Garavello W, et al. Global trends in oral and pharyngeal cancer incidence and mortality. Int J Cancer. 2020;147(4):1040-9.
13. Norway CRo. Cancer in Norway 2022: Cancer incidence, mortality, survival and prevalence in Norway. Oslo: Cancer Registry of Norway; 2023.
14. Parkin DM, Bray F, Ferlay J, Pisani P. Global cancer statistics, 2002. CA Cancer J Clin. 2005;55(2):74-108.
15. Tan Y, Wang Z, Xu M, Li B, Huang Z, Qin S, et al. Oral squamous cell carcinomas: state of the field and emerging directions. Int J Oral Sci. 2023;15(1):44.
16. Mello FW, Melo G, Pasetto JJ, Silva CAB, Warnakulasuriya S, Rivero ERC. The synergistic effect of tobacco and alcohol consumption on oral squamous cell carcinoma: a systematic review and meta-analysis. Clin Oral Investig. 2019;23(7):2849-59.
17. Asthana S, Labani S, Kailash U, Sinha DN, Mehrotra R. Association of Smokeless Tobacco Use and Oral Cancer: A Systematic Global Review and Meta-Analysis. Nicotine Tob Res. 2019;21(9):1162-71.
18. Patil S, Arakeri G, Alamir AWH, Patil S, Awan KH, Baeshen H, et al. Is toombak a risk factor for oral leukoplakia and oral squamous cell carcinoma ? A systematic review. J Oral Pathol Med. 2020;49(2):103-9.
19. Valen H, Becher R, Vist GE, Holme JA, Mdala I, Elvsaas I, et al. A systematic review of cancer risk among users of smokeless tobacco (Swedish snus) exclusively, compared with no use of tobacco. Int J Cancer. 2023;153(12):1942-53.
20. Araghi M, Galanti MR, Lundberg M, Liu Z, Ye W, Lager A, et al. No association between moist oral snuff (snus) use and oral cancer: pooled analysis of nine prospective observational studies. Scand J Public Health. 2021;49(8):833-40.
21. Hernández-Morales A, González-López BS, Scougall-Vilchis RJ, Bermeo-Escalona JR, Velázquez-Enríquez U, Islas-Zarazúa R, et al. Lip and Oral Cavity Cancer Incidence and Mortality Rates Associated with Smoking and Chewing Tobacco Use and the Human Development Index in 172 Countries Worldwide: An Ecological Study 2019-2020. Healthcare (Basel). 2023;11(8).

22.   Smokeless tobacco and some tobacco-specific N-Nitrosamines. Lyon, France: International Agency for Research on Cancer; 2007.

23.   Chen PH, Mahmood Q, Mariottini GL, Chiang TA, Lee KW. Adverse Health Effects of Betel Quid and the Risk of Oral and Pharyngeal Cancers. Biomed Res Int. 2017;2017:3904098.

24.   Lechner M, Liu J, Masterson L, Fenton TR. HPV-associated oropharyngeal cancer: epidemiology, molecular biology and clinical management. Nat Rev Clin Oncol. 2022;19(5):306-27.

25.   Jain P, Kumar N, Shetty SC, Kalladka SS, Ramesh PS, Patil P, et al. Prevalence of Epstein Barr Virus and Herpes Simplex Virus Among Human Papillomavirus Negative Oral Cancer Patients: A Cross-Sectional Study from South India. Indian J Otolaryngol Head Neck Surg. 2024;76(1):414-21.

26.   Søland TM, Bjerkli IH, Georgsen JB, Schreurs O, Jebsen P, Laurvik H, et al. High-risk human papilloma virus was not detected in a Norwegian cohort of oral squamous cell carcinoma of the mobile tongue. Clin Exp Dent Res. 2021;7(1):70-7.

27.   Rikardsen OG, Bjerkli IH, Uhlin-Hansen L, Hadler-Olsen E, Steigen SE. Clinicopathological characteristics of oral squamous cell carcinoma in Northern Norway: a retrospective study. BMC Oral Health. 2014;14:103.

28.   de Abreu PM, Có ACG, Azevedo PL, do Valle IB, de Oliveira KG, Gouvea SA, et al. Frequency of HPV in oral cavity squamous cell carcinoma. BMC Cancer. 2018;18(1):324.

29.   Rahman R, Shaikh MH, Gopinath D, Idris A, Johnson NW. Human papillomavirus and Epstein-Barr virus co-infection in oral and oropharyngeal squamous cell carcinomas: A systematic review and meta-analysis. Mol Oral Microbiol. 2023;38(4):259-74.

30.   Su ZY, Siak PY, Leong CO, Cheah SC. The role of Epstein-Barr virus in nasopharyngeal carcinoma. Front Microbiol. 2023;14:1116143.

31.   Banerjee S, Tian T, Wei Z, Peck KN, Shih N, Chalian AA, et al. Microbial Signatures Associated with Oropharyngeal and Oral Squamous Cell Carcinomas. Sci Rep. 2017;7(1):4036.

32.   Mahuli AV, Sagar V, Kumar A, Mahuli SA, Kujur A. A Systematic Review and Meta-Analysis Assessing the Role of Oral Health as a Risk Factor in Oral Cancer. Cureus. 2023;15(5):e39786.

33.   Ogden GR. Alcohol and mouth cancer. Br Dent J. 2018;225(9):880-3.

34.   Smokeless tobacco and some tobacco-specific N-nitrosamines. IARC Monogr Eval Carcinog Risks Hum. 2007;89:1-592.

35.   González-López LL, Morales-González Á, Sosa-Gómez A, Madrigal-Santillán EO, Anguiano-Robledo L, Madrigal-Bujaidar E, et al. Damage to Oral Mucosae Induced by Weekend Alcohol Consumption: The Role of Gender and Alcohol Concentration. Applied Sciences. 2022;12(7):3464.

36.   Sellæg K, Schwienbacher R, Kranz M, Aamodt AE, Wirsing AM, Berge G, et al. 4-nitroquinoline 1-oxide-induced oral epithelial lesions exhibit time- and stage-dependent changes in the tumor immune microenvironment. Front Oncol. 2024;14:1343839.

37.   Kanojia D, Vaidya MM. 4-nitroquinoline-1-oxide induced experimental oral carcinogenesis. Oral Oncol. 2006;42(7):655-67.

38.   Sequeira I, Rashid M, Tomás IM, Williams MJ, Graham TA, Adams DJ, et al. Genomic landscape and clonal architecture of mouse oral squamous cell carcinomas dictate tumour ecology. Nat Commun. 2020;11(1):5671.

39.   Wang Z, Wu VH, Allevato MM, Gilardi M, He Y, Luis Callejas-Valera J, et al. Syngeneic animal models of tobacco-associated oral cancer reveal the activity of in situ anti-CTLA-4. Nat Commun. 2019;10(1):5546.

40.   Leemans CR, Snijders PJF, Brakenhoff RH. The molecular landscape of head and neck cancer. Nat Rev Cancer. 2018;18(5):269-82.

41.   Li J, Li S, Shu M, Hu W. Unravelling the heterogeneity of oral squamous cell carcinoma by integrative analysis of single-cell and bulk transcriptome data. J Cell Mol Med. 2024;28(3):e18108.

42.   Dongre HN, Haave H, Fromreide S, Erland FA, Moe SEE, Dhayalan SM, et al. Targeted Next-Generation Sequencing of Cancer-Related Genes in a Norwegian Patient Cohort With Head and Neck Squamous Cell Carcinoma Reveals Novel Actionable Mutations and Correlations With Pathological Parameters. Front Oncol. 2021;11:734134.

43.   Warnakulasuriya S. Oral potentially malignant disorders: A comprehensive review on clinical aspects and management. Oral Oncol. 2020;102:104550.

44.   Warnakulasuriya S, Kujan O, Aguirre-Urizar JM, Bagan JV, González-Moles M, Kerr AR, et al. Oral potentially malignant disorders: A consensus report from an international seminar on nomenclature and classification, convened by the WHO Collaborating Centre for Oral Cancer. Oral Dis. 2021;27(8):1862-80.

45.   Hankinson P, Mahmood H, Walsh H, Speight PM, Khurram SA. Demystifying oral epithelial dysplasia: a histological guide. Pathology. 2024;56(1):11-23.
46.   Ranganathan K, Kavitha L. Oral epithelial dysplasia: Classifications and clinical relevance in risk assessment of oral potentially malignant disorders. J Oral Maxillofac Pathol. 2019;23(1):19-27.
47.   Brandwein-Gensler M, Teixeira MS, Lewis CM, Lee B, Rolnitzky L, Hille JJ, et al. Oral squamous cell carcinoma: histologic risk assessment, but not margin status, is strongly predictive of local disease-free and overall survival. Am J Surg Pathol. 2005;29(2):167-78.
48.   Speight PM, Farthing PM. The pathology of oral cancer. Br Dent J. 2018;225(9):841-7.
49.   Duprez F, Berwouts D, De Neve W, Bonte K, Boterberg T, Deron P, et al. Distant metastases in head and neck cancer. Head Neck. 2017;39(9):1733-43.
50.   Matsui M, Kawamura K, Kano K, Yoshimatsu H, Doi T, Miyake T. Incidence of second primary cancers in oral and pharyngeal cancer patients using a large medical claims database in Japan. J Dent Sci. 2023;18(3):1047-54.
51.   Gu X, Wang L, Coates PJ, Gnanasundram SV, Sgaramella N, Sörlin J, et al. Evidence for etiologic field changes in tongue distant from tumor in patients with squamous cell carcinoma of the oral tongue. J Pathol. 2023;259(1):93-102.
52.   Slaughter DP, Southwick HW, Smejkal W. Field cancerization in oral stratified squamous epithelium; clinical implications of multicentric origin. Cancer. 1953;6(5):963-8.
53.   Lydiatt WM, Patel SG, O'Sullivan B, Brandwein MS, Ridge JA, Migliacci JC, et al. Head and Neck cancers-major changes in the American Joint Committee on cancer eighth edition cancer staging manual. CA Cancer J Clin. 2017;67(2):122-37.
54.   Almangush A, Bello IO, Keski-Säntti H, Mäkinen LK, Kauppila JH, Pukkila M, et al. Depth of invasion, tumor budding, and worst pattern of invasion: prognostic indicators in early-stage oral tongue cancer. Head Neck. 2014;36(6):811-8.
55.   Caponio VCA, Troiano G, Togni L, Zhurakivska K, Santarelli A, Laino L, et al. Pattern and localization of perineural invasion predict poor survival in oral tongue carcinoma. Oral Dis. 2023;29(2):411-22.
56.   El-Naggar AK, Chan JKC, Grandis JR, Takata T, Slootweg PJ. WHO Classification of Head and Neck Tumours 4th edition: International Agency for Research on Cancer; 2017.
57.   Dik EA, Ipenburg NA, Kessler PA, van Es RJJ, Willems SM. The value of histological grading of biopsy and resection specimens in early stage oral squamous cell carcinomas. J Craniomaxillofac Surg. 2018;46(6):1001-6.
58.   Bjerkli IH, Hadler-Olsen E, Nginamau ES, Laurvik H, Søland TM, Costea DE, et al. A combined histo-score based on tumor differentiation and lymphocytic infiltrate is a robust prognostic marker for mobile tongue cancer. Virchows Arch. 2020;477(6):865-72.
59.   Wang C, Huang H, Huang Z, Wang A, Chen X, Huang L, et al. Tumor budding correlates with poor prognosis and epithelial-mesenchymal transition in tongue squamous cell carcinoma. J Oral Pathol Med. 2011;40(7):545-51.
60.   Almangush A, Pirinen M, Heikkinen I, Mäkitie AA, Salo T, Leivo I. Tumour budding in oral squamous cell carcinoma: a meta-analysis. Br J Cancer. 2018;118(4):577-86.
61.   Binmadi NO, Mohamed YA. Impact of worst pattern of invasion on prognosis of oral squamous cell carcinoma: a systematic review and meta-analysis. J Int Med Res. 2023;51(10):3000605231206260.
62.   Rahman N, MacNeill M, Wallace W, Conn B. Reframing Histological Risk Assessment of Oral Squamous Cell Carcinoma in the Era of UICC 8th Edition TNM Staging. Head Neck Pathol. 2021;15(1):202-11.
63.   Heikkinen I, Bello IO, Wahab A, Hagström J, Haglund C, Coletta RD, et al. Assessment of Tumor-infiltrating Lymphocytes Predicts the Behavior of Early-stage Oral Tongue Cancer. Am J Surg Pathol. 2019;43(10):1392-6.
64.   Zhou C, Diao P, Wu Y, Wei Z, Jiang L, Zhang W, et al. Development and validation of a seven-immune-feature-based prognostic score for oral squamous cell carcinoma after curative resection. Int J Cancer. 2020;146(4):1152-63.
65.   Huang Z, Xie N, Liu H, Wan Y, Zhu Y, Zhang M, et al. The prognostic role of tumour-infiltrating lymphocytes in oral squamous cell carcinoma: A meta-analysis. J Oral Pathol Med. 2019;48(9):788-98.
66.   Fang J, Li X, Ma D, Liu X, Chen Y, Wang Y, et al. Prognostic significance of tumor infiltrating immune cells in oral squamous cell carcinoma. BMC Cancer. 2017;17(1):375.

67.   Wongpattaraworakul W, Choi A, Buchakjian MR, Lanzel EA, Kd AR, Simons AL. Prognostic Role of Tumor-Infiltrating Lymphocytes in Oral Squamous Cell Carcinoma. BMC Cancer. 2024;24(1):766.

68.   Troiano G, Rubini C, Togni L, Caponio VCA, Zhurakivska K, Santarelli A, et al. The immune phenotype of tongue squamous cell carcinoma predicts early relapse and poor prognosis. Cancer Med. 2020;9(22):8333-44.

69.   Agarwal R, Chaudhary M, Bohra S, Bajaj S. Evaluation of natural killer cell (CD57) as a prognostic marker in oral squamous cell carcinoma: An immunohistochemistry study. J Oral Maxillofac Pathol. 2016;20(2):173-7.

70.   Huang Z, Lu Y, Wang W, Xie N, Yi C, Xiong G, et al. Prognostic value of tumor-infiltrating immune cells in clinical early-stage oral squamous cell carcinoma. J Oral Pathol Med. 2023;52(5):372-80.

71.   Hadler-Olsen E, Wirsing AM. Tissue-infiltrating immune cells as prognostic markers in oral squamous cell carcinoma: a systematic review and meta-analysis. Br J Cancer. 2019;120(7):714-27.

72.   Bera RN, Tandon S, Singh AK, Boojar FMA, Jaiswal G, Borse S, et al. Management and outcome of locally advanced oral squamous cell carcinoma. Natl J Maxillofac Surg. 2023;14(2):185-9.

73.   Gebre-Medhin M, Brun E, Engström P, Haugen Cange H, Hammarstedt-Nordenvall L, Reizenstein J, et al. ARTSCAN III: A Randomized Phase III Study Comparing Chemoradiotherapy With Cisplatin Versus Cetuximab in Patients With Locoregionally Advanced Head and Neck Squamous Cell Cancer. J Clin Oncol. 2021;39(1):38-47.

74.   Ferris RL, Blumenschein G, Jr., Fayette J, Guigay J, Colevas AD, Licitra L, et al. Nivolumab for Recurrent Squamous-Cell Carcinoma of the Head and Neck. N Engl J Med. 2016;375(19):1856-67.

75.   Sroussi HY, Epstein JB, Bensadoun RJ, Saunders DP, Lalla RV, Migliorati CA, et al. Common oral complications of head and neck cancer radiation therapy: mucositis, infections, saliva change, fibrosis, sensory dysfunctions, dental caries, periodontal disease, and osteoradionecrosis. Cancer Med. 2017;6(12):2918-31.

76.   Rao D, Behzadi F, Le RT, Dagan R, Fiester P. Radiation Induced Mucositis: What the Radiologist Needs to Know. Curr Probl Diagn Radiol. 2021;50(6):899-904.

77.   Frankart AJ, Frankart MJ, Cervenka B, Tang AL, Krishnan DG, Takiar V. Osteoradionecrosis: Exposing the Evidence Not the Bone. Int J Radiat Oncol Biol Phys. 2021;109(5):1206-18.

78.   Andreassen R, Jönsson B, Hadler-Olsen E. Oral health related quality of life in long-term survivors of head and neck cancer compared to a general population from the seventh Tromsø study. BMC Oral Health. 2022;22(1):100.

79.   Burian E, Palla B, Callahan N, Pyka T, Wolff C, von Schacky CE, et al. Comparison of CT, MRI, and F-18 FDG PET/CT for initial N-staging of oral squamous cell carcinoma: a cost-effectiveness analysis. Eur J Nucl Med Mol Imaging. 2022;49(11):3870-7.

80.   Maman S, Witz IP. A history of exploring cancer in context. Nat Rev Cancer. 2018;18(6):359-76.

81.   Vogelstein B, Kinzler KW. The multistep nature of cancer. Trends Genet. 1993;9(4):138-41.

82.   Hanahan D, Weinberg RA. Hallmarks of cancer: the next generation. Cell. 2011;144(5):646-74.

83.   Zhang J, Veeramachaneni N. Targeting interleukin-1β and inflammation in lung cancer. Biomark Res. 2022;10(1):5.

84.   Kalluri R. The biology and function of fibroblasts in cancer. Nat Rev Cancer. 2016;16(9):582-98.

85.   Erez N, Truitt M, Olson P, Arron ST, Hanahan D. Cancer-Associated Fibroblasts Are Activated in Incipient Neoplasia to Orchestrate Tumor-Promoting Inflammation in an NF-kappaB-Dependent Manner. Cancer Cell. 2010;17(2):135-47.

86.   Goetz JG, Minguet S, Navarro-Lérida I, Lazcano JJ, Samaniego R, Calvo E, et al. Biomechanical remodeling of the microenvironment by stromal caveolin-1 favors tumor invasion and metastasis. Cell. 2011;146(1):148-63.

87.   Orimo A, Gupta PB, Sgroi DC, Arenzana-Seisdedos F, Delaunay T, Naeem R, et al. Stromal fibroblasts present in invasive human breast carcinomas promote tumor growth and angiogenesis through elevated SDF-1/CXCL12 secretion. Cell. 2005;121(3):335-48.

88.   Al-Ansari MM, Hendrayani SF, Tulbah A, Al-Tweigeri T, Shehata AI, Aboussekhra A. p16INK4A represses breast stromal fibroblasts migration/invasion and their VEGF-A-dependent promotion of angiogenesis through Akt inhibition. Neoplasia. 2012;14(12):1269-77.

89.   DuPage M, Mazumdar C, Schmidt LM, Cheung AF, Jacks T. Expression of tumour-specific antigens underlies cancer immunoediting. Nature. 2012;482(7385):405-9.

90.   Del Prete A, Salvi V, Soriani A, Laffranchi M, Sozio F, Bosisio D, et al. Dendritic cell subsets in cancer immunity and tumor antigen sensing. Cell Mol Immunol. 2023;20(5):432-47.

91.   Curtsinger JM, Johnson CM, Mescher MF. CD8 T cell clonal expansion and development of effector function require prolonged exposure to antigen, costimulation, and signal 3 cytokine. J Immunol. 2003;171(10):5165-71.
92.   Raskov H, Orhan A, Christensen JP, Gögenur I. Cytotoxic CD8(+) T cells in cancer and cancer immunotherapy. Br J Cancer. 2021;124(2):359-67.
93.   Bos R, Sherman LA. CD4+ T-cell help in the tumor milieu is required for recruitment and cytolytic function of CD8+ T lymphocytes. Cancer Res. 2010;70(21):8368-77.
94.   Bailey SR, Nelson MH, Himes RA, Li Z, Mehrotra S, Paulos CM. Th17 cells in cancer: the ultimate identity crisis. Front Immunol. 2014;5:276.
95.   Takeuchi Y, Nishikawa H. Roles of regulatory T cells in cancer immunity. Int Immunol. 2016;28(8):401-9.
96.   Śledzińska A, Vila de Mucha M, Bergerhoff K, Hotblack A, Demane DF, Ghorani E, et al. Regulatory T Cells Restrain Interleukin-2- and Blimp-1-Dependent Acquisition of Cytotoxic Function by CD4(+) T Cells. Immunity. 2020;52(1):151-66.e6.
97.   Quezada SA, Simpson TR, Peggs KS, Merghoub T, Vider J, Fan X, et al. Tumor-reactive CD4(+) T cells develop cytotoxic activity and eradicate large established melanoma after transfer into lymphopenic hosts. J Exp Med. 2010;207(3):637-50.
98.   Xie Y, Akpinarli A, Maris C, Hipkiss EL, Lane M, Kwon EK, et al. Naive tumor-specific CD4(+) T cells differentiated in vivo eradicate established melanoma. J Exp Med. 2010;207(3):651-67.
99.   Vaidehi Narayanan H, Hoffmann A. From Antibody Repertoires to Cell-Cell Interactions to Molecular Networks: Bridging Scales in the Germinal Center. Front Immunol. 2022;13:898078.
100.   Nutt SL, Hodgkin PD, Tarlinton DM, Corcoran LM. The generation of antibody-secreting plasma cells. Nat Rev Immunol. 2015;15(3):160-71.
101.   Zahavi D, AlDeghaither D, O'Connell A, Weiner LM. Enhancing antibody-dependent cell-mediated cytotoxicity: a strategy for improving antibody-based immunotherapy. Antib Ther. 2018;1(1):7-12.
102.   Griss J, Bauer W, Wagner C, Simon M, Chen M, Grabmeier-Pfistershammer K, et al. B cells sustain inflammation and predict response to immune checkpoint blockade in human melanoma. Nat Commun. 2019;10(1):4186.
103.   DiLillo DJ, Yanaba K, Tedder TF. B cells are required for optimal CD4+ and CD8+ T cell tumor immunity: therapeutic B cell depletion enhances B16 melanoma growth in mice. J Immunol. 2010;184(7):4006-16.
104.   Montfort A, Pearce O, Maniati E, Vincent BG, Bixby L, Böhm S, et al. A Strong B-cell Response Is Part of the Immune Landscape in Human High-Grade Serous Ovarian Metastases. Clin Cancer Res. 2017;23(1):250-62.
105.   Fridman WH, Meylan M, Pupier G, Calvez A, Hernandez I, Sautès-Fridman C. Tertiary lymphoid structures and B cells: An intratumoral immunity cycle. Immunity. 2023;56(10):2254-69.
106.   Christofides A, Strauss L, Yeo A, Cao C, Charest A, Boussiotis VA. The complex role of tumor-infiltrating macrophages. Nat Immunol. 2022;23(8):1148-56.
107.   Kim JM, Rasmussen JP, Rudensky AY. Regulatory T cells prevent catastrophic autoimmunity throughout the lifespan of mice. Nat Immunol. 2007;8(2):191-7.
108.   Pelaez-Prestel HF, Sanchez-Trincado JL, Lafuente EM, Reche PA. Immune Tolerance in the Oral Mucosa. Int J Mol Sci. 2021;22(22).
109.   Takahashi T, Tagami T, Yamazaki S, Uede T, Shimizu J, Sakaguchi N, et al. Immunologic self-tolerance maintained by CD25(+)CD4(+) regulatory T cells constitutively expressing cytotoxic T lymphocyte-associated antigen 4. J Exp Med. 2000;192(2):303-10.
110.   Gunderson AJ, Yamazaki T, McCarty K, Fox N, Phillips M, Alice A, et al. TGFβ suppresses CD8(+) T cell expression of CXCR3 and tumor trafficking. Nat Commun. 2020;11(1):1749.
111.   Togashi Y, Shitara K, Nishikawa H. Regulatory T cells in cancer immunosuppression - implications for anticancer therapy. Nat Rev Clin Oncol. 2019;16(6):356-71.
112.   Shiao SL, Ruffell B, DeNardo DG, Faddegon BA, Park CC, Coussens LM. TH2-Polarized CD4(+) T Cells and Macrophages Limit Efficacy of Radiotherapy. Cancer Immunol Res. 2015;3(5):518-25.
113.   DeNardo DG, Barreto JB, Andreu P, Vasquez L, Tawfik D, Kolhatkar N, et al. CD4(+) T cells regulate pulmonary metastasis of mammary carcinomas by enhancing protumor properties of macrophages. Cancer Cell. 2009;16(2):91-102.
114.   Bosurgi L, Cao YG, Cabeza-Cabrerizo M, Tucci A, Hughes LD, Kong Y, et al. Macrophage function in tissue repair and remodeling requires IL-4 or IL-13 with apoptotic cells. Science. 2017;356(6342):1072-6.

115.   Mantovani A, Allavena P. The interaction of anticancer therapies with tumor-associated macrophages. J Exp Med. 2015;212(4):435-45.

116.   Bai R, Li Y, Jian L, Yang Y, Zhao L, Wei M. The hypoxia-driven crosstalk between tumor and tumor-associated macrophages: mechanisms and clinical treatment strategies. Mol Cancer. 2022;21(1):177.

117.   Olkhanud PB, Damdinsuren B, Bodogai M, Gress RE, Sen R, Wejksza K, et al. Tumor-evoked regulatory B cells promote breast cancer metastasis by converting resting CD4+ T cells to T-regulatory cells. Cancer Res. 2011;71(10):3505-15.

118.   Raychaudhuri B, Rayman P, Ireland J, Ko J, Rini B, Borden EC, et al. Myeloid-derived suppressor cell accumulation and function in patients with newly diagnosed glioblastoma. Neuro Oncol. 2011;13(6):591-9.

119.   Zhou X, Su YX, Lao XM, Liang YJ, Liao GQ. CD19(+)IL-10(+) regulatory B cells affect survival of tongue squamous cell carcinoma patients and induce resting CD4(+) T cells to CD4(+)Foxp3(+) regulatory T cells. Oral Oncol. 2016;53:27-35.

120.   Wang WW, Yuan XL, Chen H, Xie GH, Ma YH, Zheng YX, et al. CD19+CD24hiCD38hiBregs involved in downregulate helper T cells and upregulate regulatory T cells in gastric cancer. Oncotarget. 2015;6(32):33486-99.

121.   Lindner S, Dahlke K, Sontheimer K, Hagn M, Kaltenmeier C, Barth TF, et al. Interleukin 21-induced granzyme B-expressing B cells infiltrate tumors and regulate T cells. Cancer Res. 2013;73(8):2468-79.

122.   Noman MZ, Desantis G, Janji B, Hasmim M, Karray S, Dessen P, et al. PD-L1 is a novel direct target of HIF-1α, and its blockade under hypoxia enhanced MDSC-mediated T cell activation. J Exp Med. 2014;211(5):781-90.

123.   Dubinski D, Wölfer J, Hasselblatt M, Schneider-Hohendorf T, Bogdahn U, Stummer W, et al. CD4+ T effector memory cell dysfunction is associated with the accumulation of granulocytic myeloid-derived suppressor cells in glioblastoma patients. Neuro Oncol. 2016;18(6):807-18.

124.   Dunn GP, Old LJ, Schreiber RD. The three Es of cancer immunoediting. Annu Rev Immunol. 2004;22:329-60.

125.   Ghorani E, Swanton C, Quezada SA. Cancer cell-intrinsic mechanisms driving acquired immune tolerance. Immunity. 2023;56(10):2270-95.

126.   Gastman BR, Atarshi Y, Reichert TE, Saito T, Balkir L, Rabinowich H, et al. Fas ligand is expressed on human squamous cell carcinomas of the head and neck, and it promotes apoptosis of T lymphocytes. Cancer Res. 1999;59(20):5356-64.

127.   Schumacher TN, Thommen DS. Tertiary lymphoid structures in cancer. Science. 2022;375(6576):eabf9419.

128.   Drayton DL, Liao S, Mounzer RH, Ruddle NH. Lymphoid organ development: from ontogeny to neogenesis. Nat Immunol. 2006;7(4):344-53.

129.   Thaunat O, Patey N, Caligiuri G, Gautreau C, Mamani-Matsuda M, Mekki Y, et al. Chronic rejection triggers the development of an aggressive intragraft immune response through recapitulation of lymphoid organogenesis. J Immunol. 2010;185(1):717-28.

130.   Dieu-Nosjean MC, Antoine M, Danel C, Heudes D, Wislez M, Poulot V, et al. Long-term survival for patients with non-small-cell lung cancer with intratumoral lymphoid structures. J Clin Oncol. 2008;26(27):4410-7.

131.   Wirsing AM, Rikardsen OG, Steigen SE, Uhlin-Hansen L, Hadler-Olsen E. Characterisation and prognostic value of tertiary lymphoid structures in oral squamous cell carcinoma. BMC Clin Pathol. 2014;14:38.

132.   Hiraoka N, Ino Y, Yamazaki-Itoh R, Kanai Y, Kosuge T, Shimada K. Intratumoral tertiary lymphoid organ is a favourable prognosticator in patients with pancreatic cancer. Br J Cancer. 2015;112(11):1782-90.

133.   Wang Q, Shen X, An R, Bai J, Dong J, Cai H, et al. Peritumoral tertiary lymphoid structure and tumor stroma percentage predict the prognosis of patients with non-metastatic colorectal cancer. Front Immunol. 2022;13:962056.

134.   Wang Q, Zhong W, Shen X, Hao Z, Wan M, Yang X, et al. Tertiary lymphoid structures predict survival and response to neoadjuvant therapy in locally advanced rectal cancer. NPJ Precis Oncol. 2024;8(1):61.

135.   Halle S, Dujardin HC, Bakocevic N, Fleige H, Danzer H, Willenzon S, et al. Induced bronchus-associated lymphoid tissue serves as a general priming site for T cells and is maintained by dendritic cells. J Exp Med. 2009;206(12):2593-601.

136. Meylan M, Petitprez F, Becht E, Bougoüin A, Pupier G, Calvez A, et al. Tertiary lymphoid structures generate and propagate anti-tumor antibody-producing plasma cells in renal cell cancer. Immunity. 2022;55(3):527-41.e5.

137. Germain C, Gnjatic S, Tamzalit F, Knockaert S, Remark R, Goc J, et al. Presence of B cells in tertiary lymphoid structures is associated with a protective immunity in patients with lung cancer. Am J Respir Crit Care Med. 2014;189(7):832-44.

138. Ye BH, Cattoretti G, Shen Q, Zhang J, Hawe N, de Waard R, et al. The BCL-6 proto-oncogene controls germinal-centre formation and Th2-type inflammation. Nat Genet. 1997;16(2):161-70.

139. Muramatsu M, Kinoshita K, Fagarasan S, Yamada S, Shinkai Y, Honjo T. Class switch recombination and hypermutation require activation-induced cytidine deaminase (AID), a potential RNA editing enzyme. Cell. 2000;102(5):553-63.

140. Bombardieri M, Barone F, Humby F, Kelly S, McGurk M, Morgan P, et al. Activation-induced cytidine deaminase expression in follicular dendritic cell networks and interfollicular large B cells supports functionality of ectopic lymphoid neogenesis in autoimmune sialoadenitis and MALT lymphoma in Sjögren's syndrome. J Immunol. 2007;179(7):4929-38.

141. Chaurio RA, Anadon CM, Lee Costich T, Payne KK, Biswas S, Harro CM, et al. TGF-β-mediated silencing of genomic organizer SATB1 promotes Tfh cell differentiation and formation of intra-tumoral tertiary lymphoid structures. Immunity. 2022;55(1):115-28.e9.

142. Helmink BA, Reddy SM, Gao J, Zhang S, Basar R, Thakur R, et al. B cells and tertiary lymphoid structures promote immunotherapy response. Nature. 2020;577(7791):549-55.

143. Lee Y, Chin RK, Christiansen P, Sun Y, Tumanov AV, Wang J, et al. Recruitment and activation of naive T cells in the islets by lymphotoxin beta receptor-dependent tertiary lymphoid structure. Immunity. 2006;25(3):499-509.

144. Schrama D, Voigt H, Eggert AO, Xiang R, Zhou H, Schumacher TN, et al. Immunological tumor destruction in a murine melanoma model by targeted LTalpha independent of secondary lymphoid tissue. Cancer Immunol Immunother. 2008;57(1):85-95.

145. Sawada J, Hiraoka N, Qi R, Jiang L, Fournier-Goss AE, Yoshida M, et al. Molecular Signature of Tumor-Associated High Endothelial Venules That Can Predict Breast Cancer Survival. Cancer Immunol Res. 2022;10(4):468-81.

146. Donnem T, Hu J, Ferguson M, Adighibe O, Snell C, Harris AL, et al. Vessel co-option in primary human tumors and metastases: an obstacle to effective anti-angiogenic treatment? Cancer Med. 2013;2(4):427-36.

147. Dunleavey JM, Xiao L, Thompson J, Kim MM, Shields JM, Shelton SE, et al. Vascular channels formed by subpopulations of PECAM1+ melanoma cells. Nat Commun. 2014;5:5200.

148. Adams RH, Alitalo K. Molecular regulation of angiogenesis and lymphangiogenesis. Nat Rev Mol Cell Biol. 2007;8(6):464-78.

149. Liu ZL, Chen HH, Zheng LL, Sun LP, Shi L. Angiogenic signaling pathways and anti-angiogenic therapy for cancer. Signal Transduct Target Ther. 2023;8(1):198.

150. Cedervall J, Dimberg A, Olsson AK. Tumor-Induced Local and Systemic Impact on Blood Vessel Function. Mediators Inflamm. 2015;2015:418290.

151. Gerber HP, Condorelli F, Park J, Ferrara N. Differential transcriptional regulation of the two vascular endothelial growth factor receptor genes. Flt-1, but not Flk-1/KDR, is up-regulated by hypoxia. J Biol Chem. 1997;272(38):23659-67.

152. Forsythe JA, Jiang BH, Iyer NV, Agani F, Leung SW, Koos RD, et al. Activation of vascular endothelial growth factor gene transcription by hypoxia-inducible factor 1. Mol Cell Biol. 1996;16(9):4604-13.

153. Huinen ZR, Huijbers EJM, van Beijnum JR, Nowak-Sliwinska P, Griffioen AW. Anti-angiogenic agents - overcoming tumour endothelial cell anergy and improving immunotherapy outcomes. Nat Rev Clin Oncol. 2021;18(8):527-40.

154. Blanchard L, Girard JP. High endothelial venules (HEVs) in immunity, inflammation and cancer. Angiogenesis. 2021.

155. Pfeiffer F, Kumar V, Butz S, Vestweber D, Imhof BA, Stein JV, et al. Distinct molecular composition of blood and lymphatic vascular endothelial cell junctions establishes specific functional barriers within the peripheral lymph node. Eur J Immunol. 2008;38(8):2142-55.

156. Ager A. High Endothelial Venules and Other Blood Vessels: Critical Regulators of Lymphoid Organ Development and Function. Front Immunol. 2017;8:45.

157.   Girard JP, Moussion C, Förster R. HEVs, lymphatics and homeostatic immune cell trafficking in lymph nodes. Nat Rev Immunol. 2012;12(11):762-73.
158.   Mebius RE, Streeter PR, Michie S, Butcher EC, Weissman IL. A developmental switch in lymphocyte homing receptor and endothelial vascular addressin expression regulates lymphocyte homing and permits CD4+ CD3- cells to colonize lymph nodes. Proc Natl Acad Sci U S A. 1996;93(20):11019-24.
159.   Onder L, Danuser R, Scandella E, Firner S, Chai Q, Hehlgans T, et al. Endothelial cell-specific lymphotoxin-beta receptor signaling is critical for lymph node and high endothelial venule formation. J Exp Med. 2013;210(3):465-73.
160.   Vella G, Hua Y, Bergers G. High endothelial venules in cancer: Regulation, function, and therapeutic implication. Cancer Cell. 2023;41(3):527-45.
161.   Kawashima H, Hirakawa J, Tobisawa Y, Fukuda M, Saga Y. Conditional gene targeting in mouse high endothelial venules. J Immunol. 2009;182(9):5461-8.
162.   Rosen SD. Ligands for L-selectin: homing, inflammation, and beyond. Annu Rev Immunol. 2004;22:129-56.
163.   Hiraoka N, Petryniak B, Nakayama J, Tsuboi S, Suzuki M, Yeh JC, et al. A novel, high endothelial venule-specific sulfotransferase expresses 6-sulfo sialyl Lewis(x), an L-selectin ligand displayed by CD34. Immunity. 1999;11(1):79-89.
164.   Yeh JC, Hiraoka N, Petryniak B, Nakayama J, Ellies LG, Rabuka D, et al. Novel sulfated lymphocyte homing receptors and their control by a Core1 extension beta 1,3-N-acetylglucosaminyltransferase. Cell. 2001;105(7):957-69.
165.   Kobayashi M, Hoshino H, Masumoto J, Fukushima M, Suzawa K, Kageyama S, et al. GlcNAc6ST-1-mediated decoration of MAdCAM-1 protein with L-selectin ligand carbohydrates directs disease activity of ulcerative colitis. Inflamm Bowel Dis. 2009;15(5):697-706.
166.   de Graffenried CL, Bertozzi CR. Golgi localization of carbohydrate sulfotransferases is a determinant of L-selectin ligand biosynthesis. J Biol Chem. 2003;278(41):40282-95.
167.   Yang WH, Nussbaum C, Grewal PK, Marth JD, Sperandio M. Coordinated roles of ST3Gal-VI and ST3Gal-IV sialyltransferases in the synthesis of selectin ligands. Blood. 2012;120(5):1015-26.
168.   Homeister JW, Thall AD, Petryniak B, Malý P, Rogers CE, Smith PL, et al. The alpha(1,3)fucosyltransferases FucT-IV and FucT-VII exert collaborative control over selectin-dependent leukocyte recruitment and lymphocyte homing. Immunity. 2001;15(1):115-26.
169.   Hemmerich S, Bistrup A, Singer MS, van Zante A, Lee JK, Tsay D, et al. Sulfation of L-selectin ligands by an HEV-restricted sulfotransferase regulates lymphocyte homing to lymph nodes. Immunity. 2001;15(2):237-47.
170.   Bistrup A, Bhakta S, Lee JK, Belov YY, Gunn MD, Zuo FR, et al. Sulfotransferases of two specificities function in the reconstitution of high endothelial cell ligands for L-selectin. J Cell Biol. 1999;145(4):899-910.
171.   Kawashima H, Petryniak B, Hiraoka N, Mitoma J, Huckaby V, Nakayama J, et al. N-acetylglucosamine-6-O-sulfotransferases 1 and 2 cooperatively control lymphocyte homing through L-selectin ligand biosynthesis in high endothelial venules. Nat Immunol. 2005;6(11):1096-104.
172.   Uchimura K, Gauguet JM, Singer MS, Tsay D, Kannagi R, Muramatsu T, et al. A major class of L-selectin ligands is eliminated in mice deficient in two sulfotransferases expressed in high endothelial venules. Nat Immunol. 2005;6(11):1105-13.
173.   Liao S, Ruddle NH. Synchrony of high endothelial venules and lymphatic vessels revealed by immunization. J Immunol. 2006;177(5):3369-79.
174.   Rodriguez AB, Parriott G, Engelhard VH. Tumor necrosis factor receptor regulation of peripheral node addressin biosynthetic components in tumor endothelial cells. Front Immunol. 2022;13:1009306.
175.   Menzel L, Zschummel M, Crowley T, Franke V, Grau M, Ulbricht C, et al. Lymphocyte access to lymphoma is impaired by high endothelial venule regression. Cell Rep. 2021;37(4):109878.
176.   Stein JV, Rot A, Luo Y, Narasimhaswamy M, Nakano H, Gunn MD, et al. The CC chemokine thymus-derived chemotactic agent 4 (TCA-4, secondary lymphoid tissue chemokine, 6Ckine, exodus-2) triggers lymphocyte function-associated antigen 1-mediated arrest of rolling T lymphocytes in peripheral lymph node high endothelial venules. J Exp Med. 2000;191(1):61-76.
177.   Choe K, Moon J, Lee SY, Song E, Back JH, Song JH, et al. Stepwise transmigration of T- and B cells through a perivascular channel in high endothelial venules. Life Sci Alliance. 2021;4(8).
178.   Ager A, May MJ. Understanding high endothelial venules: Lessons for cancer immunology. Oncoimmunology. 2015;4(6):e1008791.

179. Anderson ND, Anderson AO, Wyllie RG. Specialized structure and metabolic activities of high endothelial venules in rat lymphatic tissues. Immunology. 1976;31(3):455-73.

180. Martinet L, Garrido I, Filleron T, Le Guellec S, Bellard E, Fournie JJ, et al. Human solid tumors contain high endothelial venules: association with T- and B-lymphocyte infiltration and favorable prognosis in breast cancer. Cancer Res. 2011;71(17):5678-87.

181. Wang B, Han Y, Liu J, Zhang X, Deng Y, Jiang Y. Intratumoral high endothelial venules in solid tumors: a pooled study. Front Immunol. 2024;15:1401118.

182. Yoshida H, Hoshino H, Imamura Y, Yoshimura H, Sano K, Kobayashi M. Role of sialyl 6-sulfo Lewis X in antitumor immunity against oral squamous cell carcinoma. J Oral Pathol Med. 2017;46(9):759-65.

183. Li Q, Liu X, Wang D, Wang Y, Lu H, Wen S, et al. Prognostic value of tertiary lymphoid structure and tumour infiltrating lymphocytes in oral squamous cell carcinoma. Int J Oral Sci. 2020;12(1):24.

184. Hyytiäinen A, Mroueh R, Peltonen J, Wennerstrand P, Mäkitie A, Al-Samadi A, et al. Prognostic histological markers in oral tongue squamous cell carcinoma patients treated with (chemo)radiotherapy. Apmis. 2023;131(4):142-51.

185. Lee SY, Qian CN, Ooi AS, Chen P, Tan VK, Chia CS, et al. 2011 Young Surgeon's Award Winner: high endothelial venules: a novel prognostic marker in cancer metastasis and the missing link? Ann Acad Med Singap. 2012;41(1):21-8.

186. Wirsing AM, Rikardsen OG, Steigen SE, Uhlin-Hansen L, Hadler-Olsen E. Presence of tumour high-endothelial venules is an independent positive prognostic factor and stratifies patients with advanced-stage oral squamous cell carcinoma. Tumour Biol. 2016;37(2):2449-59.

187. Martinet L, Le Guellec S, Filleron T, Lamant L, Meyer N, Rochaix P, et al. High endothelial venules (HEVs) in human melanoma lesions: Major gateways for tumor-infiltrating lymphocytes. Oncoimmunology. 2012;1(6):829-39.

188. Avram G, Sánchez-Sendra B, Martín JM, Terrádez L, Ramos D, Monteagudo C. The density and type of MECA-79-positive high endothelial venules correlate with lymphocytic infiltration and tumour regression in primary cutaneous melanoma. Histopathology. 2013;63(6):852-61.

189. Milutinovic S, Abe J, Jones E, Kelch I, Smart K, Lauder SN, et al. Three-dimensional Imaging Reveals Immune-driven Tumor-associated High Endothelial Venules as a Key Correlate of Tumor Rejection Following Depletion of Regulatory T Cells. Cancer Research Communications. 2022;2(12):1641-56.

190. Lauder SN, Smart K, Kersemans V, Allen D, Scott J, Pires A, et al. Enhanced antitumor immunity through sequential targeting of PI3Kδ and LAG3. J Immunother Cancer. 2020;8(2).

191. Martinet L, Garrido I, Girard JP. Tumor high endothelial venules (HEVs) predict lymphocyte infiltration and favorable prognosis in breast cancer. Oncoimmunology. 2012;1(5):789-90.

192. Hong SA, Hwang HW, Kim MK, Lee TJ, Yim K, Won HS, et al. High Endothelial Venule with Concomitant High CD8+ Tumor-Infiltrating Lymphocytes Is Associated with a Favorable Prognosis in Resected Gastric Cancer. J Clin Med. 2020;9(8).

193. Park HS, Kim YM, Kim S, Lee WS, Kong SJ, Yang H, et al. High endothelial venule is a surrogate biomarker for T-cell inflamed tumor microenvironment and prognosis in gastric cancer. J Immunother Cancer. 2021;9(10).

194. Wirsing AM, Ervik IK, Seppola M, Uhlin-Hansen L, Steigen SE, Hadler-Olsen E. Presence of high-endothelial venules correlates with a favorable immune microenvironment in oral squamous cell carcinoma. Mod Pathol. 2018;31(6):910-22.

195. Asrir A, Tardiveau C, Coudert J, Laffont R, Blanchard L, Bellard E, et al. Tumor-associated high endothelial venules mediate lymphocyte entry into tumors and predict response to PD-1 plus CTLA-4 combination immunotherapy. Cancer Cell. 2022.

196. Carrière V, Colisson R, Jiguet-Jiglaire C, Bellard E, Bouche G, Al Saati T, et al. Cancer cells regulate lymphocyte recruitment and leukocyte-endothelium interactions in the tumor-draining lymph node. Cancer Res. 2005;65(24):11639-48.

197. Qian CN, Berghuis B, Tsarfaty G, Bruch M, Kort EJ, Ditlev J, et al. Preparing the "soil": the primary tumor induces vasculature reorganization in the sentinel lymph node before the arrival of metastatic cancer cells. Cancer Res. 2006;66(21):10365-76.

198. Moussion C, Girard JP. Dendritic cells control lymphocyte entry to lymph nodes through high endothelial venules. Nature. 2011;479(7374):542-6.

199. Browning JL, Allaire N, Ngam-Ek A, Notidis E, Hunt J, Perrin S, et al. Lymphotoxin-beta receptor signaling is required for the homeostatic control of HEV differentiation and function. Immunity. 2005;23(5):539-50.

200. Lacorre DA, Baekkevold ES, Garrido I, Brandtzaeg P, Haraldsen G, Amalric F, et al. Plasticity of endothelial cells: rapid dedifferentiation of freshly isolated high endothelial venule endothelial cells outside the lymphoid tissue microenvironment. Blood. 2004;103(11):4164-72.

201. Onder L, Danuser R, Scandella E, Firner S, Chai Q, Hehlgans T, et al. Endothelial cell-specific lymphotoxin-β receptor signaling is critical for lymph node and high endothelial venule formation. J Exp Med. 2013;210(3):465-73.

202. Lu TT, Browning JL. Role of the Lymphotoxin/LIGHT System in the Development and Maintenance of Reticular Networks and Vasculature in Lymphoid Tissues. Front Immunol. 2014;5:47.

203. Chyou S, Ekland EH, Carpenter AC, Tzeng TC, Tian S, Michaud M, et al. Fibroblast-type reticular stromal cells regulate the lymph node vasculature. J Immunol. 2008;181(6):3887-96.

204. Hendriks HR, Eestermans IL. Disappearance and reappearance of high endothelial venules and immigrating lymphocytes in lymph nodes deprived of afferent lymphatic vessels: a possible regulatory role of macrophages in lymphocyte migration. Eur J Immunol. 1983;13(8):663-9.

205. Kumar V, Scandella E, Danuser R, Onder L, Nitschké M, Fukui Y, et al. Global lymphoid tissue remodeling during a viral infection is orchestrated by a B cell-lymphotoxin-dependent pathway. Blood. 2010;115(23):4725-33.

206. Colbeck EJ, Jones E, Hindley JP, Smart K, Schulz R, Browne M, et al. Treg Depletion Licenses T Cell-Driven HEV Neogenesis and Promotes Tumor Destruction. Cancer Immunol Res. 2017;5(11):1005-15.

207. Hua Y, Vella G, Rambow F, Allen E, Antoranz Martinez A, Duhamel M, et al. Cancer immunotherapies transition endothelial cells into HEVs that generate TCF1(+) T lymphocyte niches through a feed-forward loop. Cancer Cell. 2022;40(12):1600-18.e10.

208. Allen E, Jabouille A, Rivera LB, Lodewijckx I, Missiaen R, Steri V, et al. Combined antiangiogenic and anti-PD-L1 therapy stimulates tumor immunity through HEV formation. Sci Transl Med. 2017;9(385):eaak9679.

209. Johansson-Percival A, He B, Li ZJ, Kjellén A, Russell K, Li J, et al. De novo induction of intratumoral lymphoid structures and vessel normalization enhances immunotherapy in resistant tumors. Nat Immunol. 2017;18(11):1207-17.

210. He B, Jabouille A, Steri V, Johansson-Percival A, Michael IP, Kotamraju VR, et al. Vascular targeting of LIGHT normalizes blood vessels in primary brain cancer and induces intratumoural high endothelial venules. J Pathol. 2018;245(2):209-21.

211. Ramachandran M, Vaccaro A, van de Walle T, Georganaki M, Lugano R, Vemuri K, et al. Tailoring vascular phenotype through AAV therapy promotes anti-tumor immunity in glioma. Cancer Cell. 2023;41(6):1134-51.e10.

212. Peske JD, Thompson ED, Gemta L, Baylis RA, Fu YX, Engelhard VH. Effector lymphocyte-induced lymph node-like vasculature enables naive T-cell entry into tumours and enhanced anti-tumour immunity. Nat Commun. 2015;6:7114.

213. Brener ND, Billy JO, Grady WR. Assessment of factors affecting the validity of self-reported health-risk behavior among adolescents: evidence from the scientific literature. J Adolesc Health. 2003;33(6):436-57.

214. Association WM. WMA Declaration of Helsinki – Ethical Principles for Medical Research Involving Human Subjects [Available from: https://www.wma.net/policies-post/wma-declaration-of-helsinki-ethical-principles-for-medical-research-involving-human-subjects/.

215. Sauerbrei W, Taube SE, McShane LM, Cavenagh MM, Altman DG. Reporting Recommendations for Tumor Marker Prognostic Studies (REMARK): An Abridged Explanation and Elaboration. J Natl Cancer Inst. 2018;110(8):803-11.

216. Li Q, Dong H, Yang G, Song Y, Mou Y, Ni Y. Mouse Tumor-Bearing Models as Preclinical Study Platforms for Oral Squamous Cell Carcinoma. Front Oncol. 2020;10:212.

217. Tang XH, Knudsen B, Bemis D, Tickoo S, Gudas LJ. Oral cavity and esophageal carcinogenesis modeled in carcinogen-treated mice. Clin Cancer Res. 2004;10(1 Pt 1):301-13.

218. Vitale-Cross L, Czerninski R, Amornphimoltham P, Patel V, Molinolo AA, Gutkind JS. Chemical carcinogenesis models for evaluating molecular-targeted prevention and treatment of oral cancer. Cancer Prev Res (Phila). 2009;2(5):419-22.

219. Chang NW, Pei RJ, Tseng HC, Yeh KT, Chan HC, Lee MR, et al. Co-treating with arecoline and 4-nitroquinoline 1-oxide to establish a mouse model mimicking oral tumorigenesis. Chem Biol Interact. 2010;183(1):231-7.

220.   Guo Y, Wang X, Zhang X, Sun Z, Chen X. Ethanol promotes chemically induced oral cancer in mice through activation of the 5-lipoxygenase pathway of arachidonic acid metabolism. Cancer Prev Res (Phila). 2011;4(11):1863-72.
221.   Ishida K, Tomita H, Nakashima T, Hirata A, Tanaka T, Shibata T, et al. Current mouse models of oral squamous cell carcinoma: Genetic and chemically induced models. Oral Oncol. 2017;73:16-20.
222.   Caulin C, Nguyen T, Longley MA, Zhou Z, Wang XJ, Roop DR. Inducible activation of oncogenic K-ras results in tumor formation in the oral cavity. Cancer Res. 2004;64(15):5054-8.
223.   Li Z, Gonzalez CL, Wang B, Zhang Y, Mejia O, Katsonis P, et al. Cdkn2a suppresses metastasis in squamous cell carcinomas induced by the gain-of-function mutant p53(R172H). J Pathol. 2016;240(2):224-34.
224.   DuPage M, Jacks T. Genetically engineered mouse models of cancer reveal new insights about the antitumor immune response. Curr Opin Immunol. 2013;25(2):192-9.
225.   Watanabe H, Numata K, Ito T, Takagi K, Matsukawa A. Innate immune response in Th1- and Th2-dominant mouse strains. Shock. 2004;22(5):460-6.
226.   Reilly KM. The Effects of Genetic Background of Mouse Models of Cancer: Friend or Foe? Cold Spring Harb Protoc. 2016;2016(3):pdb.top076273.
227.   Riolobos L, Gad EA, Treuting PM, Timms AE, Hershberg EA, Corulli LR, et al. The Effect of Mouse Strain, Sex, and Carcinogen Dose on Toxicity and the Development of Lung Dysplasia and Squamous Cell Carcinomas in Mice. Cancer Prev Res (Phila). 2019;12(8):507-16.
228.   Mohideen K, Krithika C, Jeddy N, Bharathi R, Thayumanavan B, Sankari SL. Meta-analysis on risk factors of squamous cell carcinoma of the tongue in young adults. J Oral Maxillofac Pathol. 2019;23(3):450-7.
229.   Yamaguchi H, Hiroi M, Mori K, Ushio R, Matsumoto A, Yamamoto N, et al. Simultaneous Expression of Th1- and Treg-Associated Chemokine Genes and CD4(+), CD8(+), and Foxp3(+) Cells in the Premalignant Lesions of 4NQO-Induced Mouse Tongue Tumorigenesis. Cancers (Basel). 2021;13(8).
230.   Bouaoud J, Foy JP, Tortereau A, Michon L, Lavergne V, Gadot N, et al. Early changes in the immune microenvironment of oral potentially malignant disorders reveal an unexpected association of M2 macrophages with oral cancer free survival. Oncoimmunology. 2021;10(1):1944554.
231.   Vered M, Allon I, Buchner A, Dayan D. Stromal myofibroblasts and malignant transformation in a 4NQO rat tongue carcinogenesis model. Oral Oncol. 2007;43(10):999-1006.
232.   Lykidis D, Van Noorden S, Armstrong A, Spencer-Dene B, Li J, Zhuang Z, et al. Novel zinc-based fixative for high quality DNA, RNA and protein analysis. Nucleic Acids Res. 2007;35(12):e85.
233.   Grillo F, Pigozzi S, Ceriolo P, Calamaro P, Fiocca R, Mastracci L. Factors affecting immunoreactivity in long-term storage of formalin-fixed paraffin-embedded tissue sections. Histochem Cell Biol. 2015;144(1):93-9.
234.   O'Hurley G, Sjöstedt E, Rahman A, Li B, Kampf C, Pontén F, et al. Garbage in, garbage out: a critical evaluation of strategies used for validation of immunohistochemical biomarkers. Mol Oncol. 2014;8(4):783-98.
235.   Remark R, Merghoub T, Grabe N, Litjens G, Damotte D, Wolchok JD, et al. In-depth tissue profiling using multiplexed immunohistochemical consecutive staining on single slide. Sci Immunol. 2016;1(1):aaf6925.
236.   Liu W, Xiong W, Liu W, Hirakawa J, Kawashima H. A novel monoclonal antibody against 6-sulfo sialyl Lewis x glycans attenuates murine allergic rhinitis by suppressing Th2 immune responses. Sci Rep. 2023;13(1):15740.
237.   Pontén F, Jirström K, Uhlen M. The Human Protein Atlas--a tool for pathology. J Pathol. 2008;216(4):387-93.
238.   Pablos JL, Santiago B, Tsay D, Singer MS, Palao G, Galindo M, et al. A HEV-restricted sulfotransferase is expressed in rheumatoid arthritis synovium and is induced by lymphotoxin-alpha/beta and TNF-alpha in cultured endothelial cells. BMC Immunol. 2005;6:6.
239.   Magness A, Colliver E, Enfield KSS, Lee C, Shimato M, Daly E, et al. Deep cell phenotyping and spatial analysis of multiplexed imaging with TRACERx-PHLEX. Nat Commun. 2024;15(1):5135.
240.   Jhaveri N, Ben Cheikh B, Nikulina N, Ma N, Klymyshyn D, DeRosa J, et al. Mapping the Spatial Proteome of Head and Neck Tumors: Key Immune Mediators and Metabolic Determinants in the Tumor Microenvironment. GEN Biotechnology. 2023;2(5):418-34.

241.   Cuff CA, Sacca R, Ruddle NH. Differential induction of adhesion molecule and chemokine expression by LTalpha3 and LTalphabeta in inflammation elucidates potential mechanisms of mesenteric and peripheral lymph node development. J Immunol. 1999;162(10):5965-72.

242.   Madge LA, Kluger MS, Orange JS, May MJ. Lymphotoxin-alpha 1 beta 2 and LIGHT induce classical and noncanonical NF-kappa B-dependent proinflammatory gene expression in vascular endothelial cells. J Immunol. 2008;180(5):3467-77.

243.   Sawa Y, Sugimoto Y, Ueki T, Ishikawa H, Sato A, Nagato T, et al. Effects of TNF-alpha on leukocyte adhesion molecule expressions in cultured human lymphatic endothelium. J Histochem Cytochem. 2007;55(7):721-33.

244.   Sikorski EE, Hallmann R, Berg EL, Butcher EC. The Peyer's patch high endothelial receptor for lymphocytes, the mucosal vascular addressin, is induced on a murine endothelial cell line by tumor necrosis factor-alpha and IL-1. J Immunol. 1993;151(10):5239-50.

245.   Li X, Tu L, Murphy PG, Kadono T, Steeber DA, Tedder TF. CHST1 and CHST2 sulfotransferase expression by vascular endothelial cells regulates shear-resistant leukocyte rolling via L-selectin. J Leukoc Biol. 2001;69(4):565-74.

246.   Cook-Mills JM, Gallagher JS, Feldbush TL. Isolation and characterization of high endothelial cell lines derived from mouse lymph nodes. In Vitro Cell Dev Biol Anim. 1996;32(3):167-77.

247.   Baekkevold ES, Jahnsen FL, Johansen FE, Bakke O, Gaudernack G, Brandtzaeg P, et al. Culture characterization of differentiated high endothelial venule cells from human tonsils. Lab Invest. 1999;79(3):327-36.

248.   Freemont AJ, Stoddart RW, Steven F, Jones CJ, Matthews S. The structure of the basement membrane of human lymph node high endothelial venules: an ultrastructural, histochemical and immunocytochemical study. Histochem J. 1986;18(8):421-8.

249.   Nowak-Sliwinska P, Alitalo K, Allen E, Anisimov A, Aplin AC, Auerbach R, et al. Consensus guidelines for the use and interpretation of angiogenesis assays. Angiogenesis. 2018;21(3):425-532.

250.   Hayashi Y, Emoto T, Futaki S, Sekiguchi K. Establishment and characterization of a parietal endoderm-like cell line derived from Engelbreth-Holm-Swarm tumor (EHSPEL), a possible resource for an engineered basement membrane matrix. Matrix Biol. 2004;23(1):47-62.

251.   Montesano R, Pepper MS, Möhle-Steinlein U, Risau W, Wagner EF, Orci L. Increased proteolytic activity is responsible for the aberrant morphogenetic behavior of endothelial cells expressing the middle T oncogene. Cell. 1990;62(3):435-45.

252.   Staton CA, Reed MW, Brown NJ. A critical analysis of current in vitro and in vivo angiogenesis assays. Int J Exp Pathol. 2009;90(3):195-221.

253.   Andrique L, Recher G, Alessandri K, Pujol N, Feyeux M, Bon P, et al. A model of guided cell self-organization for rapid and spontaneous formation of functional vessels. Sci Adv. 2019;5(6):eaau6562.

254.   Wimmer RA, Leopoldi A, Aichinger M, Kerjaschki D, Penninger JM. Generation of blood vessel organoids from human pluripotent stem cells. Nat Protoc. 2019;14(11):3082-100.

255.   Ponchel F, Toomes C, Bransfield K, Leong FT, Douglas SH, Field SL, et al. Real-time PCR based on SYBR-Green I fluorescence: an alternative to the TaqMan assay for a relative quantification of gene rearrangements, gene amplifications and micro gene deletions. BMC Biotechnol. 2003;3:18.

256.   Livak KJ, Schmittgen TD. Analysis of relative gene expression data using real-time quantitative PCR and the 2(-Delta Delta C(T)) Method. Methods. 2001;25(4):402-8.

257.   Holland PM, Abramson RD, Watson R, Gelfand DH. Detection of specific polymerase chain reaction product by utilizing the 5'----3' exonuclease activity of Thermus aquaticus DNA polymerase. Proc Natl Acad Sci U S A. 1991;88(16):7276-80.

258.   Perl K, Ushakov K, Pozniak Y, Yizhar-Barnea O, Bhonker Y, Shivatzki S, et al. Reduced changes in protein compared to mRNA levels across non-proliferating tissues. BMC Genomics. 2017;18(1):305.

259.   Da Silva L, Bray JK, Bulut G, Jiang J, Schmittgen TD. Method for improved integrity of RNA isolated from Matrigel cultures. MethodsX. 2020;7:100966.

260.   Schrader C, Schielke A, Ellerbroek L, Johne R. PCR inhibitors - occurrence, properties and removal. J Appl Microbiol. 2012;113(5):1014-26.

261.   Chang YH, Hsieh SL, Chao Y, Chou YC, Lin WW. Proinflammatory effects of LIGHT through HVEM and LTbetaR interactions in cultured human umbilical vein endothelial cells. J Biomed Sci. 2005;12(2):363-75.

262.   Greenland S, Senn SJ, Rothman KJ, Carlin JB, Poole C, Goodman SN, et al. Statistical tests, P values, confidence intervals, and power: a guide to misinterpretations. Eur J Epidemiol. 2016;31(4):337-50.

263.   Royston P, Altman DG, Sauerbrei W. Dichotomizing continuous predictors in multiple regression: a bad idea. Stat Med. 2006;25(1):127-41.

264.   Leeflang MM, Moons KG, Reitsma JB, Zwinderman AH. Bias in sensitivity and specificity caused by data-driven selection of optimal cutoff values: mechanisms, magnitude, and solutions. Clin Chem. 2008;54(4):729-37.

265.   Veerman K, Tardiveau C, Martins F, Coudert J, Girard JP. Single-Cell Analysis Reveals Heterogeneity of High Endothelial Venules and Different Regulation of Genes Controlling Lymphocyte Entry to Lymph Nodes. Cell Rep. 2019;26(11):3116-31.e5.

266.   Bistrup A, Tsay D, Shenoy P, Singer MS, Bangia N, Luther SA, et al. Detection of a sulfotransferase (HEC-GlcNAc6ST) in high endothelial venules of lymph nodes and in high endothelial venule-like vessels within ectopic lymphoid aggregates: relationship to the MECA-79 epitope. Am J Pathol. 2004;164(5):1635-44.

267.   Milutinovic S, Gallimore A. The link between T cell activation and development of functionally useful tumour-associated high endothelial venules. Discov Immunol. 2023;2(1):kyad006.

268.   Hindley JP, Jones E, Smart K, Bridgeman H, Lauder SN, Ondondo B, et al. T-cell trafficking facilitated by high endothelial venules is required for tumor control after regulatory T-cell depletion. Cancer Res. 2012;72(21):5473-82.

269.   Joshi NS, Akama-Garren EH, Lu Y, Lee DY, Chang GP, Li A, et al. Regulatory T Cells in Tumor-Associated Tertiary Lymphoid Structures Suppress Anti-tumor T Cell Responses. Immunity. 2015;43(3):579-90.

270.   Mitsuoka C, Sawada-Kasugai M, Ando-Furui K, Izawa M, Nakanishi H, Nakamura S, et al. Identification of a major carbohydrate capping group of the L-selectin ligand on high endothelial venules in human lymph nodes as 6-sulfo sialyl Lewis X. J Biol Chem. 1998;273(18):11225-33.

271.   Kimura N, Mitsuoka C, Kanamori A, Hiraiwa N, Uchimura K, Muramatsu T, et al. Reconstitution of functional L-selectin ligands on a cultured human endothelial cell line by cotransfection of alpha1-->3 fucosyltransferase VII and newly cloned GlcNAcbeta:6-sulfotransferase cDNA. Proc Natl Acad Sci U S A. 1999;96(8):4530-5.

272.   Erdmann I, Scheidegger EP, Koch FK, Heinzerling L, Odermatt B, Burg G, et al. Fucosyltransferase VII-deficient mice with defective E-, P-, and L-selectin ligands show impaired CD4+ and CD8+ T cell migration into the skin, but normal extravasation into visceral organs. J Immunol. 2002;168(5):2139-46.

273.   Hiraoka N, Petryniak B, Kawashima H, Mitoma J, Akama TO, Fukuda MN, et al. Significant decrease in alpha1,3-linked fucose in association with increase in 6-sulfated N-acetylglucosamine in peripheral lymph node addressin of FucT-VII-deficient mice exhibiting diminished lymphocyte homing. Glycobiology. 2007;17(3):277-93.

274.   Yang J, Rosen SD, Bendele P, Hemmerich S. Induction of PNAd and N-acetylglucosamine 6-O-sulfotransferases 1 and 2 in mouse collagen-induced arthritis. BMC Immunol. 2006;7:12.

275.   Chen Y, Wu Y, Yan G, Zhang G. Tertiary lymphoid structures in cancer: maturation and induction. Front Immunol. 2024;15:1369626.

276.   An D, Chen G, Cheng WY, Mohrs K, Adler C, Gupta NT, et al. LTβR Agonism Promotes Anti-Tumor Immune Responses via Modulation of the Tumor Microenvironment. Cancer Res. 2024.

277.   Jansen CS, Prokhnevska N, Master VA, Sanda MG, Carlisle JW, Bilen MA, et al. An intra-tumoral niche maintains and differentiates stem-like CD8 T cells. Nature. 2019;576(7787):465-70.

FoxP3+ regulatory T cells were independent predictors of disease-free survival in oral tongue squamous cell carcinoma whereas tumour-associated CD163+ macrophages and high endothelial venules were not

Ibrahim Afolabi Abdulsalam, Kjersti Sellæg, Faith O. Benebo, Nancy C. Ojei, Beate Hegge, Sonja Eriksen Steigen, Lars Uhlin-Hansen, Inger-Heidi Bjerkli, Anna M. Wirsing, Synnøve Norvoll Magnussen, Elin Hadler-Olsen

Manuscript

FoxP3+ regulatory T cells were independent predictors of disease-free survival in oral tongue squamous cell carcinoma whereas tumour-associated CD163+ macrophages and high endothelial venules were not

Ibrahim Afolabi Abdulsalam[1*], Kjersti Sellæg[1], Faith O. Benebo[2], Nancy C. Ojei[2], Beate Hegge[1], Sonja E. Steigen[1,3], Lars Uhlin-Hansen[1,3], Inger-Heidi Bjerkli[1,3], Anna M. Wirsing[1,3], Synnøve Norvoll Magnussen[1], Elin Hadler-Olsen[1,4*]

[1]Department of Medical Biology, Faculty of Health Sciences, UiT – The Arctic University of Norway, Tromsø, Norway, [2]Department of Community Medicine, Faculty of Health Sciences, UiT – The Arctic University of Norway, Tromsø, Norway, [3]Department of Clinical Pathology, University Hospital of North Norway, Tromsø, Norway, [4]The Public Dental Health Service Competence Center of Northern Norway, Tromsø, Norway

*Corresponding authors:
Elin Hadler-Olsen, elin.hadlerolsen@tromsfylke.no/elin.hadler-olsen@uit.no
Ibrahim Afolabi Abdulsalam, ibrahim.abdulsalam@uit.no

Keywords: Oral cancer, oral tongue squamous cell carcinoma (OTSCC), biomarker, regulatory T cells, tumour-associated macrophages (TAMs), tumour-associated high endothelial venules (TA-HEVs), Immunohistochemistry

Abstract

Introduction and aims: Oral squamous cell carcinoma of the tongue (OTSCC) is the most common OSCC subtype characterized by significant immune cell infiltration. In head and neck SCC, biomarkers such as tumour-associated high endothelial venules (TA-HEVs), and CD163+ TA-macrophages (TAMs) have been associated with favourable and unfavourable prognosis respectively, whereas the prognostic value of FoxP3+ regulatory T cells (Tregs) is controversial. This study aims to evaluate the prognostic roles of these biomarkers individually and in combination within a homogeneous cohort of OTSCC patients. **Materials and methods**: This retrospective study included 126 primary, treatment-naïve OTSCC patients diagnosed between 2005 and 2009 in Norway. Immunohistochemical staining was performed on OTSCC patient tissue to determine the densities of PNAd+ TA-HEVs, CD163+ TAMs, and FoxP3+Tregs. A high and low score was generated using either manual or automated methods. Associations between the scores and clinical and pathological variables were analysed by cross-tabulations and Chi-square tests. The markers' potential for predicting 5-year disease-specific survival (DSS) were assessed with Kaplan-Meier survival analyses, the Log-rank test and multivariate Cox regression analyses. **Results**: Our cohort comprised 60% male patients with a mean age of 62.9 years. High TA-HEV score and low FoxP3 score were significantly associated with improved five-year DSS in univariate analyses, but only FoxP3 score remained an independent predictor in multivariate models. The combination of a high TA-HEVs and a low FoxP3 score identified a subgroup of patients with particularly favourable outcome. CD163+ score was not significantly associated with DSS, and combining CD163 scores with TA-HEVs or FOXP3 scores reduced their individual prognostic value. **Conclusions:** FoxP3+ Tregs were independent predictors of disease-specific survival in OTSCC, whereas TA-HEVs and CD163+ macrophages were not. These findings support the potential of FoxP3 as a prognostic marker and its utility in clinical practice for improving patient stratification and treatment outcomes in OTSCC. Further research is necessary to confirm the prognostic value of FoxP3 alone or in combination with TA-HEV score in larger cohorts and to explore the underlying mechanisms.

Introduction

Oral squamous cell carcinoma (OSCC) is a major subtype of head and neck cancers (1). OSCC arises from the mucosal epithelium in the oral cavity (2,3), with excessive tobacco and alcohol consumption being the best-established risk factors (4–6). The most common OSCC subsite is the mobile tongue accounting for approximately 40% of cases, denoted oral tongue SCC (OTSCC) (1,7). The tumours are generally heterogeneous (8), locally invasive and display a significant risk of cervical lymph node metastases (9,10). Surgery is the primary treatment for most OSCC patients, often combined with radiotherapy. Chemotherapy and immunotherapy are rarely employed for primary tumours (6). Currently, therapy is largely based on their Tumour-Node-Metastasis (TNM) stage (11). Nonetheless, patients with identical TNM stages frequently exhibit different therapeutic outcomes (12). The identification of new biomarkers that reflect OSCC pathogenesis, patient outcome (13) and the biological heterogenicity of these tumours therefore becomes imperative to improve treatment approaches and disease management (12).

OSCCs are highly immunogenic tumours, usually characterised by considerable immune cell infiltration (12). Tumour infiltrating lymphocytes (TILs) (14) and especially cytotoxic CD8 + T cells are associated with improved patients' survival (15). Studies have found that TILs may induce the development of specialised blood vessels known as high endothelial venules (HEVs) (16). HEVs can facilitate additional TIL recruitment into tumours, strengthening the anti-tumour immune response which in turn may improve clinical outcomes. HEVs found within the tumour microenvironment (TME), designated as tumour associated (TA)-HEVs (16,17), have been associated with better prognosis in HNSCC (18), particularly in OSCC (19,20) We have previously demonstrated a significant association between presence of TA-HEVs, elevated lymphocytic infiltration and favourable clinical outcome in OSCC patients. Additionally, we identified TA-HEVs as an independent positive prognosticator in an OSCC patient cohort (19).

Macrophages residing in the TME are referred to as TA-macrophages (TAMs) (21) and are often the most prevalent of all the immune cells (22). TAMs are highly plastic and exhibit at least two phenotypes depending on their activation status; M1(classically activated) exhibiting pro-inflammatory and tumour-suppressive functions or M2 (alternatively activated) which are anti-inflammatory and pro-oncogenic (21,23,24). TAMs mostly exhibit the M1 phenotype during the early stages of OSCC development. However, as the tumour progresses, TAMs can polarize to an M2 phenotype via a variety of pathways, such as through their interaction with CSF-1-expressing tumour cells (21,25). CD163 (also known as M2 macrophage class B scavenger receptor) is widely recognized as a marker for M2 macrophages (24). The presence of CD163+ TAMs has previously

been associated with unfavourable patient outcomes in HNSCC (26). Additionally, in OSCC, increased densities of CD163+ TAMs was positively associated with both histopathological stage (27) and LN metastasis (21,28). This implies a significant correlation between the density of M2-polarized TAMs and OSCC advancement (21,28).

An immunosuppressive and pro-tumoral TME can be promoted by M2-polarized TAMs, via recruitment of CD4+FoxP3+ TILs, known as regulatory T cells (Tregs). Tregs release anti-inflammatory cytokines (29) that repress pathological and physiological immune responses (30,31). The prognostic significance of Tregs in cancer has been quite controversial. High densities of FoxP3+ Tregs have been associated with better survival in HNSCC (14) and established to be an independent prognosticator for improved overall survival in several solid tumours (32,33). Conversely, increased influx of FoxP3+ Tregs was correlated with lymph node metastasis in colorectal cancer (34), and worsened prognosis in OSCC (35). Moreover, high infiltration of FoxP3+ Tregs in OTSCC has been reported to be associated with poor survival (36).

In summary, TA-HEVs, Tregs and CD163+ TAMs are inherent constituents of the TME that play critical roles in tumour progression, immunoregulation, and TME modulation (19,22,37). Studies indicate that TA-HEVs (19), and CD163+ TAMs (21,27,28) exhibit favourable and unfavourable prognostic impact on OSCC, respectively, while the role of FoxP3+ remains controversial (14,30). Before these potential prognostic markers can be implemented in clinical practice, their relevance must be confirmed in several independent patient cohorts. The aim of the current study was to evaluate the prognostic value of these biomarkers individually and combined, in a homogeneous cohort of OTSCC patients.

Materials and methods

Patient cohort and specimens

This study is part of the retrospective Norwegian Oral Cancer Study (NOROC) (38). In the present study, we included 126 patients diagnosed with primary, treatment naïve OSCC of the mobile tongue (OTSCC). Patients were diagnosed between January 1st, 2005, and December 31st, 2009, at one of the four Norwegian university hospitals treating OSCC (Bergen, Oslo, Trondheim, and Tromsø). Clinical and pathological data were extracted from the patients' hospital files and pathology reports. The cause of death was retrieved from the Cause of Death Registry if not reported in the patients' hospital files. The last day of follow up was June 1st, 2015 (38). Experienced and calibrated pathologists reclassified the tumours according to the current TNM classification of Malignant

tumours, 8th edition, 2016, as established by the Union for International Cancer Control (UICC) (11). Identification and recruitment of patients as well as retrieval of clinical data has been described previously (39). The Regional Committee for Medical and Health Research Ethics of Northern Norway gave its approval to the use of the patients' specimen and the collecting of clinical data (Protocol number 2013/1786 and 2015/1381). Patients still alive were given the opportunity to opt-out of the study, but the need to obtain written or oral consent was waived. The Reporting Recommendations for Tumour Marker Prognostic Studies (REMARK) guidelines (40) were followed in this study.

Inclusion and exclusion criteria

The inclusion criteria for the current study were availability of tissue from primary OTSCC tumour, clinical data and follow-up, and treatment with curative-intent. Excluded were patients with previous radiotherapy involving the head and neck, patients formerly diagnosed with oral or pharyngeal cancer, malignancy with histopathology different from SCC and patients receiving palliative treatment only.

Immunohistochemical staining

Immunohistochemistry (IHC) was used to stain four micrometre-thick formalin-fixed, paraffin-embedded (FFPE) tissue sections for the MECA-79 epitope to detect Peripheral Node Addressin (PNAd) specifically expressed by HEVs (41) and the immune cell markers FoxP3 and CD163 to detect regulatory T cells and M2 macrophages, respectively. Both automated (CD163) and manual (PNAd and FoxP3) staining procedures were employed.

CD163 staining was performed, using the automated IHC slide staining system Ventana Benchmark, XT (Ventana, Tucson, AZ, USA), at the Diagnostic Clinic-Department of Clinical pathology, University Hospital of North Norway. A Ventana Enhanced DAB detection kit (Ventana, Tucson, AZ) and commercially available prediluted monoclonal mouse primary CD163 antibody (Clone MRQ-26 from Roche, Cell marque, Cat.No: 760-4437) were used and staining was completed in accordance with the standard procedures. In summary, deparaffinized and blocked sections were heated in a 0.01M sodium citrate buffer at pH 6.0 for antigen retrieval. For visualisation, an antibody cocktail of horseradish peroxidase (HRP)-labelled goat anti-mouse IgG/IgM and mouse anti-rabbit secondary antibodies (Ventana UltraView Universal DAB Detection Kit, Roche, Mannheim, Germany, Cat.No 760–500) as well as diaminobenzidine were used. The duration of secondary antibody incubation was regulated by the manufacturer. Each run included a control slide with known positivity for each antibody (tonsil or lymph node) (42).

For PNAd and FoxP3 staining, tissue sections were incubated at 60 °C for at least one hour or overnight, deparaffinized in xylene and rehydrated in graded ethanol baths. Antigen retrieval was performed by boiling the sections in sodium citrate buffer (pH 6.0) for 20 minutes and 3% H_2O_2 (Dako Glostrup Denmark) was used for blocking of endogenous peroxidase activity. Sections were incubated with rat anti-PNAd (1:25, clone: MECA-79, Biolegend, San Diego, USA, Cat.No 120801,) or mouse anti-FoxP3 antibody (1:50, Clone:235/E7, Abcam, Cambridge, UK, Cat.No ab20034,) in room temperature for 30 minutes or at 4°C overnight, respectively. Detection was thereafter carried out by incubating sections for 30 minutes with HRP-labelled secondary goat anti-rat light chain (1:250, Millipore, Temecula, California, USA, Cat.No AP202P,) or anti-mouse IgG antibody (1:100, Sigma-Aldrich, St. Louis, Missouri, USA, Cat.No A2554), followed by diaminobenzidine (Dako EnVision + System-Horseradish Peroxidase, Dako) for visualization. Harris haematoxylin (Sigma-Aldrich, St. Louis, Missouri, USA) was used for counterstaining. FFPE human lymph nodes or spleen tissue were used as positive controls for PNAd and FoxP3, respectively, and for negative control the primary antibody was omitted. Assessment of PNAd antibody specificity was performed as described by Wirsing and colleagues (19).

Immunohistochemical evaluation

Stained sections were scanned with the Olympus VS120 automated slide scanner (Olympus Germany). For PNAd and CD163, the OlyVIA software version 1.06 (Olympus Germany) was used to digitally capture and evaluate micrographs, while QuPath software version 0.3.2. (43) was used to evaluate whole slide Foxp3-stained images.

PNAd+ TA-HEVs: Two trained observers who were calibrated prior to the study, independently performed identification, histological evaluation, and manual scoring of IHC-stained TA-HEVs. Manual scoring was chosen over automated scoring because HEVs have a unique morphology that requires expert visual judgement for reliable identification and quantification (44,45). TA-HEVs were defined as distinct brown PNAd staining in aggregates of cells greater than 1. To eliminate HEVs that were not TA, only HEVs that were present within one field of vision of tumour cells, were considered. At a low power magnification (5x), five tissue areas with the highest TA-HEVs density (hotspots), were identified for each tissue section. Micrographs of these TA-HEVs hotspots were captured at X20 power magnification. The number of TA-HEVs in each hotspot was manually counted and the mean number per hotspot calculated for each tumour section as previously described (19). In situations of disparate scores between the observers, the staining was re-evaluated and discussed to reach an

agreement. An inter-rater reliability test was conducted to evaluate the consistency and agreement between the observers' scores.

FoxP3+ Tregs: QuPath was used to evaluate FoxP3 staining because it possesses advanced cell segmentation algorithms that enables identification of individual cells and nuclei (46). Automated estimation of stain vectors was performed in a representative image to optimize digital separation of the Haematoxylin and DAB channels and was applied to all images before cell detection. Parameters for positive cell detection were optimized on several images before deciding on a threshold level (0.100). Automated positive cell detection was compared to manual count of positively stained cells in 15 areas corresponding to 20X field of view (1100x1100µm; 950331µm^2) to check whether the settings were satisfactory. The threshold was adjusted to 0.150 or 0.175 for a few images with particularly strong staining intensities and/or high background. Five circular annotations corresponding to 20X field of view were applied to areas with the highest density of FoxP3 cells, referred to as hotspots, in all sections. The number of FoxP3 cells in each of the five hotspots was summated and the mean number per hotspot was calculated for each section. Each hotspot contained tumour cells and stroma. Areas with high background staining due to red blood cells, blood vessels or tissue artefacts were excluded from annotations to prevent false positive count.

CD163+ TAMs: CD163 staining of M2 TAMs showed cytoplasmic and membrane staining in cells that were irregularly shaped, overlapping and appearing in clusters, making them difficult to count as individual cells. Thus, the stain was quantified as the mean percentage of positively stained area in five hotspots, each with a magnification of 20X. Quantification was performed using ImageJ (Fiji version 2.9.0/1.54d; Java 1.8.0_322) (47). This is because the software sufficiently handles overlapping staining and accounts for spatial distribution of CD163+ macrophages (48). Briefly and chronologically, using ImageJ, micrographs of CD163+ hotspots were selected and converted into 8-bit image. Under measurements, the area and area fraction boxes were checked to set the quantification of the micrograph. Next, the threshold was adjusted to ensure that only the positively stained CD163+ cells were visible by setting the positive and negative (including background) areas to display contrasting colours. Background staining is a major challenge during quantification of CD163+ macrophages. On each image to be quantified, background staining was eliminated while ensuring that the total area of interest to be quantified remained unchanged before and after background stain elimination. (49). Subsequently, we juxtaposed the original unedited CD163+ micrograph with the ImageJ adjusted micrograph to ensure the best possible elimination of the background staining. This also aided identifying an optimal threshold as the staining intensities of sections varied somewhat. We used 3 different thresholds: 165, 175 and 150, for weak, optimal, and

extremely high staining intensities respectively after a consensus among the observers. The quantification was expressed as the mean percentage of the total area measured in the five hotspots.

Dichotomization for marker scoring

For each patient, we calculated a mean staining score per hotspot for the different markers. Based on these mean scores, we divided the patient sample into quintiles (20%) where the first and fifth quintiles had the lowest and highest scores, respectively for each of the three markers. We tested cut-off points for dichotomizing the scores into low and high staining between these quintiles, to identify the best separation of survival curves based on median survival time (50). For all markers, cut-off between the first quintile (low density) and the combined second through fifth quintiles (high density), gave the best separation of survival times and was used for dichotomization. Additionally, we generated variables based on combinations of high and low expression for pairs of markers to assess whether considering two markers together could enhance their prognostic value.

Clinical and pathological variable coding

In this study, our primary outcome was five-year disease-specific survival (DSS), from the time of diagnosis. Our independent variables were the IHC scores (high versus low) for TA-HEVs, CD163 and FoxP3. Covariates included were sex, age, T-status, N-status, and tumour grade. Based on age at time of diagnosis, patients were divided into a younger (≤ 60 years) and an older (> 60 years) age group. T-status were used both without recoding as well as dichotomized into T1 vs T2/T3 to increase statistical power in regression analyses. The N status was based on histopathological analysis (pN) for patients who underwent neck surgery, otherwise it was based on clinical/radiological examination (cN). It was dichotomized into: N0 (no signs of lymph node involvement pathologically and/or clinically) and N+ (lymph node metastasis). Tumour grade was based on the histopathological differentiation where the moderate and well-differentiated tumours were categorized as low-grade tumours, and poorly differentiated tumours were categorized as high-grade. This approach improves power, simplifies interpretation, and is consistent with the underlying biology of tumours (51,52).

Statistical analysis

The intraclass correlation (ICC) was used to assess the inter-rater reliability of the HEV scores between the two observers. The ICC estimates and their 95% confidence intervals were calculated using a 2-way mixed-effects model based on a mean rating (K=2) and absolute agreement (53). The distribution of variables across IHC scores for TA-HEVs, CD163 and FoxP3 were analysed with cross-tabulations and the statistical significance of differences were assessed with the Pearson's Chi-square test. Kaplan-Meier analyses were used to calculate mean DSS time with 95% confidence

intervals (CI) and survival curves, and statistical significance was analysed with the Log-rank test. Cox-regression analyses were used to calculate hazard ratio (HR) for disease specific death with 95% (CI). The proportional hazard assumption of the cox regression models was tested using the Schoenfeld residual test, showing that our analysis did not violate the assumption. We tested for significant multiplicative interactions by including the cross-products in the regression models, none were found. Differences between groups with a p-value < 0.05 were considered statistically significant. Stata software version 18.0 (Stata Corp, College Station, TX, USA) and Microsoft Excel 2013 were used for all statistical analyses (Microsoft, Redmond, WA).

Results

This study includes a cohort of 126 patients (60% men) diagnosed with OTSCC between January 1st, 2005, and December 31st, 2009, in Norway. Mean age at diagnosis was 62.9 years (standard deviation 14.2, range 24-90 years). The characteristics of the cohort are summarized in Table 1. At the time of diagnosis, one third of the patients had T1 tumours and 85% had no lymph node metastasis. During the 5-year follow up period 30% of the patients had died of the disease.

Identification, distribution and staining characteristics of TA-HEVs, CD163, and FOXP3+ cells in OTSCC tissues

TA-HEVs were easily identifiable and unevenly distributed in the tumour stroma. They appeared as brown-stained vessel structures with or without a visible lumen (Fig.1). TA-HEVs displayed heterogeneous morphology with varied vessel wall thickness, and the staining appeared patchy in some vessel walls. Most TA-HEVs were found in areas with a dense lymphocyte infiltration. Only one tumour specimen was negative for TA-HEVs. The interclass correlation coefficient of the two observers' TA-HEVs scores was 0.997 (95% CI: 0.995 – 0.998), which is regarded an excellent reliability (53). In most tumours, CD163 staining was quite prominent with positive cells densely distributed throughout the tumour stroma. CD163 staining was seen in both the cell membrane and cytoplasm of cells with irregular shape (Fig.1). FoxP3+ cells were typically observed infiltrating the stroma rather than the tumour areas. Most FoxP3+ cells exhibited a small size with a darkly stained and round-shaped nucleus, suggestive of lymphocytes (Fig.1). However, the exact location of FoxP3+ staining in the nucleus versus cytoplasm was difficult to assess due to sparse cytoplasm in most FoxP3+ cells. They were evenly dispersed in areas with prominent lymphocyte infiltration. No significant associations were seen between scores for the three markers, although tumours with high FoxP3 score tended to also have high CD163 score (p=0.088) (Table 1). Distribution of patient characteristics across the scores for TA-HEVs, FoxP3 and CD163 IHC staining is described in Table

1. Large (T3) tumours more often had a high FoxP3 score than T1 and T2 tumours (p=0.034). Furthermore, 5-year DSS rate was significantly higher for patients with TA-HEVs high than TA-HEVs low score (p=0.03), whereas patients with high FoxP3 score had significantly lower 5-year DSS rate than those with FoxP3 low tumours (p=0,009, Table 1). Otherwise, there were no significant differences in clinical or pathological characteristics based on the IHC markers (Table 1).

Survival analyses

Mean DSS time stratified on clinicopathological variables and staining characteristics for TA-HEVs, FoxP3 and CD163 was calculated by Kaplan-Meier analyses and the statistical differences were analysed by the Log-rank test (Table 2). Survival time varied significantly with T-status, N-status, TA-HEVs-status and FoxP3 status, and the same variables had significant impact on the hazard ratio (HR) in unadjusted Cox-regressions (Table 2). High T-stage, N+ stage and high FoxP3 score were associated with shorter DSS and higher risk of dying of the disease, whereas high TA-HEVs score was associated with lower risk of dying of the disease (Table 2). Survival curves based on TA-HEV, CD163, and FoxP3 scores are displayed in Fig.2A-C. We also assessed if combinations of high and low scores for the three markers could increase their prognostic potential. The combination of TA-HEVs and FoxP3 scores identified groups with very different survival trajectories, where those having a combination of a high TA-HEVs score and a low FoxP3 score had none suffering 5-year disease-specific death, whereas those having a combination of TA-HEVs low and FoxP3 high scores had particularly low 5-year DSS (Figure 2d). Except for the Log-rank test, survival statistics could not be computed for these combinations due to lack of disease-specific death in one of the groups (all censored). Combinations of TA-HEVs and CD163 scores (Fig.2E) or FoxP3 and CD163 scores (Fig.2F) showed lower prognostic potential than the individual TA-HEVs (Fig.2A) and FoxP3 (Fig.2D) scores.

To adjust for putative confounding factors, we further ran multivariate Cox regression analyses. We ran separate models for each of the markers as well as a model including scores for both TA-HEVs and FoxP3 as these markers seemed to enhance each other (Table 3). A high FoxP3 score was an independent risk factor for disease-specific survival both when included as the only IHC marker (HR=8.02, 95% CI: 1.77, 36.44) and in the model including both FoxP3 and TA-HEV score (OR=27.77, 95% CI: 3.86, 199.77). TA-HEVs and CD163 score were not significantly associated with DSS in the adjusted models, but the prognostic value of TA-HEVs was substantially higher in the model including both TA-HEVs and FoxP3 (HR=2.39, 95% CI:0.96, 5.98 for low versus high TA-HEV score) compared to the model without FoxP3 score (HR=1.18, 95% CI: 0.49, 2.80). In line with previous studies on this cohort (19,38,39), N-status and tumour grade were significantly

associated with DSS in all models. Age and T-status showed borderline significant associations with DSS in the various models, most often with a p-value >0.05 (Table 3). There were no significant multiplicative interactions between variables included in the models.

Discussion

In the present study we have explored the prognostic value of TA-HEVs, M2 TAMs and Tregs in OTSCC, identified by immunohistochemical staining for PNAd, CD163, and FoxP3, respectively. We found that a high number of FoxP3+ cells in the TME was an independent predictor of increased risk of disease-specific death within five years of the OTSCC diagnosis. A high TA-HEVs score was significantly associated with higher 5-year DSS in univariate-, but not in multivariate analyses. Additionally, OTSCCs with a combination of a high TA-HEV score and a low FoxP3 score were associated with a particularly favourable outcome, whereas tumours with the opposite combination (low TA-HEV and high FoxP3 score) showed the worst survival outcome in univariate analyses. CD163 score was not significantly associated with DSS in any of the analyses.

In the TME, there is a complex interplay between anti-inflammatory and pro-inflammatory cells, which may impact disease progression and patient outcomes (54). Transformed cells express neoantigens that evoke an adaptive immune response, which may supress tumour growth (14,55). Cytotoxic T cells are major effector cells in the anti-tumour immune response, and TA-HEVs are important gateways for their entry into the TME (16,17,56). However, in line with the trajectory of immune responses to other challenges, the anti-tumour immune response is usually downregulated over time, partly due to the influence of anti-inflammatory cells. M2 macrophages and Tregs often cooperate to establish an immunosuppressive TME (57,58). CD163+ macrophages produce and release immunosuppressive cytokines, including interleukin-10 (IL-10) and TGF-Beta β, which play a crucial role in recruiting and activating FoxP3+ Tregs (59,60). Tregs have been shown to inhibit the proliferation of effector T cells within solid malignancies (61,62). In line with this, we found that the density of Tregs was significantly higher in T3 tumours relative to T1 or T2 tumours, suggesting a shift towards a more suppressive and anti-inflammatory TME as the tumours progress. However, no significant associations were found between TA-HEVs or M2 TAMs with T stage, and none of the markers varied significantly with N stage. Furthermore, there were no significant association between high- and low scores of the various markers, although there was a tendency that tumours with high CD163 score also had a high FoxP3 score. This demonstrates the intricate interactions among the

immune components in OTSCC, with Tregs playing a significant role in larger tumours while TA-HEVs and M2 TAMs may have a more subtle or independent function.

Previous studies on the prognostic value of FoxP3+ Treg show conflicting results. A high density of FoxP3+ Tregs was significantly associated with improved survival in patients with lymphoma (63), bladder (64), colorectal cancer (65), and HNSCC (14,32). However, a high density of infiltrating FOXP3+ Tregs was associated with an unfavourable prognosis in cervical (66), liver (67), ovarian (68), pancreatic (69) and renal cancer (70). Additionally, a meta-analysis comprising seventeen solid cancers found that an elevated influx of FoxP3+ Tregs significantly correlated with poor prognosis (33). In line with results from the present study, most studies on OTSCC, most studies found that a low number of FoxP3+ Tregs was associated with longer survival (71,72). Qualitative analysis of FoxP3 immunofluorescence staining has shown that FoxP3 may reside either in the nucleus or the cytoplasm of lymphocytes. Cytoplasmic FoxP3 expression was associated with a favourable prognosis, whereas nuclear expression was significantly associated with tumour recurrence and poor prognosis in OTSCC (73). The nuclear localization of FoxP3 is essential for the transcriptional regulatory activity and immunosuppressive function of Tregs (74). This suggests that the different subcellular localization of FoxP3 in Tregs (cytoplasmic vs nuclear) may explain the contrasting associations between FoxP3+ Tregs and prognosis in OTSCC, emphasizing the complex role of FoxP3 in tumour immunity (14). We did not discriminate between nuclear and cytoplasmic FoxP3 staining in the

HEVs have previously been found to be a promising prognostic factor in several cancers (16,56) including OSCC (19,20).In the present study a high TA-HEV score was associated with longer DSS in univariate analyses, but not in multivariate analyses. However, the regression model including both TA-HEVs and FoxP3 score markedly increased the statistical significance of the TA-HEVs score, suggesting that prognostic value TA-HEVs is improved when they are assessed within a broader immunological milieu, particularly alongside FoxP3+ Tregs.

Indeed, when we assessed survival in patients with various combinations of high and low TA-HEV and FoxP3 scores, we found that patients having tumours with a high TA-HEV score and a low FoxP3 score had the highest survival rate over the 5-year follow-up period. Conversely, patients with tumours with a low TA-HEV score and a high FoxP3 score had the lowest disease-specific survival rate.

Carcinogen-induced tumour models in mice have shown that FoxP3 depletion triggers the development of TA-HEVs, indicating that Tregs suppress HEV neogenesis. Specifically, Treg depletion facilitates T cell activation, which subsequently stimulates HEV development, promotes T

cell recruitment, and eventually leads to the elimination of cancer cells (75,76). This further supports the idea that the combined evaluation of TA-HEVs and FoxP3 in the TME may be of particular prognostic value as it may help identify tumours in the transition from a tumour-promoting to a tumour-suppressive immune response. Both TA-HEVs and FoxP3 staining was distinct and easy to interpret and score, either manually or digitally, suggesting that their implementation in clinical practice could be feasible.

Although, patients with a high CD163 score had a slightly lower 5-year DSS compared to those with a low score, there was no statistically significant association between CD163 density and survival in univariate or multivariate analyses. Additionally, assessing the CD163 score in combination with TA-HEVs or FoxP3 score reduced the prognostic value of TA-HEVs and FoxP3 compared to when these markers were assessed alone. Our findings are in conflict with several previous studies that reported a significant inverse correlation between the density of CD163+ TAMs and survival rates in numerous cancer types (77), including OSCC (12,24). Additionally, in colorectal cancer, CD163+TAMs have been found to promote an immunosuppressive TME (78). The dissonance could be due to a small cohort with and insufficient statistical power to detect a difference in survival, variability in the patient population, and method of scoring. Our study's approach, particularly the criteria for categorizing patients into high- and low-level CD163+ TAM infiltration groups, might not have adequately captured the nuances of TAM distribution within OTSCC tissues. Differences in CD163+TAM localization (e.g., tumour centre vs. invasive front or/ stromal vs. intra-tumoral expression) could alter their prognostic significance. Some studies have highlighted stromal expression, but not intratumoral CD163+ TAMs, as being significantly associated with patient survival (24,79). We did not differentiate between these locations in the present study, which might have lessened the impact of CD163+ TAMs on survival outcomes.

Study strengths and limitations.

Our study includes a homogeneous cohort of patients with primary OTSCC, with validated diagnosis and cause of death. Histopathological characteristics have been re-evaluated by calibrated, experienced clinical pathologists. The most important weakness of the study is the size of the cohort, which may have rendered some of the analyses under-powered with risk of type II errors. Due to small group sizes we had to merge some variable categories, with risk of losing information. In multivariate regressions the 95% CI was very large for several of the included parameters, most notably for the FoxP3 score. This indicates low precision, uncertainty in the effect size, and difficulty in assessing clinical relevance. It also poses challenges for research validity and the generalizability

of our results. Addressing these limitations typically requires larger sample sizes and better control of potential confounders to achieve higher statistical power and precision with meaningful outcomes.

Conclusion and Future Perspectives

We found FoxP3 to be an independent predictor of DSS, and that the combined evaluation of TA-HEVs score and FoxP3 score could identify patients with particularly favourable and unfavourable outcomes. Further research should aim to validate these findings in several, and preferably larger cohorts. This would provide a more comprehensive understanding of the immunological landscape in OTSCC and its implications for patient management.

References

1.   Rivera C. Essentials of oral cancer. Int J Clin Exp Pathol [Internet]. 2015 Sep 1 [cited 2023 Jan 20];8(9):11884–94. Available from: https://www.ncbi.nlm.nih.gov/pmc/articles/PMC4637760/

2.   Ng JH, Iyer NG, Tan MH, Edgren G. Changing epidemiology of oral squamous cell carcinoma of the tongue: A global study. Head Neck. 2017 Feb;39(2):297–304.

3.   Tan Y, Wang Z, Xu M, Li B, Huang Z, Qin S, et al. Oral squamous cell carcinomas: state of the field and emerging directions. Int J Oral Sci [Internet]. 2023 Sep 22 [cited 2023 Sep 27];15(1):1–23. Available from: https://www.nature.com/articles/s41368-023-00249-w

4.   Sung H, Ferlay J, Siegel RL, Laversanne M, Soerjomataram I, Jemal A, et al. Global Cancer Statistics 2020: GLOBOCAN Estimates of Incidence and Mortality Worldwide for 36 Cancers in 185 Countries. CA Cancer J Clin. 2021 May;71(3):209–49.

5.   Tenore G, Nuvoli A, Mohsen A, Cassoni A, Battisti A, Terenzi V, et al. Tobacco, Alcohol and Family History of Cancer as Risk Factors of Oral Squamous Cell Carcinoma: Case-Control Retrospective Study. Applied Sciences [Internet]. 2020 Jan [cited 2024 Jan 4];10(11):3896. Available from: https://www.mdpi.com/2076-3417/10/11/3896

6.   Zanoni DK, Montero PH, Migliacci JC, Shah JP, Wong RJ, Ganly I, et al. Survival outcomes after treatment of cancer of the oral cavity (1985–2015). Oral Oncology [Internet]. 2019 Mar 1 [cited 2023 Jan 20];90:115–21. Available from: https://www.sciencedirect.com/science/article/pii/S1368837519300387

7.   Stepan KO, Mazul AL, Larson J, Shah P, Jackson RS, Pipkorn P, et al. Changing Epidemiology of Oral Cavity Cancer in the United States. Otolaryngology–Head and Neck Surgery [Internet]. [cited 2023 Feb 16];n/a(n/a). Available from: https://onlinelibrary.wiley.com/doi/abs/10.1177/01945998221098011

8.   Chen D, Wang CY. Targeting cancer stem cells in squamous cell carcinoma. Precis Clin Med. 2019 Sep;2(3):152–65.

9.   Lampri ES, Chondrogiannis G, Ioachim E, Varouktsi A, Mitselou A, Galani A, et al. Biomarkers of head and neck cancer, tools or a gordian knot? Int J Clin Exp Med. 2015;8(7):10340–57.

10.   Koyfman SA, Ismaila N, Crook D, D'Cruz A, Rodriguez CP, Sher DJ, et al. Management of the Neck in Squamous Cell Carcinoma of the Oral Cavity and Oropharynx: ASCO Clinical Practice Guideline. J Clin Oncol. 2019 Jul 10;37(20):1753–74.

11.   Brierley JD, Gospodarowicz MK, Wittekind C. TNM Classification of Malignant Tumours. John Wiley & Sons; 2017. 272 p.

12.   Hadler-Olsen E, Wirsing AM. Tissue-infiltrating immune cells as prognostic markers in oral squamous cell carcinoma: a systematic review and meta-analysis. Br J Cancer. 2019 Apr;120(7):714–27.

13.   Gattuso G, Crimi S, Lavoro A, Rizzo R, Musumarra G, Gallo S, et al. Liquid Biopsy and Circulating Biomarkers for the Diagnosis of Precancerous and Cancerous Oral Lesions. Noncoding RNA. 2022 Aug 10;8(4):60.

14.   Wondergem NE, Nauta IH, Muijlwijk T, Leemans CR, van de Ven R. The Immune Microenvironment in Head and Neck Squamous Cell Carcinoma: on Subsets and Subsites. Curr Oncol Rep [Internet]. 2020 Jun 29 [cited 2023 Oct 23];22(8):81. Available from: https://doi.org/10.1007/s11912-020-00938-3

15.   Shimizu S, Hiratsuka H, Koike K, Tsuchihashi K, Sonoda T, Ogi K, et al. Tumor-infiltrating CD8+ T-cell density is an independent prognostic marker for oral squamous cell carcinoma. Cancer Med [Internet]. 2019 Jan 1 [cited 2023 Nov 23];8(1):80–93. Available from: https://www.ncbi.nlm.nih.gov/pmc/articles/PMC6346233/

16.   High endothelial venules (HEVs) in immunity, inflammation and cancer - PMC [Internet]. [cited 2023 Nov 23]. Available from: https://www.ncbi.nlm.nih.gov/pmc/articles/PMC8487881/

17.   Asrir A, Tardiveau C, Coudert J, Laffont R, Blanchard L, Bellard E, et al. Tumor-associated high endothelial venules mediate lymphocyte entry into tumors and predict response to PD-1 plus CTLA-4 combination immunotherapy. Cancer Cell [Internet]. 2022 Mar 14 [cited 2023 Nov 27];40(3):318-334.e9. Available from: https://www.sciencedirect.com/science/article/pii/S1535610822000046

18.   Karpathiou G, Dumollard JM, Gavid M, Casteillo F, Vieville M, Prades JM, et al. High endothelial venules are present in pharyngeal and laryngeal carcinomas and they are associated with better prognosis. Pathol Res Pract. 2021 Apr;220:153392.

19.   Wirsing AM, Rikardsen OG, Steigen SE, Uhlin-Hansen L, Hadler-Olsen E. Presence of tumour high-endothelial venules is an independent positive prognostic factor and stratifies patients with advanced-stage oral squamous cell carcinoma. Tumour Biol. 2016 Feb;37(2):2449–59.

20.   Li Q, Liu X, Wang D, Wang Y, Lu H, Wen S, et al. Prognostic value of tertiary lymphoid structure and tumour infiltrating lymphocytes in oral squamous cell carcinoma. Int J Oral Sci [Internet]. 2020 Sep 15 [cited 2024 Aug 28];12(1):1–8. Available from: https://www.nature.com/articles/s41368-020-00092-3

21.   Xue Y, Song X, Fan S, Deng R. The role of tumor-associated macrophages in oral squamous cell carcinoma. Front Physiol. 2022;13:959747.

22.   Caponio VCA, Zhurakivska K, Lo Muzio L, Troiano G, Cirillo N. The Immune Cells in the Development of Oral Squamous Cell Carcinoma. Cancers [Internet]. 2023 Jan [cited 2024 Apr 24];15(15):3779. Available from: https://www.mdpi.com/2072-6694/15/15/3779

23.   Cendrowicz E, Sas Z, Bremer E, Rygiel TP. The Role of Macrophages in Cancer Development and Therapy. Cancers (Basel). 2021 Apr 18;13(8):1946.

24.   Chohan MH, Perry M, Laurance-Young P, Salih VM, Foey AD. Prognostic Role of CD68+ and CD163+ Tumour-Associated Macrophages and PD-L1 Expression in Oral Squamous Cell Carcinoma: A Meta-Analysis. Br J Biomed Sci [Internet]. 2023 [cited 2023 Dec 4];80:11065. Available from: https://www.frontierspartnerships.org/articles/10.3389/bjbs.2023.11065/full

25.   Ai Y, Liu S, Luo H, Wu S, Wei H, Tang Z, et al. lncRNA DCST1-AS1 Facilitates Oral Squamous Cell Carcinoma by Promoting M2 Macrophage Polarization through Activating NF-κB Signaling. J Immunol Res [Internet]. 2021 Aug 8 [cited 2023 Feb 9];2021:5524231. Available from: https://www.ncbi.nlm.nih.gov/pmc/articles/PMC8369177/

26.   Bisheshar SK, van der Kamp MF, de Ruiter EJ, Ruiter LN, van der Vegt B, Breimer GE, et al. The prognostic role of tumor associated macrophages in squamous cell carcinoma of the head and neck: A systematic review and meta-analysis. Oral Oncology [Internet]. 2022 Dec 1 [cited 2023 Feb 9];135:106227. Available from: https://www.sciencedirect.com/science/article/pii/S1368837522005164

27.   Mori K, Hiroi M, Shimada J, Ohmori Y. Infiltration of M2 Tumor-Associated Macrophages in Oral Squamous Cell Carcinoma Correlates with Tumor Malignancy. Cancers (Basel) [Internet]. 2011 Sep 28 [cited 2023 Feb 10];3(4):3726–39. Available from: https://www.ncbi.nlm.nih.gov/pmc/articles/PMC3763393/

28.   Chaudhari N, Prakash N, Pradeep GL, Mahajan A, Lunawat S, Salunkhe V. Evaluation of density of tumor-associated macrophages using CD163 in histological grades of oral squamous cell carcinoma, an immunohistochemical study. J Oral Maxillofac Pathol. 2020;24(3):577.

29.   Boxberg M, Leising L, Steiger K, Jesinghaus M, Alkhamas A, Mielke M, et al. Composition and Clinical Impact of the Immunologic Tumor Microenvironment in Oral Squamous Cell Carcinoma. The Journal of Immunology [Internet]. 2019 Jan 1 [cited 2023 Dec 4];202(1):278–91. Available from: https://doi.org/10.4049/jimmunol.1800242

30.   Liu S, Liu D, Li J, Zhang D, Chen Q. Regulatory T cells in oral squamous cell carcinoma. J Oral Pathol Med. 2016 Oct;45(9):635–9.

31.   Wang J, Gong R, Zhao C, Lei K, Sun X, Ren H. Human FOXP3 and tumour microenvironment. Immunology [Internet]. 2023 [cited 2023 Dec 6];168(2):248–55. Available from: https://onlinelibrary.wiley.com/doi/abs/10.1111/imm.13520

32.   Seminerio I, Descamps G, Dupont S, de Marrez L, Laigle JA, Lechien JR, et al. Infiltration of FoxP3+ Regulatory T Cells is a Strong and Independent Prognostic Factor in Head and Neck Squamous Cell Carcinoma. Cancers (Basel) [Internet]. 2019 Feb 15 [cited 2024 Jun 12];11(2):227. Available from: https://www.ncbi.nlm.nih.gov/pmc/articles/PMC6406934/

33.   Shang B, Liu Y, Jiang S juan, Liu Y. Prognostic value of tumor-infiltrating FoxP3+ regulatory T cells in cancers: a systematic review and meta-analysis. Sci Rep [Internet]. 2015 Oct 14 [cited 2024 Jun 3];5:15179. Available from: https://www.ncbi.nlm.nih.gov/pmc/articles/PMC4604472/

34.   Suzuki H, Chikazawa N, Tasaka T, Wada J, Yamasaki A, Kitaura Y, et al. Intratumoral CD8+ T/FOXP3+ cell ratio is a predictive marker for survival in patients with colorectal cancer. Cancer Immunol Immunother [Internet]. 2010 May 1 [cited 2024 Jun 14];59(5):653–61. Available from: https://doi.org/10.1007/s00262-009-0781-9

35.   Hayashi T, Yoshikawa K, Suzuki S, Gosho M, Ueda R, Kazaoka Y. Tumor-infiltrating FoxP3+ T cells are associated with poor prognosis in oral squamous cell carcinoma. Clinical and Experimental Dental Research [Internet]. 2022 [cited 2023 Dec 6];8(1):152–9. Available from: https://onlinelibrary.wiley.com/doi/abs/10.1002/cre2.477

36.   Hanakawa H, Orita Y, Sato Y, Takeuchi M, Ohno K, Gion Y, et al. Regulatory T-cell infiltration in tongue squamous cell carcinoma. Acta Otolaryngol. 2014 Aug;134(8):859–64.

37.   Wirsing AM, Ervik IK, Seppola M, Uhlin-Hansen L, Steigen SE, Hadler-Olsen E. Presence of high-endothelial venules correlates with a favorable immune microenvironment in oral squamous cell carcinoma. Modern Pathology [Internet]. 2018 Jun 1 [cited 2023 Nov 23];31(6):910–22. Available from: https://www.sciencedirect.com/science/article/pii/S0893395222014922

38.   Bjerkli IH, Jetlund O, Karevold G, Karlsdóttir Á, Jaatun E, Uhlin-Hansen L, et al. Characteristics and prognosis of primary treatment-naïve oral cavity squamous cell carcinoma in Norway, a descriptive retrospective study. PLoS One. 2020;15(1):e0227738.

39.   Bjerkli IH, Laurvik H, Nginamau ES, Søland TM, Costea D, Hov H, et al. Tumor budding score predicts lymph node status in oral tongue squamous cell carcinoma and should be included in the pathology report. PLOS ONE [Internet]. 2020 Sep 25 [cited 2023 Dec 21];15(9):e0239783. Available from: https://journals.plos.org/plosone/article?id=10.1371/journal.pone.0239783

40.   Sauerbrei W, Taube SE, McShane LM, Cavenagh MM, Altman DG. Reporting Recommendations for Tumor Marker Prognostic Studies (REMARK): An Abridged Explanation and Elaboration. J Natl Cancer Inst. 2018 Aug 1;110(8):803–11.

41.   Girard JP, Springer TA. High endothelial venules (HEVs): specialized endothelium for lymphocyte migration. Immunol Today. 1995 Sep;16(9):449–57.

42.   Wirsing AM, Rikardsen OG, Steigen SE, Uhlin-Hansen L, Hadler-Olsen E. Characterisation and prognostic value of tertiary lymphoid structures in oral squamous cell carcinoma. BMC Clin Pathol. 2014;14:38.

43.   Bankhead P, Loughrey MB, Fernández JA, Dombrowski Y, McArt DG, Dunne PD, et al. QuPath: Open source software for digital pathology image analysis. Sci Rep [Internet]. 2017 Dec 4 [cited 2024 Apr 26];7(1):16878. Available from: https://www.nature.com/articles/s41598-017-17204-5

44.   Vella G, Guelfi S, Bergers G. High Endothelial Venules: A Vascular Perspective on Tertiary Lymphoid Structures in Cancer. Front Immunol. 2021;12:736670.

45.   Sawada J, Hiraoka N, Qi R, Jiang L, Fournier-Goss AE, Yoshida M, et al. Molecular Signature of Tumor-Associated High Endothelial Venules That Can Predict Breast Cancer Survival. Cancer Immunol Res [Internet]. 2022 Apr 1 [cited 2024 Apr 26];10(4):468–81. Available from: https://www.ncbi.nlm.nih.gov/pmc/articles/PMC8976767/

46.   Mi H, Gong C, Sulam J, Fertig EJ, Szalay AS, Jaffee EM, et al. Digital Pathology Analysis Quantifies Spatial Heterogeneity of CD3, CD4, CD8, CD20, and FoxP3 Immune Markers in Triple-Negative Breast Cancer. Front Physiol [Internet]. 2020 Oct 19 [cited 2024 Apr 26];11:583333. Available from: https://www.ncbi.nlm.nih.gov/pmc/articles/PMC7604437/

47.   A versatile toolbox for semi-automatic cell-by-cell object-based colocalization analysis | Scientific Reports [Internet]. [cited 2023 Dec 13]. Available from: https://www.nature.com/articles/s41598-020-75835-7

48.   Van Elsas MJ, Labrie C, Etzerodt A, Charoentong P, Van Stigt Thans JJC, Van Hall T, et al. Invasive margin tissue-resident macrophages of high CD163 expression impede responses to T cell-based immunotherapy. J Immunother Cancer [Internet]. 2023 Mar [cited 2024 May 1];11(3):e006433. Available from: https://jitc.bmj.com/lookup/doi/10.1136/jitc-2022-006433

49.   Quantification of Immunohistochemistry images using ImageJ | How to remove background in ImageJ [Internet]. 2021 [cited 2023 Dec 13]. Available from: https://www.youtube.com/watch?v=gxnWYhZ0z4k

50.   Wirsing AM, Bjerkli IH, Steigen SE, Rikardsen O, Magnussen SN, Hegge B, et al. Validation of Selected Head and Neck Cancer Prognostic Markers from the Pathology Atlas in an Oral Tongue Cancer Cohort. Cancers (Basel). 2021 May 14;13(10):2387.

51.   Nagy Á, Munkácsy G, Győrffy B. Pancancer survival analysis of cancer hallmark genes. Sci Rep. 2021 Mar 15;11(1):6047.

52.   Bradburn MJ, Clark TG, Love SB, Altman DG. Survival analysis part II: multivariate data analysis--an introduction to concepts and methods. Br J Cancer. 2003 Aug 4;89(3):431–6.

53.   Liljequist D, Elfving B, Roaldsen KS. Intraclass correlation – A discussion and demonstration of basic features. PLoS ONE [Internet]. 2019 [cited 2024 Apr 11];14(7). Available from: https://www.ncbi.nlm.nih.gov/pmc/articles/PMC6645485/

54.   Greten FR, Grivennikov SI. Inflammation and Cancer: Triggers, Mechanisms and Consequences. Immunity [Internet]. 2019 Jul 16 [cited 2024 May 8];51(1):27–41. Available from: https://www.ncbi.nlm.nih.gov/pmc/articles/PMC6831096/

55.   Xie N, Shen G, Gao W, Huang Z, Huang C, Fu L. Neoantigens: promising targets for cancer therapy. Sig Transduct Target Ther [Internet]. 2023 Jan 6 [cited 2024 Jun 21];8(1):1–38. Available from: https://www.nature.com/articles/s41392-022-01270-x

56.   Vella G, Hua Y, Bergers G. High endothelial venules in cancer: Regulation, function, and therapeutic implication. Cancer Cell [Internet]. 2023 Mar 13 [cited 2023 Nov 27];41(3):527–45. Available from: https://www.sciencedirect.com/science/article/pii/S1535610823000120

57.   Sun W, Wei FQ, Li WJ, Wei JW, Zhong H, Wen YH, et al. A positive-feedback loop between tumour infiltrating activated Treg cells and type 2-skewed macrophages is essential for progression of laryngeal squamous cell carcinoma. Br J Cancer [Internet]. 2017 Nov [cited 2024 May 8];117(11):1631–43. Available from: https://www.nature.com/articles/bjc2017329

58.   Huang L, Zhao Y, Shan M, Wang S, Chen J, Liu Z, et al. Targeting crosstalk of STAT3 between tumor-associated M2 macrophages and Tregs in colorectal cancer. Cancer Biol Ther [Internet]. [cited 2024 May 13];24(1):2226418. Available from: https://www.ncbi.nlm.nih.gov/pmc/articles/PMC10312030/

59.   Skytthe MK, Graversen JH, Moestrup SK. Targeting of CD163+ Macrophages in Inflammatory and Malignant Diseases. Int J Mol Sci [Internet]. 2020 Jul 31 [cited 2024 May 13];21(15):5497. Available from: https://www.ncbi.nlm.nih.gov/pmc/articles/PMC7432735/

60.   Basak U, Sarkar T, Mukherjee S, Chakraborty S, Dutta A, Dutta S, et al. Tumor-associated macrophages: an effective player of the tumor microenvironment. Front Immunol [Internet]. 2023 Nov 16 [cited 2024 May 13];14:1295257. Available from: https://www.ncbi.nlm.nih.gov/pmc/articles/PMC10687432/

61.   Kim JH, Kim BS, Lee SK. Regulatory T Cells in Tumor Microenvironment and Approach for Anticancer Immunotherapy. Immune Netw [Internet]. 2020 Feb 11 [cited 2024 May 13];20(1):e4. Available from: https://www.ncbi.nlm.nih.gov/pmc/articles/PMC7049587/

62.   Li Y, Zhang C, Jiang A, Lin A, Liu Z, Cheng X, et al. Potential anti-tumor effects of regulatory T cells in the tumor microenvironment: a review. Journal of Translational Medicine [Internet]. 2024 Mar 20 [cited 2024 May 13];22(1):293. Available from: https://doi.org/10.1186/s12967-024-05104-y

63.   Tzankov A, Meier C, Hirschmann P, Went P, Pileri SA, Dirnhofer S. Correlation of high numbers of intratumoral FOXP3+ regulatory T cells with improved survival in germinal center-like diffuse large B-cell lymphoma, follicular lymphoma and classical Hodgkin's lymphoma. Haematologica. 2008 Feb;93(2):193–200.

64.   Winerdal ME, Marits P, Winerdal M, Hasan M, Rosenblatt R, Tolf A, et al. FOXP3 and survival in urinary bladder cancer. BJU Int. 2011 Nov;108(10):1672–8.

65.   Salama P, Phillips M, Grieu F, Morris M, Zeps N, Joseph D, et al. Tumor-infiltrating FOXP3+ T regulatory cells show strong prognostic significance in colorectal cancer. J Clin Oncol. 2009 Jan 10;27(2):186–92.

66.   Shah W, Yan X, Jing L, Zhou Y, Chen H, Wang Y. A reversed CD4/CD8 ratio of tumor-infiltrating lymphocytes and a high percentage of CD4(+)FOXP3(+) regulatory T cells are significantly associated with clinical outcome in squamous cell carcinoma of the cervix. Cell Mol Immunol. 2011 Jan;8(1):59–66.

67.   Fu J, Xu D, Liu Z, Shi M, Zhao P, Fu B, et al. Increased Regulatory T Cells Correlate With CD8 T-Cell Impairment and Poor Survival in Hepatocellular Carcinoma Patients. Gastroenterology [Internet]. 2007 Jun 1 [cited 2024 Jun 12];132(7):2328–39. Available from: https://www.sciencedirect.com/science/article/pii/S0016508507006282

68.   Curiel TJ, Coukos G, Zou L, Alvarez X, Cheng P, Mottram P, et al. Specific recruitment of regulatory T cells in ovarian carcinoma fosters immune privilege and predicts reduced survival. Nat Med. 2004 Sep;10(9):942–9.

69.   Hiraoka N, Onozato K, Kosuge T, Hirohashi S. Prevalence of FOXP3+ regulatory T cells increases during the progression of pancreatic ductal adenocarcinoma and its premalignant lesions. Clin Cancer Res. 2006 Sep 15;12(18):5423–34.

70.   Siddiqui SA, Frigola X, Bonne-Annee S, Mercader M, Kuntz SM, Krambeck AE, et al. Tumor-infiltrating Foxp3-CD4+CD25+ T cells predict poor survival in renal cell carcinoma. Clin Cancer Res. 2007 Apr 1;13(7):2075–81.

71.   Chen WY, Wu CT, Wang CW, Lan KH, Liang HK, Huang BS, et al. Prognostic significance of tumor-infiltrating lymphocytes in patients with operable tongue cancer. Radiat Oncol [Internet]. 2018 Aug 28 [cited 2024 Jun 12];13:157. Available from: https://www.ncbi.nlm.nih.gov/pmc/articles/PMC6114480/

72.   Zhou X, Su YX, Lao XM, Liang YJ, Liao GQ. CD19(+)IL-10(+) regulatory B cells affect survival of tongue squamous cell carcinoma patients and induce resting CD4(+) T cells to CD4(+)Foxp3(+) regulatory T cells. Oral Oncol. 2016 Feb;53:27–35.

73.   Weed DT, Walker G, De La Fuente AC, Nazarian R, Vella JL, Gomez-Fernandez CR, et al. FOXP3 subcellular localization predicts recurrence in oral squamous cell carcinoma. PLoS One. 2013;8(8):e71908.

74.   Grimmig T, Kim M, Germer CT, Gasser M, Waaga-Gasser AM. The role of FOXP3 in disease progression in colorectal cancer patients. Oncoimmunology [Internet]. 2013 Jun 1 [cited 2024 Jun 12];2(6):e24521. Available from: https://www.ncbi.nlm.nih.gov/pmc/articles/PMC3716747/

75.   Blanchard L, Girard JP. High endothelial venules (HEVs) in immunity, inflammation and cancer. Angiogenesis. 2021 Nov;24(4):719–53.

76.   Colbeck EJ, Jones E, Hindley JP, Smart K, Schulz R, Browne M, et al. Treg Depletion Licenses T Cell–Driven HEV Neogenesis and Promotes Tumor Destruction. Cancer Immunol Res [Internet]. 2017 Nov [cited 2024 May 30];5(11):1005–15. Available from: https://www.ncbi.nlm.nih.gov/pmc/articles/PMC5668144/

77.   Jung KY, Cho SW, Kim YA, Kim D, Oh BC, Park DJ, et al. Cancers with Higher Density of Tumor-Associated Macrophages Were Associated with Poor Survival Rates. J Pathol Transl Med. 2015 Jul;49(4):318–24.

78.   Xue T, Yan K, Cai Y, Sun J, Chen Z, Chen X, et al. Prognostic significance of CD163+ tumor-associated macrophages in colorectal cancer. World J Surg Oncol [Internet]. 2021 Jun 24 [cited 2024 Jun 2];19:186. Available from: https://www.ncbi.nlm.nih.gov/pmc/articles/PMC8229299/

79.   Suárez-Sánchez FJ, Lequerica-Fernández P, Suárez-Canto J, Rodrigo JP, Rodriguez-Santamarta T, Domínguez-Iglesias F, et al. Macrophages in Oral Carcinomas: Relationship with Cancer Stem Cell Markers and PD-L1 Expression. Cancers [Internet]. 2020 Jul [cited 2024 Jun 3];12(7):1764. Available from: https://www.mdpi.com/2072-6694/12/7/1764

Figure legends

Figure 1. Immunohistochemical staining of OTSCC tumour tissue. Representative images of tumour tissue sections of primary treatment naïve OTSCC patients immunohistochemically stained for PNAd (n=126), CD163 (n=122), and FoxP3 (n=118). Five areas (hotspots) with the highest density of each of the markers were identified to generate a low and high score for the density of TA-HEVs, CD163+TAMs, and FoxP3+Tregs. The number of TA-HEVs were manually counted, while the number of Tregs was quantified by automated cell detection. TAMs were quantified as percentage of the total area measured. Scale bar indicates 100μm.

Figure 2. Kaplan-Meier curves showing the five-year disease-specific survival in a cohort of OTSCC patients for selected biomarkers; (**A**) TA-HEVs (N=126) (**B**) CD163 (N= 122) (**C**) FoxP3 (N= 118),

(**D**) TA-HEVs and FOXP3 (N=118), (**E**) TA-HEVs and CD163 (N=122) (**F**) FoxP3 and CD163 (N=116). P-values were estimated using the log-rank test.
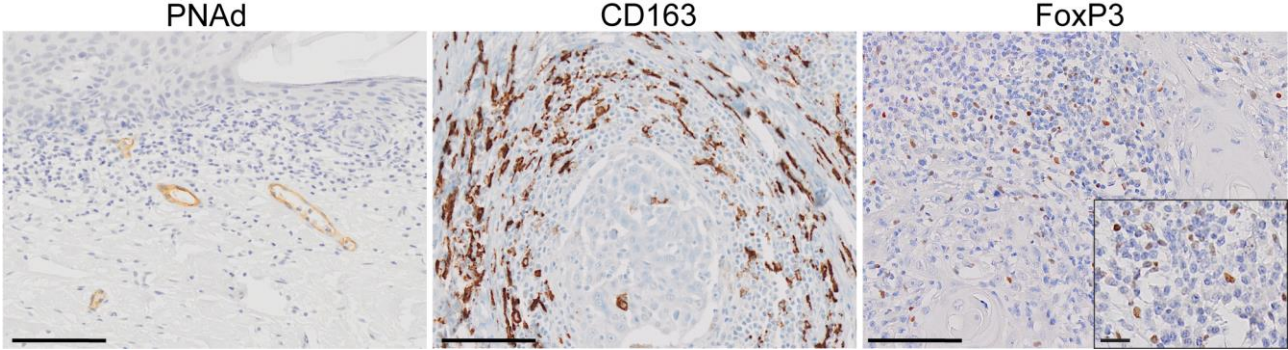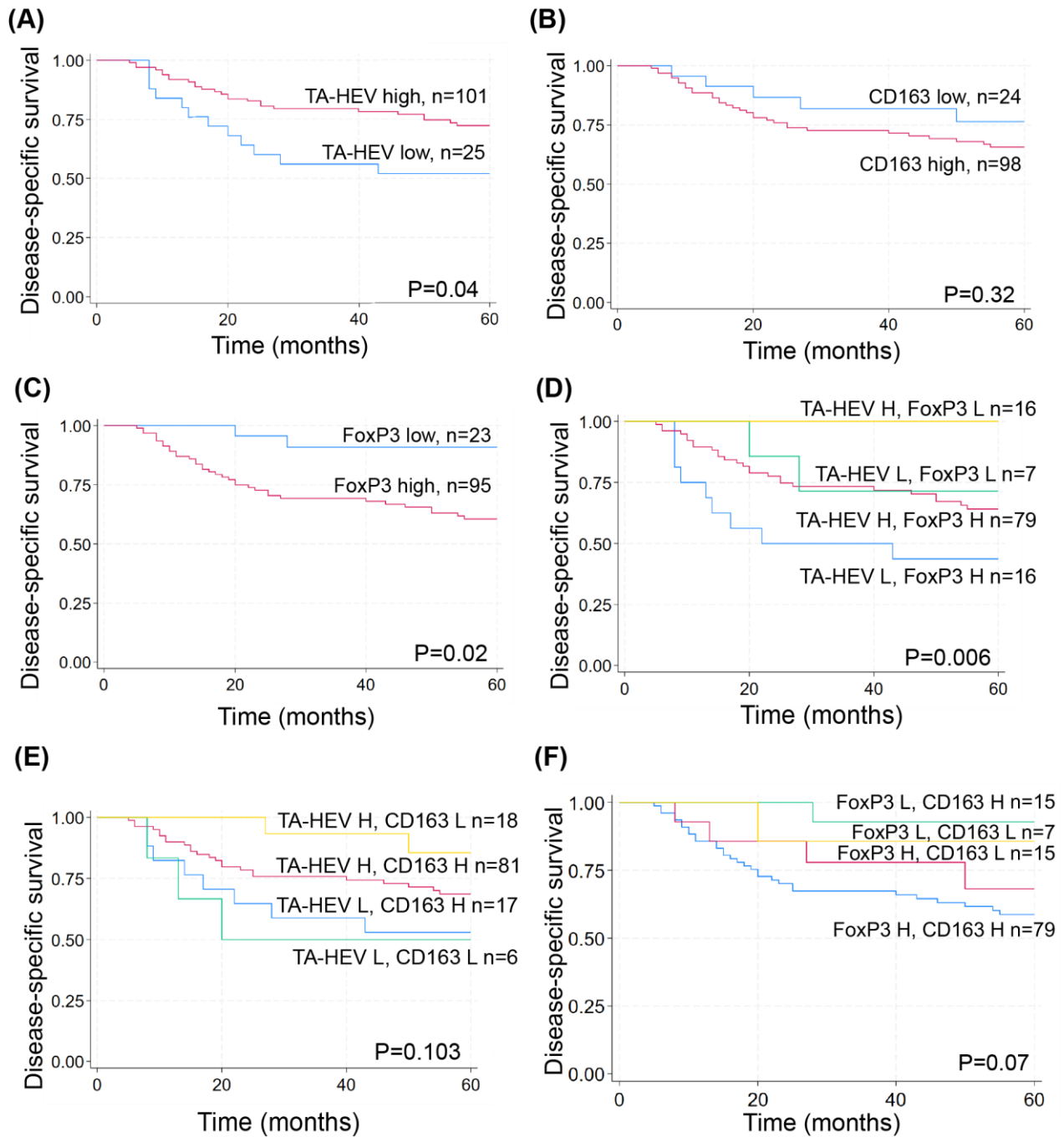
Figures

Figure 1

Figure 2

Tables

Table 1: Demographic, clinical, and pathological features of oral tongue squamous cell carcinoma patients and their association with scores for TA-HEVs-, FoxP3-, and CD163 immunohistochemical staining.

	All	TA-HEVs			FoxP3			CD163		
		Low	High	p	Low	High	p	Low	High	P
	n	n (%)	n (%)		n (%)	n (%)		n (%)	n (%)	
All		25 (19.8)	61 (80.2)		23 (19.5)	95 (80.5)		24 (19.7)	98 (80.3)	
Sex										
Male	76	15 (19.7)	61 (80.3)	.971	12 (16.7)	60 (83.3)	.332	12 (16.2)	62 (83.8)	.233
Female	50	10 (20.0)	40 (80.0)		11 (23.9)	35 (76.1)		12 (25.0)	36 (75.0)	
Age										
≤60 years	50	11 (22.0)	39 (78.0)	.622	11 (23.4)	36 (76.6)	.383	12 (25.09	36 (75.0)	.233
>60 years	76	14 (18.4)	62 (81.6)		12 (16.9)	59 (83.1)		12 (16.2)	62 (83.8)	
T-status										
T1	41	7 (17.1)	34 (82.9)	.878	8 (20.5)	31 (79.5)	.034	10 (26.3)	28 (73.7)	.305
T2	53	11 (20.8)	42 (79.2)		14 (28.6)	35 (71.4)		7 (13.5)	45 (86.5)	
T3	29	5 (17.2)	24 (82.8)		1 (3.7)	26 (96.3)		6 (20.7)	23 (79.3)	
N-status										
N0	89	15 (16.9)	74 (83.1)	.167	17 (20.2)	67 (79.8)	.801	20 (23.3)	66 (76.7)	.139
N+	16	10 (27.8)	26 (72.2)		6 (18.2)	27 (81.8)		4 (11.4)	31 (88.6)	
Grade										
Low	111	21 (18.9)	90 (81.1)	.400	19 (18.4)	84 (81.6)	.904	22 (20.6)	85 (79.4)	.967
High	10	3 (30.0)	7 (70.0)		2 (20.0)	8 (80.0)		2 (20.0)	8 (80.0)	
5-year DSS										
Alive	88	13 (14.8)	75 (85.2)	.030	21 (25.9)	60 (74.1)	.009	19 (22.4)	66 (77.6)	.259
Dead	38	12 (31.6)	101 (68.4)		2 (5.4)	35 (94.6)		5 (13.5)	32 (86.5)	
FoxP3										
Low	23	7 (30.4)	16 (69.6)	.140						
High	95	16 (16.8)	79 (83.2)							
CD163										
Low	24	6 (25.0)	18 (75.0)	.390	7 (31.8)	15 (68.2)	.088			
High	98	17 (17.3)	81 (82.7)		15 (16.0)	79 (84.0)				

P-values were calculated using the Pearson Chi-square test. N0: no lymph node metastases. N+: Lymph node metastases. N: number of patients. DSS: Disease specific survival. Variation in number was due to missing data or availability of tissue sections.

Table 2: Mean disease-specific survival time and unadjusted risk of dying of disease.

	Mean disease specific survival months (95% CI)	p	Unadjusted HR (95% CI)	p
All	47.90 (44.43, 51.36)			
Sex				
Male	47.71 (43.27, 52.15)	.818	1.08 (0.56, 2.09)	.818
Female	48.20 (42.65, 53.74)		Ref.	
Age				
≤60 years	50.07 (45.16, 54.98)	.397	Reference	.400
>60 years	46.42 (41.68, 51.16)		1.33 (0.69, 2.57)	
T-status				
T1	55.36 (51.48, 59.24)		Reference	
T2	46.32 (40.96, 51.68)	.040	2.83 (1.13, 7.09)	.026
T3	43.57 (35.04, 52.09)		3.14 (1.14, 8.65)	.027
N-status				
N0	52.54 (49.20, 55.87)	<.001	Reference	<.001
N+	35.57 (27.90, 43,24)		3.87 (2.04, 7.34)	
Grade				
Low	49.53 (46.03, 53.04)	<.001	Reference	
High	28.40 (14.42, 42.38)		4.44 (1.94, 10.16)	
TA-HEVs				
Low	39.76 (31.07, 48.54)	.030	2.09 (1.05, 4.14)	.035
High	50.02 (46.40, 53.64)		Reference	
FoxP3				
Low	56.73 (52.40, 61.07)	.010	Reference	.022
High	45.02 (40.73, 49.32)		5.31 (1.28, 22.07)	
CD163				
Low	51.73 (44.82, 58.64)	.314	Reference	.320
High	46.85 (42.80, 50.90)		1.61 (0.63, 4.14)	

Mean survival with 95% confidence intervals (CI) calculated by Kaplan-Meier analyses and statistical significance of differences assessed with the Log-rank test. Hazard ratio (HR) of disease-specific death with 95% CI was calculated with Cox regression analyses.

Table 3 Multivariate survival analyses.

	Adjusted HR (95% CI)	Adjusted HR (95% CI)	Adjusted HR (95% CI)	Adjusted HR (95% CI)
Sex				
Male	0.97 (0.46, 2.08)	1.16 (0.55, 2.45)	1.01 (0.48, 2.11)	1.10 (0.51, 2.22)
Female	Reference	Reference	Reference	Reference
Age				
≤60 years	Reference	Reference	Reference	Reference
>60 years	**2.26** (1.03, 4.95)	1.68 (0.79, 3.62)	2.09 (0.94, 4.65)	1.68 (0.77, 3.67)
T-status				
T1	Reference	Reference	Reference	Reference
T2/T3	2.15 (0.78, 5.94)	2.71 (1.00, 7.38)	2.16 (0.78, 6.03)	2.50 (0.91, 6.87)
N-status				
N0	Reference	Reference	Reference	Reference
N+	**3.84 (1.75, 8.46)**	**4.61 (2.10, 10.10)**	**3.43 (1.52, 7.72)**	**5.07 (2.24, 11.45)**
Grade				
Low	Reference	Reference	Reference	Reference
High	**4.79 (1.94, 11.83)**	**6.52 (2.68, 15.83)**	**5.44 (2.21, 13.39)**	**6.88 (2.75, 17.20)**
TA-HEVs				
Low	1.17 (0.51, 2.70)			2.26 (0.91, 5.47)
High	Reference			Reference
FoxP3				
Low		Reference		Reference
High		**8.02 (1.77, 36.44)**		**13.18 (2.44, 71.08)**
CD163				
Low			Reference	
High			1.65 (0.55, 4.96)	

Hazard ratio (HR) of disease-specific death with 95% CI was calculated with Cox regression analyses. Ref indicates reference category. Numbers in bold indicates statistically significant differences.

4-nitroquinoline 1-oxide-induced oral epithelial lesions exhibit time- and stage-dependent changes in the tumor immune microenvironment

Kjersti Sellæg, Ruth Schwienbacher, Mathias Kranz, Anna Engan Aamodt, Anna M. Wirsing, Gerd Berge, Elin Hadler-Olsen, Synnøve Norvoll Magnussen

4-nitroquinoline 1-oxide-induced oral epithelial lesions exhibit time- and stage-dependent changes in the tumor immune microenvironment

Kjersti Sellæg[1]*, Ruth Schwienbacher[1,2], Mathias Kranz[3],
Anna Engan Aamodt[1], Anna M. Wirsing[1], Gerd Berge[1],
Elin Hadler-Olsen[1,4] and Synnøve Norvoll Magnussen[1]*

[1]Department of Medical Biology, Faculty of Health Sciences, University of Tromsø (UiT) — The Arctic
University of Norway, Tromsø, Norway, [2]Department of Clinical Pathology, University Hospital of
North Norway, Tromsø, Norway, [3]PET Imaging Center Tromsø, University Hospital of North Norway,
Tromsø, Norway, [4]The Public Dental Health Competence Center of Northern Norway,
Tromsø, Norway

Oral tongue squamous cell carcinoma (OTSCC) is the most common cancer of
the oral cavity and is associated with high morbidity due to local invasion and
lymph node metastasis. Tumor infiltrating lymphocytes (TILs) are associated with
good prognosis in oral cancer patients and dictate response to treatment.
Ectopic sites for immune activation in tumors, known as tertiary lymphoid
structures (TLS), and tumor-associated high-endothelial venules (TA-HEVs),
which are specialized lymphocyte recruiting vessels, are associated with a
favorable prognosis in OSCC. Why only some tumors support the
development of TLS and HEVs is poorly understood. In the current study we
explored the infiltration of lymphocyte subsets and the development of TLS and
HEVs in oral epithelial lesions using the 4-nitroquinoline 1-oxide (4NQO)-
induced mouse model of oral carcinogenesis. We found that the immune
response to 4NQO-induced oral epithelial lesions was dominated by T cell
subsets. The number of T cells (CD4+, FoxP3+, and CD8+), B cells (B220+)
and PNAd+ HEVs increased from the earliest to the latest endpoints. All the
immune markers increased with the severity of the dysplasia, while the number of
HEVs and B cells further increased in SCCs. HEVs were present already in early-
stage lesions, while TLS did not develop at any timepoint. This suggests that the
4NQO model is applicable to study the dynamics of the tumor immune
microenvironment at early phases of oral cancer development, including the
regulation of TA-HEVs in OTSCC.

1 Introduction

Oral tongue squamous cell carcinoma (OTSCC) is the most common oral malignancy. OTSCCs are aggressive due to local invasion and a tendency for early metastatic spread to regional lymph nodes (1). About half (47-52%) of the patients will die within five years after diagnosis (2, 3). The standard treatment includes surgery, and in some cases radiotherapy and chemotherapy (2).

A high density of tumor infiltrating lymphocytes (TILs) is associated with good prognosis in several cancers including melanoma, breast, colorectal, and tongue cancers (4, 5). TILs can be separated into B cells and T cells, which can be further classified into various subtypes with specific functions. CD8+ cytotoxic T cells can kill malignant cells and their presence in tumors is associated with favorable patient outcomes (6, 7). These cells are also key players in cancer immunotherapy. Indeed, boosting the presence and reactivity of cytotoxic T cells within tumors, either by blocking of immune checkpoint molecules or transplanting engineered tumor-specific T cells have shown improved clinical outcomes in human cancers (8, 9). Tumor infiltrating B cells have also been shown to correlate with improved patient survival (5), whereas regulatory T cells (Tregs), an immunosuppressive T cell subset, confers worse prognosis in oral cancer patients (10).

In inflamed tissues, B cells, T cells and specialized stromal cells (follicular dendritic cells; FDCs) sometimes form organized immune aggregates known as tertiary lymphoid structures (TLS). The structure and function of TLS resemble lymphoid follicles and act as ectopic sites for local antigen presentation and immune activation (11). Lymphocyte trafficking into lymph nodes and TLS is mediated by specialized post-capillary venules termed high-endothelial venules (HEVs) (12). HEVs with similar phenotypes to lymph node HEVs are found in chronically inflamed tissues, such as autoimmune diseases (13), allograft rejection (14), and solid tumors (15), and are considered the main gateways for lymphocyte entry into these sites. The presence of TLS and HEVs, as well as high density of HEVs within TLS, are associated with a favorable prognosis in several cancers (16–18). In our previous studies we have found that tumor-associated (TA) TLS were associated with a favorable prognosis in OSCC patients (19). Interestingly, TA-HEVs were found to be an independent positive prognostic marker associated a favorable immune microenvironment and were sometimes present independently of TLS (19–21). The specific conditions within a tumor that supports the development of TLS and HEVs remain unclear.

To study OTSCC carcinogenesis and its immune infiltrate, we chose the 4-nitroquinoline 1-oxide (4NQO) mouse model which has been widely used in studies of oral cancer (22). The genetic alterations caused by 4NQO exposure resemble that of tobacco carcinogens (23), which is an important risk factor for oral cancer in humans. To increase our understanding of the immune response in human cancer we need models that closely mimic clinical features of human disease. Our previous studies on TLS and HEVs in OSCC used human archival tissues (19–21). However, archival tissues are snapshots and do not capture the development of the microenvironment during tumor progression. In this study we aimed to determine whether HEVs and TLSs develop in the 4NQO model and to map the immune infiltrate during oral carcinogenesis. We also wanted to explore whether positron emission tomography (PET) and magnetic resonance imaging (MRI) are suitable to track the development of tongue lesions and metastasis in this model. We used immunohistochemistry together with a refined scoring approach to analyze the quantity and spatial distribution of CD4+ (T helper cells), FoxP3+ (regulatory T cells), CD8+ (cytotoxic T cells), and B220+ (B cells) cells, as well as PNAd + HEVs in tongue tissues. We also performed *in vivo* whole-body PET/MRI of 4NQO-exposed mice at different timepoints. Aggregates of B220+ cells indicative of TLS did not develop at any timepoint, however, HEVs were present already in early-stage lesions. The number of infiltrating lymphocytes and HEVs associated with oral epithelial lesions increased with time and severity of the lesions. PET/MRI efficiently detected epithelial lesions of the tongue and reactive changes in the regional lymph nodes of 4NQO-exposed mice.

2 Materials and methods

2.1 Animals and experimental protocol

Animal experiments were approved by The Norwegian Food Safety Authority (FOTS ID 15956) and adhere to the Norwegian Animal Welfare Act and the European Union directive 2010/63. For the duration of the study, the mice were maintained at controlled temperature and humidity under a 12h/12h light/dark cycle with *ad libitum* food and water access. The mice were housed at specific-pathogen free conditions and environmental enrichment was provided. Forty-eight C57BL/6 wild-type (strain:C57BL/6JRj) mice (female, 6-8 weeks; Janvier Labs, Route de Genest, France) were kept in ventilated cages (maximum five mice in each cage) with or without filtertops depending on carcinogen exposure. The mice were acclimatized for one week prior to study start. During a treatment period of 16 weeks, mice in randomly selected cages were given either 100μg/mL of the carcinogen 4-nitroquinoline 1-oxide (4NQO, Sigma, St. Louis, Missouri, USA) in the drinking water (4NQO n=30) or regular drinking water (control n=18) (Figure 1A). Freshly prepared 4NQO-water was provided every five ± three days. The 4NQO stock solution and drinking bottles were protected from light. During a 12-week follow-up period, carcinogen-exposed and control mice were sacrificed at different timepoints (weeks ≤20: 4NQO n=12, control n=6, weeks 21-24: 4NQO n=9, control n=6, and weeks 25-28: 4NQO n=9, control n=6), referred to as experimental endpoint (Figure 1A). Humane endpoints were ≥10% loss of bodyweight and signs of decreased well-being of the animals, including physical appearance and behavior, if it could not be alleviated with intervention. The mice were weighed at baseline (week 0) and weekly until week 14, whereafter the animals were weighed daily until they reached humane or experimental endpoint. Due to loss of body weight and dehydration, the carcinogen-exposed mice were given chow soaked in water in addition to dietary supplements (DietGel® Recovery, Clear H_2O, Maine, USA) from week 14. Whole-body dynamic PET and high-resolution head MRI was conducted at
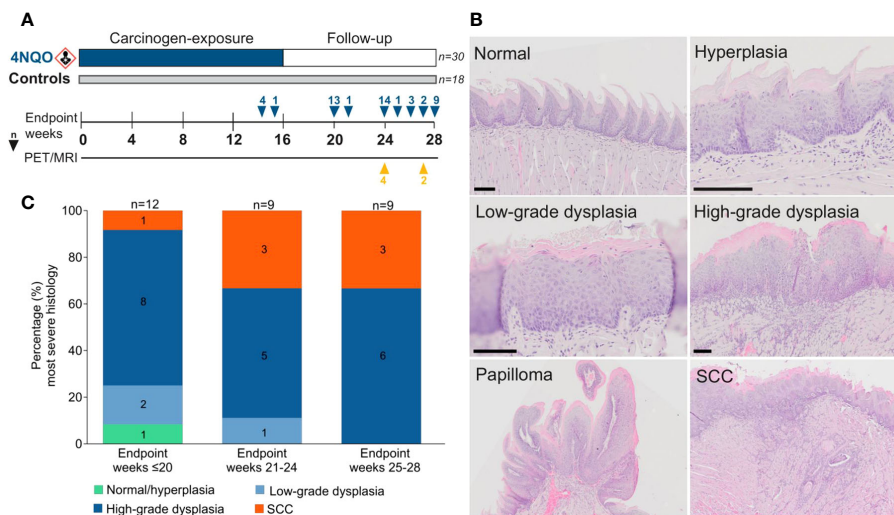
FIGURE 1

Histopathological evaluation in the 4NQO mouse model. **(A)** Forty-eight mice were given 4NQO-water (n=30) or regular drinking water (n=18) for 16 weeks, followed by 12 weeks observation where the mice were sacrificed at different timepoints. **(B)** Each tongue was assigned a score corresponding to the lesion with the most severe histopathological grade: normal/hyperplasia, low-grade dysplasia, high-grade dysplasia, or SCC. Scale bar indicates 100 μm. **(C)** The severity of epithelial lesions increased in mice sacrificed at later endpoints.

weeks 24 and 27 as described in detail below. Euthanasia was conducted by carbon dioxide inhalation. Investigators were not blinded to the allocation of animals in the control and experimental group.

2.2 Tissue preparation

Immediately after euthanasia, the tongue, cervical and inguinal lymph nodes, lungs, liver, kidneys, and urinary bladder, were collected and fixed in 4% buffered formalin overnight. Thereafter the tissue was kept in 70% ethanol until dehydration and paraffin embedding at the Department of Clinical Pathology, University of North Norway, Tromsø. Before embedding in paraffin, tongues were cut through the midline (medial sulcus) and mounted to give sagittal sections (displaying the tongue from tip to base). Four-μm-thick serial sections were cut from each paraffin-embedded tissue block and mounted on Superfrost Plus glass slides. Sections were coated with paraffin and stored at 4°C until use.

2.3 Histopathological evaluation

For histopathological examination of the tongue, one sagittal section from the medial part of the tongue and one from a more lateral part (approximately 80μm apart) were stained with hematoxylin and eosin (H&E). The sagittal sections were used to assess the histology of the whole tongue. Cervical lymph nodes were serial sectioned, and sections at 40μm intervals were H&E-stained to assess local metastatic disease and to verify PET/MRI findings. Furthermore, H&E-stained sections from inguinal lymph nodes, lungs, liver, kidneys, and urinary bladder (one from each organ) were assessed for tumors (distant metastases or primary tumors).

H&E staining was done according to standard procedures. Briefly, tissue sections were dewaxed by incubation at 60°C for at least three hours before immersion in xylene, followed by rehydration in graded ethanol baths. The sections were then stained by immersion in Harris hematoxylin (RAL diagnostics, Martillac, France), Scott's solution (in-house), and eosin (Sigma-Aldrich, St. Louis, Missouri, USA) for 30, 15, and 30 seconds, respectively. An Olympus VS120 automated slide scanner (Olympus, Tokyo, Japan) was used for scanning of stained slides at 20x magnification. Digital virtual whole-slide images were assessed in OlyVIA Image Viewer software (version 2.6) via the Olympus Net Image Server SQL at 0.31- 40x magnification. In case of poor focus of digital slides, the glass slides were studied in a Leica DM2000 light microscope (Leica Microsystems, Wetzlar, Germany).

To map the spatial histology of the tongue we applied an approach adapted from Vered and colleagues (24), where the tongues were divided into seven sectors by imaginary lines; one horizontal line separating the tongue into a dorsal half and a ventral half from tip to base, crossed by three vertical lines. The vertical lines separated the tongue into the following regions: sector 1; dorsal tip, sector 2; ventral tip, sector 3; dorsal anterior body, sector 4; ventral anterior body, sector 5; dorsal posterior body, sector 6; ventral posterior body, sector 7; tongue base. The histology of each tongue was evaluated and assigned to the specific sector. The tongue tissues were scored as normal mucosa, hyperplasia, low-grade dysplasia, high-grade dysplasia, and SCC (Figure 1B) according to the WHO classification of head and neck tumors 4th edition (25). Squamous hyperplasia was defined as the presence of a thickened epithelium in the absence of histological criteria for dysplasia (26). Because squamous hyperplasia was observed in both study groups it was considered a normal finding, and therefore, normal mucosa and hyperplasia was grouped together. Epithelial dysplasia was classified as either low- or high-grade using a simplified binary

system (26). In low-grade dysplasia, the dysplastic features were restricted to the lower third of the epithelium, and in high-grade dysplasia the dysplastic features were present in the middle- to upper-third of the epithelium. SCC was defined as neoplastic squamous epithelium that penetrated the basement membrane and infiltrated the underlying submucosa. Exophytic lesions composed of acanthotic squamous epithelium arranged along a fibrovascular stem were referred to as papilloma. Histological evaluations of all study animals were performed by KS and clinical pathologist (head- and neck specialist) RS. First, a histopathological examination of the medial tongue sections was performed, during which RS was blinded to the study groups. Next, we repeated the process for the lateral tongue sections. Finally, each tongue and each of their seven sectors were assigned a score corresponding to the most severe epithelial lesion found in the two tissue sections.

2.4 Immunohistochemical staining

Consecutive serial sections (within the distance between the two sagittal H&E-stained sections used for histological assessment) were stained for immune cell markers (CD4, FoxP3, CD8, and B220), the HEV specific marker PNAd and the proliferation marker Ki-67. Cervical lymph node sections from mice that underwent PET/MRI were also stained for Ki-67. Specifications for immunohistochemical staining are listed in Table 1. Dewaxed and rehydrated tissue sections were subjected to heat-induced antigen retrieval for 20 minutes. After blocking of endogenous peroxidase activity, 5% goat serum was added to prevent non-specific binding of primary antibody. Sections were incubated with primary antibody before adding secondary antibody. Visualization was done with DAKO EnVision DAB+ kit (Aglient, Santa Clara, CA) and counterstain with Hematoxylin (RAL Diagnostics, Martillac, France). Mouse spleen and lymph node tissue was used as positive staining control and primary antibody was omitted for the negative control.

2.5 Immunohistochemical evaluation

Immunohistochemically stained sections were assessed using the OlyVIA Image Viewer Software as described for histopathological evaluation. Each of the tongue specimens were divided into sectors (as described above) using the corresponding H&E-stained section as a guide to ensure the sectors matched as accurately as possible. We counted the total number of the various immune cell types in the epithelium and lamina propria of normal mucosa, as well as in and around epithelial lesions of the seven sectors. To evaluate the presence of TLS, we based our scoring approach on methods previously used in human OSCC tumors (19, 27). B220-stained sections were assessed for the presence of distinct aggregates of positively stained cells or more diffuse B220 staining patterns. The presence of CD4+ and CD8+ T cells, as well as PNAd-positive vessels within or adjacent to B220+ cell aggregates on consecutive sections would be considered TLS. Due to the limited presence of HEVs compared to immune cells in the tongue specimens, HEVs were analyzed in two sections per mouse (one medial and one more lateral section, approximately 80μm apart). To report the results, we chose the section that had the highest HEV count out of the two (Supplementary Figure S1). HEVs were defined as PNAd-stained vessels or clusters of >1 positively stained cells as previously described (Wirsing 2016). Qualitative assessment of Ki-67 staining was performed in 25 tongue sections (4NQO n=17, control n=8). This included the four carcinogen-exposed- and two control mice that underwent PET/MRI. For these mice, Ki-67 was also evaluated in three cervical lymph node sections at 120μm intervals. Immune cells and Ki-67 staining were analyzed by KS, and HEVs were analyzed by KS and AMW.

2.6 Imaging and monitoring with PET/MRI

Animals (4NQO n=4, control n=2) were anesthetized by inhaling 4% Isoflurane (in O_2), after which anesthesia was

TABLE 1 Specification for immunohistochemical staining.

Target/Primary antibody/Clone	Antigen retrieval	Blocking	Dilution	Incubation time (minutes)	Secondary antibody
T helper cells/Recombinant rabbit monoclonal anti-CD4 antibody/EPR19514[a]	Tris-EDTA (pH 9.0)	0.3% H_2O_2	1:1000	60	HRP-labelled polymer anti-rabbit[f]
Cytotoxic T cells/Recombinant monoclonal rabbit anti-CD8 alpha antibody/EPR21769[a]	Sodium citrate (pH 6.0)	0.3% H_2O_2	1:2000	ON	HRP-labelled polymer anti-rabbit
T regulatory cells/Rabbit anti-mouse FoxP3 antibody/D6O8R[b]	Sodium citrate (pH 6.0)	3% H_2O_2	1:75	ON	HRP-labelled polymer anti-rabbit
B cells/Rat anti-mouse B220/CD45R antibody/RA3-6B2[c]	Tris-EDTA (pH 9.0)	0.3% H_2O_2	1:600	60	Goat anti-rat HRP-conjugated (1:200)[g]
High-endothelial venules/Purified Rat anti-mouse/human PNAd antibody/MECA-79[d]	Sodium citrate (pH 6.0)	0.3% H_2O_2	1:25	30	Goat anti-rat HRP-conjugated (1:200)
Ki-67/Ki-67 recombinant rabbit monoclonal antibody/SR00-02[e]	Sodium citrate (pH 6.0)	3% H_2O_2	1:2000	60	HRP-labelled polymer anti-rabbit

[a]Abcam, Cambridge, UK; [b]Cell Signaling Technology, Dovers, Massachusetts, US; [c]R&D Systems, Minneapolis, Minnesota, US; [d]BioLegend, San Diego, California, US; [e]Invitrogen, Waltham, Massachusetts, US; [f]Agilent, Santa Clara, CA; [g]Merck, Rahway, New Jersey.

maintained at 1.8-2% for up to two hours during imaging procedure. The animals were placed prone on a dedicated heated mouse holder (MINERVE, Esternay, France) and 60 min whole-body dynamic PET imaging (PET/MRI 7T, MR solutions, Guildford, UK) was performed following i.v. application of 6.3 ± 0.3 MBq [18F]-fluorodeoxyglucose ([18F]FDG). Simultaneously, high resolution head MRI was performed in the same device applying T1- and T2-weighted fast spin echo (FSE). The radiosynthesis of [18F]FDG was performed according to standard clinical procedure at the PET Imaging Center Tromsø and approximately 1 GBq of the patient batch was used for the animal studies.

The list-mode data were reconstructed into 24x5 s -8x60 s, 10 and x300 s time frames using 3D ordered subset expectation maximization with 1 iteration, 32 subsets, VOXEL size 0.42 mm, applying correction for random coincidences-, decay-, deadtime- and scatter-correction. Subsequently, the hyper-intense lesion was segmented (PMOD v4.3, PMOD Technologies, Zurich, Switzerland) by placing a region of interest (ROI) using the MR information.

2.7 PET data analysis

The MRI-based ROI was used to extract the [18F]FDG activity concentration (Bq/ml) on the PET data. PET pharmacokinetic modeling was applied using the irreversible 2TCM (PMOD v.4.3, PMOD technologies) and its suitability evaluated by Schwartz Criterion (SC), Akaike Information Criterion (AIK) and Model Selection Criterion (MSC). Furthermore, rate constants were calculated for K1, k2, k3, and macro parameters MRGlu and Flux derived. The image derived input function (idIF) was segmented from the inferior vena cava as it provides a robust estimation of the idIF [28] with special regard to the spill-in contamination from neighboring tissue when using the heart [29].

2.8 Statistical analysis

GraphPad Prism version 10.0.2 (https://www.graphpad.com/) was used for statistical analyses and graphical visualization of data. Quantile-quantile (QQ) plots and the Shapiro-Wilk test were used to assess sample distributions. Mann-Whitney U test or Kruskal-Wallis H test (with Dunn's multiple comparisons test) was used to analyze difference between two or more groups, respectively, of non-normal distributed data. Student's t-test or one-way ANOVA (with Tukey's *post hoc* test for multiple comparisons) was applied to analyze difference between two or more groups, respectively, when the data met the assumption of normal distribution. Statistical analyses were performed using two-tailed tests. Data were transformed for visualization purposes in some instances by log2 (y+1). P-value <0.05 was considered statistically significant. In all graphs, asterisks indicate significant differences: *p<0.05, **p<0.01, ***p>0.001, and ****p<0.0001.

3 Results

3.1 Histopathological characterization of the 4NQO mouse model of oral carcinogenesis

In the current study we used the 4NQO mouse model to analyze the time- and stage-dependent development of the immune infiltrate during oral carcinogenesis. A total of 30 4NQO-exposed mice and 18 healthy controls were sacrificed at different timepoints during the study and were grouped by the weeks at which they reached humane- or experimental endpoint; weeks ≤20 (4NQO: n=12, controls: n=6), weeks 21-24 (4NQO: n=9, controls: n=6), and weeks 25-28 (4NQO: n=9, controls: n=6; Figure 1A). The tongue mucosa of most control animals displayed normal histology, while a few mice exhibited features of squamous hyperplasia. Therefore, normal- and hyperplastic epithelium were categorized as one group. 4NQO exposure often induced multiple lesions of varying severity on the same tongue, including low- and high-grade dysplasias, SCC, and papilloma (Figure 1B), and each tongue, as a whole, was assigned a score based on the most severe histopathology observed. The severity of the histopathological lesions clearly increased with later endpoints (Figure 1C). Only one (3.3%) of the carcinogen-exposed mice had no histopathological lesions, and this animal was sacrificed at the earliest endpoint. High-grade dysplasias were the most common lesions across all endpoints, accounting for 63.3% (19/30) of all cases. At endpoint weeks 25-28, all 4NQO-exposed tongues had either high-grade dysplasia or SCC. Seven 4NQO-exposed mice (23.3%) developed SCC; one at week 20, three at weeks 21-24, and three at weeks 25-28. Half (15/30) of the mice developed one or more papilloma, presenting with either dysplasia or SCC (Supplementary Figure S2; Supplementary Table S1). In two animals we histologically verified the presence of lesions at other sites in the oral cavity: one in the hard palate and one in the throat. Because the tissues contained only parts of the lesions and surrounding tissue, invasive growth and stage could not be determined. In conclusion, the severity of epithelial lesions increased with time after 4NQO-exposure.

3.2 The immune infiltrate gradually increased during oral carcinogenesis and the composition differed with stage

To study the immune infiltrate during oral carcinogenesis, whole tongue sections were immunohistochemically stained for the immune cell markers CD4 (T helper cells), FoxP3 (regulatory T cells), CD8 (cytotoxic T cells), and B220 (B cells), and the HEV marker PNAd (Supplementary Figure S3). Immune cells were variably found in the epithelium and lamina propria, while HEVs were only found in the stromal compartment typically in areas with several HEVs present, close to epithelial lesions (Figure 2A; Supplementary Figure S4). For all the markers, the number of positive cells and -vessels were significantly higher in the
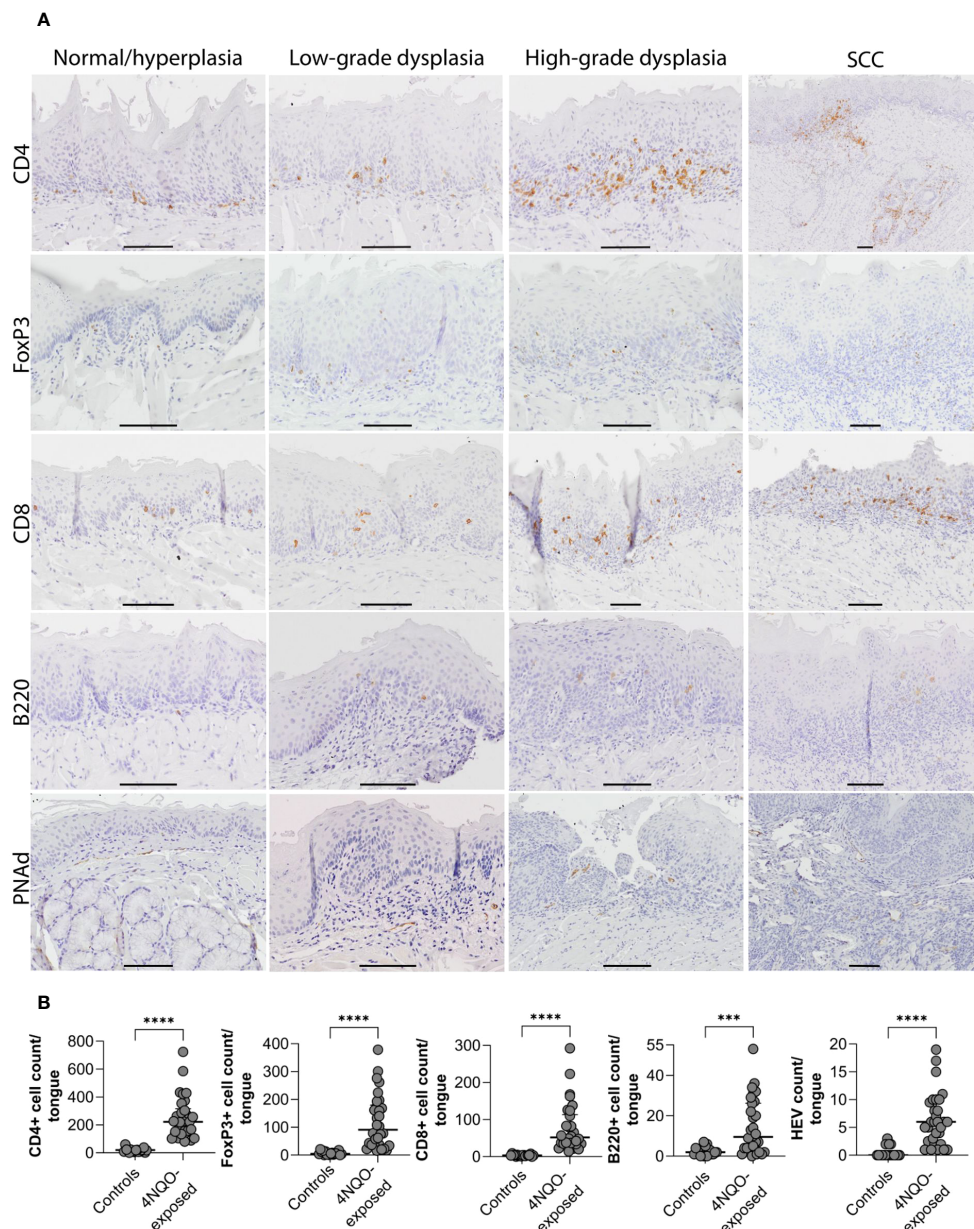
FIGURE 2

Distribution of immune cells and HEVs in relation to epithelial lesions on the tongue of 4NQO-exposed mice. **(A)** Four µm thick sagittal tongue sections (scale bar indicates 400µm) were stained with H&E and divided into seven sectors (1–7) to **(B)** map the location of epithelial lesions of the tongue following 4NQO-exposure. Data is presented as percentage, and n represents the number of sectors that were examined across all 4NQO-exposed mice. **(C-G)** Total counts of each of the immune cells and HEVs within the seven sectors of the tongue in 4NQO-exposed mice (n=30) and healthy controls (n=18). Data is log-transformed (log2(y+1)), and error bars indicate median with IQR. **(H)** Total counts of each of the immune cells and HEVs in the seven sectors for all 4NQO-exposed mice. The range in the counts for the respective markers are shown to the right where the white is the lowest count and dark purple is the highest count.

carcinogen-exposed versus control mice (P ≤ 0.0001) (Figure 2B). 4NQO-exposed tongues generally contained sparse numbers of B220+ cells. Aggregates of B220+ cells, which are considered a defining component of TLS (30), were not found in any of the tissue sections analyzed. Irrespective of the severity of the carcinogen-induced epithelial lesions, the most abundant cell type was the CD4+ T cells (Figures 3A–E). The total number of positive cells/vessels increased gradually with later endpoints for all the markers

(Figures 3F–J), though not statistically significant for B220+ cells (Figure 3I) (P=0.07). The most prominent increase was seen for FoxP3- and CD8-positive cells (weeks ≤20 n=65 and weeks 25-28 n=205, P=0.0014; weeks ≤20 n=51 and weeks 25-28 n=138, P=0.0071, respectively; Figures 3G, H). The CD4+/FoxP3+ cell ratio decreased from the first to the latest endpoint (Supplementary Figure S5). Since most FoxP3+ cells also express CD4, this indicates that the proportion of regulatory T cells versus
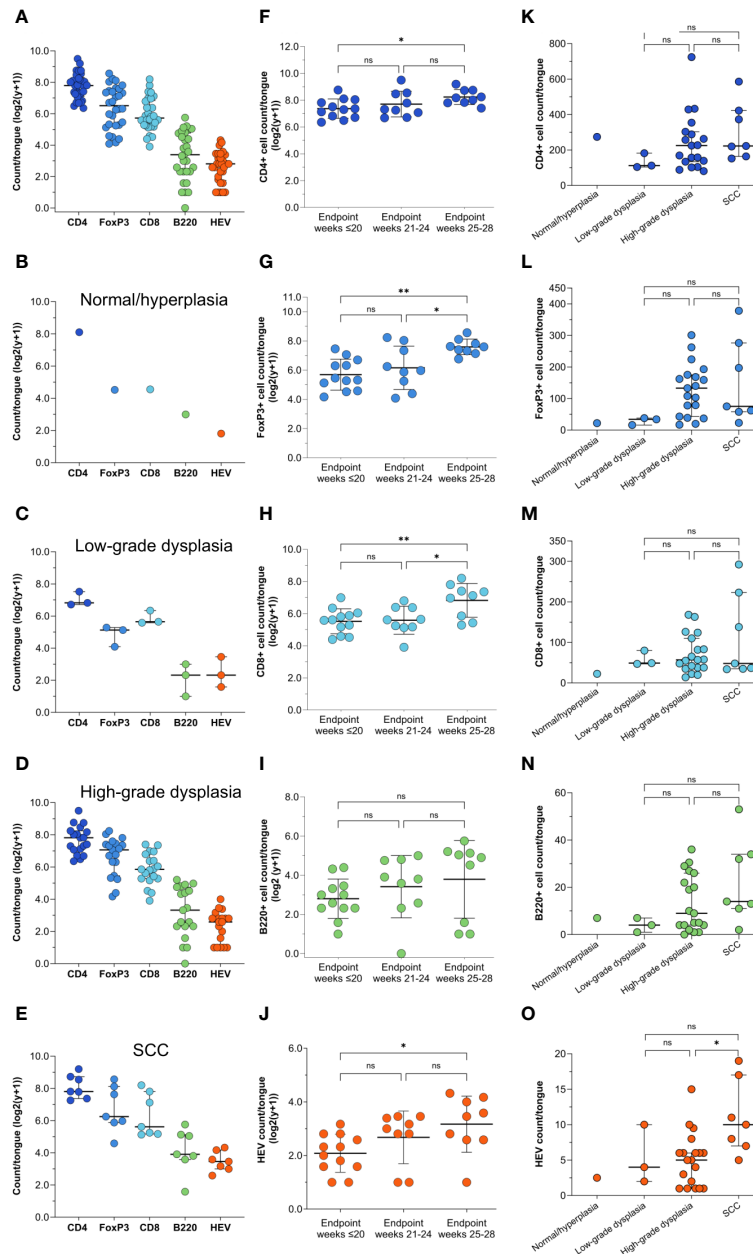
FIGURE 3

Distribution of immune cell- and HEV markers in the tongue mucosa. **(A)** Shown are representative images for the distribution of CD4-, FoxP3-, CD8-, and B220 cells, and PNAd positive vessels in areas of the tongue graded as normal/hyperplasia, low-grade dysplasia, high-grade dysplasia, and SCC. For CD4, FoxP3, and B220, the same SCC is shown, but the images for FoxP3 and B220 only show parts of the SCC that represented the staining patterns. Scale bar indicates 100µm. **(B)** The number of positively stained cells or vessels for all the markers (CD4, FoxP3, CD8, B220, and PNAd) were significantly higher (P<0.0001) in mice exposed to 4NQO (n=30) compared to healthy controls (n=18). Error bars indicate median with interquartile range (IQR).

helper T cells increased during tumor progression. The number of HEVs also increased significantly between endpoint weeks ≤20 and endpoint weeks 25-28 (P=0.0292) in carcinogen-exposed mice.

We further assessed if the number of immune cells and HEVs corresponded to the severity of the most severe histopathological lesion (Figures 3K–O). Although the differences did not reach statistical significance, the median number of all immune cells increased with the severity of the dysplasia (Figures 3K–O).

Tongues with SCC had a significantly higher number of HEVs than those with high-grade dysplasia (P=0.0397; Figures 3K–O), and the number of B220+ cells increased slightly, although not statistically significant (P=0.2077; Figure 3N). CD4+ and CD8+ T cell counts were similar (P=0.3177 and P=0.5984, respectively; Figures 3K, M), and the number of FoxP3+ cells was lower (P=0.0741; Figure 3L) in tongues with SCC than in tongues with high-grade dysplasias.

3.3 A novel scoring approach revealed that the distribution of TILs and HEVs corresponds to the site of the epithelial lesions

As previously described, several lesions developed per tongue. Hence, to correlate the immune infiltrate more precisely to the severity of the epithelial lesions, we divided each tongue section into

seven sectors and each of them were given a score corresponding to the most severe histopathological change in the sector (Figures 4A, B). Altogether, more lesions developed on the dorsal side than on the ventral side of the tongue, and most lesions were found in sectors 3 and 5. These sectors also had the most severe lesions (Figure 4B; Table 2). SCCs were only found in sector 3 and 5 and accounted for 10% and 20% of the lesions, respectively. The SCCs sometimes extended into both sectors. Large papillomas were most
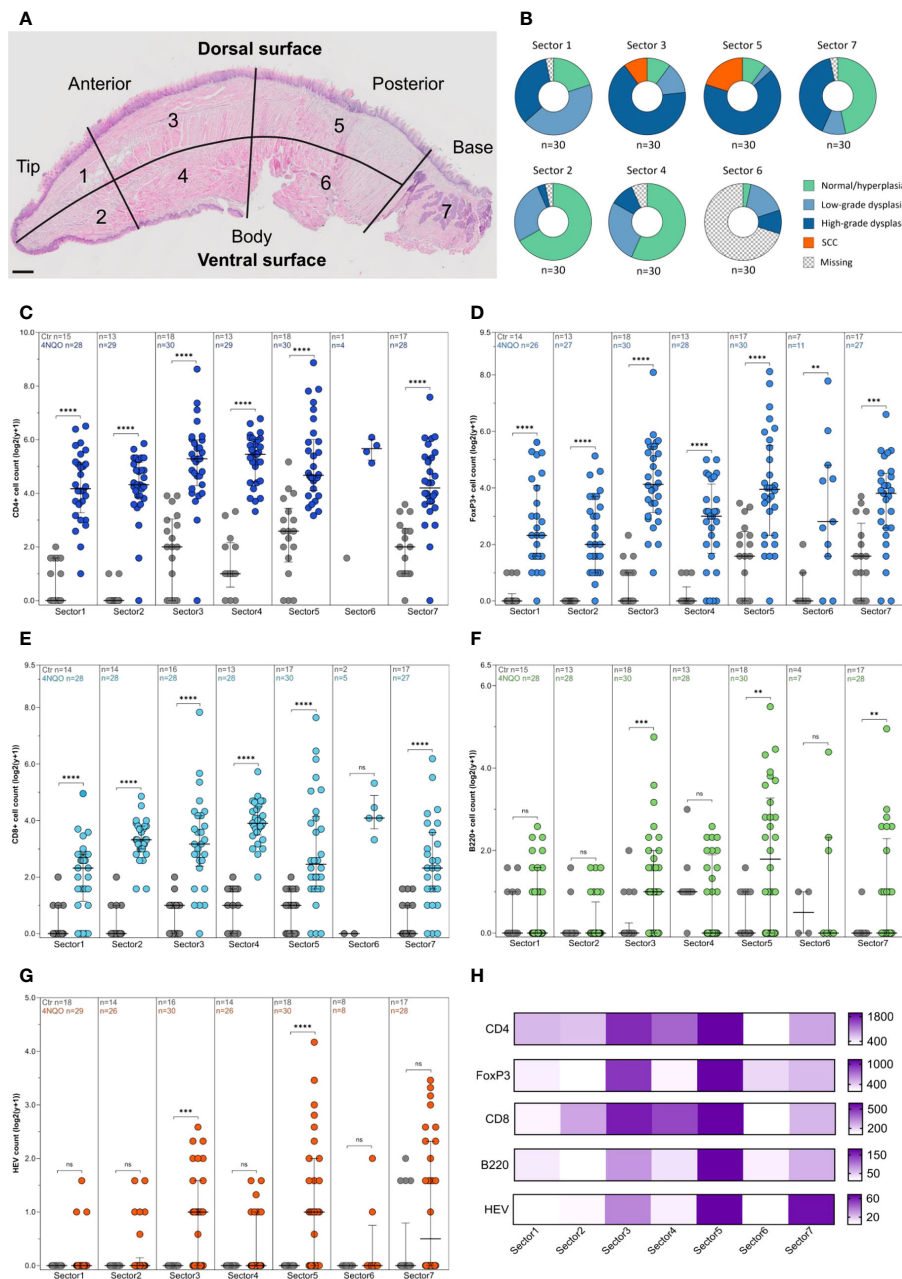

FIGURE 4

Immune cell and HEV count by endpoint and histopathological grade. **(A)** Shown are the total counts of CD4+, FoxP3+, CD8+ and B220+ cells and HEVs in the tongues of 4NQO-exposed mice (n=30), and the total counts of each of the markers in the tongues graded as **(B)** normal/hyperplasia (n=1), **(C)** low-grade dysplasia (n=3), **(D)** high-grade dysplasia (n=19), and **(E)** SCC (n=7). **(F–J)** The total counts of all the immune cell markers and HEVs in the tongues of 4NQO-exposed mice sacrificed at endpoint weeks ≤20 (n=12), endpoint weeks 21-24 (n=9), and endpoint weeks 25-28 (n=9). **(K–O)** The total counts of immune cells and HEVs in the tongues of 4NQO-exposed mice plotted against the most severe histopathological lesion. Data is log transformed (log2(y-+)). Scale bar indicates median with IQR **(A–E, K–O)** or mean with standard deviation (SD) **(F–J)**.

TABLE 2 Worst histologic grade in sectors 1-7 in the tongue of 4NQO-exposed mice.

Worst histologic grade	Sector 1 n=29 (No.(%))	Sector 2 n=29 (No.(%))	Sector 3 n=30 (No.(%))	Sector 4 n=29 (No.(%))	Sector 5 n=30 (No.(%))	Sector 6 n=9 (No.(%))	Sector 7 n=29 (No.(%))
Normal/hyperplasia	6 (20.0)	20 (66.7)	3 (10.0)	17 (56.7)	3 (10.0)	1 (3.3)	14 (46.7)
Low-grade dysplasia	13 (43.3)	8 (26.7)	4 (13.3)	8 (26.7)	1 (3.3)	5 (16.7)	3 (10.0)
High-grade dysplasia	10 (33.3)	1 (3.3)	20 (66.7)	3 (10.0)	20 (66.7)	3 (10.0)	12 (40.0)
SCC	0 (0.0)	0 (0.0)	4 (10.0)	0 (0.0)	6 (20.0)	0 (0.0)	0 (0.0)
Missing	1 (3.3)	1 (3.3)	0 (0.0)	2 (6.7)	0 (0.0)	21 (70)	1 (3.3)

common on the dorsal posterior body of the tongue (sector 5) and tongue base (sector 7) (Supplementary Figure S2; Supplementary Table S1). The area least affected by 4NQO-exposure was the ventral part of the tongue, in sectors 2 and 4, in which 66.7% and 56.7% of the mice presented with normal/hyperplastic mucosa, respectively. The ventral posterior part of the tongue (sector 6) was missing in many sections because excision of the tongue was performed in this region. The severity of the histopathological lesions increased from the earliest to the last endpoint in all areas of the tongue (Supplementary Figure S6).

Lower numbers of immune cells and HEVs were found in all seven sectors of the control tongues compared to 4NQO-exposed tongues (Figures 4C–G). Sector 3 and 5 displayed a substantial accumulation of immune cells and HEVs (Figures 4C–H), which corresponded with the severity of the epithelial lesions found in these sectors (Figure 4B). Interestingly, the median number of CD4 + and CD8+ T cells were highest in sector 4, despite the presence of few lesions in this area (Figures 4C, E). While the number of CD4+ T cells in sector 4 was associated with the presence of epithelial lesions (median CD4+ T cells without lesions n=35, and with lesions n=55, P=0.0038), the number of CD8+ T cells was not (P=0.755). For B cells and HEVs, the highest count was found in sector 5 (Figures 4F, G). Several tongues also displayed a high HEV count in sector 7. Large papillomas often displayed a strong immune infiltrate, likely reflecting the high numbers of HEVs seen in this area (Figure 4G; Supplementary Figure S2). Interestingly, sector 7 was the only area of the tongue where HEVs were observed in the control group (Figure 4G). This area of the mouse tongue has mucous- and serous salivary glands and we observed that structures characteristic of excretory ducts of the salivary glands were often surrounded by several HEVs and immune cells (Supplementary Figure S7), even in the absence of histological changes in 4NQO-exposed mice. We also found HEVs in this area in healthy controls. Additionally, sectors 2 and 4 were the only other sites of the 4NQO-exposed tongues where HEVs were present without any epithelial lesions. Finally, we calculated the number of immune cells and HEVs within sectors assigned the same histopathological score to get a more detailed image of the immune composition closely linked to the epithelial lesions (Supplementary Figure S8). In summary, the presence of immune cells and HEVs corresponded with the site and severity of epithelial lesion.

3.4 4NQO-exposed mice displayed reactive draining lymph nodes but no metastasis

A small group of mice (4NQO n=4, control n=2) underwent PET/MRI (Figure 1A) to determine whether this combined modality could be used to detect primary- and metastatic lesions as a non-invasive method to follow tumor progression. The mice were tail-vein injected with [18F]FDG, a glucose analogue radiotracer. MRI clearly revealed a hyperintense signal on the tongue, offset to the midsagittal plane, of the four 4NQO-exposed mice and PET confirmed specific [18F]FDG-uptake (Figure 5A). The radiotracer accumulation in this area increased over time and had a standardized uptake value of 8.0 ± 6.2 when compared to the muscle reference region, which reached an early plateau (Figure 5B). The [18F]FDG-uptake in this region was also distinct from the surrounding tissues, corresponding well with the PET images. The ratio of [18F]FDG-uptake in the hyper-intense lesion vs muscle varied among the different animals, with animal e4 showing the largest deviation from the mean (Figure 5C). However, this was not linked to the variation in the size of the lesion, with animal e4 having one of the smallest lesions (Figure 5D). This could indicate a difference in metabolic rate and/or cell proliferation.

Following PET pharmacokinetic modeling, the rate constants were expressed as ml/ccm/min (K1, Flux), 1/min (k2-k3) and μmol/min/100g (MRGlu) and the results are shown in Supplementary Figures S9A, B. The highest glucose uptake and retention were seen in the hyperintense lesions when comparing to the reference region, confirming increased glucose consumption in these areas of the tongue (Figures 5A, B). Histological examination based on one half of the tongue (the other half was used for other purposes) showed that all the four experimental mice had several lesions on the tongue. The most severe lesions in mice e1, e2 and e4 were high-grade dysplasias, while e3 had low-grade dysplastic lesions as the most severe score. Staining for Ki-67 showed no obvious difference in the number of positive cells in the tongue epithelium between these four mice. However, most of the 4NQO-exposed mice (13/17) displayed increased Ki-67 positivity in the tongue compared to healthy controls (n=8), and the distribution of the positively stained cells corresponded with the presence of epithelial lesions (Figure 5E).
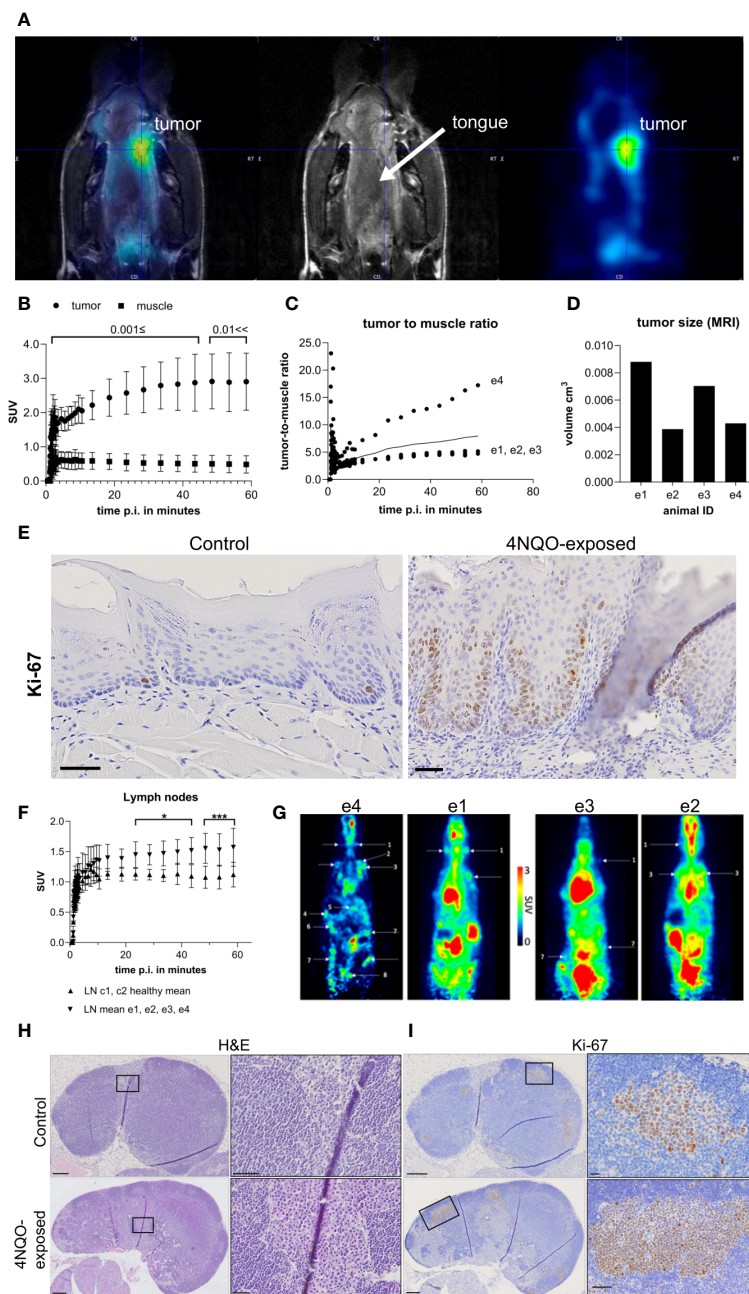
FIGURE 5

In vivo PET/MRI results of mice following i.v. injection of [18F]FDG. **(A)** PET/MRI image of a representative animal (animal e4) representing uptake of [18F]FGD in the hyperintense lesion (left and right). The T2-weightes (middle) shows the lesion on the lateral side of the tongue marked by the crosshair. Overlapping PET and MRI image is shown to the left, while the middle and right shows MRI and PET image, respectively. **(B)** Standardized uptake values (SUV) of the whole lesion (round dots) and leg muscle (square dots, reference tissue), **(C)** lesion-to-muscle ratio in the four carcinogen-exposed mice (e1-e4), and **(D)** volumes of the hyperintense lesions of each animal (e1-e4) derived from T1-weighted MRI. **(E)** Representative images of Ki-67 staining in the (dorsal) tongue of healthy controls and 4NQO-exposed mice. Scale bar indicates 50µm. **(F)** SUV of lymph nodes of 4NQO-exposed (n=4, e1-e4, upward pointing arrowheads) and control mice (n=2, c1-c2, downward pointing arrowheads). Error bars indicate mean with SD. **(G)** PET/MRI results showing SUV of the lymph nodes indicated by arrows/labels in the four 4NQO-exposed mice. Representative images of **(H)** H&E- and **(I)** Ki-67-stained sections of cervical lymph nodes in 4NQO-exposed mice and healthy controls. Detailed images of plasma cells and Ki-67+ cells from outlined areas (black box) are shown in H&E- and Ki-67-stained sections, right panels of **(H, I)**, respectively. Scale bars indicate 200µm **(H, I)** lymph node overview), 50µm **(E, H)** outlined area control and 4NQO, **(I)** outlined area 4NQO) or 20µm **(I)** outlined area control).

To assess whether PET could be used to detect lymph node metastasis, an in-depth image analysis of the cervical- and distant lymph nodes was performed. The analysis revealed increased [18F] FDG uptake in the carcinogen-exposed group compared to the healthy controls (Figures 5F, G). Animal e4 presented with higher glucose metabolism in all lymph nodes, while e1, e2, and e3 showed active [18F]FDG uptake primarily in the cervical and axillary region (Figures 5F, G). To assess whether the observed [18F]FDG uptake

was due to lymph node metastasis, H&E-stained serial sections of cervical lymph nodes from the four carcinogen-exposed mice and controls (c1-c2) were assessed for metastatic lesions. The results showed that none of the lymph nodes contained cancer cells (primary or metastatic) (Figure 5H). However, when comparing the 4NQO group to the controls, the carcinogen-exposed group had enlarged lymph nodes owing to expansion of the B and T cell compartments. We also observed a prominent accumulation of cells with abundant cytoplasm and an eccentrically located nucleus, indicative of plasma cells in the paracortex and medulla (Figure 5H). Animals e1-e3 exhibited low to moderate presence of plasma cells, while in e4, plasma cells comprised nearly half of certain lymph nodes. Ki-67 staining of cervical lymph nodes did show accumulation of positively stained cells in areas corresponding to germinal centers, which were larger in the 4NQO-exposed mice compared to healthy controls (Figure 5I). To conclude, no regional lymph node metastases or distant metastases were detected using whole-body scans, nor upon histopathological analysis of the examined tissues (cervical- and inguinal lymph nodes, lungs, liver, kidneys, and urinary bladder).

4 Discussion

The current study presents a detailed description of how the tongue epithelial lesions and associated immune infiltrate evolve in the 4NQO mouse model after oral administration of the carcinogen for 16 weeks. We evaluated the potential of PET/MRI as a tool to monitor tumor progression in this model. We showed that 4NQO exposure induced epithelial lesions in the tongue that increased in severity over time, where all mice had high-grade dysplastic lesions or SCCs at the latest timepoint (9 weeks or longer after termination of carcinogen exposure). These findings are consistent with other reports of this model (31–34), and confirm its ability to replicate the multistep carcinogenesis in humans through spontaneous tumor development and progression, alongside a functional immune system. Our results showed that the lymphocytic infiltrate and HEVs increased over time after 4NQO exposure, in concert with the severity of epithelial lesions.

A challenge we faced with this model was the development of multiple lesions with varying severity on the same tongue. Using a mouse model with transplanted cells could provide more predictable and consistent tumor development, however, we were interested in the early development of the tumor and the associated immune response. Genetically engineered models with inducible tissue-targeted expression and/or knockout of oncogenes and tumor suppressor genes could also provide more predictable tumorigenesis but are often challenged by a lack of tissue-specificity and risk of leakage of transgene expression (35). We handled the challenge of multiple lesions by using a scoring method where the tongue was divided into seven sectors. We used a similar approach as Vered et al. (24), in which they separated the tongue of rats into three equal parts: the anterior, middle, and posterior part of the tongue. Because the tongue base in mice contains the lingual salivary glands, which is distinct from the anatomy of the rest of the

tongue, we chose to separate this area into a single sector. In support of our approach of grouping lesions from small anatomical regions, Sequeira et al. (32) found that individual 4NQO-induced lesions close to each other were more likely to be clonally related. The clonal origin differed when the lesions were located some distance from each other (32). Thus, our approach can be used to study the stage-by-stage changes that occur in the tongue mucosa.

Neither local nor distant metastasis was observed in any of the 4NQO-exposed mice in our study. This is in line with other studies reporting that lymph node metastasis in this model was infrequent until week 33 post 4NQO exposure (36, 37). Some of the animals had to be sacrificed before reaching the final experimental endpoint due to a high primary tumor burden. Hence, the mice were probably terminated before the development of metastasis. Despite lack of metastases upon histopathological examination, we saw prominent PET signals from the cervical lymph nodes of the 4NQO-exposed mice. These signals were probably due to increased [18F]FDG uptake caused by reactive changes in the lymph nodes indicated by a prominent plasma cell component within the paracortex and medulla, as well as increased proliferation of B cell follicles measured by Ki-67 expression and enlarged T cell zones. Although no metastases were detected in our experiment, the strong PET-signal from reactive lymph nodes suggests that [18F]FDG is an unsuitable tracer for discriminating between metastases and reactive changes in this model. Using PET radiotracers that are more tumor- or metastasis-specific, such as [18F]FAPI-74, [18F]Fluciclovine, or [68Ga]Pentixafor, might enhance the ability to distinguish between reactive changes and metastasis in lymph nodes.

It is well established that the tumor immune infiltrate has a major influence on tumor progression and the response of solid tumors to immunotherapy (4). Similar to our current findings, previous studies on the 4NQO mouse model have demonstrated that changes in the immune infiltrate correspond with the histological grade (38, 39). This is consistent with findings in human tongue specimens of different histological grades (40), as well as across oral subsites (41, 42). Our findings together with other studies indicate that mouse and human oral lesions display a pronounced influx of T cells that increase with more severe histopathology (39, 40, 42). Consistently, OSCCs are often abundantly infiltrated with T cells (43, 44). However, marked B cell infiltrates have been found in human oral cancers (5, 45), which might reflect the presence of TLS. Consequently, tumors that lack TLS tend to display low numbers of B cells (27, 46). In the 4NQO-induced tongue lesions, we found that B cells were present at low numbers. Accordingly, we found low numbers of B cells and no aggregates resembling the formation of TLS in the tongue tissues. Sales de Sà et al. reported that among 48 OTSCC patients, 77.1% were enriched in CD20+ B cells (5). Intratumoral B cells are mostly located in TLS and aggregated with T cells (30). Indeed, the presence of B cells in OTSCC tumors positively correlated with the density of T cells (5), indicative of TLS formation. Although the presence of B cells was low in the 4NQO-exposed tongues, the number of B cells was higher in SCCs compared to earlier stages. This might indicate that TLSs develop at a later timepoint in this

model. We have earlier found that TLSs in OSCC are infrequent and heterogeneously distributed (19), and it might be that we have missed TLSs by not examining whole tongues. Alternatively, the presence of a sparse B cell infiltrate could point to a role of B cells in promoting OSCC. There is growing evidence that intratumoral B cells found outside TLS may be involved in tumor progression (47, 48). However, the role of different B cell subsets in OSCC is largely unexplored, and reliable markers for identifying B cell phenotypes remain undefined. Recently, tumor-associated lymphoid aggregates rich in T cells with a stem-cell like phenotype (CD8+TCF1+) and antigen-presenting cells (APCs) has been identified in human tumors and tumor-bearing mice (49, 50). These so-called antigen-presenting niches (APNs) resemble T cell zones in SLOs, suggesting that they may function as intra-tumoral sites for priming and activation of T cells. CD8+TCF1+ T cell niches have also been found in close proximity to TA-HEVs (51). Hence, lymphoid aggregates other than TLS can impact tumor control, however, we have yet to determine the presence of APNs in the 4NQO model. While TILs are often examined in established tumors, the tumor immune response is dynamic and constantly reshaped by interactions with neoplastic cells and the microenvironment at different stages of tumorigenesis (52). Efficient use of animal models warrants a better understanding of the immune infiltrate. Based on these results, the 4NQO mouse model is suitable for studies of T cells responses in oral carcinogenesis and perhaps tumor promoting B cells.

We found that HEVs developed in the tongue already 14 weeks after administration of the carcinogen, even when hyperplasia was the most severe histology. HEVs were found in the tongue of all 4NQO-exposed mice and in some controls. To the best of our knowledge HEVs have not been reported in this model previously. The presence of HEVs has been reported in oral lesions with malignant potential (53, 54), but HEV development at different stages of oral cancer development and progression is not well described. In OSCC, HEVs are more frequently found in early-stage tumors (T1-T2) than advanced tumors (T3-T4) (21, 55). Here we showed that the number of HEVs increased significantly during progression of tongue lesions, suggesting that early changes in the tongue mucosa initiates HEV formation that is maintained during tumor initiation and progression.

In tumors, HEVs are typically found in areas rich in lymphocytes, including TLS. TLSs share some characteristics with lymph nodes, including organized clusters of B and T cells, interspersed with antigen presenting cells and stromal cells (11). HEVs recruit lymphocytes into the TLS, which serve as a local site for adaptive immune responses. The presence of TA-HEVs and TLS is associated with a favorable prognosis in many cancers (15), including OSCC (19, 21, 27). However, the location of TA-HEVs within the tumor microenvironment could further refine their prognostic value. A high HEV density within TLS correlated with longer survival in colorectal cancer patients compared to HEV low TLS (16). These findings demonstrate a close relationship between HEVs and TLS in anti-tumor immunity. Interestingly, the presence of TA-HEVs does not always correlate with the presence of TLS (15, 19, 21). This raises the question whether TA-HEVs within TLS are

regulated differently than those independent of TLS, and whether this could impact on their functionality. Compared to homeostatic HEVs in the lymph node, that display a thick vessel wall and small lumen, more heterogenous HEV phenotypes have been found in inflamed lymph nodes and tumors (21, 56). The heterogenous morphology of these HEVs can be explained by differences in gene signatures revealed by transcriptomic analyses (57, 58), in which lymph node HEVs are considered fully differentiated (mature), and the inflamed- and TA-HEVs are dedifferentiated. Despite being dedifferentiated, spontaneously arising TA-HEVs have been shown to harbor some lymphocyte-recruiting capacity (59, 60). In a mouse model of fibrosarcoma, treatment with immune checkpoint inhibitors, (anti-PD-1 and -CTLA-4) induced the frequency and maturation of TA-HEVs and led to increased numbers of infiltrating CD4 and CD8 T cells (60). This suggests some functional impairment of TA-HEVs.

Although it is not well-known what triggers the development of TA-HEVs, some studies have proposed a positive feedback-loop mechanism. In lymph nodes, dendritic cells are recognized as main drivers of HEV formation. However, in murine tumors the presence of an active T cell response prior to or within the developing tumor appears to be essential for TA-HEV development. For instance, B16-OVA tumors grown in Rag⁻/⁻ mice, that lack mature B and T lymphocytes, also lack TA-HEVs (59). Repleting these mice with CD8 T cells induced TA-HEVs. T cell depletion using anti-CD4 and -CD8 antibodies were also shown to reduce the number of TA-HEVs in murine pancreatic neuroendocrine tumors (61). Induction of TA-HEVs by immune checkpoint inhibitors is also a strong indicator of the necessity of reactive T cells (51, 60, 61). Here we show that 4NQO does not induce TLS formation but supports TA-HEV development. Hence, the 4NQO model can be used to study mechanisms regulating HEV neogenesis. The model could furthermore be beneficial for studies aiming to understand mechanisms driving the differentiation and TA-HEVs with the aim of refining anti-cancer therapy.

In conclusion, we have shown that the 4NQO mouse model generates an immune microenvironment that reflects early stages of oral carcinogenesis and constitutes the required signals for HEV formation. While 4NQO-induced lesions display a marked T cell infiltrate, we found sparse numbers of B cells and no B cells aggregates indicating TLS. The present study is the first to report the presence of HEVs within 4NQO-induced oral lesions, making it a promising model to dissect the components involved in generating a permissive milieu for *de novo* HEV development independent of TLS. Whether these vessels have functional capabilities is yet to be answered. Understanding the mechanisms regulating TA-HEVs can permit the development of targeted therapies for oral cancer patients. PET/MRI using [18F]FDG radiotracer is efficient in detecting reactive cervical lymph nodes. Although we did not detect any metastatic lesions in the mice, the strong [18F]FDG signals in reactive lymph nodes suggests that other tracers are needed to detect lymph node metastases. Due to the low incidence of metastasis in this model while the tumor burden is manageable for the mice, the 4NQO model is best used to study early stages of oral carcinogenesis.

Data availability statement

The raw data supporting the conclusions of this article will be made available by the authors, without undue reservation.

Ethics statement

The animal study was approved by The Norwegian Food Safety Authority. The study was conducted in accordance with the local legislation and institutional requirements.

Author contributions

KS: Conceptualization, Investigation, Visualization, Writing – original draft, Writing – review & editing, Data curation, Formal analysis, Methodology, Project administration. RS: Investigation, Writing – review & editing, Formal analysis, Methodology. MK: Investigation, Writing – review & editing, Data curation, Formal analysis, Methodology, Visualization. AA: Investigation, Writing – review & editing, Formal analysis. AW: Methodology, Writing – review & editing, Conceptualization, Project administration, Supervision. GB: Investigation, Writing – review & editing, Conceptualization, Project administration, Supervision. EH-O: Conceptualization, Methodology, Project administration, Supervision, Writing – review & editing, Funding acquisition, Investigation. SM: Formal analysis, Investigation, Methodology, Writing – review & editing, Conceptualization, Data curation, Funding acquisition, Project administration, Supervision, Writing – original draft.

Funding

Acknowledgments

Conflict of interest

The authors declare that the research was conducted in the absence of any commercial or financial relationships that could be construed as a potential conflict of interest.

Publisher's note

All claims expressed in this article are solely those of the authors and do not necessarily represent those of their affiliated organizations, or those of the publisher, the editors and the reviewers. Any product that may be evaluated in this article, or claim that may be made by its manufacturer, is not guaranteed or endorsed by the publisher.

Supplementary material

The Supplementary Material for this article can be found online at: https://www.frontiersin.org/articles/10.3389/fonc.2024.1343839/full#supplementary-material

References

1. Oc P, Pillai G, Patel S, Fisher C, Archer D, Eccles S, et al. Tumour thickness predicts cervical nodal metastases and survival in early oral tongue cancer. *Oral Oncol.* (2003) 39:386–90. doi: 10.1016/S1368-8375(02)00142-2

2. Bjerkli IH, Jetlund O, Karevold G, Karlsdottir A, Jaatun E, Uhlin-Hansen L, et al. Characteristics and prognosis of primary treatment-naive oral cavity squamous cell carcinoma in Norway, a descriptive retrospective study. *PloS One.* (2020) 15:e0227738. doi: 10.1371/journal.pone.0227738

3. Sung H, Ferlay J, Siegel RL, Laversanne M, Soerjomataram I, Jemal A, et al. Global cancer statistics 2020: GLOBOCAN estimates of incidence and mortality worldwide for 36 cancers in 185 countries. *CA Cancer J Clin.* (2021) 71:209–49. doi: 10.3322/caac.21660

4. Bruni D, Angell HK, Galon J. The immune contexture and Immunoscore in cancer prognosis and therapeutic efficacy. *Nat Rev Cancer.* (2020) 20:662–80. doi: 10.1038/s41568-020-0285-7

5. Sales de Sá R, Miranda Galvis M, Mariz B, Leite AA, Schultz L, Almeida OP, et al. Increased tumor immune microenvironment CD3+ and CD20+ Lymphocytes predict a better prognosis in oral tongue squamous cell carcinoma. *Front Cell Dev Biol.* (2020) 8:622161. doi: 10.3389/fcell.2020.622161

6. Mahmoud SM, Paish EC, Powe DG, Macmillan RD, Grainge MJ, Lee AH, et al. Tumor-infiltrating CD8+ lymphocytes predict clinical outcome in breast cancer. *J Clin Oncol.* (2011) 29:1949–55. doi: 10.1200/JCO.2010.30.5037

7. Shimizu S, Hiratsuka H, Koike K, Tsuchihashi K, Sonoda T, Ogi K, et al. Tumor-infiltrating CD8(+) T-cell density is an independent prognostic marker for oral squamous cell carcinoma. *Cancer Med.* (2019) 8:80–93. doi: 10.1002/cam4.1889

8. Shoushtari AN, Olszanski AJ, Nyakas M, Hornyak TJ, Wolchok JD, Levitsky V, et al. Pilot study of ONCOS-102 and pembrolizumab: remodeling of the tumor microenvironment and clinical outcomes in anti-PD-1-resistant advanced melanoma. *Clin Cancer Res.* (2023) 29:100–9. doi: 10.1158/1078-0432.CCR-22-2046

9. Saito H, Okita K, Chang AE, Ito F. Adoptive transfer of CD8+ T cells generated from induced pluripotent stem cells triggers regressions of large tumors along with immunological memory. *Cancer Res.* (2016) 76:3473–83. doi: 10.1158/0008-5472.CAN-15-1742

10. Kouketsu A, Sato I, Oikawa M, Shimizu Y, Saito H, Tashiro K, et al. Regulatory T cells and M2-polarized tumour-associated macrophages are associated with the oncogenesis and progression of oral squamous cell carcinoma. *Int J Oral Maxillofac Surg.* (2019) 48:1279–88. doi: 10.1016/j.ijom.2019.04.004

11. Sautès-Fridman C, Petitprez F, Calderaro J, Fridman WH. Tertiary lymphoid structures in the era of cancer immunotherapy. *Nat Rev Cancer*. (2019) 19:307–25. doi: 10.1038/s41568-019-0144-6

12. Vella G, Guelfi S, Bergers G. High endothelial venules: A vascular perspective on tertiary lymphoid structures in cancer. *Front Immunol*. (2021) 12:736670. doi: 10.3389/fimmu.2021.736670

13. Middleton J, Americh L, Gayon R, Julien D, Mansat M, Mansat P, et al. A comparative study of endothelial cell markers expressed in chronically inflamed human tissues: MECA-79, Duffy antigen receptor for chemokines, von Willebrand factor, CD31, CD34, CD105 and CD146. *J Pathol*. (2005) 206:260–8. doi: 10.1002/path.1788

14. Thaunat O, Patey N, Caligiuri G, Gautreau C, Mamani-Matsuda M, Mekki Y, et al. Chronic rejection triggers the development of an aggressive intragraft immune response through recapitulation of lymphoid organogenesis. *J Immunol*. (2010) 185:717–28. doi: 10.4049/jimmunol.0903589

15. Martinet L, Garrido I, Filleron T, Le Guellec S, Bellard E, Fournie JJ, et al. Human solid tumors contain high endothelial venules: association with T- and B-lymphocyte infiltration and favorable prognosis in breast cancer. *Cancer Res*. (2011) 71:5678–87. doi: 10.1158/0008-5472.CAN-11-0431

16. Zhan Z, Shi-Jin L, Yi-Ran Z, Zhi-Long L, Xiao-Xu Z, Hui D, et al. High endothelial venules proportion in tertiary lymphoid structure is a prognostic marker and correlated with anti-tumor immune microenvironment in colorectal cancer. *Ann Med*. (2023) 55:114–26. doi: 10.1080/07853890.2022.2153911

17. Dieu-Nosjean MC, Antoine M, Danel C, Heudes D, Wislez M, Poulot V, et al. Long-term survival for patients with non-small-cell lung cancer with intratumoral lymphoid structures. *J Clin Oncol*. (2008) 26:4410–7. doi: 10.1200/JCO.2007.15.0284

18. Martinet L, Garrido I, Girard JP. Tumor high endothelial venules (HEVs) predict lymphocyte infiltration and favorable prognosis in breast cancer. *Oncoimmunology*. (2012) 1:789–90. doi: 10.4161/onci.19787

19. Wirsing AM, Rikardsen OG, Steigen SE, Uhlin-Hansen L, Hadler-Olsen E. Characterisation and prognostic value of tertiary lymphoid structures in oral squamous cell carcinoma. *BMC Clin Pathol*. (2014) 14:38. doi: 10.1186/1472-6890-14-38

20. Wirsing AM, Ervik IK, Seppola M, Uhlin-Hansen L, Steigen SE, Hadler-Olsen E. Presence of high-endothelial venules correlates with a favorable immune microenvironment in oral squamous cell carcinoma. *Mod Pathol*. (2018) 31:910–22. doi: 10.1038/s41379-018-0019-5

21. Wirsing AM, Rikardsen OG, Steigen SE, Uhlin-Hansen L, Hadler-Olsen E. Presence of tumour high-endothelial venules is an independent positive prognostic factor and stratifies patients with advanced-stage oral squamous cell carcinoma. *Tumour Biol*. (2016) 37:2449–59. doi: 10.1007/s13277-015-4036-4

22. Kanojia D, Vaidya MM. 4-nitroquinoline-1-oxide induced experimental oral carcinogenesis. *Oral Oncol*. (2006) 42:655–67. doi: 10.1016/j.oraloncology.2005.10.013

23. Wang Z, Wu VH, Allevato MM, Gilardi M, He Y, Luis Callejas-Valera J, et al. Syngeneic animal models of tobacco-associated oral cancer reveal the activity of in *situ* anti-CTLA-4. *Nat Commun*. (2019) 10:5546. doi: 10.1038/s41467-019-13471-0

24. Vered M, Allon I, Buchner A, Dayan D. Stromal myofibroblasts and Malignant transformation in a 4NQO rat tongue carcinogenesis model. *Oral Oncol*. (2007) 43:999–1006. doi: 10.1016/j.oraloncology.2006.11.007

25. El-Naggar AK, Chan JKC, Grandis JR, Takata T, Slootweg PJ. *WHO Classification of Head and Neck Tumours. 4th edition*. International Agency for Research on Cancer (2017).

26. Odell E, Kujan O, Warnakulasuriya S, Sloan P. Oral epithelial dysplasia: Recognition, grading and clinical significance. *Oral Dis*. (2021) 27:1947–76. doi: 10.1111/odi.13993

27. Li Q, Liu X, Wang D, Wang Y, Lu H, Wen S, et al. Prognostic value of tertiary lymphoid structure and tumour infiltrating lymphocytes in oral squamous cell carcinoma. *Int J Oral Sci*. (2020) 12:24. doi: 10.1038/s41368-020-00092-3

28. Espedal H, Berg HF, Fonnes T, Fasmer KE, Krakstad C, Haldorsen IS. Feasibility and utility of MRI and dynamic (18)F-FDG-PET in an orthotopic organoid-based patient-derived mouse model of endometrial cancer. *J Transl Med*. (2021) 19:406. doi: 10.1186/s12967-021-03086-9

29. Lanz B, Poitry-Yamate C, Gruetter R. Image-derived input function from the vena cava for 18F-FDG PET studies in rats and mice. *J Nucl Med*. (2014) 55:1380–8. doi: 10.2967/jnumed.113.127381

30. Fridman WH, Meylan M, Pupier G, Calvez A, Hernandez I, Sautès-Fridman C. Tertiary lymphoid structures and B cells: An intratumoral immunity cycle. *Immunity*. (2023) 56:2254–69. doi: 10.1016/j.immuni.2023.08.009

31. Bouaoud J, Foy JP, Tortereau A, Michon L, Lavergne V, Gadot N, et al. Early changes in the immune microenvironment of oral potentially Malignant disorders reveal an unexpected association of M2 macrophages with oral cancer free survival. *Oncoimmunology*. (2021) 10:1944554. doi: 10.1080/2162402X.2021.1944554

32. Sequeira I, Rashid M, Tomás IM, Williams MJ, Graham TA, Adams DJ, et al. Genomic landscape and clonal architecture of mouse oral squamous cell carcinomas dictate tumour ecology. *Nat Commun*. (2020) 11:5671. doi: 10.1038/s41467-020-19401-9

33. Wen L, Lu H, Li Q, Li Q, Wen S, Wang D, et al. Contributions of T cell dysfunction to the resistance against anti-PD-1 therapy in oral carcinogenesis. *J Exp Clin Cancer Res*. (2019) 38:299. doi: 10.1186/s13046-019-1185-0

34. Yamaguchi H, Hiroi M, Mori K, Ushio R, Matsumoto A, Yamamoto N, et al. Simultaneous expression of th1- and treg-associated chemokine genes and CD4(+), CD8(+), and foxp3(+) cells in the premalignant lesions of 4NQO-induced mouse tongue tumorigenesis. *Cancers (Basel)*. (2021) 13:1835. doi: 10.3390/cancers13081835

35. Ishida K, Tomita H, Nakashima T, Hirata A, Tanaka T, Shibata T, et al. Current mouse models of oral squamous cell carcinoma: Genetic and chemically induced models. *Oral Oncol*. (2017) 73:16–20. doi: 10.1016/j.oraloncology.2017.07.028

36. Walk EL, McLaughlin S, Coad J, Weed SA. Use of high frequency ultrasound to monitor cervical lymph node alterations in mice. *PLoS One*. (2014) 9:e100185. doi: 10.1371/journal.pone.0100185

37. Li J, Liang F, Yu D, Qing H, Yang Y. Development of a 4-nitroquinoline-1-oxide model of lymph node metastasis in oral squamous cell carcinoma. *Oral Oncol*. (2013) 49:299–305. doi: 10.1016/j.oraloncology.2012.10.013

38. Wang J, Hu Y, Escamilla-Rivera V, Gonzalez CL, Tang L, Wang B, et al. Epithelial mutant p53 promotes resistance to anti-PD-1-mediated oral cancer immunoprevention in carcinogen-induced mouse models. *Cancers (Basel)*. (2021) 13:1471. doi: 10.3390/cancers13061471

39. Chao JL, Korzinkin M, Zhavoronkov A, Ozerov IV, Walker MT, Higgins K, et al. Effector T cell responses unleashed by regulatory T cell ablation exacerbate oral squamous cell carcinoma. *Cell Rep Med*. (2021) 2:100399. doi: 10.1016/j.xcrm.2021.100399

40. Gannot G, Gannot I, Vered H, Buchner A, Keisari Y. Increase in immune cell infiltration with progression of oral epithelium from hyperkeratosis to dysplasia and carcinoma. *Br J Cancer*. (2002) 86:1444–8. doi: 10.1038/sj.bjc.6600282

41. Sun L, Kang X, Wang C, Wang R, Yang G, Jiang W, et al. Single-cell and spatial dissection of precancerous lesions underlying the initiation process of oral squamous cell carcinoma. *Cell Discovery*. (2023) 9:28. doi: 10.1038/s41421-023-00532-4

42. Gan CP, Lee BKB, Lau SH, Kallarakkal TG, Zaini ZM, Lye BKW, et al. Transcriptional analysis highlights three distinct immune profiles of high-risk oral epithelial dysplasia. *Front Immunol*. (2022) 13:954567. doi: 10.3389/fimmu.2022.954567

43. Gaafar NM, Osman TA, Ahmed IA, Elsheikh M, Dongre H, Jacobsen MR, et al. Characterization of immune cell infiltrate in tumor stroma and epithelial compartments in oral squamous cell carcinomas of Sudanese patients. *Clin Exp Dent Res*. (2022) 8:130–40. doi: 10.1002/cre2.501

44. Zhou C, Wu Y, Jiang L, Li Z, Diao P, Wang D, et al. Density and location of CD3 (+) and CD8(+) tumor-infiltrating lymphocytes correlate with prognosis of oral squamous cell carcinoma. *J Oral Pathol Med*. (2018) 47:359–67. doi: 10.1111/jop.12698

45. Quan H, Shan Z, Liu Z, Liu S, Yang L, Fang X, et al. The repertoire of tumor-infiltrating lymphocytes within the microenvironment of oral squamous cell carcinoma reveals immune dysfunction. *Cancer Immunol Immunother*. (2020) 69:465–76. doi: 10.1007/s00262-020-02479-x

46. Petitprez F, de Reyniès A, Keung EZ, Chen TW, Sun CM, Calderaro J, et al. B cells are associated with survival and immunotherapy response in sarcoma. *Nature*. (2020) 577:556–60. doi: 10.1038/s41586-019-1906-8

47. Castino GF, Cortese N, Capretti G, Serio S, Di Caro G, Mineri R, et al. Spatial distribution of B cells predicts prognosis in human pancreatic adenocarcinoma. *Oncoimmunology*. (2016) 5:e1085147. doi: 10.1080/2162402X.2015.1085147

48. Yang M, Lu J, Zhang G, Wang Y, He M, Xu Q, et al. CXCL13 shapes immunoactive tumor microenvironment and enhances the efficacy of PD-1 checkpoint blockade in high-grade serous ovarian cancer. *J Immunother Cancer*. (2021) 9:e001136. doi: 10.1136/jitc-2020-001136

49. Jansen CS, Prokhnevska N, Master VA, Sanda MG, Carlisle JW, Bilen MA, et al. An intra-tumoral niche maintains and differentiates stem-like CD8 T cells. *Nature*. (2019) 576:465–70. doi: 10.1038/s41586-019-1836-5

50. Ramachandran M, Vaccaro A, van de Walle T, Georganaki M, Lugano R, Vemuri K, et al. Tailoring vascular phenotype through AAV therapy promotes anti-tumor immunity in glioma. *Cancer Cell*. (2023) 41:1134–51.e10. doi: 10.1016/j.ccell.2023.04.010

51. Hua Y, Vella G, Rambow F, Allen E, Antoranz Martinez A, Duhamel M, et al. Cancer immunotherapies transition endothelial cells into HEVs that generate TCF1(+) T lymphocyte niches through a feed-forward loop. *Cancer Cell*. (2022) 40:1600–18.e10. doi: 10.1016/j.ccell.2022.11.002

52. Bindea G, Mlecnik B, Tosolini M, Kirilovsky A, Waldner M, Obenauf AC, et al. Spatiotemporal dynamics of intratumoral immune cells reveal the immune landscape in human cancer. *Immunity*. (2013) 39:782–95. doi: 10.1016/j.immuni.2013.10.003

53. Wang MY, Zhu WW, Zhang JY, Yu M, Zhai RD, Liu LK. Tertiary lymphoid structures in oral lichen planus and oral epithelial dysplasia with lichenoid features: A comparative study. *Oral Dis*. (2023) 29:154–64. doi: 10.1111/odi.14097

54. Yoshida H, Imamura Y, Yoshimura H, Kobayashi M. Induction of high endothelial venule-like vessels in oral and cutaneous lichen planus: A comparative study. *J Histochem Cytochem*. (2020) 68:343–50. doi: 10.1369/0022155420923272

55. Yoshida H, Hoshino H, Imamura Y, Yoshimura H, Sano K, Kobayashi M. Role of sialyl 6-sulfo Lewis X in antitumor immunity against oral squamous cell carcinoma. *J Oral Pathol Med*. (2017) 46:759–65. doi: 10.1111/jop.12585

56. Liao S, Ruddle NH. Synchrony of high endothelial venules and lymphatic vessels revealed by immunization. *J Immunol*. (2006) 177:3369–79. doi: 10.4049/jimmunol.177.5.3369

57. Veerman K, Tardiveau C, Martins F, Coudert J, Girard JP. Single-cell analysis reveals heterogeneity of high endothelial venules and different regulation of genes controlling lymphocyte entry to lymph nodes. *Cell Rep*. (2019) 26:3116–31.e5. doi: 10.1016/j.celrep.2019.02.042

58. Sawada J, Hiraoka N, Qi R, Jiang L, Fournier-Goss AE, Yoshida M, et al. Molecular signature of tumor-associated high endothelial venules that can predict breast cancer survival. *Cancer Immunol Res*. (2022) 10:468–81. doi: 10.1158/2326-6066.CIR-21-0369

59. Peske JD, Thompson ED, Gemta L, Baylis RA, Fu YX, Engelhard VH. Effector lymphocyte-induced lymph node-like vasculature enables naive T-cell entry into tumours and enhanced anti-tumour immunity. *Nat Commun*. (2015) 6:7114. doi: 10.1038/ncomms8114

60. Asrir A, Tardiveau C, Coudert J, Laffont R, Blanchard L, Bellard E, et al. Tumor-associated high endothelial venules mediate lymphocyte entry into tumors and predict response to PD-1 plus CTLA-4 combination immunotherapy. *Cancer Cell*. (2022) 40: p318-334.e9. doi: 10.1016/j.ccell.2022.01.002

61. Johansson-Percival A, He B, Li ZJ, Kjellén A, Russell K, Li J, et al. *De novo* induction of intratumoral lymphoid structures and vessel normalization enhances immunotherapy in resistant tumors. *Nat Immunol*. (2017) 18:1207–17. doi: 10.1038/ni.3836

Tumor-associated high endothelial venules in oral squamous cell carcinoma can be distinguished by Chst4 expression

Kjersti Sellæg, Anne Kristin McLaren Berge, Erik Knutsen, May-Britt Five, Elin Hadler-Olsen, Synnøve Norvoll Magnussen

Manuscript

Tumor-associated high endothelial venules in oral squamous cell carcinoma can be distinguished by Chst4 expression

Kjersti Sellæg[1]*, Anne Kristin McLaren Berge[1], Erik Knutsen[1], May-Britt Five[1], Elin Hadler-Olsen[1,2], Synnøve Norvoll Magnussen[1]*

[1]Department of Medical Biology, Faculty of Health Sciences, UiT – The Arctic University of Norway, Tromsø, Norway
[2]The Public Dental Health Competence Center of Northern Norway, Tromsø, Norway

*Corresponding authors:
Kjersti Sellæg, kjersti.sellag@uit.no
Synnøve Norvoll Magnussen, synnove.magnussen@uit.no

Keywords: High endothelial venules (HEVs), oral cancer, oral squamous cell carcinoma (OSCC), tumor microenvironment (TME), tumor infiltrating immune cells (TILs), Chst4, GlcNAc6ST-2

Abstract

Oral squamous cell carcinomas (OSCC) are aggressive cancers associated with poor patient survival. Inflamed tumors rich in effector T lymphocytes typically confer a favorable prognosis and enter the tumor microenvironment (TME) via specialized tumor vasculature, termed tumor-associated high endothelial venules (TA-HEVs). Lymphocytes bind the vessel wall through the HEV-specific marker Peripheral Node Addressin (PNAd). The absence of PNAd+ TA-HEVs is associated with an unfavorable prognosis in (late-stage) OSCC patients. In this study, we analyzed the Golgi specific enzyme GlcNAc6ST-2 (gene *Chst4*) known to be crucial for the synthesis of PNAd. We hypothesized that the TME impedes the development of fully functional TA-HEVs, ultimately impairing lymphocyte recruitment. We showed that TA-HEVs had lower expression of both GlcNAc6ST-2/*Chst4* and PNAd compared to normal HEVs in the lymph nodes (LN-HEVs), and a subset of TA-HEVs lacked GlcNAc6ST-2/*Chst4*. Using both targeted and unbiased approaches we analyzed the surrounding microenvironment of HEVs at the protein and cellular levels. We found that TA-HEVs development in mouse tongue tumors depended on the presence of mature T cells, while the role of DCs appeared to be less important. Through proteomics analysis of human OSCC, we identified tumors enriched in proteins involved in inflammatory processes were favorable for the presence of TA-HEVs.

Introduction

Oral squamous cell carcinoma (OSCC) is a heterogenous and aggressive type of cancer that accounts for approximately 90% of oral malignancies (1). About half of OSCCs develop in the mobile tongue (2). OSCC progression depends on the interactions between cancer cells and the host cells in the tissue (3). Due to the constant exposure of microbes, antigens, and environmental stimuli in the oral cavity, OSCC arises in a tissue where tolerance and immune activation needs to be tightly controlled (4).

A tumor microenvironment (TME) rich in CD8+ cytotoxic T cells promote patient survival and response to immunomodulatory treatment in cancer patients (5) + other. However, the anti-tumor immune response prompt cancer cells to evolve in order to evade destruction (6). Chemical and physical barriers such as upregulation of the inhibitory ligand PD-L1, altered expression of cytokines and chemokines, and remodeling of the tumor vasculature and extracellular matrix may promote an immune-excluded phenotype (7, 8), characterized by accumulation of T cells at the tumor periphery, that rarely respond to immunotherapy (9). These barriers must be overcome for T cells to accumulate in the tumor and exert their antitumor effects. A critical step for entering the tumor tissue is the interaction of circulating T cells with vascular endothelial cells (10, 11).

The development of a specialized type of post-capillary vessels, termed high-endothelial venules (HEVs), have been associated with clinical signs of tumor regression (12, 13), probably by mediating the entry of tumor infiltrating lymphocytes (TILs) (14). HEVs are normally exclusive to secondary lymphoid organs (SLOs) where they direct infiltration of naïve and memory lymphocytes from the blood into the tissue (15, 16). HEVs are lined with endothelial cells with a characteristic cuboidal morphology that express the specialized adhesion molecule Peripheral Node Addressin (PNAd) (17). Circulating lymphocytes expressing L-selectin adhere to the HEV lumen by binding to PNAd, which initiates a series of chemokine- and integrin-dependent steps that enables lymphocyte extravasation (diapedesis) (15, 18).

HEVs in solid tumors are typically surrounded by dense lymphocytic infiltrates, sometimes organized in lymph node-like B and T cell aggregates called tertiary lymphoid structures (TLS) (19-21). The presence of TLS is associated with a favorable prognosis in various cancer types (20, 22, 23). Unlike HEVs in lymph nodes (LN), tumor associated (TA)-HEVs display a more heterogenous phenotype, which seems to be correlated to the density and composition of the immune infiltrate (12, 24, 25) In highly inflamed areas, TA-HEVs resemble LN-HEVs with plump vessels and pronounced expression of PNAd. In less inflamed areas, TA-HEVs have a flatter endothelium with scattered/patchy PNAd expression (25). The functional role of PNAd have been demonstrated by knocking out two important

genes for PNAd biosynthesis in mice, *Chst2* and *Chst4* (26, 27). These genes code for the Golgi enzymes GlcNAc6ST-1 and GlcNAc6ST-2, respectively (28, 29). Mice deficient in both GlcNAc6ST-1 and GlcNAc6ST-2 displayed about 75% reduction in homing of lymphocytes to peripheral lymph nodes, while homing of lymphocytes in either GlcNAc6ST-1 or GlcNAc6ST-2 knock-out mice were reduced by 20% and 50%, respectively (26). Several studies using GlcNAc6ST-2 knock-out mice have shown that GlcNAc6ST-2 is important in regulating the luminal expression of PNAd (26, 27, 30) in lymph nodes and inflamed tissues (29, 31). Expression of *Chst4* and *Chst2*, as well as other genes implicated in the synthesis of PNAd are differentially expressed in HEVs in murine lymph nodes, inflamed lymph nodes, and tumors (32-35), suggesting that differences in the local microenvironment is critical for the regulation of HEV expressed genes and proteins.

We hypothesized that the microenvironment in tumors influences the expression of GlcNAc6ST-2 and PNAd in TA-HEVs, which potentially could represent a dedifferentiated phenotype with impaired function. Detection of TA-HEV differentiation status based on GlcNAc6ST-2/*Chst4* expression might have prognostic and predictive value and could potentially serve as a target for therapeutic intervention.

Materials and methods

Human specimens

Archived formalin-fixed and paraffin-embedded (FFPE) normal human lymph node tissue and tumor specimens from histologically verified primary, treatment-naïve OSCC were obtained from a patient cohort described by Bjerkli et al. which is a part of the Norwegian Oral Cancer Study (NOROC) (2). NOROC is a retrospective study including 535 OSCC patients diagnosed at one of the four university hospitals in Norway between 2005-2009. The last day of follow-up was June 1st, 2015. Clinical data were retrieved from patients' medical records, pathology reports, and Cause of Death Registry. Inclusion criteria for the current study were sufficient clinical data and available FFPE tumor resections or biopsies from patients diagnosed with OSCC of the anterior two-thirds of the mobile tongue. Study approval was granted by The Regional Committee for Medical and Health Research Ethics of Northern Norway (Protocol number REK Nord: 2013/1786 and 2015/1318).

Mouse specimens

Tongue and lymph node tissue were collected from mice exposed to the carcinogen 4-nitroquinoline 1-oxide (4NQO) or healthy controls as described earlier (36). Test animals were given 100ug/mL 4NQO in the drinking water for 16 weeks, whereas control mice were given regular drinking water. During a 12-weeks follow-up period, animals were sacrificed at different timepoints, and they presented with epithelial lesions of varying severity on the tongue. FFPE longitudinal tissue sections

of the tongues were divided into seven sectors, and we scored the histopathology of the most severe lesion within each sector as normal/hyperplasia, low-grade dysplasia, high-grade dysplasia, or invasive SCC. In the present study, low- and high-grade dysplasias were pooled and denoted dysplasia. Approval for the animal study was granted by The Norwegian Food Safety Authority (FOTS ID 15956) and adhered to the Norwegian Animal Welfare Act and the European Union directive 2010/63.

Human xenograft tumors were established in the tongue of athymic BALB/c nude mice as described in (37). The human oral squamous carcinoma cell line HSC-4 was suspended in 0.9% NaCl and injected in the tongue of individual mice at a concentration of 3×10^5. The cells were allowed to grow for 5-28 days before the mice were sacrificed and the tongue and lymph node tissues were collected. The tissue was fixed in a zinc-based fixative (ZBF) and embedded in paraffin before sectioning. Animal experiments were approved by the Norwegian Animal Research Authority.

Multi-color immunofluorescence staining of human OSCC tissue and lymph nodes

Immunofluorescence staining for GlcNAc6ST-2 and PNAd was performed on four-micrometer thick FFPE OSCC tumor specimens. Detailed information on antibodies and protocol is listed in Supplementary table S1. Tissue sections were dewaxed at 60°C and in xylene and rehydrated in graded ethanol baths. For antigen retrieval, the tissue sections were boiled for 20 minutes before adding 3% H_2O_2 with 20mM NaOH for 60 minutes to block endogenous peroxidase activity and reduce tissue autofluorescence, respectively. The tissues were then incubated with 2.5% normal goat serum for 30 minutes to prevent non-specific antibody binding. For the detection of GlcNAc6ST-2 and PNAd, the sections were first incubated with the anti-human CHST4 primary antibody and then with the anti-mouse/human PNAd antibody. Fluorescently labeled secondary antibodies were applied for one hour (Supplementary table S1). To further reduce tissue autofluorescence the TrueVIEW autofluorescence quenching kit (Vector Laboratories, Newark, California, USA) was used according to the manufacturer's procedure before adding DAPI and ProLong Gold Antifade Mountant (Thermo Fisher Scientific, Waltham, Massashusetts, US). The specificity of the primary antibodies was tested using isotype controls (Rabbit IgG polyclonal isotype control antibody, #ab37415, 1:2500, Abcam, Cambridge, UK, and Rat IgM monoclonal isotype control, #400801, 1:25, clone: RTK2118, BioLegend, San Diego, California, US). Lymph node tissue served as positive control and for negative control the primary antibody was omitted. Three-channel fluorescence images were acquired using an Olympus VS120 automated slide scanner (Olympus, Tokyo, Japan) equipped with a 20x objective and DAPI, FITC, and Cy5 filters. Images were captured in a single Z plane.

Dual RNAScope and immunofluorescence staining of mouse tissues

Four-micrometer thick FFPE mouse tongue tissue sections were stained for *Chst4* and *Pecam1* mRNA using the RNAScope Multiplex Fluorescence v2 kit (Advanced Cell Diagnostics, Minneapolis, Minnesota, US) combined with immunofluorescence staining for PNAd as described below. Details and specifications of the protocols and antibodies used for staining of mouse tissues are listed in Supplementary table S2. Tissue sections were dewaxed and pre-treated with peroxidase and normal goat serum. To permeabilize the tissue, protease treatment was performed with Protease Plus for 20 minutes at 40°C, followed by hybridization of the RNAScope probes (listed in Supplementary table S3). After probe amplification, the signal for each of the probes was developed sequentially by applying HRP for 15 minutes, followed by 30 minutes incubation with Opal dyes diluted in TSA buffer (Akoya Biosciences, Marlborough, Massachusetts, US). HRP blocker was added after incubation with each of the Opal dyes for 15 minutes to stop the reaction and enable sequential HRP-mediated signal development. Immunofluorescence was performed after the RNAScope assay at room temperature. Sections were incubated with normal goat serum for 30 minutes followed by incubation with the primary antibody. After applying the secondary antibody for 30 minutes, the fluorescent signal was developed by incubation with Opal dye for 10 minutes. The sections were stained with DAPI and mounted. Normal mouse lymph node tissue was used as positive control, and for the negative control the probes and primary antibody was excluded. Single-stained samples for each of the markers were used to optimize multichannel image acquisition with a LSM780 confocal laser scanning microscope (Zeiss, Oberkochen, Germany). Samples were illuminated with 405nm, 488nm, and 633nm lasers. Images were acquired with a water-immersion 40x objective in multiple planes (z-stack).

Immunohistochemical staining of mouse tissue

Four-micrometer thick FFPE tongue and lymph node tissue sections from 4NQO-exposed mice were stained for CD11c and PNAd using a dual immunohistochemistry protocol (Supplementary table S2). For dual staining, the sections were pre-treated and incubated with anti-mouse CD11c primary antibody, followed by incubation with the secondary antibody. The CD11c staining was visualized using the ImmPACT DAB chromogen (Vector Laboratories) for four minutes. To continue with the PNAd staining, the sections were incubated with normal goat serum for 20 minutes before adding the primary antibody, and then the secondary antibody for 30 minutes. Visualization of PNAd was achieved by incubating the sections with the ImmPACT VIP chromogen for seven minutes. Sections were counterstained with Hematoxylin and Scott's Solution for 30 and 15 seconds, respectively, before mounting. Normal lymph node tissue served as positive and negative controls for both of the markers, in which the primary antibody was excluded from the negative control. Mouse spleen tissue also served as a negative tissue control for PNAd staining in double-stained sections. ZBF paraffin-

embedded tongue and lymph node tissues from the athymic BALB/c mice were stained for PNAd using the same protocol (Supplementary table S2). Brightfield images of single and dual immunohistochemically stained mouse tissues were captured using the Olympus VS120 slide scanner.

Evaluation of stained samples

Multi-color IF: Multi-channel fluorescent images of human OSCC and lymph node tissue were analyzed in QuPath version 0.3.2 (38), allowing for the assessment of the whole tissue section. The tissue sections were scanned to identify PNAd+ HEVs. Unless the PNAd staining was observed in a vessel structure, PNAd had to be expressed on more than one cell in a cell cluster to be considered a HEV. Because the mucus in the minor salivary glands of the tongue also stained positive for PNAd, clusters of PNAd-positive cells found within the glands were not included. An annotation was drawn around individual HEVs in the entire section and the location of the HEVs in the tumor specimens were noted. HEVs were considered tumor associated (TA-HEVs) when located close to the tumor mass or adjacent to visibly thickened/disorganized epithelium adjoining the tumor mass. Other HEVs in the tissues were classified as non-tumor-associated (non-TA-HEVs) when found within minor salivary glands or distant from the tumor mass. To measure the number of GlcNAc6ST-2+ HEVs, a threshold for the Cy5 channel was optimized on several sections to classify GlcNAc6ST-2 positive pixels. In sections with particularly strong staining intensity and/or high autofluorescence the threshold was adjusted. The pixel classifier for the Cy5 channel was applied to all annotations in each tumor section. To count the relative number of cells surrounding each of the HEVs, an annotation (400x400µm circle; 125664µm^2) centered on individual HEVs was applied and the cell detection tool for the DAPI channel was used to measure the number of DAPI-stained nuclei within each annotation. The DAPI cell detection parameters were adjusted to capture small, rounded cells with minimal cytoplasm indicative of lymphocytes. Annotation size was chosen based on the largest HEV found across all tissue sections. Annotations did not include epithelium, nerves, large blood vessels, or tissue artefacts. In cases where the HEVs were located adjacent to, or partially surrounded by epithelium, for instance in narrow areas between rete ridges, the circular annotation was placed off-center to the HEV, or an annotation was drawn around the HEV including surrounding stroma.

RNAScope/IF: Images were captured of all PNAd+ and *Pecam1*+ HEVs in the stained mouse tongue tissues and the location of the vessels within the tongue (sectors) was noted during confocal imaging. Images were processed and evaluated using Fiji (version 1.54f) (39). Image processing included assigning the appropriate channels, pseudo-color processing, and adjustment of brightness and contrast. For all images processed in the current study, any adjustments made to the brightness and contrast were applied to all pixels within the image. Image stacks (z-stack) were converted to two-

dimensional images using the max intensity projection tool. Because the number of slices in the z-stack differed between images, we chose to exclude the images with the 5% lowest and highest number of slices based on the median number of slices for all the images. This was done to control for the contribution of background staining in the two-dimensional representation of the stack. The correction resulted in the exclusion of seven images with ≤3 or ≥19 slices, and the median number of slices in the remaining images was nine. An annotation was drawn around each HEV based on the *Pecam1* staining in the vessel wall, and the number of *Chst4+* punctate dots was counted manually and totaled for each HEV.

Dual IHC: Scanned brightfield images of mouse tissues were assessed in the OlyVIA Image Viewer Software (v 2.6) via the Olympus Net Image Server SQL at 0.31-40x magnification. The DAB and VIP substrates used for the dual immunohistochemical staining generates a brown and a violet color, respectively, and was used to detect CD11c+ cells and PNAd+ HEVs. HEVs were identified as PNAd+ stained vessels or clusters of >1 positively stained cells. Micrographs centered on individual HEVs were captured at 20x on a 27" monitor (Dell UltraSharp U2719D, Round Rock, Texas, US) and were imported into Microsoft PowerPoint (v 2403) without adjusting the image size. The images were overlayed with a 1x1cm grid, which corresponded to 45x45µm in the tissue (diagonal 63.6µm). Each HEV were placed in the center of four 1x1cm squares in the grid (Supplementary fig.S1) and the presence of CD11c+ cells within this area was scored as sparse, moderate or dense.

IHC: PNAd-stained tongue and lymph node tissue from BALB/c mice were evaluated by scanning through the sections in OlyVIA, and the presence of PNAd+ HEVs in the sections were noted. The presence of lymphoid cells in and around the tongue tumors was also assessed by scanning the tissue for small, rounded cells with minimal cytoplasm.

MTS assay

The bEnd.3 cell line was obtained from the American Type Culture Collection (ATCC, Manassas, Virginia, USA). Cells were kept at 37°C with 5% CO_2 and cultured in high glucose Dulbecco's Modified Eagle Medium (DMEM; Sigma-Aldrich, St. Louis, Missouri, USA) supplemented with 10% fetal bovine serum (FBS; Sigma-Aldrich). A colorimetric proliferation assay based on the conversion of a tetrazolium inner salt compound (MTS) to formazan was used to assess cell viability of bEnd.3 cells after stimulation with 1µg/mL, 200ng/mL, 20ng/mL, 2ng/mL, or 0.2ng/mL of the following cytokines: recombinant mouse LIGHT (R&D systems, Minneapolis, Minnesota, USA), LTα1β2 (R&D systems) and TNFα (Thermo Fisher Scientific). Cells were seeded at $2x10^4$ cells/well in a flat-bottom 96-well plate and incubated for 1h. Next, the cells were added 10µL of each of the stimulation agents in 100µL high glucose DMEM with 0.1% FBS at 1, 16, and 20 hours after seeding,

to enable cell viability measurements after 4, 8, and 24 hours on the same plate. DMEM with 0.1% FBS ± 5% Triton-X 100 (Sigma) served as positive and negative controls, respectively. After total 25 hours of incubation, 20µL CellTiter96® Aqueous One Solution (Promega, Madison, Wisconsin, USA) was added to each well and the plate was incubated for 60 minutes. Absorbance was measured at 490nm with a VersaMax™ Microplate reader (Molecular Devices, San Jose, CA, USA). Each experiment was run three times with triplicate wells for all conditions and cell viability percentage was calculated using the formula: ((Abs. treated – Abs pos) / (Abs negative – Abs pos)) *100.

Tube formation assay

Approximately 80% confluent bEnd.3 cells were seeded at 6×10^4 per well on 50µL Matrigel (Corning, New York, USA) or as monolayer (2D) in a flat bottom 96-well plate. The cells were left to adhere for one hour before they were stimulated for 12 hours with 1µg/mL or 200ng/mL recombinant mouse LIGHT, $LT\alpha_1\beta_2$ or TNFα in DMEM with 0.1% FBS. Tube forming capacity was observed in cells seeded on Matrigel using a light microscope (Leica, Wetzler, Germany). The experiment was repeated three times with triplicate wells per condition. Unstimulated cells served as controls.

RNA isolation

RNA isolation was performed to evaluate the expression of *Chst2*, *Chst4*, *B3gnt3*, *GCNT1*, *Fut4*, and *Fut7* genes in unstimulated or stimulated bEnd.3 cells seeded on Matrigel or as monolayer. Cell lysis and total RNA isolation was performed using the E.Z.N.A® HP Total RNA kit (Omega Bio-Tek, Norcross, Georgia, USA) according to the manufacturer's recommendations (animal cell protocol). In brief, cells were lysed in Lysis buffer with 3M (DTT) and immediately frozen at -70°C until RNA isolation. RNA was purified by multiple silica-based purification steps before eluted in 40µL nuclease-free water. RNA quantity and purity was measured on the NanoDrop 2000 spectrophotometer (Thermo Fisher).

Quantitative real-time PCR

The QuantiTect® Reverse Transcription Kit (Qiagen, Hilden, Germany) was used to reverse transcribe 200ng RNA into cDNA, which was diluted 1:30 in RNAse-free water. gDNA Wipeout Buffer was used to eliminate genomic DNA prior to cDNA synthesis. Target cDNA was amplified through 40 cycles in 20µL reactions containing FastStart Essential DNA Green Master, 8uL diluted cDNA, and 10µM forward and reverse primers. The primer sequences are provided in Supplementary Table S4. Qualitative real-time PCR (qPCR) was performed in duplicate reactions for each gene in three separate experiments using the LightCycler® 96 (Roche, Basel, Switzerland). Controls with the reverse transcriptase omitted and non-template controls were included to test for genomic DNA contamination and carry-over, respectively. To verify the specificity of the primers we performed

melting curve analysis and calculated the qPCR amplification efficiency for each gene from serially diluted cDNA (isolated and prepared from fresh frozen mouse lymph node) using the slope and correlation coefficient (R2) of the regression curves. The ΔΔCt method was used to calculate the relative gene expression in each sample (ref). The relative amount of target mRNA in each sample, measured as quantification cycle (Cq), was averaged and normalized against the geometrically averaged quantity of the reference genes (*ActB*, *Hprt,* and *Ppia*) in the sample (ΔCt). Fold change was calculated using the formula $2^{-\Delta\Delta Ct}$ and the unstimulated monolayer cells served as the reference sample.

Preparation of FFPE tissue for protein isolation

Tumor specimens from 88 patients were available for the study and three to seven 10μm thick FFPE tissue sections mounted on glass slides were used from each patient. The samples were dewaxed and rehydrated, before the tumor tissue was manually dissected by scraping with a scalpel. The dissection was guided by placing the section over an H&E-stained section of the tumor tissue where the tumor was indicated with a marker. The tumor tissue was solubilized in lysis buffer containing triethylammonium bicarbonate (TEAB) and sodium dodecyl sulfate (SDS). Samples were kept on ice and stored at -20°C until protein isolation.

Protein isolation and peptide purification

To further lyse and homogenize the tumor tissue, the samples were boiled and sonicated. Protein isolation was performed using S-Trap^{TM} micro columns (ProtiFi, Fairport, New York, US) according to the manufacturers' recommendations. Lysed samples were added 20mM Dithriothreitol (DTT) and 40mM iodacetamide to reduce and alkylate disulfide bonds, respectively. Protein denaturation and acidification with 1.2% phosphoric acid was done to eliminate any enzymatic activity in the sample. S-Trap buffer containing 90% methanol with 100mM TEAB was added and the lysate was loaded onto the column. The flow through of the column after centrifugation was reloaded three times to maximize protein binding. Captured protein was washed six times with S-Trap buffer and the column was transferred to a new Protein LoBind tube to ensure complete removal of SDS and other contaminants. Protein was digested with 0.5μg/mL Trypsin in 75mM TEAB and incubated overnight at 37°C. The next day, digested peptides were eluted consecutively with TEAB, 0.2% formic acid (FA), and 70% acetonitrile (ACN) containing 0.2% FA. Samples were dried completely using a vacuum concentrator (Concentrator Plus, Eppendorf, Hamburg, Germany) and stored in -20°C. Dried peptides were solubilized in 1% trifluoroacetic acid (TFA) before performing C18 purification and desalting. We followed the instructions in the protocol for the OMIX C18 pipette tips (Aglient, Santa Clara, California, US). The C18 matrix was wet by aspiring 50% ACN twice, followed by equilibrating the matrix twice with 0.1% TFA. The peptides were bound to the C18 matrix by

repetitive aspiration of the peptide solution, followed by washing twice with 0.1% TFA. Elution of peptides was performed in a 70% ACN solution with 0.1% FA after which the peptides were dried completely. Before proceeding to mass spectrometry (MS) the peptide output was measured on a NanoDrop microvolume spectrophotometer (Thermo Fisher).

TMT labelling and patient groups

Digested peptides were labeled with a tandem mass tag (TMT) isotope using the TMT11plex Isobaric Label Reagent Set (Thermo Fisher) according to the manufacturers protocol. The cohort was run in nine TMT-11plex sets with 100µg total protein for each set, and each set consisted of ten samples and a TMT 126 labelled bridge sample containing 5µg of 40 of the patient samples. A bridge sample was included in all TMT11plex sets. One of the TMT22plex sets included a replicate of two samples to obtain a full set of ten samples. To make sure that the patient samples within each TMT set were somewhat matched, we chose five clinical parameters, that were dichotomized, and included samples representing each of the two categories for each parameter in the TMT set. Because not all five parameters could be considered for each TMT set due to other factors, such as protein concentration, we prioritized the following parameters in descending order: five-year disease-specific survival (dead/alive), age ($\leq$ or >70 years) and stage group (stage I/II and III/IV), gender (male/female) and smoking (Current or former/never).

Mass spectrometry

Liquid chromatography coupled with mass spectrophotometry (LS-MS/MS) was used for peptide fragmentation to identify proteins. The mixing of samples was checked by analyzing 2 µl of a mix of TMT labelled peptides in the mass spec. The ratios were used to mix the TMT tagged peptides correctly. Samples were first fractionated by high salt reverse phase (40) using an Ultimate 3000 offline HPLC. 100 µg of peptides were reconstituted in 200 mM ammoniumformate, pH10 and loaded to a RP column (Waters Acquity UPLC® BEH C18 1.7 µm 2.1 x 100mm column). The samples were fractionated using a linear gradient of 0-60 % B (90% ACN, 20 mM ammonium formate, pH 10) at 150 µl/min for 60 min. 40 fractions were collected and pooled into 20 fraction using the mixing strategy Fr1 + Fr21, Fr 2 + Fr22, etc. Fractions were freezed at – 80°C. Samples were then dried and reconstituted in 0.1 % Formic acid. Peptides were fractionated further using a 2-80% acetonitrile gradient in 0.1 % formic acid over 140 min at a flow rate of 300 nl/min. The separated peptides were analyzed using a Thermo Scientific Orbitrap Fusion Lumos mass spectrometer equipped with FAIMS. Data was collected using an SPS-MS3 method. MS1 data was collected at 120k resolution over a m/z range at 400-1600 using a maximum injection time of 50ms. Three FAIMS CV's were used (-40, -60 and -80). CID fragmentation was used and MS2 was measured in the Ion Trap. Ten notches were used to isolate SPS-MS3-precursors.

Data processing

Raw data was analyzed using MaxQuant (version 1.6.17.0) with the integrated Andromeda search engine. MS/MS data was searched against the UniProt human database. An FDR ratio of 0.01 were needed to give a protein identification. To normalize the raw data, it was adjusted for total protein; to control for differential protein loading within a TMT-set of ten samples, the summed protein quantities were adjusted to be equal within a TMT-set. The data was Log2 transformed, and the bridge channel protein quantity was subtracted from each sample quantity to create a ratio to the bridge. 'Bridge' sample, now zero, was removed. Within each TMT-set, the mean protein expression was centered at zero. To identify outlier samples, we examined the expression levels of a set of housekeeping genes; GAPDH, B2M, ACTB, DIMT1, TUBA1A, GUSB, PGK1, RPL13A, PUM1, DHX9, MZT2A, UBXN4, LARP1, TAF2, STX5, SYMPK, TMEM11. The mean expression levels for all housekeeping genes within each sample was calculated and used to generate a sample mean and standard deviation. Samples exhibiting aberrant expression patterns, defined as expression levels deviating by more than three times the standard deviations from the sample mean, were removed from further analysis. This included two samples that were excluded from further analysis. Seven more samples were excluded from downstream analysis because reevaluation of patient samples (for other purposes) revealed that there was no tumor tissue present in the samples. The number of PNAd+ HEVs in the tumor specimens was scored as previously described by Abdulsalam et al. (manuscript Paper II). We chose to dichotomize the HEV score into HEV high and HEV low based on the median number of HEVs in all the patients in the current cohort (n=79).

Heatmap

In downstream analysis, only proteins with expression in all patient samples were used as input. Hierarchical clustering was performed on the normalized data normalized proteomics data to create a heatmap with the R package ComplexHeatmap (v 2.18.0) The number of optimal clusters was validated using the R package clValid (v 0.7). The number of optimal clusters was decided by assessing the stability of clusters ranging from 2-10 (Supplementary fig.S2). The Dunn index and Silhouette width takes into consideration the compactness of clusters and its values should be maximized to indicate stable clusters (41, 42). Other R packages used for creating heatmaps included RColorBrewer (v 1.1-3), gplots (v 3.1.3.1), circlize (v 0.4.16), dendextend (v 1.17.1), tidyverse (v 2.0.0), and dendsort (v 0.3.4).

Gene Set Enrichment Analysis

Gene Set Enrichment Analysis (GSEA) was performed on the proteomics data in the following three different conditions 1) HEV-high vs HEV-low between all patients, 2) HEV-high vs HEV-low between patients in patient cluster 1 from the heatmap, and 3) HEV-high vs HEV-low between

patients in cluster 2 from the heatmap. The identification of enriched pathways in the three conditions was performed using the available gene sets from the Molecular Signature Database (MSigDB) which includes the MSigDB Hallmark gene set, MSigDB BioCarta gene set, MSigDB Kyoto Encyclopedia of Genes and Genomes (KEGG) Legacy gene set (https://www.gsea-msigdb.org/gsea/msigdb/index.jsp). The analysis was performed using the default settings on the GSEA software (v 4.3.2). The shared pathways between the different conditions for each gene set was later compared using the R packages VennDetail (v 1.18.0), and ggvenn (v 0.1.10). A protein-protein interaction network was created with the proteins present in the shared Hallmarks between all conditions using the STRING database (https://string-db.org/). The network was created using the default settings in the STRING database.

Statistical analysis

GraphPad Prism (v 10.2.3) was used for statistical analyses and data visualization. Data distribution was assessed by Shapiro-Wilk test and visual inspection of quantile-quantile plots. Comparison of two or more groups with non-normal distribution was performed using Kruskal-Wallis H test with Dunn's test to correct for multiple comparisons, while One-way ANOVA was used to compare two or more groups of normal distributed data with Tukey's post hoc test. Significance level was set at $P<0.05$. In all graphs, asterisks indicate significant differences: $*P<0.05$, $**P<0.01$, $***P<0.001$, $****0.0001$.

Code availability

All scripts from analyses performed on the normalized proteomics data are available at https://github.com/AKMcB/NOROC-Project-HEV/tree/main.

Results

Tumor-associated HEVs show lower expression of GlcNAc6ST-2 than HEVs in lymph nodes

GlcNAc6ST-2 (gene *Chst4)* is pivotal in generation of the HEV-specific PNAd carbohydrate structure, and its loss causes decreased PNAd expression and impaired lymphocyte homing to murine lymph nodes (26, 29, 30). A low expression of PNAd has also been reported in a subset of TA-HEVs in human cancers (12, 25), but if this is associated with the expression of GlcNAc6ST-2 is currently unknown. To explore if GlcNAc6ST-2 is differentially expressed in normal LN-HEVs compared to TA-HEVs, we co-stained a normal human lymph node and ten OSCC tumor tissue sections for PNAd and GlcNAc6ST-2. In the OSCC specimens, 63% (79/125) of the TA-HEVs and 70% (91/130) of HEVs located at a distance from the tumor, termed non-TA-HEVs, were GlcNAc6ST-2 positive (Fig.1A and B). In the lymph node, 91% (191/210) of the HEVs were GlcNAc6ST-2 positive

(Fig.1B). The GlcNAc6ST-2 staining also appeared stronger and more abundant in LN-HEVs than in the TA-HEV and non-TA-HEVs in the tumor specimens (Fig.1C) suggesting higher expression. There was also a notable difference in the level of PNAd expression between lymph nodes and tumor tissue where PNAd covered more of the vessel wall in LN-HEVs than in TA- and non-TA-HEVs (Fig.1C). In conclusion, HEVs in the OSCC microenvironment express lower levels of GlcNAc6ST-2 and PNAd than LN-HEVs, suggesting that HEVs are regulated by factors that are inherently different between lymphoid- and tumor tissues.

HEVs associated with mouse OSCC, but not dysplastic lesions, lack *Chst4* expression

We have previously shown that HEVs were more prevalent in the TME of early-stage than late-stage OSCC, and the lack of HEVs in late-stage tumors was associated with an unfavorable prognosis for the patient (25). Whether the low number of TA-HEVs in late-stage OSCC is due to the dedifferentiation of HEVs as the tumor progresses is not known. To study TA-HEV development during tumor progression, we proceeded to analyze tissue from the 4NQO model of oral carcinogenesis. The natural progression of the TME, makes this an excellent model for studying the development of HEVs at early stages of oral carcinogenesis.

We evaluated the co-localization of *Chst4* and PNAd in tongue tissue sections from 4NQO-exposed mice with normal/hyperplastic epithelium, dysplastic lesions, and SCC (n=15) and healthy controls (n=3). Due to a lack of reliable antibodies for mouse GlcNAc6ST-2, these studies were performed using dual IF (PNAd) and RNAScope (*Chst4*). In the 15 sections from the 4NQO-exposed mice, 90.9% (50/55) of the HEVs were *Chst4+*. Though not statistically significant, HEVs within SCCs tended to express lower levels of *Chst4* (*Chst4* punctate dots: median 4, range 0-44) than HEVs associated with dysplastic or normal/hyperplastic epithelium (dysplasia: median 9 (range 1-64), normal/hyperplasia: median 8 (range 1-16); P=0.1004; Fig.2A-C). Interestingly, *Chst4-* HEVs were only found in SCCs (Fig.2A and C). In the three tongue sections from control mice, three HEVs were found close to salivary glands in the posterior parts of the tongue, which were all *Chst4+* (Supplementary Fig.S3). Normal lymph node tissue was used as a positive control wherein *Chst4* was abundantly expressed in all PNAd+ LN-HEVs (Supplementary Fig.S4). To summarize, our findings show that only TA-HEVs in OSCCs, and not HEVs associated with dysplastic- or normal/hyperplastic epithelium, lacked *Chst4* expression.

Density of cells surrounding TA-HEVs did not reflect GlcNAc6ST-2 expression

In a previous study, we found that TA-HEVs in areas with few lymphocytes exhibited an altered morphology and lower PNAd expression than TA-HEVs in areas with an abundant lymphocytic infiltration (25). This could be a consequence of impaired lymphocyte recruitment through de-

differentiated HEVs, alternatively the HEV differentiation could depend on stimuli derived from tissue residing immune cells. To assess this, we used the density of DAPI stained cell nuclei surrounding the HEVs as a rough estimate of the local inflammation in tissue sections from ten human OSCCs co-stained for PNAd and GlcNAc6ST-2. Normal human lymph node tissue served as a reference for the cell density surrounding HEVs under normal conditions. Due to the location of some TA-HEVs we had to adjust the annotation shape and size for DAPI cell detection. Thus, average annotation size for DAPI cell detection in the tumor tissues was somewhat smaller than in the lymph node ($107744\mu m^2$ versus $125664\mu m^2$). The cell density surrounding TA-HEVs and non-TA-HEVs in the tumor specimens was significantly lower than around LN-HEVs (Adj.P<0.0001; Fig.3A and Supplementary fig S5). There was no statistically significant difference in the number of DAPI+ cells/μm^2 around TA-HEVs (median 0.0069, range 0.0020-0.0170) compared to non-TA-HEVs (median 0.0061, range 0.0008-0.0138; P=0.9624; Fig.3A). Next, we compared the cell density around double positive (PNAd+GlcNAc6ST-2+) and single-positive (PNAd+) HEVs in the different locations. The number of DAPI+ cells/μm^2 did not reflect GlcNAc6ST-2 expression in any of the locations (Fig.3B). In summary, the cell infiltrate surrounding HEVs in human OSCC is less dense than the network of cells surrounding LN-HEVs, but the general cell density around the TA-HEVs or the proximity to tumor tissue did not appear to affect the expression of GlcNAc6ST-2.

No apparent association between PNAd expression and CD11c+ dendritic cells in HEVs associated with oral epithelial lesions

Signaling molecules expressed by various cell types are likely regulators of the *Chst4* expression and downstream expression of PNAd. In lymph nodes, proximal dendritic cells (DCs) maintain a differentiated HEV phenotype through lymphotoxin signaling (43). However, the role of DCs in TA-HEV formation is unclear. We performed co-staining for PNAd and CD11c on mouse tongue (n=30) and lymph node tissue (n=5) from the 4NQO-mice. In the tongue, CD11c+ cells were located within a 45µm radius of all but one (76/77) HEV (Fig.4A). We scored the density of CD11c+ cells around each HEV in the tongue tissues as sparse, moderate, and dense (Fig.4A). Most HEVs were surrounded by a sparse CD11c infiltrate, irrespective of the histological grade of the epithelial lesion (Table 1). However, within SCCs more HEVs had a moderate or dense CD11c infiltrate than in dysplastic or normal/hyperplastic lesions. In contrast, LN-HEVs were found in areas densely packed with CD11c+ cells (Fig.4A-B).

To further explore the association between dendritic cells and HEV differentiation, we quantified the expression of PNAd in a subgroup of the 4NQO tongue HEVs that displayed a lumen (n=22) and assessed the association between the relative PNAd expression and density of the surrounding CD11c+ cell infiltrate. PNAd covered ≤50% of the luminal surface in 72.7% (16/22) of the HEVs,

while the remaining 27.3% (6/22) had >50% PNAd coverage. None of the HEVs expressed PNAd on the entire circumference of the vessel wall. Sixty eight percent (15/22) of the HEVs were surrounded by a sparse CD11c+ cell infiltrate, 27% (6/22) by a moderate or dense infiltrate, and one had no surrounding CD11c+ cells. To conclude, though there was a general increase in the density of CD11c+ cells in more severe lesions, there was no clear associations between the extent of PNAd expression in the HEV vessel wall and the density of surrounding CD11c+ cells.

Mature T cells play an important role in TA-HEV induction in OSCC

Mature T cells have been postulated to play a major role in TA-HEV development (35, 44, 45). To test this, we analyzed the expression of PNAd in human xenograft tongue tumors and lymph nodes of athymic BALB/c mice (n=5). These mice have a severely compromised T cell mediated immune response and impaired B cell activation. Interestingly, no TA-HEVs were found surrounding the tongue tumors of the immunocompromised mice, while HEVs were present in their lymph nodes (Fig.5A and B). The LN-HEVs displayed characteristic cuboidal morphology similar to the LN-HEVs in immune competent mice (Fig.5C). However, some of the LN-HEVs in the athymic mice had a larger lumen, which has also been observed by others in these mice (Qian 2006). The lymph node parenchyma also appeared to be less dense and somewhat disrupted in the immune deficient compared to the immunocompetent mice (Fig.5C). We did not see any apparent inflammation in the tongue tumors, although a small number of immature or dysfunctional lymphocytes or other types of immune cells, including NK cells and myeloid cells, might be present (Fig.5A). Our results support that an adaptive immune response is necessary for the development of TA-HEVs in OSCC, and that the development of LN-HEVs is fundamentally different from TA-HEVs.

Stimulation of cultured endothelial cells with inflammatory factors enhance enzymes involved in glycan synthesis, but not PNAd-specific *Chst2* and *Chst4*

A challenge for the study of HEV regulation is that the HEV phenotype cannot be maintained in cell culture (46). This suggests that expression of HEV-specific genes, such as *Chst4* and *Chst2*, require additional signals from the natural tissue microenvironment. To explore this, we cultured mouse endothelial cells in a tube formation assay to mimic *in vivo* conditions and treated the cells with LIGHT, LTα1β2, or TNFα, which are ligands of the LTβR and TNFR, receptors shown to be important for HEV development (43-45, 47-52). An MTS assay showed no cytotoxic effects of LIGHT, LTα1β2, or TNFα on bEnd.3 cells in the concentration range 0.2 ng/mL – 1000ng/mL (supplementary fig.S6A). bEnd.3 cells cultured on Matrigel efficiently formed tube-like structures but not in monolayer culture (Supplementary fig.S6B). bEnd.3 cells stimulated with 200 or 1000ng/mL LIGHT LTα1β2, or TNFα cells were analyzed for the expression of genes associated with glycan modifications that form PNAd. On Matrigel, bEnd.3 cells displayed significantly higher expression

of *Fut4* (P=0.0156), *B3gnt3* (P<0.0001) and *Chst2* (P=0.0065) compared to monolayer cultured cells (Fig.6A). Stimulation with 1000ng/mL TNFα on Matrigel resulted in a 2-fold increase in *Fut4* expression compared to unstimulated cells (Adj.P=0.0186) and was also significantly increased after 200ng/mL TNFα stimulation (Adj.P=0.0284; Fig.6B). Similar results were observed in monolayer bEnd.3 cells, although differences did not reach statistical significance except for a significant increase in *Fut4* expression in cells stimulated with 200ng/mL TNFα compared to 1000ng/mL LTα1β2. There was no significant difference in the expression of *B3gnt3* and *Chst2* between stimulated or unstimulated cells cultured on Matrigel or monolayer (P=0.0917 and P=0.0814, respectively; Fig.6C and D). However, *Chst2* and *B3gnt3* expression was generally lower in stimulated cells than unstimulated cells for both Matrigel and monolayer culture (Fig.6C and D). Transcripts of *Chst4, Fut7,* or *Gcnt1* was not detected in the bEnd.3 cells for any of the conditions tested. To summarize, the expression of *Fut4*, *B3gnt3*, and *Chst2* was higher in endothelial cells seeded on Matrigel than as monolayers, but *Fut4* was the only PNAd-associated gene affected by stimulation with pro-inflammatory cytokines.

Human OSCC tumors with a high HEV score are enriched in inflammation-associated signatures

As an unbiased approach to investigate factors in the TME that influences the presence of TA-HEVs in human OSCC, we performed proteomic profiling of 79 archival FFPE OSCC tumors. The proteomic analysis quantified 8295 proteins in total, and 4650 proteins were quantified across all samples. Using unsupervised clustering, the protein expression generated two patient clusters, cluster 1 (n=28) and cluster 2 (n=51), with distinct protein expression patterns (Fig.7A). We found that the distribution of patients with HEV-high (n=37) and HEV-low (n=42) tumors was similar within the two patient clusters, suggesting that the presence of TA-HEVs does not drive the clustering (Fig.7B). The HEV score was significantly associated with alcohol consumption (P=0.00281) but not any other clinicopathological parameters in this patient cohort (Supplementary table S5). To identify gene signatures associated with the patient clusters independent of the HEV score, we first performed Gene Set Enrichment analysis (GSEA) with hallmark, Biocarta and KEGG gene lists between the two patient clusters as seen in figure 7A. The major hallmarks that were enriched in cluster 1 were mitotic spindle, UV response, and apical junction, while in cluster 2, MTORC1 signaling, reactive oxygen species, and DNA repair were enriched (Supplementary fig.S7) Next, GSEA was performed on all HEV-high and HEV-low patients in the cohort, and within the two patient clusters (Fig.7C) The number of shared hallmarks between the conditions are presented in Fig.7D. Though not statistically significant, OSCC tumors with a high HEV score were enriched in hallmarks linked to UV-response, apoptosis, DNA repair, and PI3K-Akt-mTOR signaling, which likely represent processes and genetic

alterations that drives OSCC carcinogenesis (Fig.7C). Hallmarks associated with inflammation, such as allograft rejection, inflammatory response, and IL-6 JAK STAT signaling were also enriched in HEV-high tumors and might reflect processes in the TME that permits the development of TA-HEVs (Fig.7C). There were no shared hallmarks between HEV-high patients in cluster 1 and HEV-high patients in cluster 2 (Fig.7D).

We extracted proteins that were differently expressed between HEV-high tumors irrespective of clusters (all patients), as well as for patients within cluster 1 and 2, from the allograft rejection, inflammatory response, IL-6 JAK STAT, and angiogenesis hallmarks, revealing 22 proteins (Supplementary table S6). We performed a STRING analysis for these 22 proteins, which showed that all but one protein was clustered into a protein-protein interaction network (Fig.7E). The top five Cellular components and Molecular function gene ontology (GO) terms (provided from the STRING database) enriched in the STRING network included MHC class I and II protein complex, MHC I peptide loading, MHC II protein complex binding, and T cell receptor binding (Supplementary table S7), suggesting that HEV-high tumors are enriched in proteins that promotes adaptive anti-tumor immune responses. BioCarta and KEGG analysis also showed that HEV-high tumors shared pathways associated with inflammatory responses (supplementary fig.S8 and S9). Some hallmarks were only enriched in HEV-high cluster 1 patients (TGF beta signaling and interferon gamma signaling) or cluster 2 patients (epithelial to mesenchymal transition). Taken together, our findings indicate that OSCC tumors enriched in processes involving adaptive immune responses may favor the development of TA-HEVs.

Discussion

In this study we show that the expression of *Chst4*/GlcNAc6ST-2, which is critical for the specific expression of PNAd in HEVs, is lower or absent in TA-HEVs compared to normal human LN-HEVs and HEVs associated with dysplastic lesions in mice. The general density of the cellular infiltrate surrounding TA-HEVs in human OSCC was not associated with the expression of GlcNAc6ST-2, but in tongue tumors of mice lacking mature T cells we found a complete absence of TA-HEVs. In line with this, we found that human OSCCs with a high number of HEVs were enriched in hallmarks or pathways associated with adaptive immunity.

The lower expression of GlcNAc6ST-2 and PNAd that we observed in TA-HEVs compared to LN-HEVs might suggest that the regulation of HEVs differ depending on the tissue type and the conditions within the tissue. In mice, LN-HEVs become fully differentiated 2-4 days after birth when the cuboidal endothelial cells express high levels of PNAd (53) and other HEV-related genes such as

Chst4, Chst2, GlyCAM-1, Fut7, Gcnt1, and *B3gnt3* (32, 54). In response to inflammation, the transient downregulation of HEV-specific genes and expression of other adhesion molecules can permit the entry of other cell types into the lymph node, such as neutrophils and monocytes (55, 56). TA-HEVs assume some of the properties of inflamed LN-HEVs (33, 35) which might enable the entry of other cell types into the tumor. It is tempting to speculate that changes in TA-HEV phenotype is involved in shaping the TME at different stages of tumor progression.

We showed that the expression of *Chst4* was absent in a subset of TA-HEVs in 4NQO-exposed mice compared to HEVs associated with dysplasia or normal/hyperplastic epithelium. This might indicate a progressive loss of *Chst4* expression in HEVs as these lesions progress into SCCs, and that the loss of *Chst4* is involved in the dedifferentiation of TA-HEVs during cancer progression. It would have been interesting to follow further progression of the 4NQO-induced tumors, however, these mice succumb to cancer-related mortality before the tumors reach advanced stages. In support of our findings, Menzel et al. reported a progressive loss of *Chst4*, and other genes related to HEV-function in dedifferentiated HEVs in response to tumor growth in lymphoma-bearing lymph nodes in mice (57). Hence, the expression of GlcNAc6ST-2/*Chst4* in TA-HEVs could be a marker for the dedifferentiation and ultimately loss of TA-HEVs, which could be used to refine the HEV score in tumors. However, it remains to be determined whether GlcNAc6ST-2 protein- or gene expression in TA-HEVs signify functionally impaired HEVs and if it has an impact on OSCC patient prognosis. Our study of GlcNAc6ST-2 expression is limited to a small number of patients and should be validated in larger patient cohorts. Gene expression in mice and humans might differ, so both the protein and gene expression of GlcNAc6ST-2 in TA-HEVs should be validated in the same species.

We found that the expression of GlcNAc6ST-2 in TA-HEVs and LN-HEVs did not differ by the density of cells surrounding the HEVs. Different regulation of TA- and LN-HEVs may instead be explained by the types of cells in their local microenvironment. In the lymph node, HEVs depend on signaling through the LTβR by DC-derived lymphotoxins (LIGHT and LTa1b2) (43, 47, 58). Impeded interaction between DCs and HEVs could possibly explain the de-differentiated phenotype observed in some TA-HEVs. In the present study we did find DCs located close to HEVs in the 4NQO-exposed mice, albeit at low numbers. This could indicate that CD11c+ DCs play a minor role in the differentiation of TA-HEVs. This is in accordance with a previous study where TA-HEVs were unaffected by the depletion of CD11c+ DCs in a fibrosarcoma mouse model (59). Alternatively, TA-HEVs might require lower levels of DC-derived signals than LN-HEVs, which we found were surrounded by abundant numbers of CD11c+ cells. Indeed, it has been postulated that the responsiveness to LTβR signaling differ between various HEV-specific genes in LN-HEVs, of which *Chst4* appeared to be the most sensitive (32). Hence, the low numbers of DCs surrounding TA-HEVs

might provide sufficient lymphotoxin signals for *Chst4,* and PNAd, to be expressed. The expression of LIGHT and LTα1β2 have also been shown to be differently expressed in DC subsets (43). Various DC populations have been identified in oral tissues and are increased during inflammation, including CD11b+, CD103+ and Langerin+ DCs (60). Hence, the DC subtypes involved in the regulation of HEVs may differ between lymph nodes and tumors.

PNAd staining of immunocompromised mice revealed that tongue tumors were completely absent of TA-HEVs, while HEVs were found in the lymph node of these mice. Because these mice lack the thymus, which is the organ responsible for the maturation of T cells, this indicates that the development of TA-HEVs, but not LN-HEVs, depend on the presence of mature and functional T cells. This is in line with previous findings by Moussion et al. which showed that LN-HEVs were not affected by the absence of endogenous B and T cells in Rag2-/- mice (43). Conversely, TA-HEVs were completely absent in Rag2-/- melanoma-bearing mice (44). Peske et al. showed that mice deficient in CD8 T cells lacked PNAd+ TA-HEVs and had more impaired lymphocyte infiltration than B cell-deficient mice. Repleting the Rag2-/- mice with CD8+ T cells rescued TA-HEV development, indicating a strong relationship between T cells and TA-HEV formation (44). However, CD4+ T cells and natural killer (NK) cells have also been implicated in the development of TA-HEVs (33, 35). Others have shown that the surrounding tissue and stromal cells appear to play a role in PNAd expression and the maintenance of a differentiated HEV phenotype (46, 57, 61). For instance, it was previously shown that the de-differentiation of LN-HEVs in tumor-bearing murine lymph nodes was concurrent with disruption of the fibroblastic reticular cell (FRC) network surrounding the HEVs (57), suggesting that cell-cell interactions might be important for maintaining a differentiated HEV phenotype. However, if such signals are required for TA-HEVs is not well understood. A dependency of cell-cell interactions could in part explain the absence of *Chst4*, *Fut7*, and *Gcnt1* transcripts in our cell culture experiments. It is, however, important to recognize that immortalized cell lines can have different properties than the normally very quiescent endothelial cells *in vivo* and that the matrix itself could influence the transcriptional program of the cells (62).

Our results indicate that a subset of TA-HEVs can exist independently of the expression of GlcNAc6ST-2/Chst4. In support of this, our findings from cultured endothelial cells might suggest that the expression of *Chst4*, *Fut7,* and *Gcnt1* is more stringent and context-dependent than the expression *Chst2* (GlcNAc6ST-1), *Fut4,* and *B3gnt3*, which was constitutively expressed in mouse endothelial cells. Since the two glycosyltransferases GlcNAc6ST-1 and GlcNAc6ST-2 catalyze the same modification in PNAd (26), there might be redundant activity between them if one of the enzymes is lost. This is supported by findings in mice where double knock-out of *Chst4* and *Chst2* caused more impaired lymphocyte homing than mice deficient in either *Chst4* or *Chst2* (26, 27).

However, loss of *Chst4* had a more adverse effect on lymphocyte homing than *Chst2,* likely due to the role of *Chst4* in directing luminal expression of PNAd. Hence, it could mean that in the event that GlcNAc6ST-2 is lost, for instance in TA-HEVs, GlcNAc6ST-1 takes over.

Unbiased proteomic profiling of human OSCC tumors could distinguish two patient clusters with different tumor protein expression patterns and enriched hallmarks. OSCCs with a high HEV score were enriched in proteins associated with inflammatory processes, more specifically proteins associated with antigen presentation and T cell response. In line with this, it is well recognized that HEV development in tumors is associated with increased numbers of infiltrating T cells and tumor regression (63). Whether the presence of a high number of TA-HEVs contribute to the protein expression in these tumors, or whether the tumor protein expression is permissive for TA-HEV development cannot be deduced by these analyses. Unique hallmarks enriched in HEV high tumors in only one of the two patient clusters indicate that different processes within these tumors could potentially influence TA-HEVs differently. Limitations with bulk analysis of tumor protein expression include the underestimation of low abundance proteins which might be overshadowed by highly abundant proteins. Tumor heterogeneity and composition of the TME within individual tumors and patients might also make it challenging to obtain protein signatures that captures the general OSCC proteome, suggesting that other techniques allowing profiling of individual cells should be applied. Further studies are needed to determine if different OSCC phenotypes are associated with TA-HEV development and if this has prognostic and predictive value in OSCC patients.

Understanding the mechanisms regulating TA-HEVs can permit the development of new strategies for patient stratification, as well as targeted induction of TA-HEVs for improved immunotherapy response and targeted drug delivery. This could also be exploited in conditions where the presence of HEVs is detrimental, such as autoimmune- and chronically inflamed diseases, and organ transplantation.

References

1.	Coletta RD, Yeudall WA, Salo T. Grand Challenges in Oral Cancers. Front Oral Health. 2020;1:3.

2.	Bjerkli IH, Jetlund O, Karevold G, Karlsdottir A, Jaatun E, Uhlin-Hansen L, et al. Characteristics and prognosis of primary treatment-naive oral cavity squamous cell carcinoma in Norway, a descriptive retrospective study. PLoS One. 2020;15(1):e0227738.

3.	Zhao Y, Chen D, Yin J, Xie J, Sun CY, Lu M. Comprehensive Analysis of Tumor Immune Microenvironment Characteristics for the Prognostic Prediction and Immunotherapy of Oral Squamous Cell Carcinoma. Front Genet. 2022;13:788580.

4.	Pelaez-Prestel HF, Sanchez-Trincado JL, Lafuente EM, Reche PA. Immune Tolerance in the Oral Mucosa. Int J Mol Sci. 2021;22(22).

5.	Bruni D, Angell HK, Galon J. The immune contexture and Immunoscore in cancer prognosis and therapeutic efficacy. Nat Rev Cancer. 2020;20(11):662-80.

6.	Chen DS, Mellman I. Oncology meets immunology: the cancer-immunity cycle. Immunity. 2013;39(1):1-10.

7.	Garrido F, Cabrera T, Concha A, Glew S, Ruiz-Cabello F, Stern PL. Natural history of HLA expression during tumour development. Immunol Today. 1993;14(10):491-9.

8.	Tang S, Ning Q, Yang L, Mo Z, Tang S. Mechanisms of immune escape in the cancer immune cycle. Int Immunopharmacol. 2020;86:106700.

9.	Chen DS, Mellman I. Elements of cancer immunity and the cancer-immune set point. Nature. 2017;541(7637):321-30.

10.	Dirkx AE, Oude Egbrink MG, Kuijpers MJ, van der Niet ST, Heijnen VV, Bouma-ter Steege JC, et al. Tumor angiogenesis modulates leukocyte-vessel wall interactions in vivo by reducing endothelial adhesion molecule expression. Cancer Res. 2003;63(9):2322-9.

11.	Amersfoort J, Eelen G, Carmeliet P. Immunomodulation by endothelial cells - partnering up with the immune system? Nat Rev Immunol. 2022;22(9):576-88.

12.	Avram G, Sánchez-Sendra B, Martín JM, Terrádez L, Ramos D, Monteagudo C. The density and type of MECA-79-positive high endothelial venules correlate with lymphocytic infiltration and tumour regression in primary cutaneous melanoma. Histopathology. 2013;63(6):852-61.

13.	Martinet L, Le Guellec S, Filleron T, Lamant L, Meyer N, Rochaix P, et al. High endothelial venules (HEVs) in human melanoma lesions: Major gateways for tumor-infiltrating lymphocytes. Oncoimmunology. 2012;1(6):829-39.

14.	Blanchard L, Girard JP. High endothelial venules (HEVs) in immunity, inflammation and cancer. Angiogenesis. 2021.

15.	Girard JP, Moussion C, Förster R. HEVs, lymphatics and homeostatic immune cell trafficking in lymph nodes. Nat Rev Immunol. 2012;12(11):762-73.

16.	von Andrian UH. Intravital microscopy of the peripheral lymph node microcirculation in mice. Microcirculation. 1996;3(3):287-300.

17.	Streeter PR, Rouse BT, Butcher EC. Immunohistologic and functional characterization of a vascular addressin involved in lymphocyte homing into peripheral lymph nodes. J Cell Biol. 1988;107(5):1853-62.

18.	Rosen SD. Ligands for L-selectin: homing, inflammation, and beyond. Annu Rev Immunol. 2004;22:129-56.

19.	Martinet L, Garrido I, Filleron T, Le Guellec S, Bellard E, Fournie JJ, et al. Human solid tumors contain high endothelial venules: association with T- and B-lymphocyte infiltration and favorable prognosis in breast cancer. Cancer Res. 2011;71(17):5678-87.

20.	Wirsing AM, Rikardsen OG, Steigen SE, Uhlin-Hansen L, Hadler-Olsen E. Characterisation and prognostic value of tertiary lymphoid structures in oral squamous cell carcinoma. BMC Clin Pathol. 2014;14:38.

21.   Li Q, Liu X, Wang D, Wang Y, Lu H, Wen S, et al. Prognostic value of tertiary lymphoid structure and tumour infiltrating lymphocytes in oral squamous cell carcinoma. Int J Oral Sci. 2020;12(1):24.

22.   Hiraoka N, Ino Y, Yamazaki-Itoh R, Kanai Y, Kosuge T, Shimada K. Intratumoral tertiary lymphoid organ is a favourable prognosticator in patients with pancreatic cancer. Br J Cancer. 2015;112(11):1782-90.

23.   Wang Q, Shen X, An R, Bai J, Dong J, Cai H, et al. Peritumoral tertiary lymphoid structure and tumor stroma percentage predict the prognosis of patients with non-metastatic colorectal cancer. Front Immunol. 2022;13:962056.

24.   Wirsing AM, Ervik IK, Seppola M, Uhlin-Hansen L, Steigen SE, Hadler-Olsen E. Presence of high-endothelial venules correlates with a favorable immune microenvironment in oral squamous cell carcinoma. Mod Pathol. 2018;31(6):910-22.

25.   Wirsing AM, Rikardsen OG, Steigen SE, Uhlin-Hansen L, Hadler-Olsen E. Presence of tumour high-endothelial venules is an independent positive prognostic factor and stratifies patients with advanced-stage oral squamous cell carcinoma. Tumour Biol. 2016;37(2):2449-59.

26.   Kawashima H, Petryniak B, Hiraoka N, Mitoma J, Huckaby V, Nakayama J, et al. N-acetylglucosamine-6-O-sulfotransferases 1 and 2 cooperatively control lymphocyte homing through L-selectin ligand biosynthesis in high endothelial venules. Nat Immunol. 2005;6(11):1096-104.

27.   Uchimura K, Gauguet JM, Singer MS, Tsay D, Kannagi R, Muramatsu T, et al. A major class of L-selectin ligands is eliminated in mice deficient in two sulfotransferases expressed in high endothelial venules. Nat Immunol. 2005;6(11):1105-13.

28.   de Graffenried CL, Bertozzi CR. Golgi localization of carbohydrate sulfotransferases is a determinant of L-selectin ligand biosynthesis. J Biol Chem. 2003;278(41):40282-95.

29.   Bistrup A, Tsay D, Shenoy P, Singer MS, Bangia N, Luther SA, et al. Detection of a sulfotransferase (HEC-GlcNAc6ST) in high endothelial venules of lymph nodes and in high endothelial venule-like vessels within ectopic lymphoid aggregates: relationship to the MECA-79 epitope. Am J Pathol. 2004;164(5):1635-44.

30.   Hemmerich S, Bistrup A, Singer MS, van Zante A, Lee JK, Tsay D, et al. Sulfation of L-selectin ligands by an HEV-restricted sulfotransferase regulates lymphocyte homing to lymph nodes. Immunity. 2001;15(2):237-47.

31.   Low S, Hirakawa J, Hoshino H, Uchimura K, Kawashima H, Kobayashi M. Role of MAdCAM-1-Expressing High Endothelial Venule-Like Vessels in Colitis Induced in Mice Lacking Sulfotransferases Catalyzing L-Selectin Ligand Biosynthesis. J Histochem Cytochem. 2018;66(6):415-25.

32.   Veerman K, Tardiveau C, Martins F, Coudert J, Girard JP. Single-Cell Analysis Reveals Heterogeneity of High Endothelial Venules and Different Regulation of Genes Controlling Lymphocyte Entry to Lymph Nodes. Cell Rep. 2019;26(11):3116-31.e5.

33.   Asrir A, Tardiveau C, Coudert J, Laffont R, Blanchard L, Bellard E, et al. Tumor-associated high endothelial venules mediate lymphocyte entry into tumors and predict response to PD-1 plus CTLA-4 combination immunotherapy. Cancer Cell. 2022.

34.   Liao S, Ruddle NH. Synchrony of high endothelial venules and lymphatic vessels revealed by immunization. J Immunol. 2006;177(5):3369-79.

35.   Hua Y, Vella G, Rambow F, Allen E, Antoranz Martinez A, Duhamel M, et al. Cancer immunotherapies transition endothelial cells into HEVs that generate TCF1(+) T lymphocyte niches through a feed-forward loop. Cancer Cell. 2022;40(12):1600-18.e10.

36.   Sellæg K, Schwienbacher R, Kranz M, Aamodt AE, Wirsing AM, Berge G, et al. 4-nitroquinoline 1-oxide-induced oral epithelial lesions exhibit time- and stage-dependent changes in the tumor immune microenvironment. Front Oncol. 2024;14:1343839.

37.   Hadler-Olsen E, Wetting HL, Rikardsen O, Steigen SE, Kanapathippillai P, Grénman R, et al. Stromal impact on tumor growth and lymphangiogenesis in human carcinoma xenografts. Virchows Arch. 2010;457(6):677-92.

38.   Bankhead P, Loughrey MB, Fernández JA, Dombrowski Y, McArt DG, Dunne PD, et al. QuPath: Open source software for digital pathology image analysis. Sci Rep. 2017;7(1):16878.

39.   Schindelin J, Arganda-Carreras I, Frise E, Kaynig V, Longair M, Pietzsch T, et al. Fiji: an open-source platform for biological-image analysis. Nat Methods. 2012;9(7):676-82.

40.   Stein DR, Hu X, McCorrister SJ, Westmacott GR, Plummer FA, Ball TB, et al. High pH reversed-phase chromatography as a superior fractionation scheme compared to off-gel isoelectric focusing for complex proteome analysis. Proteomics. 2013;13(20):2956-66.

41.   Dunn† JC. Well-Separated Clusters and Optimal Fuzzy Partitions. Journal of Cybernetics. 1974;4(1):95-104.

42.   Rousseeuw PJ. Silhouettes: A graphical aid to the interpretation and validation of cluster analysis. Journal of Computational and Applied Mathematics. 1987;20:53-65.

43.   Moussion C, Girard JP. Dendritic cells control lymphocyte entry to lymph nodes through high endothelial venules. Nature. 2011;479(7374):542-6.

44.   Peske JD, Thompson ED, Gemta L, Baylis RA, Fu YX, Engelhard VH. Effector lymphocyte-induced lymph node-like vasculature enables naive T-cell entry into tumours and enhanced anti-tumour immunity. Nat Commun. 2015;6:7114.

45.   Johansson-Percival A, He B, Li ZJ, Kjellén A, Russell K, Li J, et al. De novo induction of intratumoral lymphoid structures and vessel normalization enhances immunotherapy in resistant tumors. Nat Immunol. 2017;18(11):1207-17.

46.   Lacorre DA, Baekkevold ES, Garrido I, Brandtzaeg P, Haraldsen G, Amalric F, et al. Plasticity of endothelial cells: rapid dedifferentiation of freshly isolated high endothelial venule endothelial cells outside the lymphoid tissue microenvironment. Blood. 2004;103(11):4164-72.

47.   Browning JL, Allaire N, Ngam-Ek A, Notidis E, Hunt J, Perrin S, et al. Lymphotoxin-beta receptor signaling is required for the homeostatic control of HEV differentiation and function. Immunity. 2005;23(5):539-50.

48.   Onder L, Danuser R, Scandella E, Firner S, Chai Q, Hehlgans T, et al. Endothelial cell-specific lymphotoxin-β receptor signaling is critical for lymph node and high endothelial venule formation. J Exp Med. 2013;210(3):465-73.

49.   Cuff CA, Sacca R, Ruddle NH. Differential induction of adhesion molecule and chemokine expression by LTalpha3 and LTalphabeta in inflammation elucidates potential mechanisms of mesenteric and peripheral lymph node development. J Immunol. 1999;162(10):5965-72.

50.   Rodriguez AB, Parriott G, Engelhard VH. Tumor necrosis factor receptor regulation of peripheral node addressin biosynthetic components in tumor endothelial cells. Front Immunol. 2022;13:1009306.

51.   Madge LA, Kluger MS, Orange JS, May MJ. Lymphotoxin-alpha 1 beta 2 and LIGHT induce classical and noncanonical NF-kappa B-dependent proinflammatory gene expression in vascular endothelial cells. J Immunol. 2008;180(5):3467-77.

52.   He B, Jabouille A, Steri V, Johansson-Percival A, Michael IP, Kotamraju VR, et al. Vascular targeting of LIGHT normalizes blood vessels in primary brain cancer and induces intratumoural high endothelial venules. J Pathol. 2018;245(2):209-21.

53.   Mebius RE, Streeter PR, Michie S, Butcher EC, Weissman IL. A developmental switch in lymphocyte homing receptor and endothelial vascular addressin expression regulates lymphocyte homing and permits CD4+ CD3- cells to colonize lymph nodes. Proc Natl Acad Sci U S A. 1996;93(20):11019-24.

54.   Lee M, Kiefel H, LaJevic MD, Macauley MS, Kawashima H, O'Hara E, et al. Transcriptional programs of lymphoid tissue capillary and high endothelium reveal control mechanisms for lymphocyte homing. Nat Immunol. 2014;15(10):982-95.

55.   Bogoslowski A, Wijeyesinghe S, Lee WY, Chen CS, Alanani S, Jenne C, et al. Neutrophils Recirculate through Lymph Nodes to Survey Tissues for Pathogens. J Immunol. 2020;204(9):2552-61.

56.   Janatpour MJ, Hudak S, Sathe M, Sedgwick JD, McEvoy LM. Tumor necrosis factor-dependent segmental control of MIG expression by high endothelial venules in inflamed lymph nodes regulates monocyte recruitment. J Exp Med. 2001;194(9):1375-84.

57.   Menzel L, Zschummel M, Crowley T, Franke V, Grau M, Ulbricht C, et al. Lymphocyte access to lymphoma is impaired by high endothelial venule regression. Cell Rep. 2021;37(4):109878.

58.   Lu TT, Browning JL. Role of the Lymphotoxin/LIGHT System in the Development and Maintenance of Reticular Networks and Vasculature in Lymphoid Tissues. Front Immunol. 2014;5:47.

59.   Colbeck EJ, Jones E, Hindley JP, Smart K, Schulz R, Browne M, et al. Treg Depletion Licenses T Cell-Driven HEV Neogenesis and Promotes Tumor Destruction. Cancer Immunol Res. 2017;5(11):1005-15.

60.   Moutsopoulos NM, Konkel JE. Tissue-Specific Immunity at the Oral Mucosal Barrier. Trends Immunol. 2018;39(4):276-87.

61.   Cook-Mills JM, Gallagher JS, Feldbush TL. Isolation and characterization of high endothelial cell lines derived from mouse lymph nodes. In Vitro Cell Dev Biol Anim. 1996;32(3):167-77.

62.   Staton CA, Reed MW, Brown NJ. A critical analysis of current in vitro and in vivo angiogenesis assays. Int J Exp Pathol. 2009;90(3):195-221.

63.   Milutinovic S, Gallimore A. The link between T cell activation and development of functionally useful tumour-associated high endothelial venules. Discov Immunol. 2023;2(1):kyad006.

Figure legends

Figure 1. The colocalization of GlcNAc6ST-2 and PNAd was assessed in HEVs in human OSCC specimens and were denoted TA-HEVs (n=125) when they were located close to the tumor mass, and non-TA-HEVs when they were located at a distance from the tumor (n=130), often within minor salivary glands (n=83) **(A)**. The number of double positive (GlcNAc6ST-2+PNAd+) and single positive (GlcNAc6ST-2-PNAd) TA- or non-TA-HEVs and LN-HEVs was determined in human OSCC specimens (n=10) and normal human lymph node tissue (n=1), respectively, and is presented as percentage of the total number of HEVs for each group. The number of HEVs in each category is plotted within the bar of each group **(B)**. Representative images of GlcNAc6ST-2 (magenta) and PNAd (green) staining in LN-, TA-, and non-TA-HEVs (distant from the tumor and within salivary gland) from multi-color immunofluorescence-stained lymph node and tumor tissue are shown in **(C)**. Cell nuclei were stained with DAPI (blue). Scale bar indicates 20μm.

Figure 2. Graph shows the number of *Chst4+* punctate dots in individual PNAd+*Pecam1+* HEVs in tongue tissue from 4NQO-exposed mice (n=15) presenting with normal/hyperplastic epithelium, dysplasia, or SCC. Data is presented as log2(y+1). Statistical differences were calculated by Kruskal-Wallis test (ns; non-significant P>0.05). Median values are presented as horizontal lines and whiskers represent interquartile range **(A)**. Representative images of HEVs in normal/hyperplasia, dysplasia or SCC tongue tissue stained for *Pecam1* mRNA (red), PNAd (green), *Chst4* mRNA (magenta) **(B)**. SCC images in **(B)** and **(C)** shows HEVs with positive and negative *Chst4* mRNA staining, respectively. The left and right arrowheads (white) in **(C)** indicates the two HEVs represented in the left and right inserts below, respectively. Cell nuclei were stained with DAPI (blue). Scale bar indicates 20μm and 5μm (insert).

Figure 3. The number of DAPI+ cells/μm surrounding individual LN-HEVs (n=210) in human lymph node tissue (n=1) and TA-HEVs (n=125) and non-TA-HEVs (=130) in OSCC specimens (n=10) **(A)**, and the number of DAPI+ cells/μm surrounding single- (GlcNAc6ST-2-PNAd+) and double-positive

(GlcNAc6ST-2+PNAd+) LN-, TA-, and non-TA-HEVs **(B)**. Statistical differences were calculated by Kruskal-Wallis test with **(A)** or without **(B)** *post hoc* Dunn's test (ns; non-significant P>0.05). Dotted line in **(B)** indicates that the pairwise comparison does not apply for the respective group. Error bars indicate median with interquartile range.

Figure 4. The presence of CD11c+ cells (brown) within 45μm of PNAd+ HEVs (violet) in the tongue of 4NQO-exposed mice (n=30) or normal lymph nodes (n=5) was scored as sparse, moderate, or dense **(A)**. Representative image of CD11c+ cells and PNAd+ HEVs in normal mouse lymph node **(B)**. Arrowheads (black) indicates PNAd+ HEVs in tongue tissue. Scale bar indicates 50μm.

Figure 5. The presence of HEVs (PNAd) in human xenograft tongue tumors **(A)** and lymph nodes **(B)** in immunocompromised mice (n=5) was determined. Representative image of HEVs in the lymph node of immune competent mice **(C)**. Scale bar indicates 50μm (**(A)** top, and **(B)** top/bottom right), 100μm (**(B)** top/bottom right), or 200μm (**(A)** bottom).

Figure 6. RT-qPCR data showing the fold change of *Fut4, B3gnt3,* and *Chst2* in bEnd.3 cells seeded on Matrigel or as monolayer and stimulated with 200 or 1000ng/mL LIGHT, LTα1β2, or TNFα, or unstimulated. Each point represents the mean or median for each condition on Matrigel or monolayer and is based on three independent experiments. Error bars indicate median with interquartile range (*Fut4*) or mean with SD (*B3gnt3* and *Chst2*), and statistical differences were calculated by Wilcoxon signed-rank test or paired T-rest, respectively **(A)**. The fold change of *Fut4* **(B)**, *B3gnt3* **(C)** and *Chst2* **(D)** was determined for each condition and the bars represent the mean of three independent experiments. Standard deviation is indicated by whiskers. Statistical differences between ΔCt values were calculated by One-way ANOVA with **(B)** or without **(C and D)** Tukey's test (ns; non-significant P>0.05).
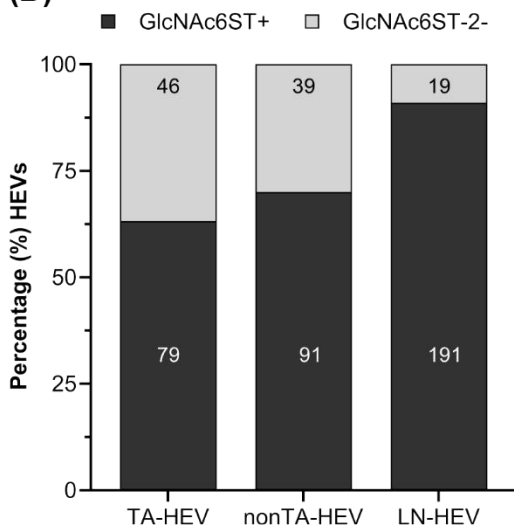
Fig.7. Heatmap representing the scaled protein expression patterns in OSCC patient tumor tissues in patient cluster 1 (n=28) and cluster 2 (n=51). The top annotation displays the HEV-score in the patient tumors as HEV-high or HEV-low **(A)**. Barplot showing the distribution of HEV-high and HEV-low tumors/patients from the heatmap patient clusters as seen in (A) **(B)**. Enriched Hallmarks Between HEV-high Associated Patients. Tile plot represents the normalized enrichment score (NES) from the GSEA of each of the three conditions, HEV-high vs HEV-low All Patients, HEV-high vs HEV-low Cluster 1 and HEV-high vs HEV-low Cluster 2. The higher the NES value the more enriched the Hallmarks are, and only the enriched Hallmarks associated with HEV-high patients from all three conditions are included in the figure. The tiles are ordered according whether the Hallmarks are shared between all conditions, between two of the three conditions or only present in one of the conditions **(C)**. Venn-diagram illustrating the shared hallmarks between the three conditions as seen in (C). Red represents HEV-high all patients, blue represents HEV-high cluster 1, and green represents HEV-high cluster 2 **(D)**. A protein-protein interaction network was created with the STRING database. The input are proteins in she shared Hallmarks between all conditions as seen in (C). Duplicated genes were removed. The colors between each node represent the evidence for the interaction; turquoise and purple represent known interactions from curated databases or experimentally determined, green or blue represent predicted interactions from gene neighborhood, gene fusion or gene co-occurrence, respectively. Light green, black, or light blue represent predicted interactions through text mining, co-expression or protein homology. An interactive presentation of the STRING network can be found here: [21 items (human) - STRING interaction network (string-db.org)](string-db.org) **(E)**.
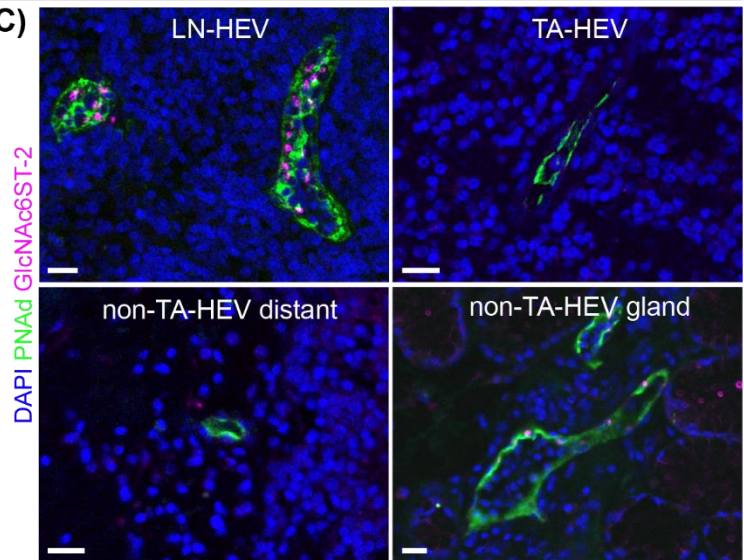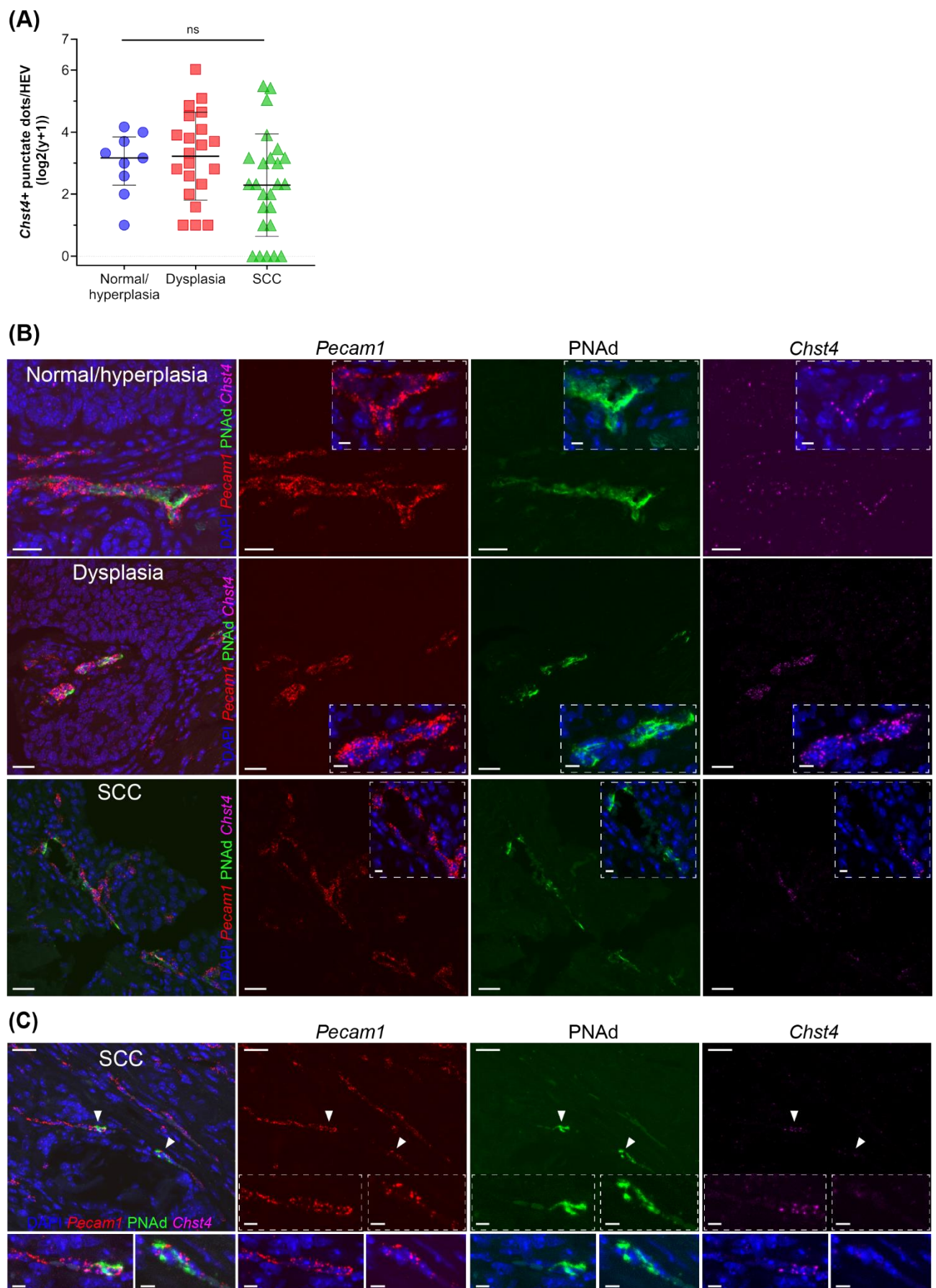
Figure 1

(A)

○ TA-HEV, n=125
○ non TA-HEV, n=130

(B)

(C)

Figure 2

Figure 3

(A)

(B)

Figure 4

(A)

Tongue

Sparse   Moderate   Dense

(B)

Lymph node

Figure 5

(A) Xenograft tumor

(B) Immune deficient

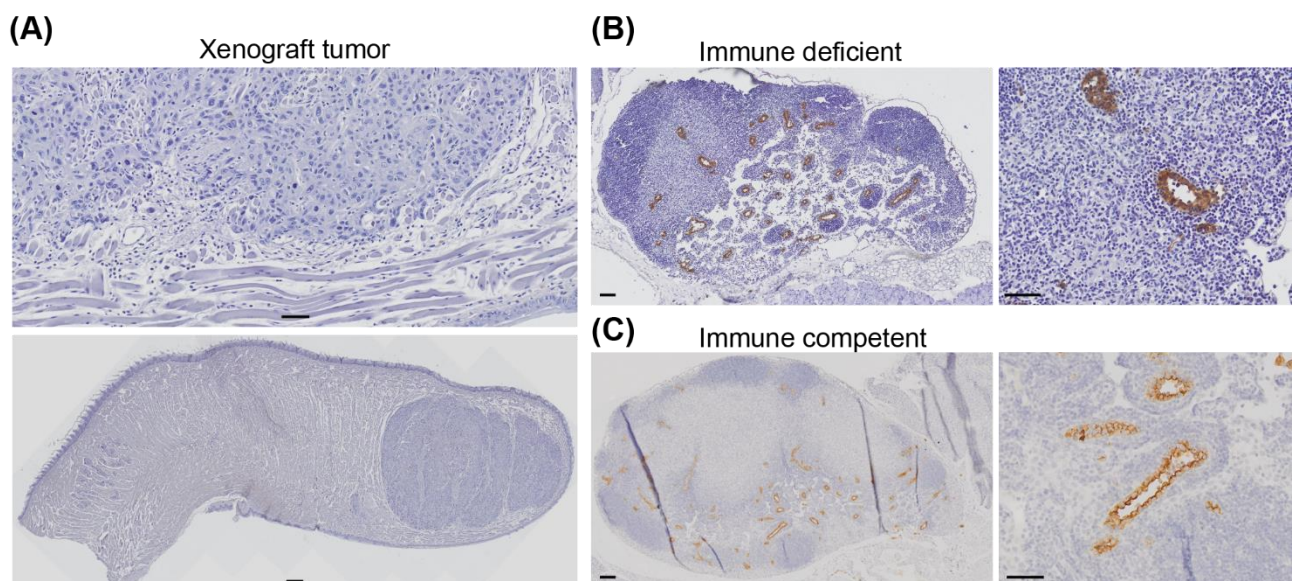**(C)** Immune competent
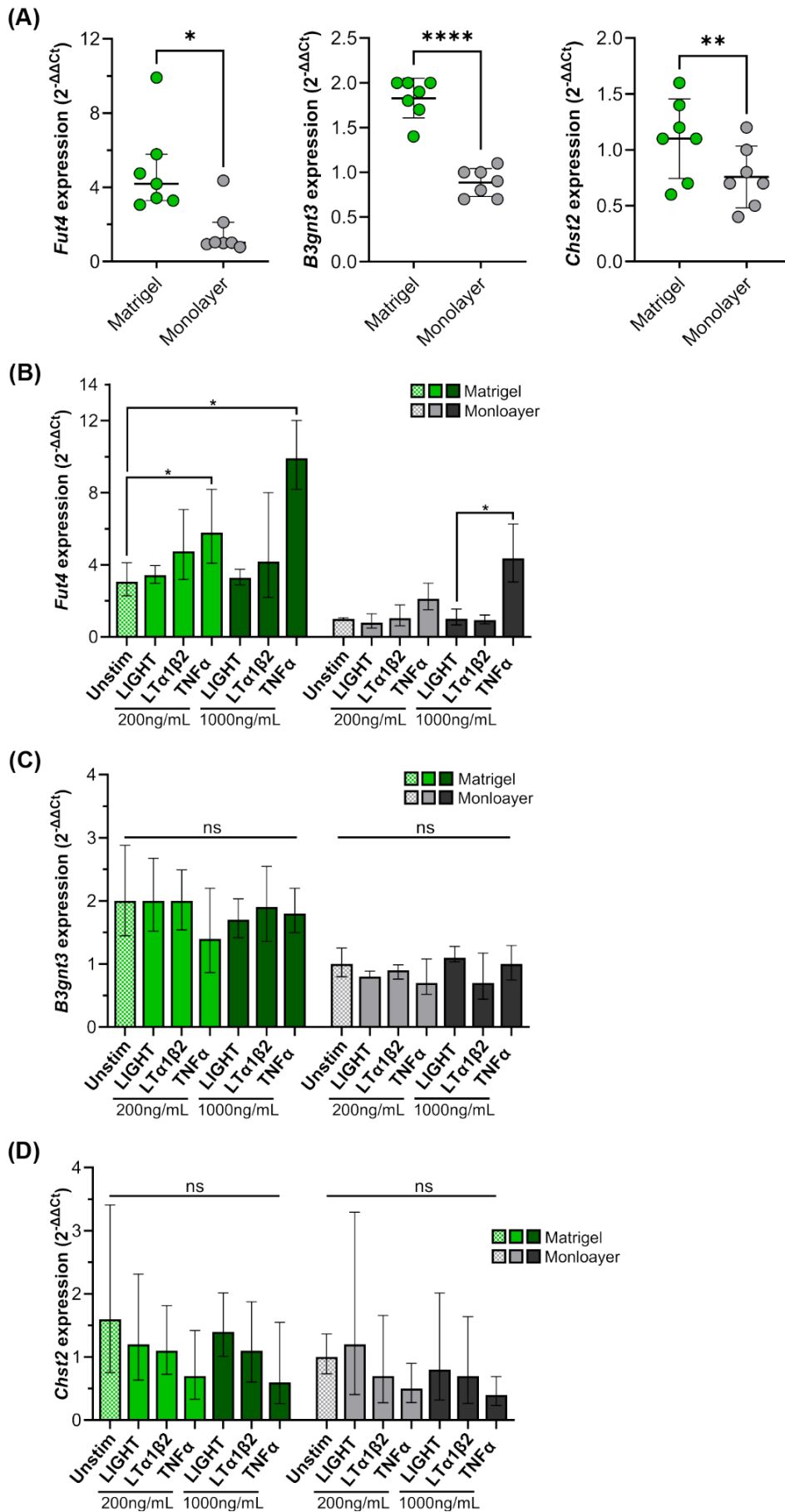
Figure 6
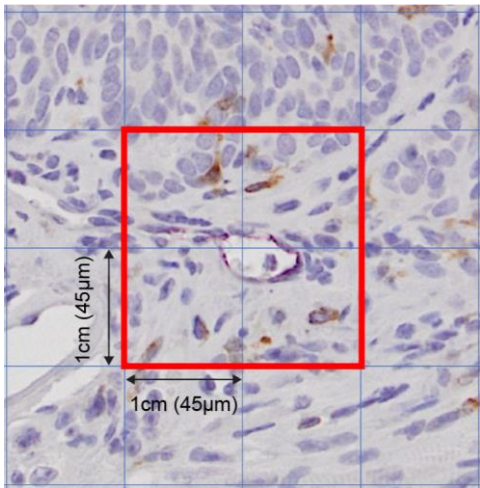
(A)

(B)

(C)

(D)
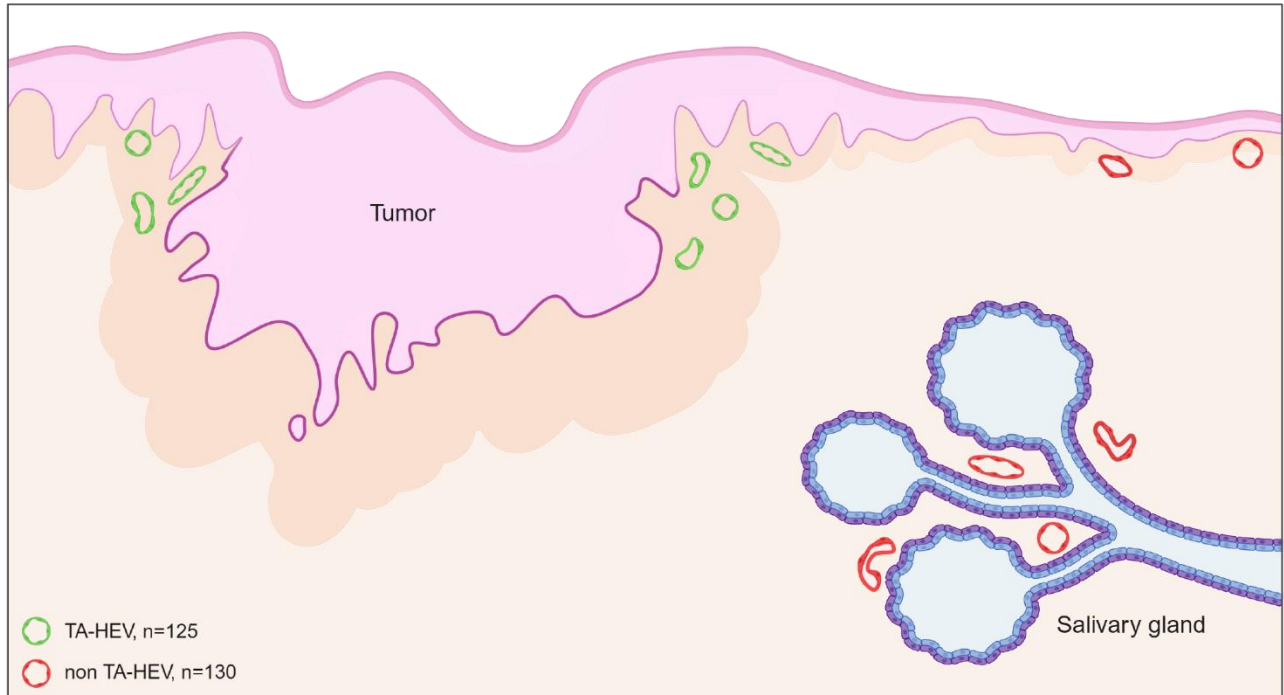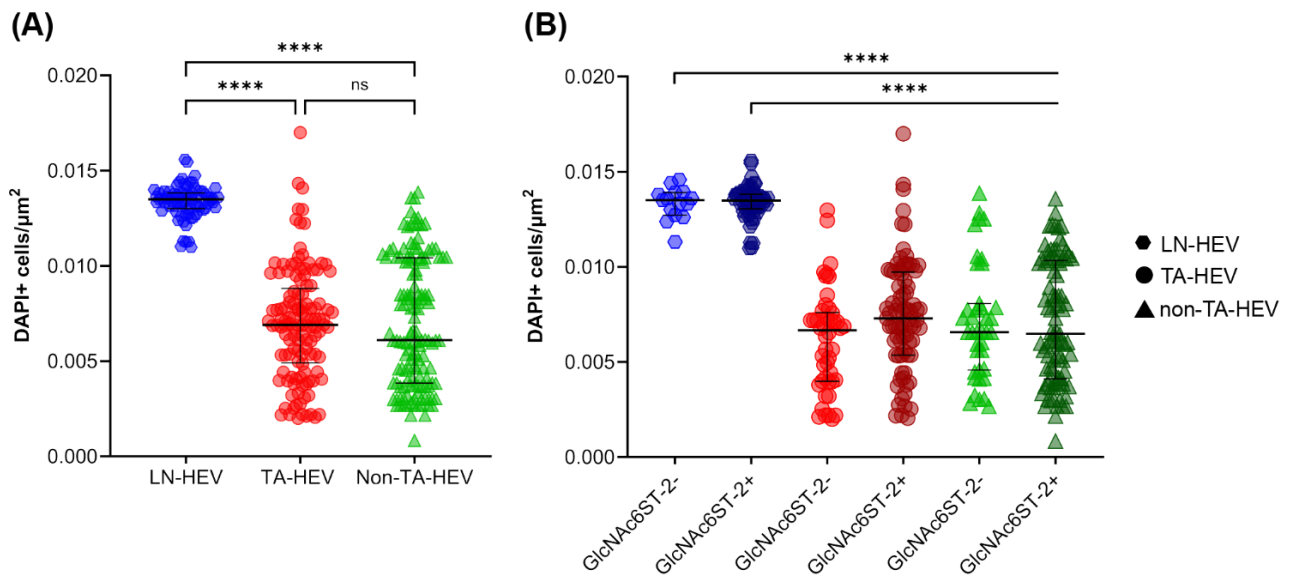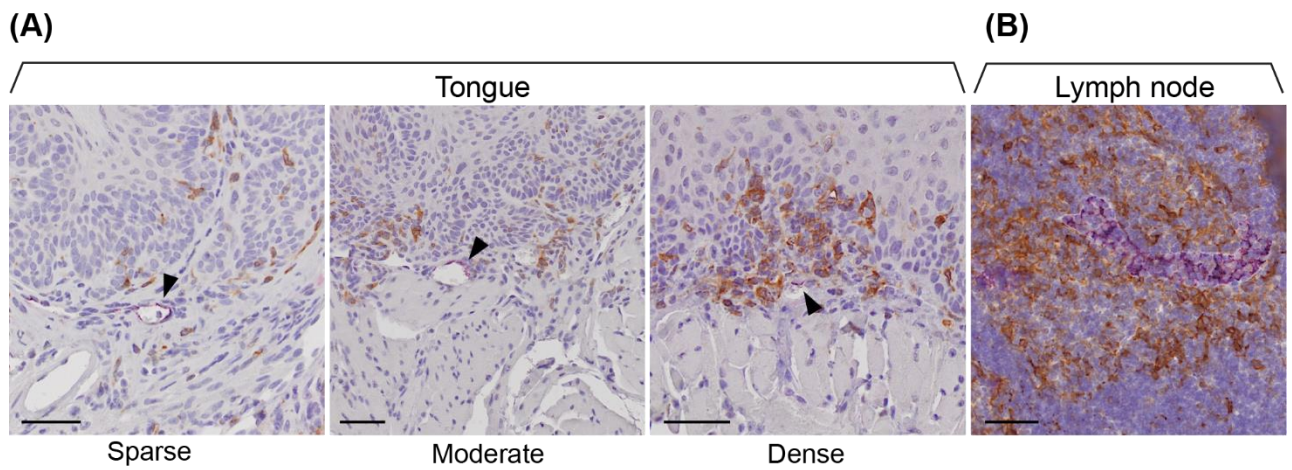
Figure 7
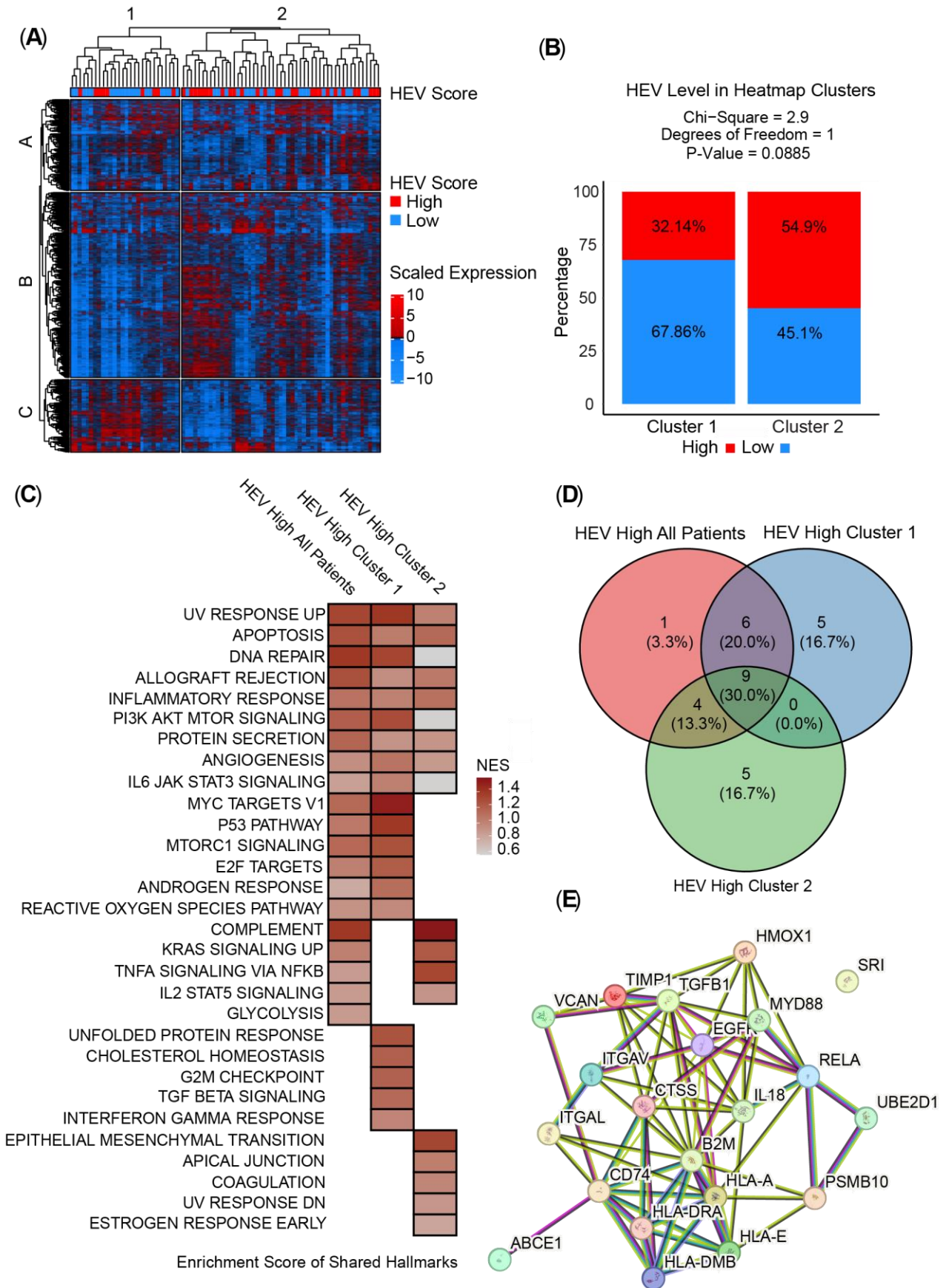
Tables

Table 1: CD11c density surrounding HEVs associated with different histological grade

| Histologic grade	Total N	CD11c density			
		Negative % (n)	Sparse % (n)	Moderate % (n)	Dense % (n)
Normal/hyperplasia	13	0.0 (0)	84.6 (11)	15.4 (2)	0.0 (0)
Dysplasia	37	0.0 (0)	75.7 (28)	21.9 (7)	6.3 (2)
SCC	26	3.8 (1)	53.8 (14)	34.6 (9)	7.4 (2)

Supplementary material
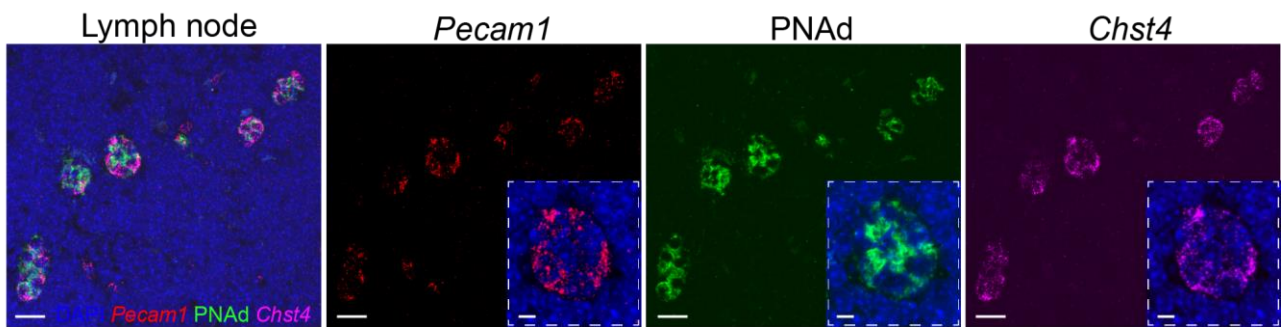
Supplementary figures

Supplementary figure S1. The density of CD11c+ cells (brown) around PNAd+ HEVs (violet) in mouse tongue tissue was assessed within four 1x1cm (45x45µm) squares centered on individual HEVs in mouse tongue tissues.
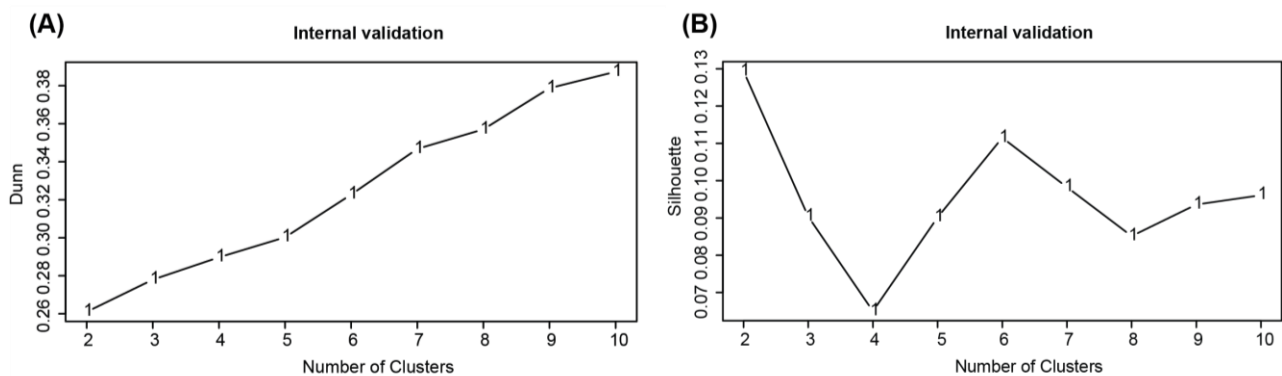

Supplementary fig S2. Internal validation of clustering was performed using the Dunn Index **(A)** and Silhouette width **(B)** showing that two clusters was the most optimal by the maximum value in **(B)**.
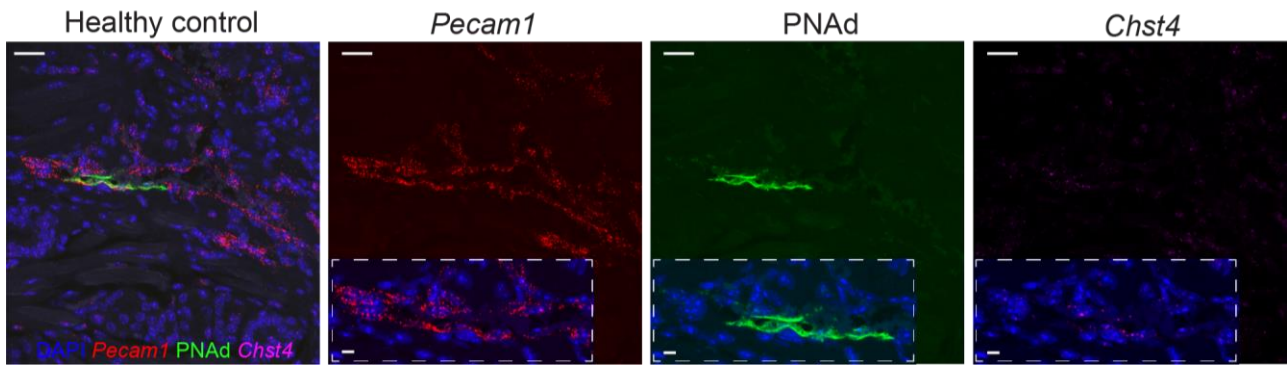
Supplementary fig S3. Representative image of *Pecam1+* (red), PNAd+, (green) and *Chst4+* (magenta) HEV in the tongue of a healthy control mouse. Cell nuclei were stained with DAPI (blue). Scale bar indicates 20µm and 5µm (insert).


Supplementary fig S4. Representative image of *Pecam1+* (red), PNAd+, (green) and *Chst4+* (magenta) HEV in normal mouse lymph node. Cell nuclei were stained with DAPI (blue). Scale bar indicates 20µm and 5µm (insert).
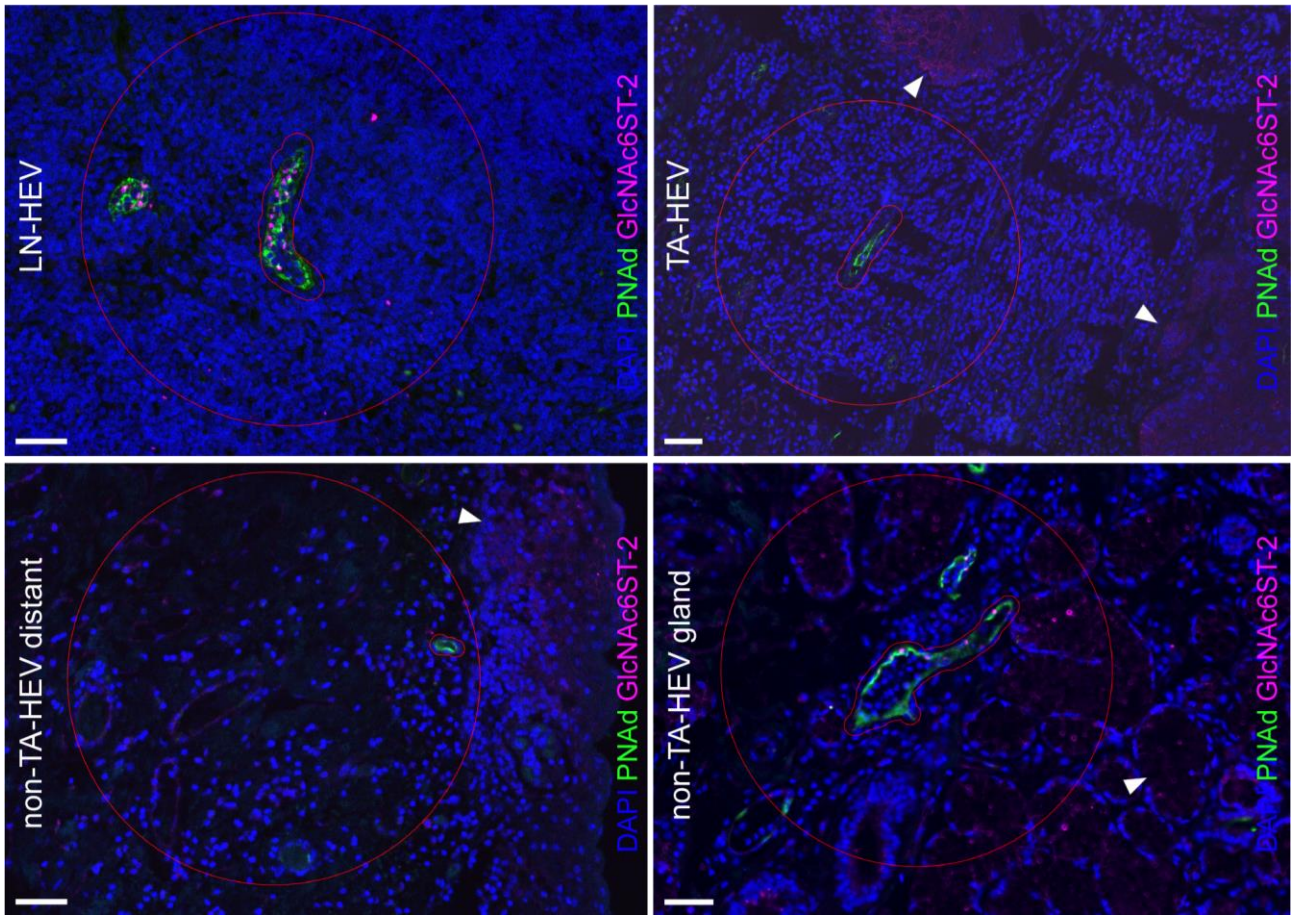
Supplementary fig S5. An annotation (400x400µm circle; 125664µm^2) centered on individual HEVs was used for automatic cell detection in QuPath of the number of DAPI+ cells surrounding LN-HEVs in normal human lymph node and TA- and non-TA-HEVs in OSCC tissue. The annotation was placed off-center to the HEV in cases there the HEVs were located close to epithelium (bottom left). Scale bar indicates 50µm.

(A)

(B)
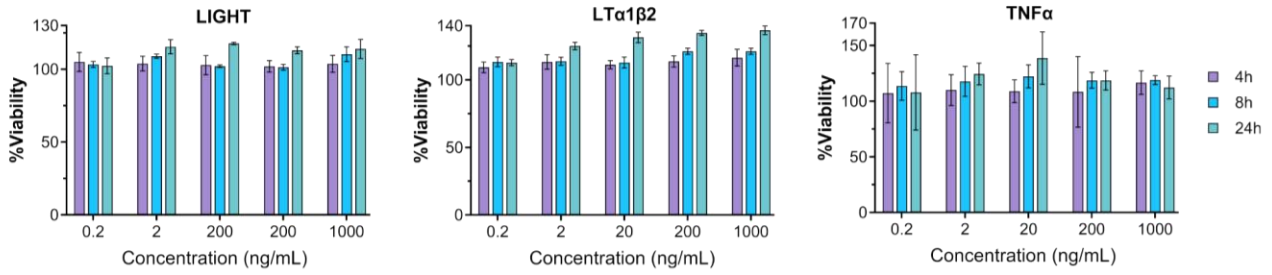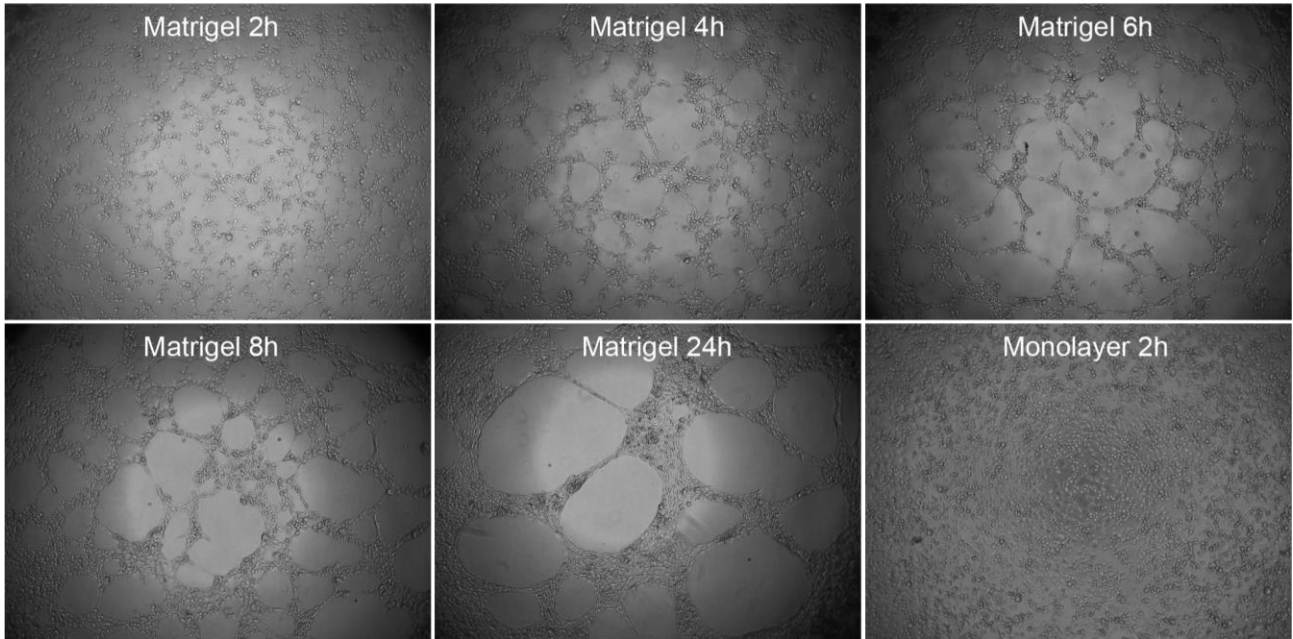
Supplementary figure S6. Viability of bEnd.3 cells after stimulation with 0.2, 2, 20, 200, and 1000ng/mL LIGHT-, LTα1β2-, or TNFα was determined by MTS assay. Bars represent the means from three independent experiments and the whiskers represents the standard deviation **(A)**. Tube formation assay was performed by seeding of bEnd.3 cells (6×10^4/well) on Matrigel. Shown are representative images of unstimulated bEnd.3 cells seeded on Matrigel for 2, 4, 6, 8, and 24 hours and unstimulated cells seeded as monolayer for 8 hours. Images were captured with 5X or 10X objectives on an inverted light microscope **(B).**

Enrichment Score of Hallmarks Between Patient Clusters
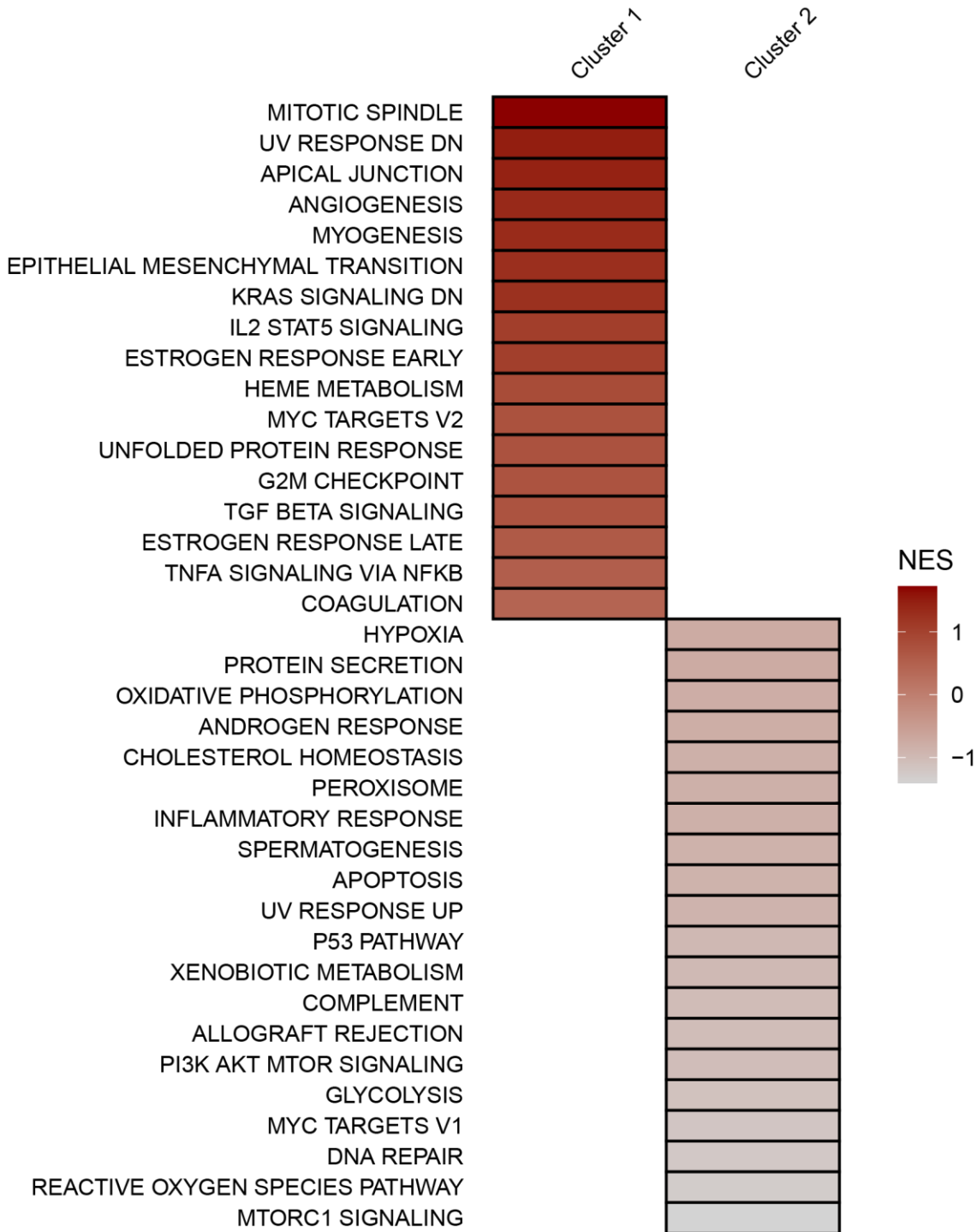
Supplementary figure S7. Enriched Hallmarks in Patient Clusters. Tile plot represents the normalized enrichment score (NES) from the GSEA. The positive or negative values are used to distinguish the groups. Patient Cluster 1 is associated with a positive NES (red,0 to 1), 1 indicating the highest enrichment within Cluster 1. Patient Cluster 2 is associated with a negative NES score (grey,0 to -1), -1 indicating the highest enrichment within Cluster 2.
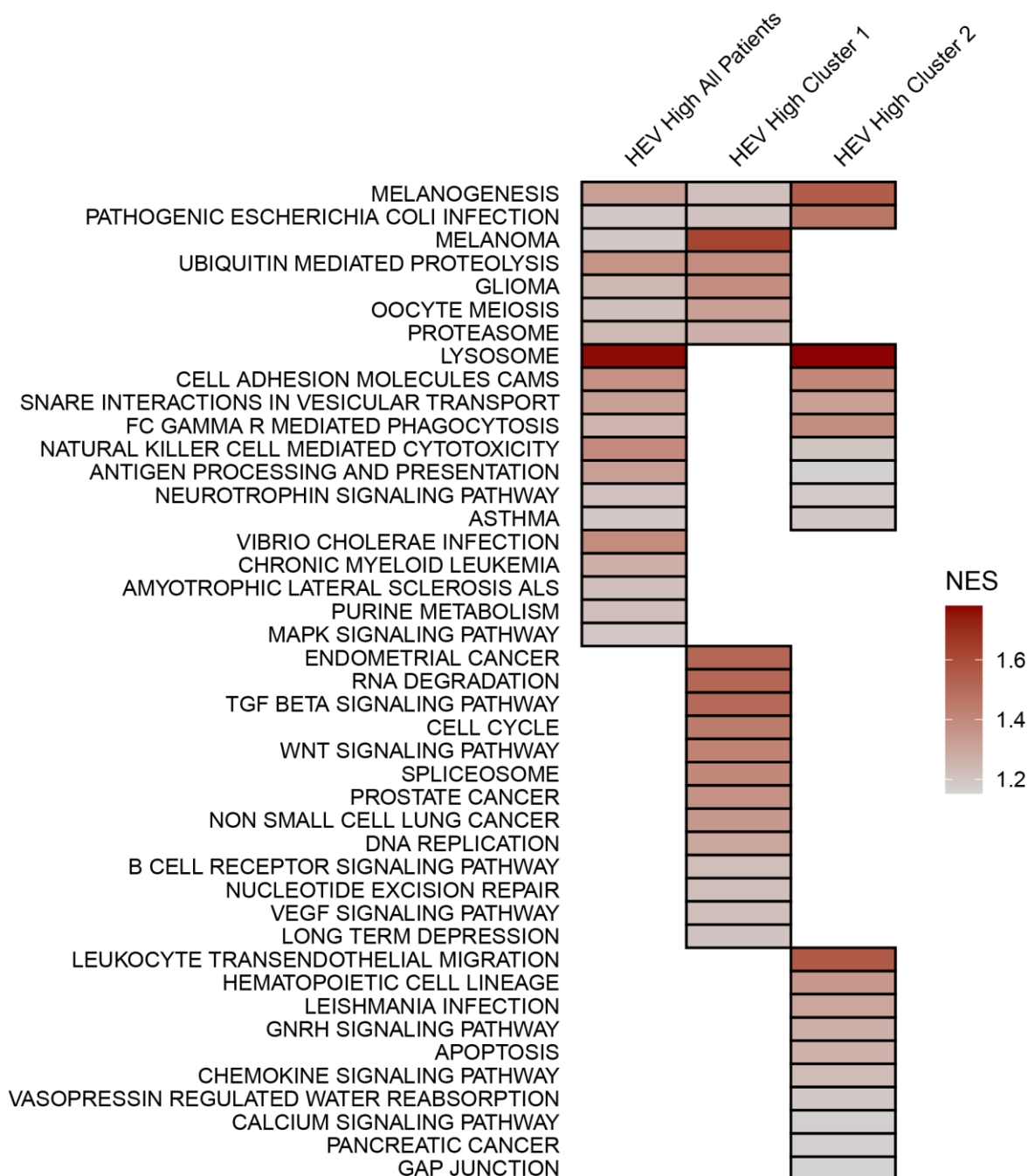
Supplementary figure S8. Enriched KEGG pathways between HEV-high patients. Tile plot represents the normalized enrichment score (NES) from the GSEA of each of the three conditions, HEV-high vs HEV-low All Patients, HEV-high vs HEV-low Cluster 1 and HEV-high vs HEV-low Cluster 2. The higher the NES value the more enriched the KEGG pathways are, and only the enriched KEGG pathways associated with HEV-high patients from all three conditions are included in the figure. The tiles are ordered according whether the KEGG pathways are shared between, all conditions, between two of the three conditions or only present in one of the conditions.
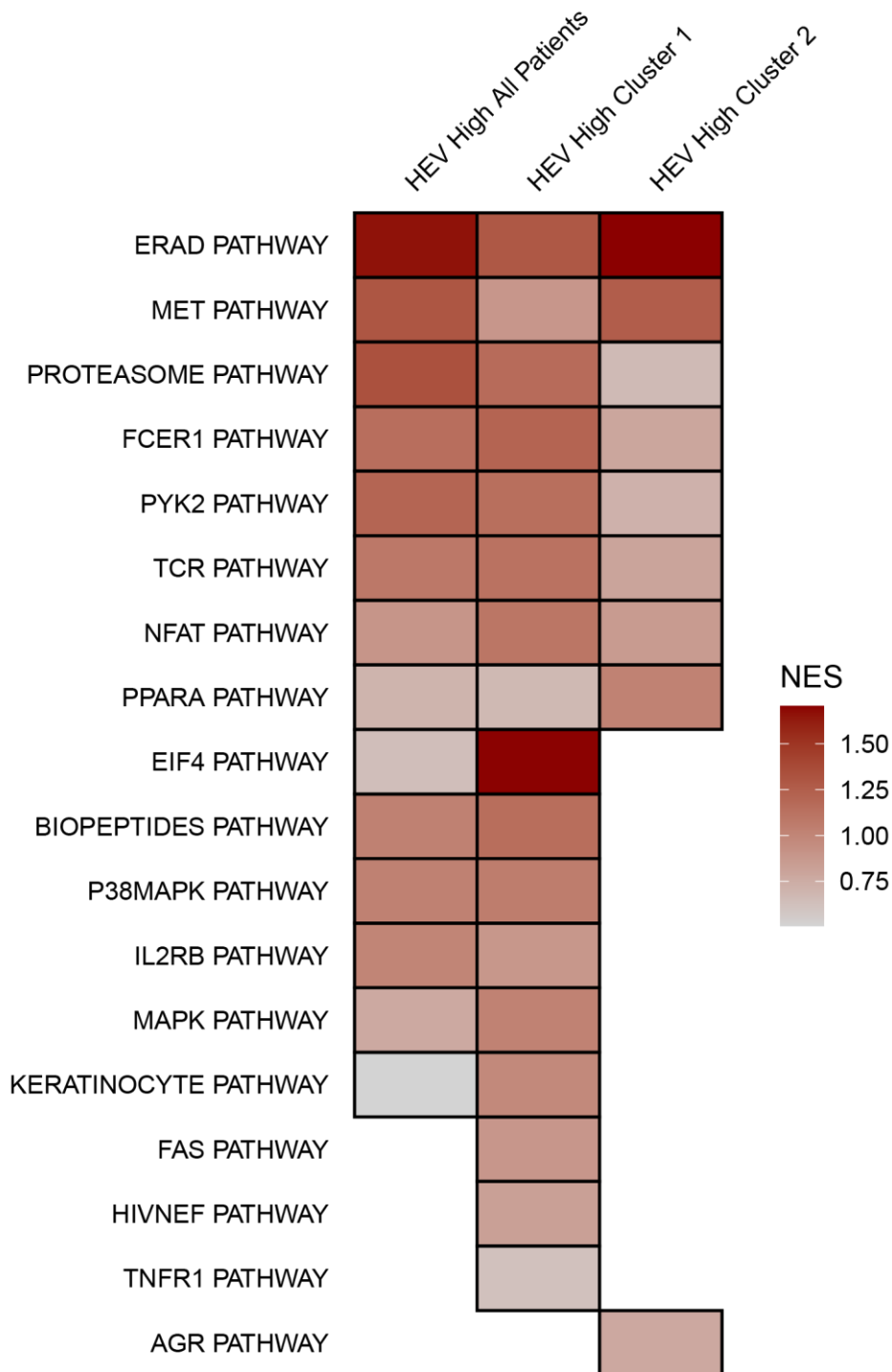
Supplementary figure S9. Enriched BioCarta pathways between HEV-high patients. Tile plot represents the normalized enrichment score (NES) from the GSEA of each of the three conditions, HEV-high vs HEV-low All Patients, HEV-high vs HEV-low Cluster 1 and HEV-high vs HEV-low Cluster 2. The higher the NES value the more enriched the BioCarta pathways are, and only the enriched BioCarta pathways associated with HEV-high patients from all three conditions are included in the figure. The tiles are ordered according whether the BioCarta pathways are shared between, all conditions, between two of the three conditions or only present in one of the conditions.

Supplementary tables

Supplementary table S1. Specification for multi-color immunofluorescence staining of human OSCC tissue

Target)/primary antibody/clone	Antigen retrieval	Dilution	Incubation time (minutes)	Secondary antibody	Dilution
GlcNAc6ST-2/Rabbit anti-CHST4 antibody/polyclonal[a]	Sodium citrate (pH 6.0)	1:50	ON	Goat anti-rabbit IgG Alexa Fluor 647[c]	1:300
Rat anti-mouse/human PNAd antibody/MECA-79[b]	Sodium citrate (pH 6.0)	1:25	60	Donkey anti-rat IgG Alexa Fluor 488[c]	1:300

[a]Merck, Darmstadt, Germany, [b]Biolegend, San Diego, California, US, [c]Thermo Fisher Scientific, Waltham, Massachusetts, US

Supplementary table S2. Specification of the methods used for staining of mouse tissue

Method	Probe or primary antibody/clone	Antigen retrieval	Peroxidase block	Serum block	Dilution	Incubation time (minutes)	Signal development/ secondary antibody (dilution)
RNAScope/ IF	*Chst4* mRNA/ RNAScope Mm-*Chst4* probe[a]	RNAScope target retrieval buffer	RNAScope H2O2 block		Ready-to-use	120	HRP-C1, Opal 650 (1:1000)
	PeCAM-1 mRNA/ RNAScope Mm-*PeCAM-1*-C2 probe[a]	RNAScope target retrieval buffer	RNAScope H2O2 block		1:50	120	HRP-C2, Opal 570 (1:1500)
	Rat anti-mouse/human PNAd antibody/MECA-79[b]	RNAScope target retrieval buffer	RNAScope H2O2 block	10% normal goat serum	1:25	30	HRP goat anti-rat secondary antibody (1:200), Opal 520 (1:1000)
Dual IHC	Rabbit anti-CD11c[c]	Sodium citrate (pH 6.0) with 0.05% Tween-20	3% H2O2	5% normal goat serum	1:300	ON	ImmPRESS HRP goat anti-rabbit secondary antibody
	Rat anti-mouse/human PNAd antibody/MECA-79[b]	Sodium citrate (pH 6.0) with 0.05% Tween-20	3% H2O2	5% and 2.5% normal goat serum	1:25	30	ImmPRESS HRP goat anti-rat secondary antibody
IHC	Rat anti-mouse/human PNAd antibody/MECA-79[b]		3% H2O2	2.5% normal goat serum	1:25	30	HRP goat anti-rat secondary antibody (1:200)

[a]Advanced Cell Diagnostics, Minneapolis, Minnesota, US, [b]Biolegend, San Diego, California, US, [c]Cell Signaling Technology, Danvers, Massachusetts, US

Supplementary table S3. RNAScope probes

Probe	Target region	Accession number
Mm-Chst4	491-1446	NM_011998.4
Mm-PeCAM-1-C2	915-1827	NM_001032378.1

Supplementary table S4. qPCR primer sequences

Gene	Forward primer sequence	Reverse primer sequence
ActB	AGCCTTCCTTCTTGGGTATGGA	GCATAGAGGTCTTTACGGATGTCAA
B3gnt3	AGCTGGAAGCGCAGAAATACG	GGTTAGCTGCCACTCCAGGAA
Chst2	GTGCAAAAAGTGCCCACCTC	CCAACACAGCCACATCGAAGA
Chst4	AAGAAAGGGAGGCTGCTGATG	TGGACTCCTCCCTCTGGGAA
Fut4	GGAGGGAGCAGTGACGCTAA	GTATGGGAGGGCGATTCGA
Fut7	TACCCTTACTTGCCCCGCA	ACATCAGTCTCCCACCCATCC
Gcnt1	ACTAAGGCCGTTGCTAAGCCC	CCAGAATGCCACCACCTGAG
Hprt	AAGACTTGCTCGAGATGTCATGAAG	CCAGCAGGTCAGCAAAGAACTTATA
Ppia	TGGGAAGGTGAAAGAAGGCAT	TGTCCACAGTCGGAAATGGTG

Supplementary table S5. Clinicopathological parameters proteomics patients

	High (N=37)	Low (N=42)	p-value	Overall (N=79)
Gender			0.745^{ns}	
Female	11 (29.7%)	15 (35.7%)		26 (32.9%)
Male	26 (70.3%)	27 (64.3%)		53 (67.1%)
Age at diagnosis (years)			0.595^{ns}	
Mean (SD)	62.5 (14.0)	64.1 (13.3)		63.3 (13.5)
T Status			0.184^{ns}	
T1	9 (24.3%)	18 (42.9%)		27 (34.2%)
T2	18 (48.6%)	18 (42.9%)		36 (45.6%)
T3	10 (27.0%)	6 (14.3%)		16 (20.3%)
T4	0 (0%)	0 (0%)		0 (0%)
N Status			0.334^{ns}	
N0	33 (89.2%)	33 (78.6%)		66 (83.5%)
N+	4 (10.8%)	9 (21.4%)		13 (16.5%)
Stage			0.101^{ns}	
Stage I	8 (21.6%)	17 (40.5%)		25 (31.6%)
Stage II	17 (45.9%)	13 (31.0%)		30 (38.0%)
Stage III	9 (24.3%)	5 (11.9%)		14 (17.7%)
Stage IV	3 (8.1%)	7 (16.7%)		10 (12.7%)
Smoking			0.0865^{ns}	
Current	16 (47.1%)	13 (32.5%)		29 (39.2%)
Former	13 (38.2%)	12 (30.0%)		25 (33.8%)
Never	5 (14.7%)	15 (37.5%)		20 (27.0%)
Missing	3 (8.1%)	2 (4.8%)		5 (6.3%)
Alcohol			0.00281^{**}	
Current	21 (100%)	19 (65.5%)		40 (80.0%)
Never	0 (0%)	10 (34.5%)		10 (20.0%)
Missing	16 (43.2%)	13 (31.0%)		29 (36.7%)
5-Year DSS			1^{ns}	
Alive	19 (59.4%)	21 (60.0%)		40 (59.7%)
Dead of disease	13 (40.6%)	14 (40.0%)		27 (40.3%)
Missing	5 (13.5%)	7 (16.7%)		12 (15.2%)

T-Equal = T.Test with Equal Variance Chi-Squared Test Fisher`s Exact Test ns= Not Significant SD = Standard Deviation DSS = Death Specific Survival

<0.0001 = **** <0.001 = *** <0.01 = ** <=0.05 = *

Supplementary table S6. Twenty-two common proteins expressed in HEV-high tumors from the shared hallmarks allograft rejection, inflammatory response, IL-6 JAK STAT, and angiogenesis

Angiogenesis	Allograft rejection	Inflammatory response	IL-6 JAK STAT
TIMP1	IL18	SRI	HMOX1
VCAN	CTSS	RELA	TGFB1
ITGAV	HLA-DRA		MYD88
	CD74		
	B2M		
	TGFB1		
	HLA-E		
	PSMB10		
	HLA-A		
	UBE2D1		
	HLA-DMB		
	ABCE1		
	ITGAL		
	EGFR		

Supplementary table S7. Cellular component and Molecular function Gene Ontology (GO) terms enriched in the STRING network.

Cellular component				
GO-term	**Description**	**Count in network[1]**	**Strength[2]**	**False discovery rate[3]**
GO:0042612	MHC class I protein complex	3 of 8	2.55	2.16e-05
GO:0042611	MHC protein complex	6 of 24	2.37	7.96e-10
GO:0042613	MHC class II protein complex	4 of 17	2.34	2.83e-06
GO:0042824	MHC class I peptide loading complex	2 of 9	2.32	0.0026
GO:0071556	Integral component of lumenal side of endoplasmic reticulum membrane	4 of 26	2.16	8.73e-06
Molecular function				
GO-term	**Description**	**Count in network[1]**	**Strength[2]**	**False discovery rate[3]**
GO:0042608	T cell receptor binding	3 of 10	2.45	0.00029
GO:0030881	beta-2-microglobulin binding	2 of 7	2.43	0.0212
GO:0023026	MHC class II protein complex binding	4 of 26	2.16	6.31e-05
GO:0042605	Peptide antigen binding	3 of 24	2.07	0.0021
GO:0003823	Antigen binding	4 of 71	1.72	0.00090

[1]The first number indicates how many proteins in the network that are annotated with a particular term and the second number indicates how many proteins in total in the network (and in the background) have this term assigned. [2]Measure of how large the enrichment effect is (log10). [3]P-values corrected for multiple testing within each category (21 items (human) - STRING interaction network (string-db.org)).